Springer Theses
Recognizing Outstanding Ph.D. Research

Holger Schmeckebier

Quantum-Dot-Based Semiconductor Optical Amplifiers for O-Band Optical Communication

Springer

Springer Theses

Recognizing Outstanding Ph.D. Research

Aims and Scope

The series "Springer Theses" brings together a selection of the very best Ph.D. theses from around the world and across the physical sciences. Nominated and endorsed by two recognized specialists, each published volume has been selected for its scientific excellence and the high impact of its contents for the pertinent field of research. For greater accessibility to non-specialists, the published versions include an extended introduction, as well as a foreword by the student's supervisor explaining the special relevance of the work for the field. As a whole, the series will provide a valuable resource both for newcomers to the research fields described, and for other scientists seeking detailed background information on special questions. Finally, it provides an accredited documentation of the valuable contributions made by today's younger generation of scientists.

Theses are accepted into the series by invited nomination only and must fulfill all of the following criteria

- They must be written in good English.
- The topic should fall within the confines of Chemistry, Physics, Earth Sciences, Engineering and related interdisciplinary fields such as Materials, Nanoscience, Chemical Engineering, Complex Systems and Biophysics.
- The work reported in the thesis must represent a significant scientific advance.
- If the thesis includes previously published material, permission to reproduce this must be gained from the respective copyright holder.
- They must have been examined and passed during the 12 months prior to nomination.
- Each thesis should include a foreword by the supervisor outlining the significance of its content.
- The theses should have a clearly defined structure including an introduction accessible to scientists not expert in that particular field.

More information about this series at http://www.springer.com/series/8790

Holger Schmeckebier

Quantum-Dot-Based Semiconductor Optical Amplifiers for O-Band Optical Communication

Doctoral Thesis accepted by
the Technical University of Berlin, Germany

Springer

Author
Dr. Holger Schmeckebier
Institute of Solid State Physics
Technical University of Berlin
Berlin
Germany

Supervisor
Prof. Dieter Bimberg
Institute of Solid State Physics
Technical University of Berlin
Berlin
Germany

Zugl.: Berlin, Technische Universität, Diss., 2016

ISSN 2190-5053 ISSN 2190-5061 (electronic)
Springer Theses
ISBN 978-3-319-44274-7 ISBN 978-3-319-44275-4 (eBook)
DOI 10.1007/978-3-319-44275-4

Library of Congress Control Number: 2016949569

Printed on acid-free paper

This Springer imprint is published by Springer Nature
The registered company is Springer International Publishing AG
The registered company address is: Gewerbestrasse 11, 6330 Cham, Switzerland

Supervisor's Foreword

Next to the invention of printing by Gutenberg, there is probably no technology that has changed the way of life for human beings as much as the Internet. Our books are now in the cloud; our home movies and videos are stored in the cloud; our Brockhaus or Encyclopaedia Britannica is now called Wikepedia; and with the rise in online dating, we often even meet our future partners first in the cloud. All that and more is based around the Internet, which allows instantaneous communication at the speed of light, from everybody to everywhere. In 2017, three times more devices will be connected to the Internet than there will be people living on earth. In addition, the consumption of electrical energy by the internet has increased rapidly: in 2015, 6 % of the raw electricity production in the USA was used to power its Internet. The number of fundamental changes to our social and economic life based on the Internet seem unlikely to end in the foreseeable future. Remote health control of individuals is just one of many such examples. To date, two Nobel Prizes have been bestowed upon those who paved the way through their discoveries, inventions, and developments of the so-called physical layer enabling the Internet Zh. I. Alferov and H. Kroemer for semiconductor lasers and C. K. Kao for glass fibers.

Everything started in the second half of the last century with the development of active optical cables spanning the continents. The invention and further development of a few photonic devices that convert electrical pulses to optical ones or vice versa and amplify them, paved the way for the internet, made the dreams possible. The proposal of the double-heterostructure semiconductor laser by Alferov and Kroemer and its room temperature realization by Alferov in 1970 was the first step. Low-noise erbium-doped fiber amplifiers (EDFAs), and InGaAs/InP p-i-n diodes were the other essential and already conclusive prerequisites for the replacement of copper by glass for long distance communication and the deployment of the first continental and intercontinental cables enabling the wide area networks (WANs), bridging thousands of kilometres. Usually semiconductor lasers are in the limelight of the public as the enabling devices and stand in the limelight of the public. However, each of these active cables has many more EDFAs than emitters or receivers. The reason for the little attention that EDFAs receive might be

due to the fact that they are not single devices that are easy to explain, but rather they are complex modules consisting of passive and active optical elements, and are expensive to produce.

Ultrahigh speed/bit rate access to the home at Gbit/s levels will be the next step with the largest social and economic impact for the consumer. Quantum leaps in the properties of the metropolitan area and access networks will be necessary; simple improvements and extensions will not be sufficient. Novel device technologies and materials for photonic devices are needed. Wavelength windows different from those used for WANs will also be exploited in the future. The O-band, spanning the wavelength range 1260–1360 nm is of paramount importance. Again, amplifiers that act both in the linear amplifying regimes as well as functioning as nonlinear optical devices, such as wavelength converters, are needed at these much shorter distances. They must be simple, low cost, reliable, low power, temperature-stable and versatile. EDFAs do not operate in the O-band. Other rare element based amplifiers do not cover the whole O-band and are prohibitively expensive for large-scale deployment.

Semiconductor optical amplifiers (SOAs) are here making the race. The structural design of such a device is very close to that of a laser, except that they definitely should not be used as such. Ultralow reflection coatings, which represent a technological challenge cover their windows. Devices operating in the O-band based on InP technology do not completely satisfy the demands of circuit designers: They are neither low power nor very temperature stable.

The discovery of quantum dots (QDs) as an enabling epitaxial technology to extend the wavelength window covered by GaAs-based photonic devices to the O-band stood at the advent of the development of both QD-lasers and QD SOAs. InAs/GaAs-based QD structures enable coverage of a wavelength range that was thought to be only accessible by InP-based quantum wells (QWs), until the nineties. Lasers based on QDs were the first photonic devices to be thoroughly investigated for the window 1.1–1.35 μm. Larger material gain of QDs compared with that of classical QWs overcompensates the impact of the Gaussian-like broad distribution of emission energies on modal gain, still showing sufficient amplification. The large gain bandwidth was in fact found to be very favorable, enabling simple generation of fs-pulses of high peak power by mode locking of QD-lasers. The threshold current density of QD-lasers was observed to be almost one order of magnitude lower than that of standard QW-lasers. Thus, their conversion efficiency for electrical to optical energy is larger: QD-lasers are more energy efficient.

A decade after research on QD-lasers started it was realized that the same inherent property of large gain bandwidth together with the strong spatial localization of charge carriers in the QDs, ultrafast gain recovery times from massively populated reservoirs and the resulting decoupling of gain and index of refraction present decisive advantages for novel types of SOAs.

The present dissertation of Holger Schmeckebier surveys the decisive advantages of SOAs based on QDs. Many essential breakthroughs are presented that could only be achieved using QDs as active media. Amongst them are:

- distinct excited states of QDs are used together with the ground state for dual-band-amplification of up-and down-stream signals by the same device, thus reducing the energy consumption by half,
- differential quadrature phase shift keying signals are successfully amplified;
- QD SOAs are demonstrated as direct phase modulators while still operating as amplifiers;
- four-wave mixing is used for converting wavelengths within SOAs, including phase coded signals.

Reading this thesis is a must for all scientists and engineers interested in the impact that modern semiconductor nanotechnology has on novel device designs, leading to breakthroughs for the physical layer of metropolitan and access networks, supporting higher data rates and, at the same time, energy efficiency.

Berlin, Germany
June 2016

Prof. Dieter Bimberg

Abstract

The social and economic life of today's modern society is characterized by nearly instantaneous distribution of information, access to almost unlimited sources of knowledge and entertainment, and globalized communication between everybody and everything at any time. To keep up with future demands, new advanced optical communication networks are required providing e.g. larger bandwidth and new functionalities. These networks will require optical amplifiers to overcome losses on the transmission line and devices for optical signal processing. Semiconductor optical amplifiers (SOAs) are promising candidates for both, amplification and signal processing.

This thesis considers the design, fabrication and experimental and numerical investigation of SOA for future optical communication networks used in metropolitan areas. It begins with a brief overview of the topic of optical communication networks and the demand of optical amplifiers as well as of devices for signal processing. The reader is thoroughly introduced to semiconductor gain media and their interaction with light, the parameters of optical amplifiers as well as the static and dynamic properties of SOA. The thesis focuses on SOA with quantum dots (QDs) as the active gain material and discusses their advantages for the generation, amplification and processing of optical data signals. The reader is than slowly introduced to various measurement methods and parameters for optical communication experiments, in particular system experiments. Optical data signals are generated by encoding the information in varying properties of light, commonly its amplitude and/or phase. The different types of modulation are called modulation formats. Multiple data signals are coded, e.g., on different wavelength channels.

The quality of the amplified optical data signal depends on the optical power level at the input of the amplifiers. Hence, the range of power levels—the so-called (IPDR)—in which the amplifier doesn't decrease the signal quality significantly is of utmost importance. The thesis presents (QD SOA) based single- and multi-wavelength-channel amplification of amplitude- and phase-coded signals with data rates as large as 80 Gb/s per channel using system experiments. The appropriate power ranges and the influences of different wavelength channels and modulation formats are discussed.

Two novel device concepts are developed and demonstrated by exploiting the unique advantages of QD SOAs. Both concept could drastically simplify the network architecture and thus reduce their investment and maintenance costs. The first concept allows the amplification of data signals with a large spectral separation. This enables the realization of a single amplifier device with the ability to amplify data signals from different communication bands. The second concept enables the generation of phase-coded data signals by direct modulation of the drive current of the amplifier. The advantages and performance of both concepts are extensively discussed. The concepts are proven by performing system experiments with data rates as large as 40 Gb/s per channel.

The final part of the thesis deals with optical signal processing. All-optical wavelength conversion as the fundamental building block for optical signal processing is the conversion of the information from one wavelength channel to another. The reader is introduced into nonlinear effects of semiconductor gain media, i.e., four-wave mixing. The advantages of QD SOAs are addressed and a guideline for the optimization of the conversion performance is given. The conversion of phase-coded data signals with a data rate as large as 80 Gb/s is proven in a wavelength span as large as 45 nm using system experiments.

List of Publications

Parts of This Work Have Been Previously Published as:
Reviewed Papers:

1. A. Zeghuzi, H. Schmeckebier, M. Stubenrauch, C. Meuer, C. Schubert, C.-A. Bunge, and D. Bimberg, 25 Gbit/s differential phase-shift-keying signal generation using directly modulated quantum-dot semiconductor optical amplifiers, Appl. Phys. Lett. **106**(21), 213501 (2015).
2. Y. Kaptan, A. Röhm, B. Herzog, B. Lingnau, H. Schmeckebier, D. Arsenijević, V. Mikhelashvili, O. Schöps, M. Kolarczik, G. Eisenstein, D. Bimberg, U. Woggon, N. Owschimikow, and K. Lüdge, Stability of quantum-dot excited-state laser emission under simultaneous ground-state perturbation, Appl. Phys. Lett. **105**(19), 191105 (2014).
3. Y. Kaptan, H. Schmeckebier, B. Herzog, D. Arsenijević, M. Kolarczik, V. Mikhelashvili, N. Owschimikow, G. Eisenstein, D. Bimberg, and U. Woggon, Gain dynamics of quantum dot devices for dual-state operation, Appl. Phys. Lett. **104**(26), 261108 (2014).
4. H. Schmeckebier, C. Meuer, D. Arsenijević, G. Fiol, C. Schmidt-Langhorst, C. Schubert, G. Eisenstein, and D. Bimberg, Wide-Range Wavelength Conversion of 40-Gb/s NRZ-DPSK Signals Using a 1.3- m Quantum-Dot Semiconductor Optical Amplifier, IEEE Photonics Technol. Lett. **24**(13), 1163–1165 (2012).
5. H. Schmeckebier, C. Meuer, D. Bimberg, C. Schmidt-Langhorst, A. Galperin, and C. Schubert, Quantum dot semiconductor optical amplifiers at 1.3 m for applications in all-optical communication networks, Semicond. Sci. Technol. **26**(1), 14009 (2011).
6. C. Meuer, C. Schmidt-Langhorst, G. Fiol, D. Arsenijević, C. Schubert, and D. Bimberg, 40 Gb/s wavelength conversion via four-wave mixing in a quantum-dot semiconductor optical amplifier., Opt. Express **19**(4), 3788{3798 (2011).

7. C. Meuer, C. Schmidt-Langhorst, R. Bonk, H. Schmeckebier, D. Arsenijević, G. Fiol, A. Galperin, J. Leuthold, C. Schubert, and D. Bimberg, 80 Gb/s wavelength conversion using a quantum-dot semiconductor optical amplifier and optical filtering, Opt. Express **19**(6), 5134–5142 (2011).
8. A. V. Uskov, C. Meuer, H. Schmeckebier, and D. Bimberg, Auger Capture Induced Carrier Heating in Quantum Dot Lasers and Amplifiers, Appl. Phys. Express **4**(2), 22202 (2011).
9. G. Fiol, C. Meuer, H. Schmeckebier, D. Arsenijević, S. Liebich, M. Laemmlin, M. Kuntz, and D. Bimberg, Quantum-Dot Semiconductor Mode-Locked Lasers and Amplifiers at 40 GHz, IEEE J. Quantum Electron. **45**(11), 1429–1435 (2009).

Conference Contributions:

10. H. Schmeckebier, B. Lingnau, S. Koenig, K. Lüdge, C. Meuer, A. Zeghuzi, D. Arsenijević, M. Stubenrauch, R. Bonk, C. Koos, C. Schubert, T. Pfeiffer, and D. Bimberg, Ultra-Broadband Bidirectional Dual-Band Quantum-Dot Semiconductor Optical Amplifier, in *Optical Fiber Communication Conf. (OFC)*, page Tu3I.7, 2015.
11. H. Schmeckebier, Quantum dot based semiconductor optical amplifiers: Gain dynamics of quantum-dot states, in *Int. Symposium Nanostructures Physics and Technology*, pages –, 2014.
12. C. Meuer, H. Schmeckebier, C. Schmidt-Langhorst, G. Fiol, D. Arsenijević, C. Schubert, G. Eisenstein, and D. Bimberg, Wavelength conversion of 40-Gb/s NRZ DPSK signals within a 45-nm range using a 1.3 m quantum-dot semiconductor optical amplifier, in *European Conf. and Exhibition on Optical Communication (ECOC)*, page We.10.P1.26, 2011.
13. C. Schmidt-Langhorst, C. Meuer, A. Galperin, H. Schmeckebier, R. Ludwig, D. Puris, D. Bimberg, K. Petermann, and C. Schubert, 80 Gb/s multi-wavelength booster amplification in an InGaAs/GaAs quantum-dot semiconductor optical amplifier, in *European Conf. and Exhibition on Optical Communication (ECOC)*, page Mo.1.F.6, 2010.
14. D. Bimberg, C. Meuer, G. Fiol, H. Schmeckebier, and D. Arsenijević, Four-wave mixing in 1.3 m quantum-dot semiconductor optical amplifiers, in *Int. Conf. on Transparent Optical Networks (ICTON)*, page We.D4.2, 2010.
15. D. Bimberg, G. Fiol, C. Meuer, D. Arsenijević, J. Kim, S. Liebich, M. Laemmlin, M. Kuntz, H. Schmeckebier, and G. Eisenstein, Ultra high-speed nanophotonics, in *Proc. SPIE*, page 721117, 2009.
16. D. Bimberg, C. Meuer, G. Fiol, H. Schmeckebier, D. Arsenijević, and G. Eisenstein, Influence of P-doping in quantum dot semiconductor optical amplifiers at 1.3 m, in *Int. Conf. on Transparent Optical Networks (ICTON)*, page We.C5.5, 2009.

Acknowledgments

This thesis originated in the course of several years during my work at the institute of solid state physics at the Technische Universität Berlin. During this time, many people contributed to the success of this thesis. I would like to express my heartfelt thanks to all of these people with the following paragraphs.

First of all, my sincerest thanks go to Prof. Dieter Bimberg (TU Berlin) for the opportunity to work on this interesting topic and his continuous interest in the progress of this work. I appreciated his excellent allocation of resources, the forming of a sparkling team and his wealth of experience. I am very thankful that he granted me enormous freedom of action and especially his unconditional trust in my scientific, administrative and managing activities over the entire period. Thank you very much!

I am very grateful to Prof. Gadi Eisenstein (Technion) for taking over the second review of my thesis. Moreover, I am greatly appreciative of the numerous loose scientific discussions without any restrictions in thinking and assumptions as well as for all the private conversations during this time. Finally, I also thank him for the opportunity to visit his institute and lovely home country.

I want like to thank Prof. Michael Lehmann (TU Berlin) for taking over the presidency of the exam.

I am deeply indebted to my former colleague, early supervisor and good friend Christian Meu(r?)er. In the course of our long acquaintance ship, he has not only coined my current way of approaching scientific problems, but also contributed with numerous discussions to the success of this work. A welcome distraction was the Friday lunch time as well as his song writing and singing performance. And of course, I still have to smile about his talent to always finding a way to give my wording a different interpretation as intended as well as the way of linking the words “networking”, “management” and “consultant” to my person. Furthermore, I would like to thank him for the many years of sharing the office. Finally, I thank him especially for the short nights during proofreading of this manuscript. Infinite thanks!

I am very grateful to my colleagues Mirko Stubenrauch and Dejan Arsenijević for the many years of successful cooperation, uncountable interesting discussions and conversations as well as their friendship. In particular I thank Mirko for processing a plurality of samples used in this thesis and Dejan for the collaboration in the implementation of the OMA, the associated transmitter as well as taking care of all the HF equipment. Many thanks to Mirko also for the coffee-owl and its active application. I also thank him for the two years of the shared work for the SoN. A decisive part to the realization of this work was contributed by Anissa Zeghuzi whose thesis I have supervised with great pleasure. Thank you very much for the productive year, many conversations, sympathy during harder times and the lot of fun.

I sincerely thank René Bonk and Swen König (both former KIT) for the cooperation and the very intensive measuring time in Karlsruhe including the unforgotten "Fleischkäse"-night and the soccer game. Specifical thanks to René for his ideas, support and his constant interest in the progress of this work.

I want to acknowledge the contribution of Prof. Christian Bunge (HfTL) in terms of scientific discussions and ideas to this work.

I thank Yücel Kaptan, Bastian Herzog, Nina Owschimikow und Prof. Ulrike Woggon as well as Benjamin Lingnau, André Röhm and Prof. Kathy Lüdge for their cooperation and contribution to this work.

My special thanks to Carsten Schmidt-Langhorst and Colja Schubert (both HHI). Without their providing of equipment, numerous experiments would not have been possible. Furthermore I thank Greta Ropers (HHI) for the AR coating of the samples.

I would like to thank the current and former members of AG Bimberg. In particular, I am very grateful to Jan-Hindrik Schulze and David Quandt for many humorously conversations and especially for spending time to my endless questions during writing this manuscript. I am appreciative Tobias Nowozin for the experience during the trip to St Petersburg (especially the last morning) as well as his numerous excursions to the sublime German language, e.g. "Aufbruch—Keramik, Mörtel". Thanks also go to Gernot Stracke for its continuous maintenance of the IT infrastructure. He is a man a few word, but if he speaks, you better be there. I thank Tagir Sadev for the very relaxed and quiet atmosphere in the office. Thanks also to all not explicitly mentioned members for their cooperation.

I express my thankfulness to the staffs of the institute who have supported me throughout all my activities. Specifical thanks to Roswitha Koskinas, Ines Rudolph, Doreen Nitzsche, Thu Hoang and Ulrike Grupe for their kindness and help with the administrative problems of the daily routine and beside. Furthermore, thanks to Silke Hönert for all her support in managing PROPHET. Our research would be so much harder without the many small works in the background performed by Kathrin Schatke, René Linke and Ronny Schmidt. I have to thank the employees of the fine mechanical workshop for their skill and their technical expertise. Their support enabled nearly all experimental setups.

Meanwhile, many thanks to the badminton group for so much fun and fights in all the years, namely Gerrit Fiol, Mirko Stubenrauch, Christian Meuer, Philip Wolf und Mark Spiegelberg.

Overflowing gratitude to my family, especially to my parents Ute and Karsten Schmeckebier for their unlimited support, encouragement and unswerving belief in me. Furthermore, cheerful thanks to Jürgen and Mandi for the great weekend distractions. I really appreciate it.

My last words are dedicated to you, Sabine Alamé. My loving thanks to you for all your care, support, motivation and understanding during all these years, and especially for all your love.

Contents

Acronyms

AC	Alternating current
AN	Access network
AOWC	All-optical wavelength conversion
AR	Anti-reflection
ASE	Amplified spontaneous emission
Att	Attenuator
BPG	Bit-pattern generator
BtB	Back-to-back
C-band	Conventional band
CDP	Carrier density pulsation
CI	Carrier injection
D(Q)PSK	Differential (quadrature) phase-shift keying
DC	Direct current
DD MZM	Dual-drive Mach-Zehnder modulator
DFB laser	Distributed feedback laser
DI	Delay interferometer
DPSK	Differential phase-shift keying
DQPSK	Differential quadrature phase-shift keying
DSP	Digital signal processing
DUT	Device under test
EA	Error analyzer
EAM	Electro-absorption modulator
ECL	External cavity laser
EDFA	Erbium-doped fiber amplifier
EQ	Equalizer
ES	Excited state
FBG	Fiber-Bragg grating
FEC	Forward-error correction
FROG	Frequency-resolved optical gating
FTTH	Fiber-to-the home

FTTx	Fiber-to-the x
FWM	Four-wave mixing
GS	Ground state
HF	High-frequency
HH	Heavy-hole
HMLL	Hybrid mode-locked laser
IP	Internet protocol
IPDR	Input power dynamic range
LH	Light-hole
LIV	Light-intensity-voltage
MAN	Metropolitan area network
MLL	Mode-locked laser
MZM	Mach-Zehnder modulator
O-band	Original band
OFDM	Orthogonal frequency-division multiplexing
OMA	Optical modulation analyzer
ONT	Optical network termination
OOK	On-off keying
OSA	Optical spectrum analyzer
OSNR	Optical signal-to-noise ratio
OTDM	Optical time-division multiplexing
PAM	Pulse amplitude modulation
PD	Photodiode
PDFA	Praseodymium-doped fiber amplifier
PMF	Polarization-maintaining fiber
PRBS	Pseudo-random binary sequence
PRBS-7	PRBS with the length of 2^7–1
PRBS-15	PRBS with the length of 2^{15}–1
PRBS-31	PRBS with the length of 2^{31}–1
PSK	Phase-shift keying
PWM	Power meter
QAM	Quadrature amplitude modulation
QD	Quantum dot
QD SOA	Quantum-dot semiconductor optical amplifier
QPSK	Quadrature phase-shift keying
QW	Quantum-well
QW SOA	Quantum-well semiconductor optical amplifier
RF	Radio frequency
rms	Root-mean square
RT Osci	Real-time oscilloscope
Rx	Receiver
S-band	Short-wavelengths band
SBR	Signal-to-background ratio
SHG	Second-harmonic generation
SMF	Single-mode fiber

SO	Split off
SOA	Semiconductor optical amplifier
SPM	Self-phase modulation
TDM	Time division multiplexing
TE	Transverse electric
TEC	Thermoelectric cooler
TF	Wavelength tunable filter
TM	Transverse magnetic
Tx	Transmitter
VOA	Variable optical attenuator
WAN	Wide-area network
WDM	Wavelength division multiplexing
XGM	Cross-gain modulation
XPM	Cross-phase modulation

Chapter 1
Preamble

Today's modern society is commonly called a digital- and knowledge/information society in the media. Our present social and economic life is characterized by nearly instantaneous distribution of news and information, access to almost unlimited sources of knowledge and entertainment and globalized communication between everybody and everything at any time. This was enabled by a rapid evolution of communication networks and by the innovation of new services within the past few decades.

Optical interconnects are decisive for contemporary communication networks. Information is encoded in various physical properties of light emitted by semiconductor lasers and transmitted across optical fibers [1]. The invention and improvement of both, the semiconductor lasers and fibers have been honored often over the years. The highlights are the Nobel prizes awarded (in half) to Z. I. Alferov and H. Kroemer "for developing semiconductor heterostructures used in high-speed- and opto-electronics" [2] in 2000, and (in half) to C. K. Kao "for groundbreaking achievements concerning the transmission of light in fibers for optical communication" [3] in 2009. Besides semiconductor lasers and fibers, the development of erbium-doped fiber amplifiers (EDFAs) was a crucial part for the triumph of optical communication network technologies enabling transmission across distances of up to 10,000 km without signal regeneration [4].

The global internet protocol (IP) traffic handled by the communication network has increased tremendously in the last two decades, e.g. by approximately 37 % from 2012 to 2014 resulting in a traffic of almost 60 exabytes per month[1] [5, 6]. The traffic increase in the few past years was mainly driven by consumer video services like video-telephony, social movie sharing and internet TV or video on demand. But also the traffic based on business and other consumer services like data exchange, social media and gaming increases rapidly. Cisco System Inc. forecasts in [6] a still large

[1] One exabyte corresponds to 10 to the power of 18 byte.

H. Schmeckebier, *Quantum-Dot-Based Semiconductor Optical Amplifiers for O-Band Optical Communication*, Springer Theses,
DOI 10.1007/978-3-319-44275-4_1

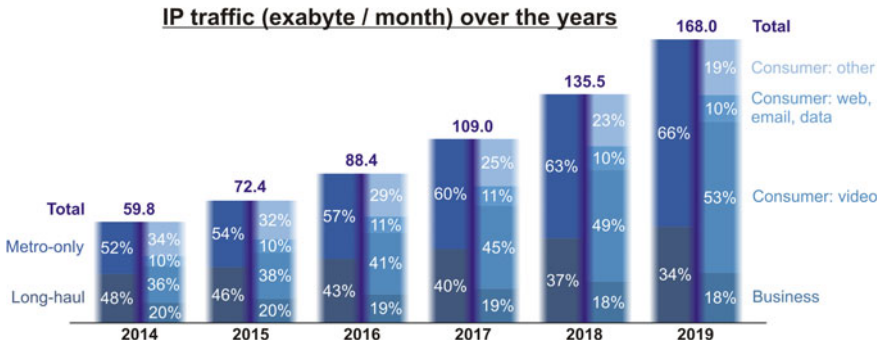

Fig. 1.1 Forecast of total global internet protocol (IP) traffic over the years. The ratio of long-haul and metro-only traffic (*left part of each bar*) as well as the ratio of different services (*right part of each bar*) on the total traffic is given. Data extracted from [6]

annual traffic increase of 23 % per year resulting in 168 exabytes per month in 2019 as depicted in Fig. 1.1. The global traffic managed per year will exceed one zetabyte (1000 exabyte) already in the year 2016 [6]. Hence, this era is called the "Zetabyte Era" [7].

Another very important issue is the traffic allocation across the network architecture. Two main traffic allocations must be distinguished: IP traffic within a metropolitan area bypassing long-haul links (connection between metropolitan areas) is called metro-only traffic. IP traffic traversing long-haul links is called long-haul traffic. Today, metro-only and long-haul traffic contribute each almost half-and-half to the total traffic [6]. Metro-only traffic is forecast to grow significantly faster than long-haul traffic resulting in a two-to-one ratio in 2019 [6].

Beside the traffic, also the number of devices connected to the IP networks increases rapidly and is forecast to grow to nearly three times the global population in the year 2017 [6]. To satisfy future requirements, the markets for communication and network products require innovative solutions. Today, the global optical networking and communications market reaches a volume of approximately USD 16 billion per year and is forecast to reach a volume of USD 26 billion per year in 2020 [8].

Network Architecture

The state-of-the-art communication network is divided into network classes, such as wide area network (WAN), metropolitan area network (MAN) and access network (AN) which are distinguished by their span, task and structure. The following introductions to the network architecture, the physical layer and future networks are based on [9–14].

A simplified schematic of a network is shown in Fig. 1.2. WANs, also called backbone or long-haul networks, span over up to thousands of kilometers and handle the global data exchange across terrestrial or undersea systems. These networks are organized in mesh topology to guarantee a large redundancy. The backbone network connects MANs most commonly realized in a ring topology. A typical MAN is

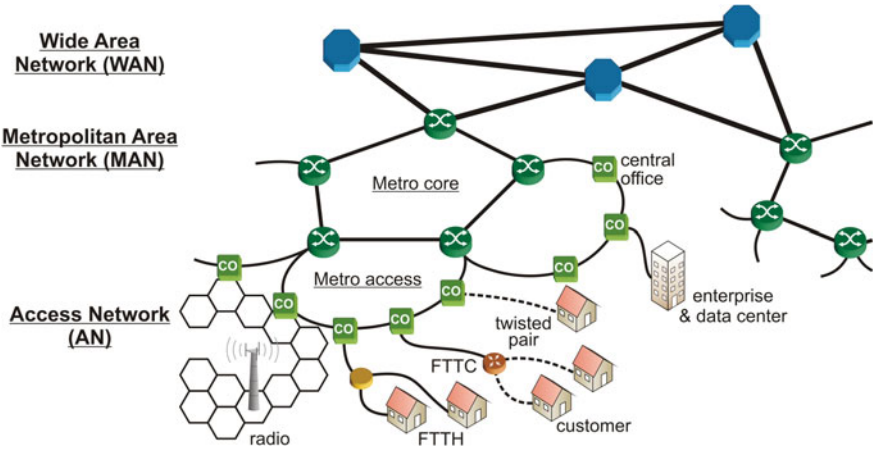

Fig. 1.2 Sketch of common communication network architecture. Redrawn after [14–16]. *FTTC* fiber-to-the curb, *FTTH* fiber-to-the home

subdivided into a ring metro core network with a circumference in the order of 100 km and multiple ring metro access networks with a circumference of 30–60 km. The customer premises are connected via ANs to central offices located in the metro access networks. A couple of different implementation of ANs are realized ranging from a few kilometers up to more than 60 km. Traditionally, the customer premises are connected by twisted pair copper cables to the central office. These copper-based ANs already reached their capacity limit which is overcome by shorter reach and/or more complexity. Instead, these connections are more and more replaced by fiber which is called fiber-to-the x (FTTx), where x stands either for curb, building or home. Pushing the fiber connections from curb to building to home reduces the span of limiting copper connections from a few kilometer in the case of xDSL (digital subscriber line) to below one hundred meters in the case of fiber-to-the home (FTTH). Future AN designs will finally be based on FTTH due to their significantly increased bandwidth.

Physical Layer

The physical layer of an optical point-to-point transmission link consist of a transmitter, inline components, a receiver and fiber connecting all components. The transmitter emits the optical data signal and is based on a directly modulated semiconductor laser or a continuous wave laser in combination with a modulator. The receiver detects the optical data signal using semiconductor photodiode(s). A more detailed description is given in Chap. 4. However, the properties of the fiber are important as it routes the information across large distances.

Exclusively single-mode fibers (SMFs) (e.g. specified in [17]) are used in global communication networks. The characteristics of the SMF lead to the definition of several communication bands in the near-infrared region as listed in Table 1.1 [12].

Table 1.1 List of defined single-mode fiber (SMF) communication bands

Band	Description	Wavelength range (nm)
O-band	Original	1260–1360
E-band	Extended	1360–1460
S-band	Short wavelength	1460–1530
C-band	Conventional	1530–1565
L-band	Long wavelength	1565–1625
U-band	Ultralong wavelength	1625–1675

The conventional band (C-band) is currently the most commonly used wavelength band because the fiber provides the lowest attenuation of below 0.2 dB/km [18].[2] In comparison, the attenuation in the original band (O-band) is about 50 % larger with 0.35 dB/km. The C-band is thus of great importance for long-haul communication across thousands of kilometers for which the fiber attenuation is the dominating factor. The C-band fiber attenuation is compensated after transmission distances of at the most 100 km (typical about 80 km) commonly using EDFAs. A second important SMF parameter is the dispersion. The O-band is characterized by the zero dispersion of the SMF at a wavelength around 1300 nm. Hence, the O-band is particularly interesting for low-cost networks for medium and short distances, like MANs and ANs, since costly dispersion compensating techniques can be avoided at the expense of a slightly larger fiber attenuation. In today's networks, the O-band is typically used for up-streaming the data from the customer premises to the central office [9, 14]. Some of them use the O-band also for down-stream [19] which will be expanded in the future.

This thesis is focusing on devices for O-band communication applications but the presented results are not restricted to these.

Networks implemented as FTTH are commonly designed in a point-to-multi-point topology which multiplexes the fibers of multiple customer premises to a single fiber connected with the central office. The separation of the individual user information channels is commonly realized by time division multiplexing (TDM) or wavelength division multiplexing (WDM). In TDM-based networks, the time domain is divided into multiple periodic time slots, where each customer premise is assigned to a specific time slot. Down- and up-stream,[3] implemented in different wavelength bands (commonly S-band and O-band), are split and combined using a symmetric power splitter, whereas the information is multiplexed in time. In contrast, WDM networks are implemented by assigning individual wavelength channels to each customer premises. The channel splitting and combining is realized by a wavelength division multiplexer. Increasing the splitting ratio e.g. from currently 16 to 512 will

[2] This attenuation is reached in modern SMFs. Typical deployed links exhibit values of e.g. 0.275 dB/km [17].

[3] Down-stream describes the transmission of information from the central office to the customer premises and up-stream vice versa.

increase the power splitting losses for TDM implementation by 15 dB. In contrast, the losses in WDM implementation do not scale with the number of connected customer premises and reach values in the order of 3 dB per port [14]. The research and development for near future access technologies tends to combine both TDM and WDM approaches [14, 19, 20].

Future Metro & Access Networks and the Demand for Optical Amplifiers
State-of-the-art ANs and MANs technologies use up to 40 wavelength channels each carrying a data stream of up to 10 Gb/s [14, 19, 21–23] increasing to 40 Gb/s in near future [19–21]. The data up- and down-stream are often realized with asymmetric transmission bandwidth, the down-stream having a significantly higher data rate [19]. In the course of web 2.0, e.g. cloud computing and video streaming, the bandwidth of both, up- and down-stream have been increasing and could become more and more symmetric in the future [21].

The requirements for the next-generation optical MANs and ANs are determined by a significantly increased number of customer premises and increased transmission rates per costumer. The former can be realized by combining the TDM and the WDM approaches [14, 19, 20]. The latter can be realized by boosting the modulation speed of the current widely used intensity modulation, i.e. on-off keying (OOK), or by the implementation of more advanced modulation formats encoding multiple bits per transmitted symbol [14, 16]. Advanced modulation formats code multiple symbol levels on the same and/or different physical properties of light, i.e. intensity, amplitude, phase or polarization, and thus multiply the transmission rate [24]. Approaches for next-generation optical networks, such as converged MANs and reach extended ANs, will cover long distances of up to 100 km, larger splitting ratios up to 512 and the use of advanced modulation formats [14–16, 19, 21, 22, 25]. In this respect, optical amplifiers are essential to compensate the additional losses caused by the extended reach and larger splitting ratios. Such amplifiers have to support multiple modulation formats, particularly intensity and phase-coded formats, as well as multi-wavelength channel amplification with low channel crosstalk. Additional specifications will be desirable, such as low energy consumption, support of multiple communication bands and above all low investment and maintenance cost as ANs and MANs components are mass market products.

Optical Amplifiers and Advantages of QD SOAs
Various realizations of optical amplifiers have been developed for optical communication networks, such as rare-doped fiber amplifiers, Raman amplifiers and semiconductor optical amplifiers (SOAs). Doped fiber amplifiers use optically pumped doped fibers as a gain medium. Most established are erbium-doped fiber amplifiers (EDFAs) and praseodymium-doped fiber amplifiers(PDFAs) providing gain in the C-band and O-band, respectively [12, 26, 27]. Raman amplifiers use stimulated Raman scattering in a fiber to provide gain [12, 26]. SOAs use electrically pumped semiconductor diode structures to provide gain [12, 27, 28].

EDFAs are widely used in C-band-based optical communication networks as they offer large gain and excellent noise performance, but the spectral gain bandwidth is typically limited and the investment and maintenance costs are large. The limited gain bandwidth is overcome by combining EDFAs and Raman-amplifiers [12]. In comparison to fiber amplifiers, SOAs offer low-cost mass production typical for semiconductor devices, reduced power consumption, smaller footprint, ease of integration in photonic integrated circuits, and broad gain spectra, but at the expense of a slightly increased noise [27]. The decisive advantages of SOAs outweigh the noise performance in case of networks spanning medium distances that subject an intensive cost-pressure mass-market like MANs and ANs. Thus, SOAs are a superior alternative to the costly fiber amplifiers that are used for the linear amplification in such networks and particular for approaches for next-generation all-optical high-speed ANs and MAN [16, 21, 25, 29–32]. In addition, increasing network integration and modulation speed rise the demand for optical signal processing, such as switching, add-drop multiplexing and conversion of information between individual wavelength channels (called wavelength conversion) [33].

The performance of SOAs in terms of the requirements listed above and particularly for signal processing depend on the nature of the semiconductor gain media. Two main classes are distinguished, the conventional bulk semiconductors and semiconductor nanostructures. In contrast to bulk semiconductors, semiconductor nanostructures exhibit a confinement of the charge carriers in one, two or three spatial directions and are called quantum-well (QW), quantum wire and quantum dot (QD), respectively [34, 35]. The carrier confinement strongly influences the optical, electronic and thermal properties of the gain media. In comparison to conventional bulk or QW SOAs, QD-based SOAs benefit from a number of unique properties [36].

QDs exhibit discrete bound states, a ground state (GS) and typically excited state (ESs) [35, 37, 38]. A QD ensemble exhibits an inhomogeneously broadened optical emission [35] resulting in a large spectral gain bandwidth of up to 120 nm [39, 40]. The separation of the energy states into gain providing QD states and carrier reservoir providing higher energy states results—in case of a highly populated reservoir—in a decoupling of gain and phase dynamics [41] and a presumably low α-factor [42–44]. Therefore, very fast gain dynamics is achieved, demonstrated by a complete GS gain recovery down to a few hundred femtoseconds found in pump-probe measurements [45, 46] and below 10 ps under system environment-like conditions [47, 48].

State-of-the Art and Focus of this Work

When this thesis was initiated, the fast gain dynamics of QD SOAs had been utilized very successfully for single and multi-channel amplification of intensity-coded (OOK) signals with symbol rates up to 80 GBd [44, 49–53]. Also nonlinear effects, like cross-gain modulation (XGM), cross-phase modulation (XPM) and four-wave mixing (FWM), benefit from the fast QD gain dynamics even beyond saturation input power levels. Subsequently, these nonlinear effects have been used successfully to demonstrate single and multi-channel AOWC of OOK signals with symbol rates up to 320 GBd [47, 50, 51, 54–60].

All these results have been achieved with OOK modulated signals. Beside the common OOK format, future networks will use advanced modulations formats, which are mainly based on phase or phase and intensity modulation. Thus, not only the gain dynamics but also the phase dynamics of QD SOAs are important. In addition, XGM and XPM are inappropriate to convert the wavelength of phase-coded signals. Only FWM remains for signal processing of phase-coded signals.

This thesis is focusing on the investigation of amplification and wavelength conversion for both, conventional and advanced modulation formats in single and multi-wavelength channel configurations. Within the last few years, error-free amplification and wavelength conversion of phase-coded signals has been demonstrated with symbol rates of up to 28 GBd [61–63] and 40 GBd [64–70], respectively.

The second focus of this thesis is on the development of novel concepts based on the unique properties of QDs. One novel concept is based on the decoupling of gain and phase dynamics in a saturated QD SOA. Taking advantage of this feature, a directly modulated QD SOA is used for generation of phase-coded signals. This concept has a large potential for future color-free AN.

The above listed results of both, intensity and phase-coded signals, have been achieved utilizing the QD GS emission. A second novel concept presented in this thesis exploits the QD GS and ES for simultaneous amplification of data signals with a spectral separation in the order of 100 nm. This ultra-broadband dual-band amplifier concept has a large potential to replace two amplifiers commonly required for the up- and downstream in different communication bands.

Structure of This Thesis

This thesis investigates the properties of GaAs-based QD SOAs emitting in the O-band and is organized as follows:

Chapter 2 introduces the basics of QD SOA, starting with a brief introduction to semiconductor gain media and their interaction with light. The basic parameters of optical amplifiers are defined. Dynamics of SOAs are discussed and the advantages of QD SOAs are presented.

Chapter 3 presents the design and characteristics of the devices investigated in this thesis. First, the QD SOA design and the characterization stage are described. The dependence of the static performance on the design parameters is shown. Finally, results on the gain and phase dynamics of QDs are presented.

Chapter 4 describes the basics of modulated signals and system experiments, starting with an overview of modulation formats. Subsequently, the optical test setup and the evaluation of the signal quality are introduced.

Chapter 5 presents a novel concept based on the decoupling of gain and phase dynamics in a saturated QD SOA. First, the concept of directly modulated phase-coded signal generation is motivated and introduced. The proof of concept is demonstrated by generating DPSK signals up to 25 GBd using a direct modulated QD SOA.

Chapter 6 covers single- and multi-wavelength channel amplification of intensity and phase-coded binary as well as quadrature signals. The first part concentrates on the single-channel amplification of OOK, and D(Q)PSK using QD SOAs with symbol rates of up 80 GBd. The latter part investigates the cross-talk of 40 GBd OOK

interfering wavelength channels on one 80 GBd OOK and one 40 GBd D(Q)PSK wavelength channel.

Chapter 7 presents a novel concept for a dual-band optical amplifier. It exploits the QD GS and ESs to amplify data signals. First, the proof of concept is demonstrated by amplifying bidirectional 40 GBd OOK data signals with a spectral spacing of 93 nm representing the two bands. The second part presents a theoretical description of QD SOAs and models the experimental results.

Chapter 8 is dedicated to nonlinear wavelength conversion in QD SOAs, in particular the conversion of phase-coded signals. It starts with an introduction to wavelength conversion and four-wave mixing in QD SOAs. Optimization of the static FWM performance is presented. The chapter closes with the demonstration of wavelength conversion of 40 GBd D(Q)PSK.

Chapter 9 completes this thesis by summarizing the results and an outlook.

References

1. C. Tocci, H.J. Caulfield (eds.), *Optical Interconnection Foundations and Applications*, 1st edn. (Artech House, 1994), p. 383
2. http://www.nobelprize.org/nobel_prizes/physics/laureates/2000/index.html (2015)
3. http://www.nobelprize.org/nobel_prizes/physics/laureates/2009/index.html (2015)
4. A.A. Huurdeman, *The Worldwide History of Telecommunications*, 1st edn. (Wiley, New York, 2003), p. 638
5. Cisco Systems Inc., *Cisco Visual Networking Index: Forecast and Methodology, 2012–2017*. WHITE PAPER (2013)
6. Cisco Systems Inc., *Cisco Visual Networking Index: Forecast and Methodology, 2014–2019*. WHITE PAPER (2015)
7. Cisco Systems Inc., *The Zettabyte Era-Trends and Analysis*. WHITE PAPER (2015)
8. Optical Networking and Communications Market by Technology (Wavelength Division Multiplexing (WDM), Synchronous Optical Networking (SONET)/Synchronous Digital Hierarchy (SDH) and Fiber Channel), by Verticals Aerospace and Defense, Government, Manufactur. Markets and Markets (2015)
9. M. Sexton, A. Reid, *Transmission Networking: SONET and the Synchronous Digital Hierarchy*, 1st edn. (Artech House, 1992), p. 360
10. J. Prat (ed.), *Next-Generation FTTH Passive Optical Networks: Research Towards Unlimited Bandwidth Access*, 1st edn. (Springer, Berlin, 2008), p. 188
11. M. Azadeh, *Fiber Optics Engineering*, 1st edn. (Springer, Berlin, 2009), p. 376
12. J.M. Senior, M.Y. Jamro, *Optical Fiber Communications: Principles and Practice*, 3rd edn. (Financial Times/Prentice Hall, Englewood Cliffs, NJ, 2009)
13. A. Shami, M. Maier, C. Assi (eds.), *Broadband Access Networks: Technologies and Deployments*, 1st edn. (Springer, Berlin, 2010)
14. R. Bonk, *Linear and Nonlinear Semiconductor Optical Amplifiers for Next-Generation Optical Networks*. Doctoral Thesis. (Karlsruher Institut für Technologie, 2013), p. 278
15. T. Pfeiffer, Converged heterogeneous optical metro-access networks, in *European Conference and Exhibition on Optical Communication (ECOC)* (2010), Tu.5.B.1
16. H. Schmuck. *Breitband-Zugangsnetze der nächsten Generation Verbundprojekt: CONDOR - Converged Heterogeneous Metro/Access Infrastructure (Project Report)* (2013)
17. ITU-T, *ITU-T G.652 06/2005, Series G: Transmission Systems and Media, Digital Systems and Networks; Transmission Media Characteristics—Optical Fibre Cables; Characteristics of a Single-Mode Optical Fibre and Cable* (2005)

18. Corning Inc., *Data Sheet: Corning SMF-28e+ Photonic Optical Fiber* (2010)
19. P. Vetter, Next generation optical access technologies, in *Communication (ECOC), European Conference and Exhibition on Optical* (2012), pp. 1–42
20. D. Nesset, NG-PON2 technology and standards. J. Lightwave Technol. **33**(5), 1136–1143 (2015)
21. K.C. Reichmann et al., A symmetric-rate, extended-reach 40 Gb/s CWDM-TDMA PON with downstream and upstream SOA-Raman amplification. J. Lightwave Technol. **30**(4), 479–485 (2012)
22. ITU-T, *ITU-T G.989.1 03/2013, Series G: Transmission Systems and Media, Digital Systems and Networks; Digital Sections and Digital Line System - Optical Line Systems for Local and Access Networks* (2013)
23. Infinera, *Product Brochure: State-of-the-Art Metro WDM Extension for Intelligent Transport Networks* (2015)
24. P.J. Winzer, R.J. Essiambre, Advanced optical modulation formats. Proc. IEEE **94**(5), 952–985 (2006)
25. N. Suzuki, S. Yoshima, J. Nakagawa, Extended reach bidirectional optical amplified GE-PON with a high 46 dB span-budget for 64 far-end user ONUs, in *Joint International Conference on the Optical Internet (COIN) and Australian Conference on Optical Fibre Technology (ACOFT)* (2007), pp. 1–3
26. M.J. Digonnet (ed.), *Rare-Earth-Doped Fiber Lasers and Amplifiers (revised and expanded)*, 2nd edn. (CRC Press, Boca Raton, 2005), p. 798
27. D.R. Zimmerman, L.H. Spiekman, Amplifiers for the masses: EDFA, EDWA, and SOA amplets for metro and access applications. J. Lightwave Technol. **22**(1), 63–70 (2004)
28. G.P. Agrawal, *Lightwave Technology: Telecommunication Systems*, 1st edn. (Wiley, New York, 2005), p. 480
29. L. Spiekman et al., Semiconductor optical amplifiers for FTTx, in *International Conference on Transparent Optical Networks (ICTON)*, vol. 2. (2007), Mo.D2.4
30. P.P. Iannone et al., Four extended-reach TDM PONs sharing a bidirectional hybrid CWDM amplifier. J. Lightwave Technol. **26**(1), 138–143 (2008)
31. P.P. Iannone et al., Bi-directionally amplified extended reach 40 Gb/s CWDM-TDM PON with burst-mode upstream transmission, in *Optical Fiber Communication Conference (OFC) and National Fiber Optic Engineers Conference (NFOEC)* (2011), PDPD6
32. K. Taguchi et al., 40-km reach symmetric 40-Gbit/s λ-tunable WDM/TDM-PON using synchronized gain-clamping SOA, in *Optical Fiber Communication Conference. (OFC) and National Fiber Optic Engineers Conference (NFOEC)* (2013), OW4D.6
33. A.E. Willner et al., Optically efficient nonlinear signal processing. IEEE J. Sel. Top. Quantum Electron. **17**(2), 320–332 (2011)
34. M. Asada, Y. Miyamoto, Y. Suematsu, Gain and the threshold of three-dimensional quantum-box lasers. IEEE J. Quantum Electron. **22**(9), 1915–1921 (1986)
35. D. Bimberg, M. Grundmann, N.N. Ledentsov, *Quantum Dot Heterostructures*, 1st edn. (Wiley, New York, 1998)
36. D. Bimberg, Quantum dot based nanophotonics and nanoelectronics. Electron. Lett. **44**(3), 168–170 (2008)
37. M. Sugawara et al., Theory of optical signal amplification and processing by quantum-dot semiconductor optical amplifiers. Phys. Rev. B **69**(23), 235332 (2004)
38. D. Bimberg (ed.), *Semiconductor Nanostructures*, 2nd edn. (Springer, Berlin, 2008)
39. L.H. Li et al., Wide emission spectrum from superluminescent diodes with chirped quantum dot multilayers. Electron. Lett. **41**(1), 41–43 (2005)
40. T. Akiyama et al., An ultrawide-band semiconductor optical amplifier having an extremely high penalty-free output power of 23 dBm achieved with quantum dots. IEEE Photonics Technol. Lett. **17**(8), 1614–1616 (2005)
41. A.V. Uskov et al., On ultrafast optical switching based on quantum-dot semiconductor optical amplifiers in nonlinear interferometers. IEEE Photonics Technol. Lett. **16**(5), 1265–1267 (2004)

42. T. Akiyama et al., Symmetric highly effcient (~0 dB) wavelength conversion based on four-wave mixing in quantum dot optical amplifiers. IEEE Photonics Technol. Lett. **14**(8), 1139–1141 (2002)
43. T. Vallaitis et al., Slow and fast dynamics of gain and phase in a quantum dot semiconductor optical amplifier. Opt. Express **16**(1), 170–178 (2008)
44. G. Contestabile et al., Regenerative amplification by using self-phase modulation in a quantum-dot SOA. IEEE Photonics Technol. Lett. **22**(7), 492–494 (2010)
45. P. Borri et al., Spectral hole-burning and carrier-heating dynamics in InGaAs quantumdot amplifiers. IEEE J. Sel. Top. Quantum Electron. **6**(3), 544–551 (2000)
46. T.W. Berg et al., Ultrafast gain recovery and modulation limitations in self-assembled quantum-dot devices. IEEE Photonics Technol. Lett. **13**(6), 541–543 (2001)
47. C. Meuer et al., 80 Gb/s wavelength conversion using a quantum-dot semiconductor optical amplifier and optical filtering. Opt. Express **19**(6), 5134–5142 (2011)
48. C. Meuer, GaAs-Based Quantum-Dot Semiconductor Optical Amplifiers at 1.3 μm for All-Optical Networks. Doctoral Thesis. (Technical University of Berlin, 2011), p. 155
49. M. Sugawara et al., Recent progress in self-assembled quantum-dot optical devices for optical telecommunication: temperature-insensitive 10 Gb/s directly modulated lasers and 40 Gb/s signal-regenerative amplifiers. J. Phys. D. Appl. Phys. **38**(13), 2126–2134 (2005)
50. T. Akiyama, M. Sugawara, Y. Arakawa, Quantum-dot semiconductor optical amplifiers. Proc. IEEE **95**(9), 1757–1766 (2007)
51. C. Schmidt-Langhorst et al., 80 Gb/s multi-wavelength booster amplification in an InGaAs/GaAs quantum-dot semiconductor optical amplifier, in *European Conference and Exhibition on Optical Communication (ECOC)* (2010), Mo.1.F.6
52. H. Schmeckebier et al., Quantum dot semiconductor optical amplifiers at 1.3 μm for applications in all-optical communication networks. Semicond. Sci. Technol. **26**(1), 14009 (2011)
53. R. Bonk et al., The input power dynamic range of a semiconductor optical amplifier and its relevance for access network applications. IEEE Photonics J. **3**(6), 1039–1053 (2011)
54. G. Contestabile et al., 160 Gb/s cross gain modulation in quantum dot SOA at 1550 nm, in *Communication (ECOC), European Conference and Exhibition on Optical* (2009), pp. 1–2
55. G. Contestabile et al., Cross-gain modulation in quantum-dot SOA at 1550 nm. IEEE J. Quantum Electron. **46**(12), 1696–1703 (2010)
56. G. Contestabile et al., All-optical wavelength multicasting in a QD-SOA. IEEE J. Quantum Electron. **47**(4), 541–547 (2011)
57. M. Matsuura et al., 320-Gb/s wavelength conversion based on cross-gain modulation in a quantum-dot SOA, in *European Conference and Exhibition on Optical Communication (ECOC)* (Washington, DC, 2011), Mo.1.A.1
58. M. Matsuura et al., 320 Gbit/s wavelength conversion using four-wave mixing in quantumdot semiconductor optical amplifiers. Opt. Lett. **36**(15), 2910–2912 (2011)
59. C. Meuer et al., 40 Gb/s wavelength conversion via four-wave mixing in a quantum-dot semiconductor optical amplifier. Opt. Express **19**(4), 3788–3798 (2011)
60. M. Matsuura et al., 320-to-40-Gb/s optical demultiplexing by means of optical filtering of chirped signal using a quantum-dot SOA, in *Optical Fiber Communication Conference (OFC) and National Fiber Optic Engineers Conference (NFOEC)* (2012), OTh3H.4
61. T. Vallaitis et al., Quantum dot SOA input power dynamic range improvement for differential-phase encoded signals. Opt. Express **18**(6), 6270–6276 (2010)
62. R. Bonk et al., Linear semiconductor optical amplifiers for amplification of advanced modulation formats. Opt. Express **20**(9), 9657–9672 (2012)
63. S. Lange et al., Phase-transparent amplification of 16 QAM signals in a QD-SOA. IEEE Photonics Technol. Lett. **25**(24), 2486–2489 (2013)
64. M. Matsuura, N. Kishi, 40-Gbit/s RZ-DPSK wavelength conversion using four-wave mixing in a quantum dot SOA, in *Optical Fiber Communication Conference (OFC) and National Fiber Optic Engineers Conference (NFOEC)* (2011), JThA024
65. M. Matsuura et al., Multichannel wavelength conversion of 50-Gbit/s NRZ-DQPSK signals using a quantum-dot semiconductor optical amplifier. Opt. Express **19**(26), B560–B566 (2011)

66. M. Matsuura, N. Kishi, High-speed wavelength conversion of RZ-DPSK signal using FWM in a quantum-dot SOA. IEEE Photonics Technol. Lett. **23**(10), 615–617 (2011)
67. C. Meuer et al., Wavelength conversion of 40-Gb/s NRZ DPSK signals within a 45-nm range using a 1.3 μm quantum-dot semiconductor optical amplifier, in *European Conf. and Exhibition on Optical Communication (ECOC)* (2011), We.10.P1.26
68. G. Contestabile et al., Ultra-broad band, low power, highly effcient coherent wavelength conversion in quantum dot SOA. Opt. Express **20**(25), 27902–27907 (2012)
69. H. Schmeckebier et al., Wide-range wavelength conversion of 40-Gb/s NRZ-DPSK signals using a 1.3 μm quantum-dot semiconductor optical amplifier. IEEE Photonics Technol. Lett. **24**(13), 1163–1165 (2012)
70. G. Contestabile, All optical processing in QD-SOAs, in *Optical Fiber Communication Conference (OFC)* (2014), W4F.6

Chapter 2
Introduction to Semiconductor Optical Amplifiers (SOAs)

This chapter is dedicated to the basics and key parameters of semiconductor optical amplifiers (SOAs). The beginning of Sect. 2.1 provides a general introduction to semiconductor gain media and theory of interaction of light and semiconductors. Fundamental physical concepts and properties like band structure, inversion, nanostructures, gain and phase are introduced and discussed. This text-book knowledge can be found in more detail e.g. in [1–4]. Subsequently, Sect. 2.2 defines basic parameters of optical amplifiers, such as gain, saturation power levels and noise figure, characterizing the static performance of optical amplifiers. Section 2.2 addresses the gain, phase and carrier dynamics of SOA and discusses the advantages of QD gain media. Finally, this chapter is summarized in Sect. 2.4.

2.1 Basics of SOAs

The following paragraphs introduce the fundamentals of SOAs. The conditions to achieve optical gain in a simplified two level energy system neglecting higher or lower levels is given. The details of semiconductor gain media, the interaction of light and semiconductors are explained.

Three fundamental radiative processes important for the optoelectronic devices are sketched in Fig. 2.1. The device media is represented exemplarily as a two level energetic system with $E_1 < E_2$. An incoming photon with the energy $E_{ph} = \hbar\omega = E_2 - E_1$ can be absorbed by excitation of an electron from the energy level E_1 to

Parts of this chapter have been previously published in A. Zeghuzi, H. Schmeckebier, M. Stubenrauch, C. Meuer, C. Schubert, C.-A. Bunge, and D. Bimberg, 25 Gbit/s differential phase-shift-keying signal generation using directly modulated quantum-dot semiconductor optical amplifiers, Appl. Phys. Lett. **106**(21), 213501 (2015).

H. Schmeckebier, *Quantum-Dot-Based Semiconductor Optical Amplifiers for O-Band Optical Communication*, Springer Theses,
DOI 10.1007/978-3-319-44275-4_2

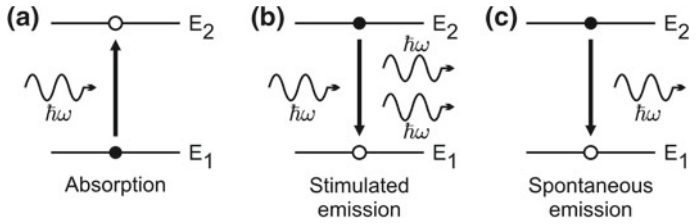

Fig. 2.1 Sketch of the three fundamental radiative processes in a medium

E_2. This process requires an empty state E_2 and tthus also called induced absorption. The quantum mec anics inverse process is the stimulated emission. In this case, the photon field can stimulate a relaxation of an excited electron from level E_2 to the empty level E_1 resulting in the coherent emission of a photon $\hbar\omega$. Instead of stimulated emission, the excitation system can relax by spontaneous emission of an photon $\hbar\omega$. The spontaneous emission appears thus without the presence of an external field. Indeed, the spontaneous emission can by described as stimulated emission induced by vacuum fluctuations, e.g. [5].

The amplification of an optical signal (photon field) is given by the stimulated emission whereas absorption results in attenuation of the photon field. Spontaneous emission on the other hand, results in noise background of the amplified signal. The stimulated emission has to be the dominating process to achieve gain of an optical signal.

The spontaneous emission rate depends on the life time of the state and the absolute number of excited carriers. In contrast, the absorption depends on the number of photons and the number of carriers in the lower energy level as well as the number of empty states in the upper level ("missing carriers"). The stimulated emission as the inverse process depends also on the number of photons but on the number of carriers in the upper level and empty states in the lower level. Hence, all three processes compete with each other. However, two main conditions have to be fulfilled to ensure the domination of stimulated emission:

- The carrier population probability of a simple level system in thermal equilibrium is given by the Boltzmann distribution and thus the carrier density N_1 is larger than N_2. Hence, the carrier population probability has to be inverted (called: population inversion) to suppress the absorption which is realized by pushing the medium out of thermal equilibrium.
- The electron lifetime on the upper energy level, the "missing electron" lifetime on the lower level and the photon density have to be sufficiently long to suppress the spontaneous emission.

The simple two level systems is sufficient to introduce the radiative processes but indeed it cannot be inverted in steady state condition. Thus, multi-level systems are used.

The following Sect. 2.1.1 introduces the fundamentals of semiconductor gain media in terms of energy structure and inversion. The subsequent Sect. 2.1.2 discusses the fundamentals of light-semiconductor interaction. Finally, the dynamics of SOAs are discussed in Sect. 2.3.

2.1.1 Semiconductor Gain Media

The discrete energy levels of distinct atoms are superimposed in crystalline solids resulting in the formation of quasi continuous energy bands [4]. In crystalline semiconductors, the energetically highest fully occupied band, called valence band, and the next higher empty band, called conduction band, are separated by an energy gap E_g [6]. Charge carriers can be described by a material wave with a quasi-momentum k [6]. The structure of the energy bands plotted in the momentum space (k-space) usually has a complicated structure.

The most important semiconductor optoelectronic emitters base on direct semiconductors like GaAs, InP or GaN. These materials exhibit a direct band gap given by the coincidence of the maximum of the valence band and minimum of the conduction band at $k = 0$, called the Γ point in k-space. In general, direct semiconductors exhibit a larger radiative recombination probability than indirect semiconductors which require the assistant of e.g. phonons [6].

The direct semiconductor band structure around the Γ point can be approximated by parabolic shaped bands using the effective mass approximation which describes the charge carriers at the direct semiconductor band edges with an constant effective mass m_b^* with $b \in \{e, h\}$ for electrons and holes, whereat holes are defect electrons (missing electrons). The valance band in semiconductors splits at the band edge into three bands, the heavy-hole (HH) band, light-hole (LH) band and split off (SO) band, each described by an effective mass $2m_o^*$ with $o \in \{HH, LH, SO\}$ (see Fig. 2.2a). The HH and LH states are degenerated at the Γ point in semiconductors with a cubic crystal structure like GaAs [4]. The low energy band edge of the conduction band E_C and the high energy band edge of the three valance bands E_V are given by

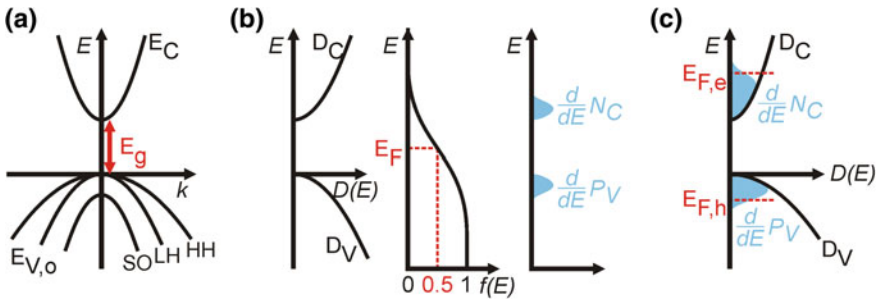

Fig. 2.2 **a** Sketch of the band structure of a direct semiconductor in k-space around the Γ point with conduction band and the three valance bands: *HH* heavy-hole, *LH* light-hole, *SO* split off. **b** Density of states $D(E)$, Fermi-Dirac distribution $f(E, T)$ for $T > 0$ K, electron density $\frac{d}{dE}N_C(E)$ in the conduction band and hole density $\frac{d}{dE}P_V(E)$ in the valance band. **c** Sketch of density of states $D(E)$, electron density $\frac{d}{dE}N_C(E)$ in the conduction band and hole density $\frac{d}{dE}P_V(E)$ in the valance band for an inverted semiconductor p-n junction

$$E_C(\mathbf{k}) = E_g + \frac{\hbar k^2}{2m_e^*},$$
$$E_{V,o}(\mathbf{k}) = -\frac{\hbar k^2}{2m_o^*}, \tag{2.1}$$

with $\hbar$: Plank constant [6]. The respective density of states within the conduction $D_C(E)$ and valance band $D_V(E)$ are given by [4]:

$$D_c(E) = \frac{(2m_e^*)^{3/2}}{2\pi^2\hbar^3}\sqrt{E - E_C} \quad \text{for} \quad E > E_C,$$
$$D_V(E) = \frac{(2m_h^*)^{3/2}}{2\pi^2\hbar^3}\sqrt{E_V - E} \quad \text{for} \quad E < E_V. \tag{2.2}$$

The electron occupation probability of a state with the energy E follows the Fermi-Dirac-statistics and is given by the temperature T dependent Fermi-Dirac-distribution $f(E, T)$

$$f(E, T) = \left(exp\left[\frac{E - E_F\left(T, m_h^*/m_e^*\right)}{k_B T} \right] - 1 \right)^{-1}, \tag{2.3}$$

with E_F: Fermi-energy, k_B: Boltzmann constant [4]. The occupation probability for the holes is given by $1 - f(E, T)$. The electron occupation probability changes from $f(E, T) \approx 1$ for $E \ll E_F$ to $f(E, T) \approx 0$ for $E \gg E_F$ and reaches exactly 0.5 at the Fermi-energy (see Fig. 2.2b). For intrinsic semiconductors and a temperature above 0 K, the Fermi-energy is usually localized above but close to the center of the band gap. The charge-carrier density within the bands is than given by the multiplication of the density of states and the occupation probability [4]. The electron density in the conduction band $\frac{d}{dE}N_C$ and the hole density in the valance band $\frac{d}{dE}P_V$ are then given by

$$\frac{d}{dE}N_C = D(E)f(E, T) \quad \text{for} \quad E > E_C,$$
$$\frac{d}{dE}P_V = D(E)(1 - f(E, T)) \quad \text{for} \quad E < E_V, \tag{2.4}$$

with N_C (P_V): electron (hole) volume concentration in the conduction (valance) band.

Semiconductor Doping and p-n Junction

The population inversion required for optical gain is preferably realized by electrical pumping of a p-n junction.

Undoped semiconductors are called intrinsic semiconductors. Doping the semiconductor material by introducing impurity atoms into the crystal leads to additional energy states in the band gap close to the band edges. For temperatures above 0 K, n-doping leads to donator levels next to the conduction band which donate electrons to the conduction band. In contrast, p-doping leads to acceptor levels close to the valance band accepting electrons from the valance band. Consequently, the Fermi-energy is shifted towards the corresponding band edge [4].

Nearly all semiconductor devices are realized as p-n junctions consisting in the simplest case of a semiconductor which is p- and n-doped on opposite sides of the junction. The equilibrium condition of a p-n junction described by the constant Fermi-energy across the complete junction leads to energy band bending and an intrinsic region in the transient region of the junction [4]. Pushing the junction out of thermal equilibrium by injecting charge carriers into the structure, e.g. via electrical pumping, leads to a reduction of the band bending and to injection of charge carriers into the former intrinsic region. For a constant carrier injection in time, new quasi thermal equilibrium condition can be deduced separately for the p- and n-region as well as separately for the conduction and valance band in the former intrinsic region [4]. Consequently, quasi-Fermi-energies are defined for holes $E_{F,h}$ and electrons $E_{F,e}$. At sufficient carrier injection, the quasi-Fermi-levels are pushed above the band edges when Eq. (2.5) is fulfilled, and population inversion of the charge carriers occurs (see Fig. 2.2c). The population inversion is mandatory to achieve optical gain in semiconductor material as will be described in the subsequent section.

$$E_{F,e} - E_{F,h} > E_g. \tag{2.5}$$

Semiconductor Nanostructures

So far, the description given above was obtained for bulk semiconductors in which the motion of the charge carriers is not restricted. Placing semiconductor layers or structures with a reduced dimensionality in the active region of a semiconductor p-i-n junction results in restriction of the carrier motion and has a huge impact on the later device properties [6, 7]. A charge carrier is restricted in its motion (confined) if the material dimension is on the order of the de Broglie wavelength[1] $\lambda_{de\ Broglie}$ of the carrier, given by

$$\lambda_{de\ Broglie} = \frac{2\pi\hbar}{\sqrt{2m^*E}}. \tag{2.6}$$

The de Broglie wavelengths of typical semiconductors are on the order of 7–70 nm [9]. Reducing the material dimension in one (quantum-well (QW)), two (quantum wire) and three dimensions (quantum dot (QD)) results in a confinement of the carriers in one, two and finally all three space directions, see Fig. 2.3. The restriction of the spacial dimension translates directly into a restriction of the corresponding momentum and as a result the square-root shaped density of states for a bulk semiconductor is modified as depicted in Fig. 2.3. The QW density of state can be described by a staircase function whereas the quantum wire exhibits a density of state proportional to the sum of inverse square roots of the energy [7, 10]. Finally, the QD has a delta function like density of states similar to the states of a single atom.

Semiconductors with a reduced dimensionality are called semiconductor nanostructures. They are usually imbedded in a bulk semiconductor exhibiting a larger

[1] Indeed, the more correct definition is based on the exciton Bohr radius [8].

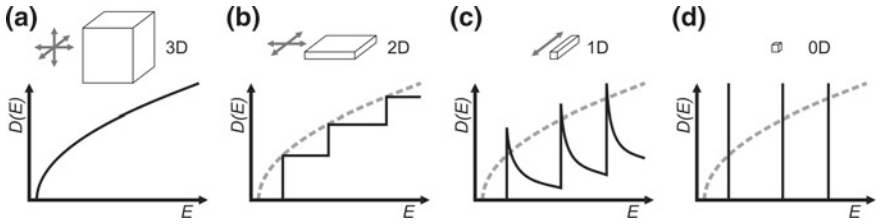

Fig. 2.3 Sketch of dimensionality and density of states $D(E)$ for **a** bulk semiconductor, **b** quantum well, **c** quantum wire and **d** quantum dot. Redrawn after [11]

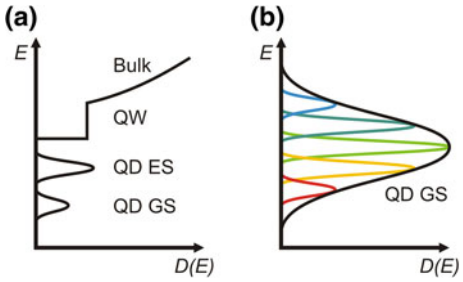

Fig. 2.4 **a** Sketch of the density of states $D(E)$ for a QD gain media with **b** a zoom into the inhomogeneously broadened QD GS resulting from the overlap of different numbers of homogeneous linewidth of equivalent QDs (*color coded*). Redrawn after [17]

band gap. The gain media used in this thesis are InGaAs/GaAs QDs (In: indium, Ga: gallium, As: arsenic) imbedded in an InGaAs QW which is surrounded by GaAs bulk material. These QDs exhibit one bound GS and a twofold degenerated ES [12, 13]. Both, the GS and ES are twofold spin degenerated [10]. Possible further upper QD states are neglected throughout this thesis. The optical emission of a single QD state is given by a Lorentzian and its linewidth is called homogeneous linewidth [10, 14–16]. Variations among different QDs lead to a shift of the levels resulting in an inhomogeneously broadened ensemble of states [10]. The resulting density of states are sketched in Fig. 2.4. Typically, the QD GS is used for amplification whereas in this thesis the ES will be used in addition. The upper density of states, i.e. of QW and bulk, can serve as a carrier reservoir for the optically active QD states.

2.1.2 Theory of Semiconductor-Light Interaction

The previous section briefly introduced band structure and population inversion of semiconductor gain media. This section gives a brief semi-classical description of the interaction of light and semiconductor. This description is valid for macroscopic scales of the material and for classical light description.

Light traveling through a dielectric, non-magnetic and non-charged semiconductor can be described by its space and time dependent electric field $\boldsymbol{\mathcal{E}}(\boldsymbol{r}, t)$. For an improved readability, the dependency of the electric field will not be written in the following. The response of the semiconductor is described by the Maxwell-equations, e.g. given in [3]. The light propagation is than given by the solution of the following wave equation

$$\nabla^2 \boldsymbol{\mathcal{E}} - \frac{1}{c^2}\frac{\partial}{\partial t}\boldsymbol{\mathcal{E}} = \frac{1}{\epsilon_0 c^2}\frac{\partial^2}{\partial t^2}\boldsymbol{\mathcal{P}}(\boldsymbol{r}, t) + \frac{\sigma}{\epsilon_0 c^2}\frac{\partial}{\partial t}\boldsymbol{\mathcal{E}}, \tag{2.7}$$

with ∇^2: Laplace operator, c_m: vacuum speed of light, ϵ_0: vacuum permittivity, $\boldsymbol{\mathcal{P}}$: electric polarization written in the following without the dependency, σ: material conductivity [3]. Under steady state conditions, the polarization response of the semiconductor to electric fields can be expressed as a function of the electric field by

$$\boldsymbol{\mathcal{P}} = \epsilon_0 \widehat{\chi}, (\omega, \boldsymbol{\mathcal{E}})\boldsymbol{\mathcal{E}}, \tag{2.8}$$

with $\widehat{\chi}(\omega, \boldsymbol{\mathcal{E}})$: susceptibility, ω: light angular frequency [3]. The frequency dependence of the susceptibility carries the dispersion properties of the material. This section assumes a linear response of the polarization to the electric field, which is valid for small field strength. A description of the nonlinear response will be given in Sect. 8.2.1.

Waiving the steady state condition, the polarization is obtained similar as an integral over time [18]. In general, the susceptibility is in general a tensor but becomes a scalar χ for isotropic media. Inserting Eq. (2.8) into Eq. (2.7) and assuming a monochromatic wave $\mathcal{E} = Re[\widetilde{E}(r)exp(-i\omega t)]$,[2] Eq. (2.7) can be simplified according to [3] to

$$\nabla^2 \widetilde{E} + \underbrace{\left(1 + \chi + \frac{i\sigma}{\epsilon_0 \omega}\right)}_{=:\epsilon_r(\omega)} \frac{\omega^2}{c^2}\widetilde{E} = 0. \tag{2.9}$$

The relative complex dielectric function ϵ_r can be defined, which is directly linked to the complex refractive index $\bar{n}$ by $\epsilon_r(\omega) = \bar{n}(\omega)^2$. The real part of the complex refractive index $\bar{n}$ equals the refractive index n indicating the phase velocity. The imaginary part κ describes the attenuation of the field within the semiconductor.

$$\begin{aligned} \bar{n} &= n + i\kappa = n + i\frac{\alpha c}{2\omega}, && \text{with} \\ n &= \sqrt{1 + Re(\chi)} && \text{and} \\ \alpha &= \frac{\omega}{cn} Im(\chi) + \frac{\sigma}{\epsilon_0 \omega}, \end{aligned} \tag{2.10}$$

[2] This equation is written in complex notation and thus Re stands for the real part whereas Im would represent the imaginary part.

with α: absorption coefficient [3]. Thus, the refractive index and the attenuation of the electric field of the propagating wave is now directly connected to the real and imaginary part of the susceptibility describing the material properties. The susceptibility can be described as the sum of a background susceptibility χ_0 describing the medium without carrier injecting, and an additional part χ_{pump}. The latter part scales with the number of injected carries and can result in an amplification of the electric field. Introducing the internal or intrinsic material losses α_{loss}, the material gain $g_{material}$ and the phenomenological confinement factor Γ describing the overlap of the electric field with the gain material, the absorption coefficient can be replaced by the more convenient net gain g_{net} [3]. The net gain describes the effective gain ($g_{net} > 0$) or loss ($g_{net} < 0$) when passing the material:

$$-\alpha = g_{net} = \Gamma g_{material} - \alpha_{loss}. \tag{2.11}$$

The exact description of the susceptibility in dependence of the carrier density $\frac{d}{dE}\tilde{N}$ (joined electron and hole density, see Eq. (2.2), p. 16) depends among others on the band structure and can be very complicated [19]. Simple phenomenological models usually assume a linear dependence on the carrier density and thus an unsaturated media[3] [3, 19]. However, the amplitude of the electric field of the wave is now connected to the material gain and losses via the imaginary part of the susceptibility which depends on the carrier density. The phase of the field ϕ is determined by the real part of the susceptibility and thus to the refractive index. While traveling through the material, the field experiences a phase change described by

$$\frac{d}{dz}\phi(z) = -\frac{1}{2} g_{material}(N)\alpha_H, \tag{2.12}$$

with α_H: α-factor or Henry factor or linewidth enhancement factor [19]. The α-factor is defined by the Kramers-Kronig relation of the change of the refractive index with the change of the carrier density as shown in Eq. (2.13) [20]. In case of large material gain ($\alpha_{loss} \ll g_{material}$) the α-factor can be approximated by the relation of the change of the real part of the refractive index n to the gain change according to [17].

$$\alpha_H = \frac{\frac{\partial}{\partial \tilde{N}} n}{\frac{\partial}{\partial \tilde{N}} \kappa} \approx -2\frac{\omega}{c}\frac{\Delta n}{\Delta g_{material}}. \tag{2.13}$$

A time dependent gain or refractive index induced by carrier density changes result also in a time dependent phase change. Hence, the α-factor is typically time dependent. Under certain condition, the Kramers-Kronig relation is abrogated for QD-based gain media [21, 22] and the time dependence of the gain and phase are decoupled. In selected configuration, the gain becomes even time independent whereas

[3] QD-based gain media are usually completely inverted at larger bias levels. Hence, more sophisticated models are required for an accurate description which are beyond the scope of this thesis.

the phase remains time dependent. These particular QD gain media characteristics will be experimentally discussed in Sect. 3.6.1 and exploited in Sect. 5.

In summary, the resonant light ($\hbar\omega = E \geq E_g$) experiences amplitude and phase changes described by complex susceptibility or the refractive index and net gain. However, the gain and phase are frequency dependent as is the susceptibility. Taking into account the semiconductor band structure, the frequency ($\hbar\omega = E$) dependent gain $g(E)$ is described by Fermi's golden rule [3]

$$g(E) \propto \int_{-\infty}^{+\infty} D_C(E_2) D_V(E_1) \, |M|^2 \left[f_C(E_2) + f_V(E_1) - 1 \right] dE_2, \tag{2.14}$$

with $|M|^2$: squared dipole matrix element describing the quantum mechanical transition property, D_C and D_V: density of states in conduction and valance band, f_C and f_V: occupation probability of electrons in the conduction band and holes in the valance band. An increase of the carrier density results according to Sect. 2.1.1 in an increase of the Fermi-energy level difference of the conduction $E_{F,e}$ and valance band $E_{F,h}$ for electrons and holes. Due to increasing density of states within the bands starting from the band edges (see Fig. 2.2), the peak carrier densities and shift more into the bands. The peak gain is shifted accordingly towards larger transition energies respectively shorter wavelengths. This blue shift of the wavelength with increasing carrier density is called band-filling effect. This effect appears similar in QW and QD gain media whereas the effect in QD devices is given by the inhomogeneous broadening of the ensemble sketched in Fig. 2.4 [23].

So far, only the gain of the material has been considered. However, the material also shows spontaneous emission experiencing gain as well. This amplified spontaneous emission (ASE) is the main source of noise in lasers and optical amplifiers and will be further discussed in Sect. 2.2.5. Here for the moment, the spontaneous emitted optical power in the direction of the income light is addressed by P_{sp}. According to [24], the power of the light P at a position r is given by the following differential equation:

$$\frac{d}{dr} P(r) = g_{net} P(r) + g_{net} P_{sp}. \tag{2.15}$$

Assuming that the net gain g_{net} and thus also the spontaneous emission are independent of the position r, this equation is solved by

$$P(r) = P_{in} e^{g_{net} r} + \underbrace{P_{sp}(e^{g_{net} r} - 1)}_{=:P_{ASE}}, \tag{2.16}$$

with P_{ASE}: the power of the amplified spontaneous emission. Introducing the more common amplification factor $G = e^{g_{net} r}$, which is used as a key parameter of optical amplifiers the total output power after a length L of material can be calculated to

$$P_{out} = P(L) = P_{in} G + P_{ASE}. \tag{2.17}$$

The amplification factor G is usually called gain and accordingly, gain refers in the following always to this factor.

2.2 Parameters of Optical Amplifiers

Optical amplifiers[4] are characterized by key parameters, such as gain, noise figure and saturation power level. This chapter will define these parameters which will be used as basic specifications of the different QD SOAs and commercial amplifiers throughout this thesis.

2.2.1 Gain

In Sect. 2.1.2 the gain G was defined as the amplification factor. Solving Eq. (2.17) for G, the gain can be calculated from the input signal power P_{in}, total output signal power P_{out} and amplified spontaneous emission (ASE) output power P_{ASE} by

$$G = \frac{P_{out} - P_{ASE}}{P_{in}}. \tag{2.18}$$

The optical power and gain values throughout this thesis are usually given in logarithmic units. The power is given in relation to 1 mW and the so obtained logarithmic power unit dBm is an absolute unit. In contrast, power differences, such as gain or losses, are given in dB, which is a relative unit.

$$P\,[\text{dBm}] = 10\ log_{10}\left(\frac{P\,[\text{mW}]}{1\,[\text{mW}]}\right) \quad \text{and} \quad G\,[dB] = 10\ log_{10}G. \tag{2.19}$$

To characterize the amplifier, the gain is typically measured as a function of the signal input or output power, which are extracted from optical spectra as standardized in e.g. [26]. The amplifier's continuous wave input signal is given by a polarized narrow bandwidth source[5] with a wavelength λ_S whereas an attenuator (Att) is used to vary the input power into the amplifier. The amplified signal is spectrally resolved and detected, e.g. using an optical spectrum analyzer (OSA). The resolution of the OSA is typically set to 0.1 nm which is significantly larger than the source signal bandwidth. The output power (P_{out}) can then be taken from the peak power level of the measured spectra, as depicted in Fig. 2.5a. The ASE power P_{ASE} at the signal wavelength λ_S is interpolated either by line approximation (in linear units) between the wavelength λ_1 and λ_2. Alternatively, the ASE background floor can be approximated e.g. by a

[4] The review given in this Sect. 2.2 follows closely the description given e.g. in [17, 25].

[5] A calculation for broad bandwidth sources is given in Appendix A.

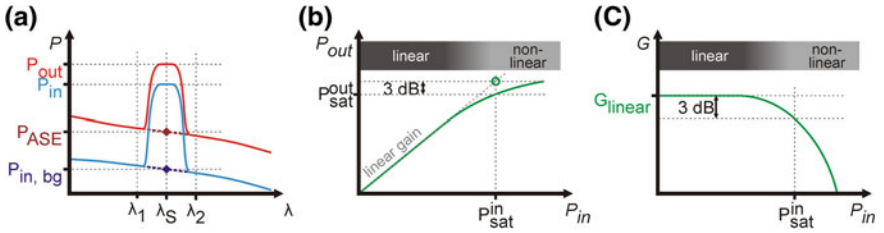

Fig. 2.5 Sketch of **a** optical power P versus wavelength λ of an amplifier input and output signal as well as marked quantities to obtain gain and noise figure. Sketch of **b** optical output power P_{out} and **c** gain G versus optical input power P_{in} of an amplifier displaying characteristic quantities of gain, saturation power levels and highlighting the linear and nonlinear gain region

polynomial function excluding the signal part between the wavelength λ_1 and λ_2. Both methods lead usually to comparable results for narrow bandwidth sources.[6] Similar measurements are performed for the input signal bypassing the amplifier. Thus, the input power (P_{in}) can be extracted if the total background power of the source signal is sufficiently small and can be neglected, which is usually the case. The internal losses of the OSA are taking into account by comparing the input power measured with a power meter (PWM) with the integrated OSA input power deconvoluted by the resolution bandwidth.

For fiber-coupled devices, the calculated gain is commonly called fiber-to-fiber gain G_{fiber} as it is calculated from the in-fiber input and in-fiber output power. These gain values are practically accessible for applications. However, taking into account coupling losses from the fiber to the gain element and vice versa, the input power reaching the gain element is reduced by the coupling losses with respect to the in-fiber input power. Accordingly, the in-fiber output power is reduced by the coupling losses with respect to the output power of the gain element. Thus, the gain of the medium excluding the coupling losses is usually called chip gain G_{chip}. Comparing different gain media offering different coupling losses only due to technological different fabrication schemes being independent of the gain media itself, the chip gain G_{chip} is usually used. Knowing the coupling losses for the input $\alpha_{coupling,\,in}$ and output signal $\alpha_{coupling,\,in}$ in logarithmic units, the chip gain is derived from the fiber-to-fiber gain by

$$G_{chip}[\mathrm{dB}] = G_{fiber}[\mathrm{dB}] + \alpha_{coupling,\,in}[\mathrm{dB}] + \alpha_{coupling,\,out}[\mathrm{dB}]. \tag{2.20}$$

If not stated differently, all gain and power levels given in this thesis are in-fiber values. From the device physics point of view, the gain as well as other measured parameters are usually plotted versus the input power because the characteristics are determined by the input power levels and the gain media. Contrary, the parameters are often plotted versus the output power from the optical communication application

[6] Saturated SOAs can exhibit a coherent noise spectral hole, which modifies the ASE spectrum in a narrow bandwidth. Hence, gain values calculated in deep saturation properly suffer from this small modification [25, 27].

point of view because the achieved output power is essential for the performance of the network. The measured parameters in this thesis are often plotted versus both, input power and output power.

2.2.2 Gain Saturation—Saturation Power

For given operating condition, i.e. current for electrical pumped SOAs, the gain is found to be independent of the optical input power for small input power levels. In this configuration, the output power scales linearly with increasing input power, see Fig. 2.5b. For a sufficient large input power, the gain starts to depend on the input signal due to a decrease of the inversion level. This is called gain saturation or gain compression and is inherent to all amplifiers for sufficient large input power levels and results in a maximal extractable output power.

Characterizing the gain saturation, the 3-dB saturation input power (P_{sat}^{in}) is defined as the input power at which the interpolated linear output power (P_{out}) is reduced by 3 dB (see Fig. 2.5b), i.e. halved. Thus, the gain is reduced by 3 dB with respect to the constant so called linear gain or unsaturated gain (see Fig. 2.5c). Correspondingly, the 3-dB saturation output power (P_{sat}^{out}) is defined as the output power level, at which the linear gain is reduced by 3 dB.

The gain saturation divides the amplifier operation condition into two regimes. The linear or small-signal regime is usually used for amplification of signals because the gain does not depend on the input power levels of the signal(s). Consequently, single and multi-channel amplification are feasible with low signal degradation and cross-talk between the channels. In contrast, cross-talk between the channels appears in the nonlinear regime which can be utilize for processing of the signals. Typically, linear amplification is achieved up to input power levels around the 3-dB saturation input power whereas efficient signal processing is usually obtained for input power levels much larger than the 3-dB saturation input power.

2.2.3 Gain Bandwidth

The linear spectral gain peak and gain bandwidth characterize the accessible wavelength range for amplification of signals. The gain bandwidth is typically defined as the spectral range in which the gain reduction is less than 3 dB with respect to the peak gain. As the ASE represents the small-signal amplification of an internally generated signal, both the spectral gain peak and gain bandwidth can be estimated from the ASE spectra. Figure 2.6 shows an ASE spectra and wavelength dependent gain measured exemplary for a QD SOA. Both curves are normalized to their peaks for easier comparison. The 3-dB ASE bandwidth is here about 15 % smaller than the 3-dB gain bandwidth. Similar results are measured for QW SOAs and PDFAs. Thus, the 3-dB ASE slightly underestimates the 3-dB gain bandwidth.

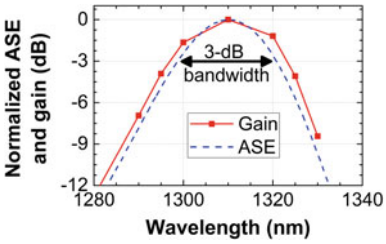

Fig. 2.6 ASE spectra and wavelength dependent gain for a QD SOA. Both curves are normalized to their peaks

2.2.4 Polarization Dependent Gain

The polarization state of an electromagnetic wave can be described by the superposition of two perpendicularly polarized electromagnetic waves. For SOAs the two perpendicular axes are called transverse electric (TE) and transverse magnetic (TM). For TE and TM polarized light the electric and magnetic field, respectively, are polarized along the growth direction of the structure. Two properties define the polarization dependent gain of a SOA. First, the typically asymmetric and tilted SOA waveguide structure[7] prefers TE polarized light [28, 29]. Secondly, the gain media itself can exhibit a polarization dependent gain [29].

SOAs usually have a polarization dependence due to their waveguide design which can be compensated by an opposed polarization dependence of the gain material. The QD SOAs used in this thesis exhibit a predominant TE polarized gain which will be discussed in detail in Sect. 3.5.2. Bulk, QW and QD gain material can be designed in their polarization dependence as briefly discussed in Sect. 3.4.

2.2.5 Noise Figure

In communication systems, the optical signal-to-noise ratio (OSNR) of a data signal is a figure of merit for the quality of the signal. The OSNR is defined as the ratio of the time-averaged signal power to the averaged noise background power [30]. Section 2.1.1 deduced the output power of the amplifier as the sum of the amplified input power and the ASE power described by Eq. (2.17) (p. 21). In consequence, ASE represents a noise floor which degrades the amplified signal quality with respect to the input signal, i.e. lowering the optical signal-to-noise ratio (OSNR). The ratio of the optical signal-to-noise ratio of the input signal $OSNR_{in}$ to the output signal $OSNR_{out}$ is called noise factor F, respectively noise figure NF in logarithmic units [31].

[7]Details of the ridge waveguide structure of the device used throughout this thesis are given in Sects. 3.1.2 and 3.1.3.

$$F = \frac{OSNR_{in}}{OSNR_{out}} \quad \text{and} \quad NF[dB] = 10log_{10}(F). \tag{2.21}$$

Detecting the amplified optical signal with a photodetector, the noise factor of the resulting photocurrent is given by the sum of noise factors due to different processes [32]:

- Shot noise of the amplified signal.
- Beating of the signal and the ASE co-polarized to the signal.
- Shot noise of the ASE.
- Beating of the ASE with itself.
- Noise due to multi-path interference.

The last three contributions are neglected in the following because on the one hand multi-path interferences are usually sufficiently suppressed. On the other hand, the ASE shot noise and ASE-ASE beating scale with $1/G^2$ whereas the shot noise and the signal-ASE beating scale with $1/G$ [32]. The ASE power level at the signal wavelength is usually significantly lower than the signal output power and hence, the noise factor contributions depend only on the ASE. The noise factor can be calculated by [17, 25, 32]

$$F \approx \frac{1}{G} + \frac{2P_{ASE,\,||}}{GhcB_{0,\,\lambda}/\lambda_S} = \frac{1}{G} + 2\underbrace{\frac{f_C}{f_C - f_V}}_{\substack{inversion\\ factor}}\frac{G-1}{G}, \tag{2.22}$$

with $P_{ASE,\,||}$: power level of ASE co-polarized to the signal, h: Planck constant, c: vacuum speed of light, $B_{0,\,\lambda}$: 3-dB filter bandwidth used to determine the ASE at the signal wavelength λ_S, $f_{C/V}$: occupation probability of conduction and valance band. In case of an input signal exhibiting a significant ASE background $P_{in,\,bg}$ (see Fig. 2.5, p. 23), the ASE power added by the amplifier has to be reduced by these values.

The minimum noise factor is achieved in case of large gain ($G \gg 1$) and total inversion ($f_C \gg f_V$) and is $F = 2$ corresponding to a noise figure of $NF = 3$ dB. However, this is valid only as long as nonlinear interaction between the ASE and signal can be neglected. If this is not the case, noise figure values below 3 dB are found, e.g. [33].

The ASE power level co-polarized to the linear polarized input signal can be measured using a co-polarized polarization filter in front of the spectrometer. Alternatively, the co-polarized ASE power level can be calculated from the measured total ASE power level P_{ASE} within the linear gain regime if the ratio of the co-polarized ($||$) and rectangular ($|-$) ASE is known [17, 25]:

$$P_{ASE,\,||} = P_{ASE}\frac{1}{1 + \frac{P_{ASE,\,|-}}{P_{ASE,\,||}}}. \tag{2.23}$$

Similar to the gain, the chip noise figure can be calculated from the in-fiber noise figure by

$$NF_{chip}[dB] = NF_{fiber}[dB] - \alpha_{coupling,\ in}[dB]. \tag{2.24}$$

If not stated differently, all noise-figure values given in this thesis are in-fiber values.

2.3 Dynamics of Conventional and QD SOAs

The previous sections introduced the gain of an externally pumped optical amplifier as a function of the carrier density. If the carrier density becomes time dependent e.g. by modulation of the electrical pump current or by a strong modulated optical input signal, the gain becomes time dependent as well. This section[8] focus on the strength of the modulated optical input signal.

2.3.1 About Slow and Fast Amplifiers

The gain is divided into a linear and a nonlinear gain regime as discussed in Sect. 2.2.2. In the linear regime the output power is mainly limited by the number of the input photons (constant gain) whereas it is mainly limited by the number of charge carriers in the nonlinear regime. Thus, the carrier dynamics in the nonlinear gain regime determine the amplification performance for modulated signals.

Slow Amplifiers
Assuming the carrier dynamics to be orders of magnitudes slower than the temporal amplitude changes of the optical input signal, the gain material cannot respond to the time dependence of the modulated signal. Simply spoken, the amplifier cannot distinguish between an unmodulated and a modulated optical input signal. From the amplifier's point of view, the modulated signal appears like an unmodulated signal with an averaged input power. Consequently, the gain remains time independent but is reduced to a steady state condition determined by a temporal average over the carrier depletion (amplification) and injection (pumping). This assumption is valid e.g. for doped fiber amplifiers like EDFAs which are widely used in today's optical communication networks.

Fiber amplifiers exhibit fluorescence lifetimes in the millisecond regime [35] whereas the modulated signal is in the range of 25–100 ps (10–40 GBd). The advantage are input power independent pattern-effect-free amplification[9] and multi-wavelength channel amplification without a cross-gain modulation (XGM) induced crosstalk between the channels. But of course, the averaged gain of each channel is

[8] The review given in this Sect. 2.3 follows closely the description given e.g. in [17, 25, 34].

[9] Patterning of optical amplifiers is explained in Sect. 4.3.2.

influenced by the others and nonlinear effects like e.g. the Kerr effect can still cause crosstalk. Among others, the important disadvantage of fiber amplifiers is usually the unsuitability for processing of optical data signals due to the slow response.

Fast Amplifiers
Amplifiers exhibiting a much fast dynamics in the order of the signal changes can respond to the signal changes and processing of the signals becomes feasible. Patterning-free amplification and multi-wavelength channel amplification are usually feasible as long as the amplifiers is operated in the linear gain regime. Commonly, SOAs belong to this amplifier type as they show carrier dynamics in the picosecond regime, e.g. characterized for bulk, QW and QD gain material in [36–49]. For this type of amplifiers the gain remains time independent in the linear gain regime, but commonly is time dependent in the nonlinear gain regime. Hence, the carrier dynamics will be discussed in the next section for both, QD SOA and conventional SOAs exemplary for bulk material.

2.3.2 Semiconductor Optical Amplifiers

Phenomenologically, inter-band processes as well as intra-band processes contribute to the carrier dynamics. Inter-band processes describe the generation and recombination of charge carriers, i.e. electrons and holes, between the valance and conduction band, and hence a change of the carrier density of the bands. Intra-band processes describe the change of the charge-carrier distribution within the valance and conduction band.

In an electrical pumped semiconductor gain media inter-band effects account to [3, 6, 17, 25]:

- Carrier injection (CI) via the applied forward bias increasing the charge-carrier density.
- Radiative recombination, i.e. absorption, stimulated and spontaneous emission, which have been introduced in the beginning of Sect. 2.1. Stimulated and spontaneous emission decrease the carrier density whereas absorption result in an increase of the carrier density.
- Non-radiative processes like leakage current, defect recombination (via phonon emission), Shockley-Read-Hall recombination (recombination via forbidden levels in the band gap) and inter-band Auger recombination (excitation of a second carrier) decrease the charge-carrier density.

Intra-band effects account to [3, 17, 25]:

- Auger scattering describe the relaxation of an excited charge carrier into a lower empty energy state while energy and momentum is transferred to a second carrier in the identical band. Thus, the second carrier is excited.

- Phonon processes describe the relaxation and excitation of carriers due to phonon emission (carrier relaxation) and phonon absorption (carrier excitation) joined to carrier-phonon scattering.

The temporal gain dynamics are strongly determined by the lifetimes of the individual intra-band and inter-band processes. According to [17], the effective carrier lifetime τ can be described as a sum of the lifetime of the individual processes $\tau_{process}$ by

$$\frac{1}{\tau} = \sum_{processes} \frac{1}{\tau_{process}}. \tag{2.25}$$

The different processes are experimentally accessible by various techniques, as exemplarily addressed in Sect. 3.6. The most common technique is the pump-probe configuration which will be discussed in more detail in Sect. 3.6. A sufficiently short (usually a few hundred femtoseconds) and intense (nonlinear gain regime) optical pump pulse depletes a specific part of the density of states. Hence, the pulse pushes the gain media out of the steady state condition. The appearing gain and phase change as well as the recovery of the system back to the steady state condition are probed using a sufficiently short and weak (linear gain regime) probe pulse. This pulse is temporally delayed with respect to the perturbing pump pulse. For a detailed introduction to pump-probe spectroscopy, please consider e.g. [50].

Typical pump-probe traces and the involved processes will be discussed phenomenologically in the following paragraphs based on [17, 25, 34]. A sketch of a pump-probe curve is shown in Fig. 2.7a, c for conventional and QD SOAs, respectively. The corresponding change of the carrier density is depicted in Fig. 2.7b, d. For the sake of simplicity, only a joined electron-hole density for conduction and valance band is discussed.

Conventional SOAs

We start with the dynamics of conventional gain media sketched in Fig. 2.7a, b. The amplification of the pump pulse injected at time $t = 0$ causes a reduction of the gain G called gain compression. The carrier density is depleted in a narrow energy interval determined by the spectrum of optical pulse. This carrier depletion is called spectral hole burning (SHB). The gain recovers partly in a time scale of about 100 fs by intra-band Auger scattering resulting in closing of the spectral hole [34, 40, 51]. The resulting carrier distribution equals a Fermi-distribution with a temperature larger than the lattice temperature. Thus, this effect is called carrier heating (CH). The carrier distribution relaxes by intra-band phonon scattering within a few picoseconds, called carrier cool down (CCD) [22, 34, 36, 37, 51]. Finally, inter-band carrier injection (CI) refills the carrier density to its origin within a nanosecond time scale [34]. In consequence, the gain recovery is divided into three main time constants and requires for conventional gain media up to 1 ns. But the time can be drastically reduced to the tens picosecond range by an increased carrier injection and other techniques [34]. According to Sect. 2.1.2 the time dependent gain and carrier density results in a change of the refractive index and accordingly into phase changes in a comparable

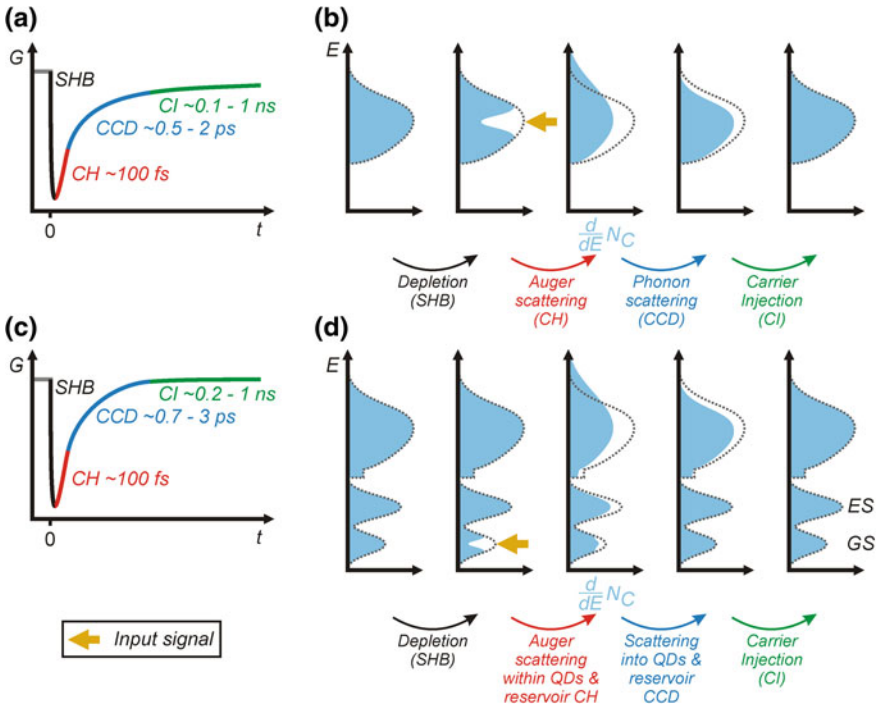

Fig. 2.7 Sketch of the pump-probe curve for **a** conventional and **c** QD gain media. The corresponding change of the carrier density $d/dEN(E)$ is sketched in (**b**) and (**d**). For the sake of simplicity, only a joined electron-hole density for conduction and valance band is plotted. *SHB* spectral hole burning, *CH* carrier heating, *CCD* carrier cool down, *CI* carrier injection. Redrawn after [17, 25, 34]

time scale. In case of a repeating optical signal, carrier depletion and CI are repeated resulting in a dynamic equilibrium called carrier density pulsation (CDP).

Quantum-Dot SOAs

QD gain media show superior advantages of the gain recovery dynamics if the structure exhibits a large carrier density as discussed in the following. As mentioned before in Sect. 2.1.1, the carriers in the QW and bulk serve as a carrier reservoir refilling the QD states. For the QD GS, also the ESs serve as a reservoir. The QD density of states are smaller than conventional gain material. Hence, the above claimed large carrier density is achieved when the carrier density in the reservoir is at least a factor of 10^4 larger than in the QDs [25]. This situation is reached for the QD GS at moderate currents but appears for the QD ES at a much larger current due to the twofold carrier density and the smaller energy separation to the carrier reservoir. The lower QD carrier density as well as their position well below the quasi Fermi-energy results in a maximum carrier population inversion even at moderate drive currents. Hence, the

linear gain is saturated under these conditions and is independent of the total carrier density [52]. The focus is here on the GS dynamics but also applies for the ES [41].

Similar to the conventional gain media, SHB occurs in the inhomogeneously broadened QD GS carrier density due to amplification of the pump pulse. The refilling of the QD GS starts predominantly by Auger scattering from the reservoir into the GS in a time range down to 100 fs [40]. This results similar to the conventional gain material into CH of the reservoir and partially the ES carrier distribution [22, 40, 41]. Subsequently, Auger scattering into the QD levels, both GS and ES as well as the CCD of the reservoir carrier distribution takes place on time scale of a few picoseconds [22, 40, 41, 53]. At this stage, the QD GS gain recovery is completed whereas the CI refills the reservoir on a longer time scale. As long as the carrier reservoir is and remains highly populated after QD state replenishment (see above request), the QD gain recovery is only limited by the closure of the SHB as well as by the intra-dot relaxation time for larger depletion and/or durations [52]. Additionally, the gain of QDs with a different homogenous center wavelength as the perturbed QDs could be expected to be uninfluenced. Indeed, the perturbation can be mediated between the QDs via the carrier reservoir as will be further discussed in the framework of a macroscopic rate-equation model in the Sects. 3.6.2, 3.6.3 and 7.3 or in more detail in [54, 55].

In case the carrier reservoir is not highly populated as requested above, the QD refilling is limited by carrier density of the reservoir and thus follows the reservoir dynamics. In particular, the QD gain recovery is then limited by CDP similar to the conventional gain media [25].

Therefore, the QD gain dynamics are independent of the total carrier density if the reservoir carrier density is sufficient large. At this point of operation, the QD gain media demonstrate one of its superior advantages.

The phase dynamics are determined according to Sect. 2.1.2 by the carrier density change within the complete structure (Kramers-Kronig relation). Precisely, each group of states, i.e. QD GS, ES and the reservoir, exhibit carrier density changes and thus contribute to the phase dynamics. But due to the much larger number of carriers in the reservoir and the fast gain recovery of the QDs states, the mid- and long-term phase dynamics are dominated by the reservoir carrier dynamics. The phase recovery times of conventional and QD gain media are therefore comparable. In consequence, the gain and phase dynamics are decoupled assuming ideal QD gain media [21, 56]. Indeed, this behavior is another unique feature of QD gain media and will be exploit in Chap. 5.

2.4 Summary

This chapter gave an introduction to the physics, dynamics and parameters of semiconductor optical amplifiers (SOAs). The amplification of these devices base upon stimulated emission of an inverted semiconductor gain medium. Hence, semiconductor p-n junctions and their inversion via electrical pumping, and subsequently

the interaction of inverted semiconductor gain media and light as well as the origin of gain have been introduced. In addition, the carrier density change induced phase change of the light has been addressed.

Important parameters of optical amplifiers have been defined, e.g. gain, gain saturation and noise figure.

Nanostructured gain materials, in particular QDs have been introduced. In comparison to bulk or QW, QDs exhibit a discrete energy spectrum with delta function like density of states [10, 57]. The optical emission of a QD ensemble shows an inhomogeneously broadened emission due to variations between the QDs [10]. The population inversion is achieved for QD devices at much lower currents demonstrated by very low laser threshold [10, 58–60]. The separation of gain providing QD states and the bulk or QW-based carrier reservoir results in record fast gain recovery dynamics and a separation of phase and gain dynamics [21, 22, 40–44, 47]. Particularly, QD SOAs exhibit a fast gain recovery in the linear and nonlinear gain regime as long as the reservoir remains highly populated. Hence, QD-based SOAs enable plenty of applications which will be addressed in this thesis.

References

1. S.M. Sze, K.K. Ng, *Physics of Semiconductor Devices*, vol. 3 (Wiley, London, 2006), p. 832
2. S.-L. Chuang, *Physics of Photonic Devices*, 2nd edn. (Wiley, London, 2009)
3. G.P. Agrawal, N.K. Dutta, *Semiconductor Lasers*, 2nd edn. (Springer, London, 2001), p. 616
4. H. Ibach, H. Lüth, *Solid-State Physics: An Introduction to Principles of Materials Science*, 3rd edn. (Springer, Berlin, 2013), p. 503
5. E.V. Goldstein, P. Meystre, Spontaneous emission in optical cavities: a tutorial review, in *Spontaneous Emission and Laser Oscillation in Microcavities*, 1st edn., ed. by H. Yokoyama, K. Ujihara (CRC Press, London, 1995), p. 384
6. C. Kittel, *Einführung in die Festkörperphysik*, 15th edn. (Oldenbourg Verlag, Munchen, 2013), p. 754
7. M. Asada, Y. Miyamoto, Y. Suematsu, Gain and the threshold of three-dimensional quantum-box lasers. IEEE J. Quantum Electron. **22**(9), 1915–1921 (1986)
8. H. Eisele, The atomic composition of semiconductor quantum dots and related nanostructures. Professorial dissertation. TU Berlin, 2013, p. 462
9. V.V. Mitin, V.A. Kochelap, M.A. Stroscio, *Introduction to Nanoelectronics: Science, Nanotechnology, Engineering, and Applications*, 1st edn. (Cambridge University Press, Cambridge, 2008), p. 329
10. D. Bimberg, M. Grundmann, N.N. Ledentsov, *Quantum Dot Heterostructures*, 1st edn. (Wiley, London, 1998)
11. D. Bimberg (ed.), *Semiconductor Nanostructures*, 2nd edn. (Springer, Berlin, 2008)
12. A. Schliwa, Electronic properties of quantum dots. Doctoral Thesis. Technische Universitaet Berlin, 2007
13. D. Arsenijević et al., Comparison of dynamic properties of ground- and excited-state emission in p-doped InAs/GaAs quantum-dot lasers. Appl. Phys. Lett. **104**(18), 181101 (2014)
14. K. Brunner et al., Photoluminescence from a single GaAs/AlGaAs quantum dot. Phys. Rev. Lett. **69**(22), 3216–3219 (1992)
15. M. Grundmann et al., Ultranarrow luminescence lines from single quantum dots. Phys. Rev. Lett. **74**(20), 4043–4046 (1995)

16. D. Gammon et al., Homogeneous linewidths in the optical spectrum of a single galliumarsenide quantum dot. Science **273**(5271), 87–90 (1996)
17. R. Bonk. Linear and nonlinear semiconductor optical amplifiers for next-generation optical networks. Doctoral Thesis. Karlsruher Institut für Technologie, 2013, p. 278
18. J.-C. Diels, W. Rudolph, *Ultrashort Laser Pulse Phenomena*, 2nd edn. (Academic Press, London, 2006)
19. G.P. Agrawal, N.A. Olsson, Self-phase modulation and spectral broadening of optical pulses in semiconductor laser amplifiers. IEEE J. Quantum Electron. **25**(11), 2297–2306 (1989)
20. C.H. Henry, Theory of the linewidth of semiconductor lasers. IEEE J. Quantum Electron. **18**(2), 259–264 (1982)
21. A.V. Uskov et al., Carrier-induced refractive index in quantum dot structures due to transitions from discrete quantum dot levels to continuum states. Appl. Phys. Lett. **84**(2004), 272–274 (2004)
22. A.V. Uskov, T.W. Berg, J. Mørk, Theory of pulse-train amplification without patterning effects in quantum-dot semiconductor optical amplifiers. IEEE J. Quantum Electron. **40**(3), 306–320 (2004)
23. R. Heitz et al., Many-body effects on the optical spectra of InAs/GaAs quantum dots. Phys. Rev. B **62**(24), 16881–16885 (2000)
24. M.J. Connelly, *Semiconductor Optical Amplifiers*, 1st edn. (Kluwer Academic, London, 2007)
25. C. Meuer, GaAs-based quantum-dot semiconductor optical amplifiers at 1.3 μm for all-optical networks. Doctoral Thesis. Technical University of Berlin, 2011, p. 155
26. Internatinal norm IEC 61290-1-1:1998, optical spectrum analyzer
27. M. Shtaif, G. Eisenstein, Noise properties of nonlinear semiconductor optical amplifiers. Opt. Lett. **21**(22), 1851–1853 (1996)
28. N.K. Dutta, Basic principles of laser diodes, in *Handbook of Laser Technology and Applications: Laser Design and Laser Systems*, vol. 2, 1st edn., ed. by C.E. Webb, J.D.C. Jones (CRC Press, London, 2004)
29. H. Kawaguchi, Semiconductor lasers and optical amplifiers for switching and signal processing, in *Handbook of Laser Technology and Applications: Laser Design and Laser Systems*, vol. 2, 1st edn., ed. by C.E. Webb, J.D.C. Jones (CRC Press, London, 2004)
30. J. Thompson, E.E. Bergmann, Stress tests in high-speed serial links, in *Digital Communications Test and Measurement: High-Speed Physical Layer Characterization*, 1st edn., ed. by D. Derickson, M. Muller (Prentice Hall, Upper Saddle River, 2007)
31. H. Haus, Noise figure definition valid from RF to optical frequencies. IEEE J. Sel. Top. Quantum Electron. **6**(2), 240–247 (2000)
32. Internatinal norm IEC 61290-3:2000, optical fibre amplifiers. Basic specification. Test methods for noise figure parameters, 2000
33. A. Bilenca, G. Eisenstein, On the noise properties of linear and nonlinear quantumdot semiconductor optical amplifiers: the impact of inhomogeneously broadened gain and fast carrier dynamics. IEEE J. Quantum Electron. **40**(6), 690–702 (2004)
34. J. Mørk, M.L. Nielsen, T.W. Berg, The dynamics of semiconductor optical amplifiers: modeling and applications. Opt. Photonics News **14**(7), 42–48 (2003)
35. M.J. Digonnet (ed.), *Rare-Earth-Doped Fiber Lasers and Amplifiers (Revised and Expanded)*, 2nd edn. (CRC Press, London, 2005), p. 798
36. G. Eisenstein et al., Ultrafast gain dynamics in 1.5 μm multiple quantum well optical amplifiers. Appl. Phys. Lett. **58**(2), 158 (1991)
37. S. Weiss et al., Carrier capture times in 1.5 μm multiple quantum well optical amplifiers. Appl. Phys. Lett. **60**(1), 9 (1992)
38. J. Wang et al., Carrier capture times in quantum-well, -wire, and -box distributed feedback lasers characterized by dynamic lasing emission measurements. IEEE J. Sel. Top. Quantum Electron. **3**(2), 223–229 (1997)
39. F. Girardin, G. Guekos, A. Houbavlis, Gain recovery of bulk semiconductor optical amplifiers. IEEE Photonics Technol. Lett. **10**(6), 784–786 (1998)

40. P. Borri et al., Spectral hole-burning and carrier-heating dynamics in InGaAs quantumdot amplifiers. IEEE J. Sel. Top. Quantum Electron. **6**(3), 544–551 (2000)
41. T.W. Berg et al., Ultrafast gain recovery and modulation limitations in self-assembled quantum-dot devices. IEEE Photonics Technol. Lett. **13**(6), 541–543 (2001)
42. S. Schneider et al., Excited-state gain dynamics in InGaAs quantum-dot amplifiers. IEEE Photonics Technol. Lett. **17**(10), 2014–2016 (2005)
43. P. Borri et al., Ultrafast carrier dynamics in InGaAs quantum dot materials and devices. J. Opt. A Pure Appl. Opt. **8**(4), S33–S46 (2006)
44. A.J. Zilkie et al., Carrier dynamics of quantum-dot, quantum-dash, and quantum-well semiconductor optical amplifiers operating at 1.55 μm. IEEE J. Quantum Electron. **43**(11), 982–991 (2007)
45. T. Piwonski et al., Carrier capture dynamics of InAs/GaAs quantum dots. Appl. Phys. Lett. **90**(12), 122108 (2007)
46. I. O'Driscoll et al., Phase dynamics of InAs/GaAs quantum dot semiconductor optical amplifiers. Appl. Phys. Lett. **91**(26), 263506 (2007)
47. T. Vallaitis et al., Slow and fast dynamics of gain and phase in a quantum dot semiconductor optical amplifier. Opt. Express **16**(1), 170–178 (2008)
48. T. Erneux et al., The fast recovery dynamics of a quantum dot semiconductor optical amplifier. Appl. Phys. Lett. **94**(11), 113501 (2009)
49. J. Gomis-Bresco et al., Time-resolved amplified spontaneous emission in quantum dots. Appl. Phys. Lett. **97**(25), 251106 (2010)
50. J. Shah, *Ultrafast Spectroscopy of Semiconductors and Semiconductor Nanostructures*, vol. 11, 1st edn. (Springer, Berlin, 2013)
51. K.L. Hall et al., Femtosecond gain dynamics in InGaAsP optical amplifiers. Appl. Phys. Lett. **56**(18), 1740 (1990)
52. A.V. Uskov et al., On gain saturation in quantum dot semiconductor optical amplifiers. Opt. Commun. **248**(1–3), 211–219 (2005)
53. A.V. Uskov et al., Auger capture induced carrier heating in quantum dot lasers and amplifiers. Appl. Phys. Express **4**(2), 22202 (2011)
54. B. Lingnau, *Nonlinear and nonequilibrium dynamics of quantum-dot optoelectronic devices*. Doctoral Thesis. Technische Universität Berlin, 2015
55. A. Röhm, *Dynamic scenarios in two-state quantum dot lasers*. Master Thesis. Technische Universität Berlin, 2015
56. A.V. Uskov et al., On ultrafast optical switching based on quantum-dot semiconductor optical amplifiers in nonlinear interferometers. IEEE Photonics Technol. Lett. **16**(5), 1265–1267 (2004)
57. O. Stier, M. Grundmann, D. Bimberg, Electronic and optical properties of strained quantum dots modeled by 8-band k p theory. Phys. Rev. B **59**(8), 5688–5701 (1999)
58. N. Kirstaedter et al., Gain and differential gain of single layer InAs/GaAs quantum dot injection lasers. Appl. Phys. Lett. **69**(9), 1226 (1996)
59. R.L. Sellin et al., Close-to-ideal device characteristics of high-power InGaAs/GaAs quantum dot lasers. Appl. Phys. Lett. **78**(9), 1207 (2001)
60. D. Bimberg, U.W. Pohl, Quantum dots: promises and accomplishments. Mater. Today **14**(9), 388–397 (2011)

Chapter 3
Samples and Characterization

The previous chapter has introduced the theoretical background of semiconductor gain media and has addressed the advantages of QD-based gain material. In the first part, this chapter focuses on the realization of SOAs, particularly the realization of p-n junctions, and the guiding of light. The second part presents the series of samples used for experiments throughout this thesis and subsequently discusses various static and dynamic properties of the samples series. In detail, this chapter is organized as follows:[1]

First, the epitaxial structure as well as the device design and fabrication is described in Sect. 3.1. The waveguide design, processing and facet anti-reflection coating will be discussed in terms of confinement, direct modulation properties and cavity suppression. Section 3.2 is devoted to the standard setup stage used to characterize the QD SOA chips. An overview of the static parameters of all QD SOAs, such as light-intensity-voltage (LIV) curve, ASE spectra, gain and noise figure, are given in Sect. 3.3. The static parameters of the QD SOAs will be compared to commercially available O-band amplifiers in Sect. 3.4. Further details on the static properties of the QD SOAs are addressed in Sect. 3.5. In detail, the dependence of gain and gain bandwidth with increasing device length as well as the wavelength dependence of the polarized emission are discussed. Section 3.6 presents the characterization of gain and phase dynamics of QD SOAs focused on the intra-dot and dot-reservoir coupling. Finally, Sect. 3.7 summarizes the obtained results.

[1] Parts of this chapter have been previously published in [2–16]. 2: Fiol 2009; 3: Bimberg 2009a; 4: Bimberg 2009c; 5: Meuer 2011a; 6: Meuer 2011b; 7: Meuer 2011c; 8: Schmeckebier 2011; 9: Schmeckebier 2012; 10: Kaptan 2014a; 11: Kaptan 2014b; 12: Schmeckebier 2014a; 13: Rohm 2015a; 14: Zeghuzi 2015a; 15: Zeghuzi 2015b; 16: Schmeckebier 2015a.

H. Schmeckebier, *Quantum-Dot-Based Semiconductor Optical Amplifiers for O-Band Optical Communication*, Springer Theses,
DOI 10.1007/978-3-319-44275-4_3

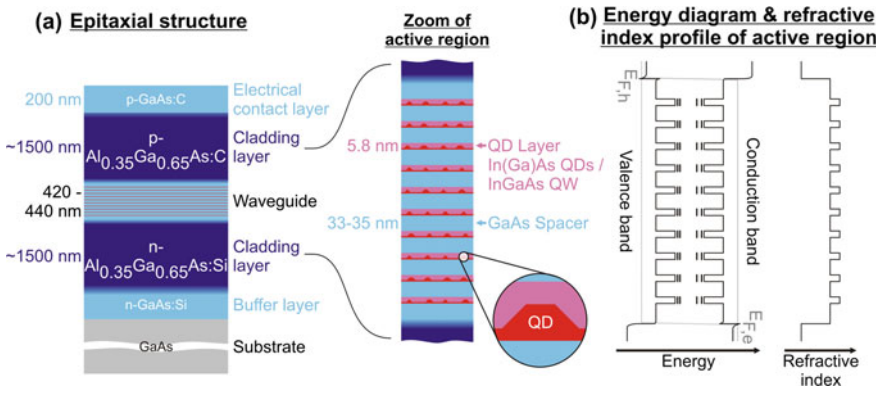

Fig. 3.1 **a** Epitaxial structure of the QD wafer with a zoom of the active region (loosely based on [5]). **b** A simplified schematic of the refractive index profile and the energy diagram is sketched including the electron $E_{F,e}$ and hole $E_{F,h}$ Fermi-levels under current injection neglecting effects like band bending. The dimensions are not in size

3.1 Epitaxial Structure, Processing and Post-processing

This section introduces and discusses the epitaxial structure, the waveguide design, and the processing and post-processing steps for the fabrication of QD SOAs.

3.1.1 Epitaxial Structure

The epitaxial structure of the QD SOAs is sketched in Fig. 3.1 and was grown on a n^+ type GaAs substrate using molecular beam epitaxy (MBE). The structure will be introduced in this section without going into the details of growth conditions and parameters. For further information please refer to the following literature [1–4].

The p-i-n-diode structure contains a separate-confinement double heterostructure in which the charge carriers and the optical mode are confined by different epitaxial layers. The optical mode is vertically guided by a waveguide, which is formed by sandwiching a GaAs core region between cladding layers with a lower refractive index. The carriers are confined within the active material located in the GaAs core region.

The waveguide is symmetrically designed with 1.5 µm thick n-doped and p-doped $Al_{0.35}Ga_{0.65}As$ bottom and top cladding. Both cladding layers exhibit a stepwise reduction of the doping from about 3×10^{18} to about 5×10^{17} cm^{-3} towards the intrinsic waveguide core. A 200 nm thick highly p-doped (10^{20} cm^{-3}) GaAs electrical contact layer is grown on top of the top cladding. GaAs/AlGaAs superlattices are used at all layer boundaries to avoid defects and to lower the series resistance.

The 420–440 nm thick active region consist of an intrinsic GaAs matrix with a stack of five or ten QD layers centered within the waveguide. The QDs are grown in self-organized Stranski-Krastanov growth mode with an areal density of typically 3×10^{10}–5×10^{10} dots/cm^2. Each QD layer is overgrown with a 5 nm thick $In_{0.15}Ga_{0.85}As$ QW in order to red-shift the emission wavelength to 1.3 μm (dot-in-a-well structure). The QDs have a truncated pyramidal shape with a base length of 15–30 nm and a height of 3–7 nm [4, 6–9]. The QD layers are separated by a 33–35 nm thick GaAs spacer layers providing strain relaxation and avoiding an electronic coupling of the QD layers.

Forward biasing the electrical p-i-n diode structure injects carriers into the active region. The carriers are predominantly concentrated within the In(Ga)As QDs and the surrounding InGaAs QW which both exhibit a lower band gap than the surrounding GaAs spacer. A carrier population inversion occurs in the active medium if the quasi-Fermi level difference of electrons and holes exceeds the bandgap enabling stimulated emission, as introduced in Sect. 2.1.1.

3.1.2 Processing

SOAs are fabricated by processing of the wafer with the epitaxial grown structure on top with the aim to apply electrical metal contacts to the p-i-n diode as well as to realize a lateral guiding of the optical mode, i.e. perpendicular to the epitaxial growth direction. The lateral confinement of the light as well as a current guiding is realized by tailoring the SOA structure using a ridge-waveguide structure.

Deeply-etched ridge waveguide structures are formed by removing the contact layer, the upper cladding layer, and the active region keeping only a few μm thick ridge (see Fig. 3.2). Contrary, for shallow-etched ridge waveguide structures only the contact and partly the upper cladding layer are etched off. The optical wave is thus gain guided and experiences a weak index guiding as well, caused by the charge carrier induced refractive index reduction in combination with the index step at the ridge edges above the active region. In contrast, the optical mode is laterally confined by the large refractive index step in deeply-etched ridge waveguides. This ridge offers therefore a stronger confinement of the optical mode but exhibits increased waveguide losses in comparison to the shallow-etched ridge. However, larger photon densities are achievable due to the stronger confinement privileging the deeply etched structures for nonlinear applications due to reduced saturation power levels (see Sect. 2.2.2). Comparing shallow and deeply-edged ridge waveguides with similar width, the former shows current spreading and thus a slight larger effective electrically pumped ridge width. The processing is briefly explained in the following. For a more detailed description please refer to the following literature [5, 11].

The 4 μm wide ridge waveguides are processed by dry etching using silicon nitride (Si_3N_4) or the metal top contact as an etch mask. For shallow-edged ridges, the etching was stopped about 170 nm above the active region. The complete structure was covered on top with a 100–300 nm thick Si_3N_4 layer for electrical isolation. For

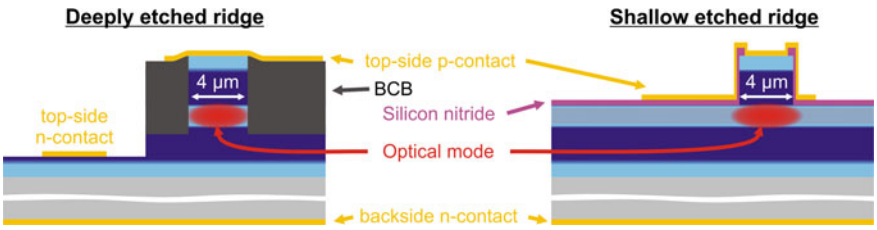

Fig. 3.2 Sketch of deeply- and shallow-etched ridge waveguide QD SOAs. The dimensions are not in size. Further description are given in the text

the deeply-etched ridges the etching was stopped about 800 nm below the active region. Depositing Benzocyclobutene (BCB, C_8H_8) on top of this structure enables an electrical isolation and planarizes the structure. The isolation of both structures was opened by selective etching on top of the ridges. The subsequent top-side p-contact metallization was applied by depositing 550–800 nm Ti/Pt/Au+Cr/Au (Ti: titan, Pt: platinum, Au: gold, Cr: chromium). In case of a shallow-etched electrically separated multi-section QD SOA, a 20 µm broad gap of the ridge was not metallized. This gap was dry etched through the highly doped upper cladding layer ensuring an electric resistance between the sections large than 10 kΩ. The deeply-etched ridge received a top-side n-contact by selective etching down to the highly doped lower cladding and the subsequent deposition of about 300 nm Ni/Au:Ge/Au (Ni: nickle, Ge: germanium). Thus, the deeply-etched structures can be electrically contacted with a high-frequency (HF) probe head. Together with the planarized structure reducing the diode parasitic capacitances, the current of the deeply etched QD SOA can be directly modulated. After thinning the wafer substrate down to a thickness of about 120 µm, a 300 nm thick Ni/Au:Ge/Au backside n-contact was applied to both structures.

3.1.3 Design and Post-processing

The QD SOAs are designed as a traveling-wave amplifier with a single pass of the input signal through the waveguide in the ideal case. For GaAs-based waveguides, the as-cleaved facet reflectivity of the waveguide is about 32–33 %. The reflection leads to standing waves within the Fabry-Pérot cavity resulting in wavelength dependent gain oscillations, the so called longitudinal modes or gain ripples. For sufficient large gain values, the amplifier usually switches into the lasing mode. To avoid the onset of lasing and to suppress the gain ripples, the facet reflection of the waveguide has to be reduced. This can be realized by tilting the waveguide by an angle θ with respect to the facet normal (see Fig. 3.3 inset) as well as by implementing an (AR) coating on the facets. Both in combination are typically used for SOAs.

The QD SOAs predominantly emit TE polarized light as will be discussed in Sect. 3.5.2. TE polarized light has the polarization along the growth plan respectively vertical to the growth direction. The polarization orthogonal to the TE axis is called transverse magnetic (TM). According to [10, 11], the reflection R of a tilted waveguide at the as-cleaved facet can be estimated for TE polarized light by Eq. 3.1 assuming a Gaussian optical mode profile.

$$R(\theta) = \left(\frac{cos\theta - n_1\sqrt{1 - n_1^2 sin^2\theta}}{cos\theta + n_1\sqrt{1 - n_1^2 sin^2\theta}} \right)^2 exp\left[-\left(\frac{\pi n_2 w\theta}{\lambda} \right)^2 \right], \tag{3.1}$$

with θ: waveguide tilt, n_1: effective waveguide refractive index, n_2: lateral cladding refractive index, λ: longitudinal wavelength, w: lateral 1/e-width of the electrical mode field. The refractive index for the deeply-etched waveguide are assumed to be $n_1 = 3.65$ [11] and $n_{2,\,deeply} = 1.54$ (BCB) [11]. The effective waveguide refractive index n_1 for the shallow-etched ridge is similar to the deeply-etched ridge whereas $n_{2,\,shallow}$ is a bit trickier. On the one hand, the refractive index of GaAs is changed by less than 0.1 under a free carrier concentration up to 10^{19} cm^{-3} [12]. On the other hand, the optical mode experiences a weak influence of the Si_3N_4-ridge isolation exhibiting a refractive index of 2.5 [13]. Thus, an effective $n_{2,shallow}$ of 2.5 is assumed allowing an worst-case approximation since a smaller refractive index difference would lead to an even lower reflectivity. Without detailed simulations, the mode width w within the 4 µm wide waveguide has to by roughly estimated and was thus varied: $w_{deeply} = 1.7$–2.3 µm and $w_{shallow} = 2.0$–3.0 µm. The reflectivity of both ridge types are shown in Fig. 3.4a for a wavelength λ of 1300 and 1220 nm.

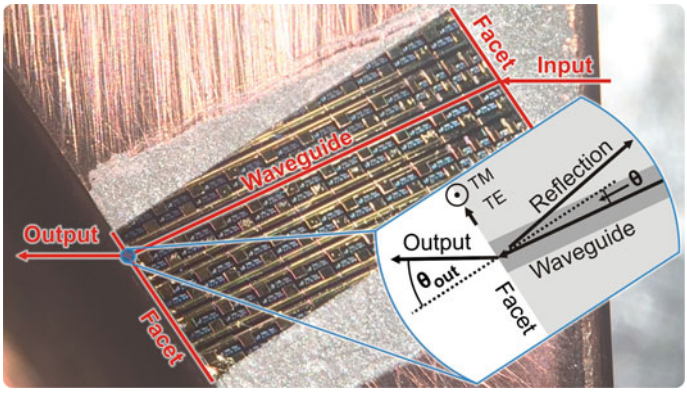

Fig. 3.3 Top view of a QD SOA chip glued on a copper mount. The chip comprises in total 6 operating QD SOAs, among others QD SOA No. 5 (see page 48) which is marked. Visible are the input and output facet as well as the top-side p-contact gold stripe with contacted gold pads. The ridge waveguide lays below the gold stripe. The *inset* depicts a general sketch for the angles and beam paths of a tilted waveguide

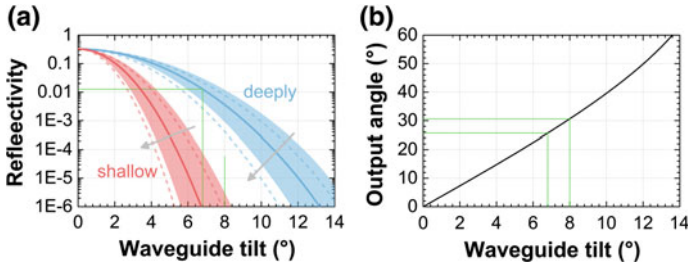

Fig. 3.4 **a** Reflectivity R and **b** output angle θ_{out} in dependence of the tilt θ of the 4 µm wide ridge waveguide. The reflectivity of the shallow-etched ridge is calculated using Eq. 3.1 with $n_1 = 3.65$, $n_2 = 2.5$, $\lambda = 1300$ nm (dashed 1220 nm) and $w = 2/2.5/3$ µm (increasing in *arrow* direction). The deeply-etched ridge reflectivity is calculated with $n_1 = 3.65$, $n_2 = 1.54$, $\lambda = 1300$ nm (dashed 1220 nm) and $w = 1.7 / 2.5 / 2.3$ µm (increasing in *arrow* direction). The shallow- and deeply-edged waveguide tilt of 8° and 6.8° used for the QD SOAs in this thesis are marked green

The angle θ_{out} of the output-coupled light with respect to the facet normal can be estimated from Snell's law by:

$$\theta_{out} = \arcsin[n_1 sin(\theta)]. \tag{3.2}$$

The optimum waveguide tilt is a trade of between a low reflectivity and low coupling losses. As shown in Fig. 3.4a, the reflectivity can be reduced for a given ridge structure by increasing the waveguide tilt as well as enlarging the lateral mode dimension. Because SOAs for present optical communication application networks require a transverse single-mode emission, the upper mode dimension is restricted. All tilted QD SOAs in this thesis have a 4 µm ridge width ensuring a single-mode operation under almost all operating conditions. Increasing the waveguide tilt results in an increased output angle hampering the light coupling into a fiber and typically increasing the coupling losses. Comparing the typical QD GS peak wavelength of 1300 nm with a QD ES peak wavelength of 1220 nm, the wavelength has a comparatively low influence on the reflectivity (see Fig. 3.4a).

The deeply-edged QD SOAs characterized in this thesis were fabricated in the framework of the thesis of M. Laemmlin [10]. They exhibit a waveguide tilt of 6.8° resulting in a simulated reflectivity of about 1 % without taking the AR coating into account. The shallow-edged QD SOAs characterized in this thesis exhibit a

waveguide tilt of 8°. The larger lateral optical mode dimension and the lower refractive index step of the shallow-edged ridge leads to an improved theoretical reflectivity below 10^{-5}.

In addition to the waveguide tilt, all QD SOAs are AR coated. A periodic dielectric layer system is deposited on the facet exhibiting alternating high and low refractive index material. The reflectivity of such a system can be calculated using a transfer-matrix method described e.g. in [14]. An AR coating has a much stronger wavelength dependence than the waveguide tilt. Thus, the fabrication of the layer system requires a very precise control of the composition and thickness of the deposited layers to match the target wavelength and to achieve a low reflection.

The AR coating of the QD SOAs was calculated and realized by the Fraunhofer Institute for Telecommunications Heinrich-Hertz Institute (HHI) taking into account the waveguide tilt and the dominating TE polarization. A two layer system was deposited. The first layer was titanium dioxide (TiO_2) and the second was silicon dioxide (SiO_2) with a refractive index difference of approximately 1 [15, 16]. More details about the layer composition and thickness are confidential and will not be given here. Simulations of such an AR coating indicate a reflection of below 10^{-3} in a range of 70 nm [17].

The processed wafer is cleaved into bars of different waveguide length. Each bar contains 6–30 waveguides. All bars are AR coated and glued on a Cu-mount (Cu: copper) using a thin film silver-filled two-component epoxy. The glue provides a high thermal conductivity and a good electrical contact. The Cu-mounts are designed with an reference angle tilting the glued chip at the waveguide output angle with respect to the fiber taper axes. Thus, SOAs with different output angles can be measured using the same setup stage without change of the fiber taper angle. Figure 3.3 (page 39) exemplary shows a glued 5 mm long bar.

3.2 SOA Coupling Stage

The setup used in this thesis is a modified version of the setup developed in [11, 17]. It allows current supply, fiber coupling and temperature control. Figure 3.5 shows a picture of the setup stage. The block "device under test (DUT)" in all setup sketches in the subsequent chapters refer to the setup sketched in Fig. 3.5 if not stated differently. The Cu-mount with the QD SOA chip glued on top is installed on the copper-based heat sink using two screws. This allows a fast and reproducible installation of the Cu-mount, on the one hand. On the other hand, it prevents a vertical lift of the Cu-mount with respect to the heat sink which could cause decreased thermal conductivity. The heat sink is thermo-electric temperature controlled at a constant heat sink temperature of 20 °C if not stated differently.

In direct current (DC) operation, the backside n-contact and top-side p-contact of the chip are used. The backside contact is fixed to the heat sink. For the top-side contact, one and two needle probers or a multi-tip DC probe head are used for shorter and longer devices, respectively. In case of a modulated current, an high-frequency

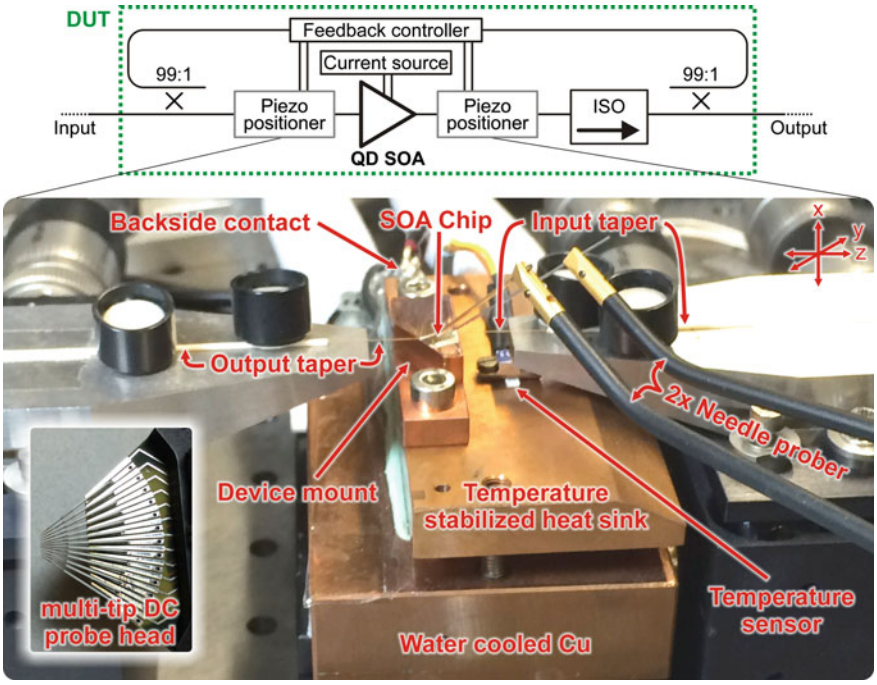

Fig. 3.5 Sketch and picture of the QD SOA characterization stage used throughout this thesis

(HF) probe head in ground-signal configuration is used (not shown in the picture) instead of the DC probes.

The ASE output of both facets are coupled using an anti-reflection coated tapered single-mode fiber (SMF) on each side. 1 % of the coupled light is taken as input of a feedback controller maximizing the coupled power by feedback-controlled readjustment of the tapered fiber. Coupling losses of about 4.5 dB per facet are obtained. The signal output path contains an isolator to prevent disturbance by reflections and other signals of subsequent components. Instead of coupling to the ASE output, the system can also couple to the optimal transmission of an input signal by aligning both tapers to the maximal output of the input signal. This option is used for all measurements with an input signal because ASE emission and the injected signal can have a different optimal coupling as shown in [11]. This system allows long-term stable measurements and simultaneously provides a high flexibility to test a large number of chips.

Reassembling of the device mount on the heat sink as well as the rough movement of the tapered fiber holder on the feedback positioning system can cause a slight change of the fiber angle with respect to the device output. Figure 3.6 shows the normalized coupling losses in dependence of the angle of the tapered fiber with respect to the optimal angle for an exemplary shallow-edged 8°-tilted ridge waveguide. An asymmetric behavior is observed for positive (towards facet plane) and negative

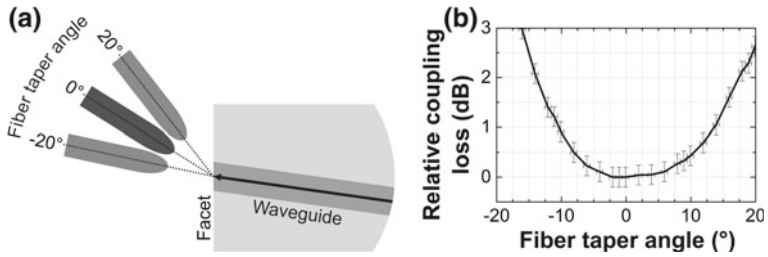

Fig. 3.6 **a** Sketch for and **b** measurement of relative coupling losses in dependence of the angle of the tapered fiber with respect to the optimal angle. The coupling losses are normalized to the lowest. The shallow-edged ridge waveguide is tilted by 8°

Table 3.1 Specifications of the sample series. AR: anti reflection

Wafer	Number of QD layers	Lateral waveguide	Ridge tilt	Facet coating	QD SOA No.
Do 520	10	Deeply	6.8°	AR, both	1
Do 957	10	Shallow	8.0°	AR, both	2
Do 1111	10	Shallow	8.0°	AR, both	3, 4, 5
Do 1202	10	Shallow	8.0°	AR, both	6

(towards facet normal) angle. The additional coupling losses are found to be below 0.2 dB for a fiber angle misalignment below 5°.

3.3 QD SOA Sample Series

This section gives an overview of the QD SOAs used for experiments throughout this thesis. Each device received a specific number for easier identification within the framework of this thesis. The devices are based on four different wafers. Table 3.1 gives a brief overview of the samples series. All devices are processed as SOAs including a waveguide tilt and anAR coating on both facets.

3.3.1 Overview

A summary of all important parameters of the different QD SOAs is given in Table 3.2. Table 3.3 gives an overview of the experiments performed with the devices. Subsequently, all devices are presented in detail. All given gain, noise figures and saturation power levels are fiber-to-fiber respectively in-fiber values. The losses of the feedback fiber coupling setup in order of 1–1.5 dB are excluded from this value to allow a com-

Table 3.2 List of characteristics of QD SOA used for experiments in this thesis

QD SOA		ASE		Amplification					
No.	Length	λ_{peak} (mm)	FWHM (nm)	λ_G (nm)	G (dB)	NF (dB)	P_{sat}^{in} (dBm)	P_{sat}^{out} (dBm)	J (kA/cm^2)
1	2	1296	33.0	1296	8.4	11.8	4.1	9.5	1.9
2	3	1284	34.0	1290	14.6	9.4	3.3	14.9	3.4
3	3	1299	28.0	1305	13.5	8.6	1.0	11.5	3.3
4	4	1304	23.2	1310	22.1	9.5	−6.3	12.8	3.1
5	5	1307	21.0	1310	25.5	10.5	−11.5	11.0	2.9
6	4	1311	24.6	1310	25.5	10.2	−14.4	8.0	4.4

J is current density at which the maximal gain is obtained for an input wavelength λ_G. J is calculated with the ridge width of 4 µm neglecting current spreading in the shallow edged active region. All gain G, noise figure NF, 3-dB saturation input power P_{sat}^{in} and output power P_{sat}^{out} values are fiber-to-fiber and in-fiber values, respectively. The given linear gain and noise figure values are averaged over all measured values within the linear gain regime

parison with packaged devices like the commercial QW SOAs presented in Sect. 3.4. The power levels presented and discussed in the subsequent chapters usually include these losses if the feedback fiber coupling setup is used. The fiber coupling losses vary from device to device and with the current between 4 and 4.5 dB per facet. The chip gain, the chip noise figure and the chip saturation power levels can be obtained by increasing the given in-fiber values by 8–9, 4–4.5, and 4–4.5 dB, respectively (see Sect. 2.2).

Table 3.3 Overview of experiments performed throughout this thesis with the samples

QD SOA no	Experiment (chapter number)
1	Phase-coded signal generation (5)
2	Self-phase modulation (3)
	Static FWM (8)
3	Gain dependence on SOA length (3)
	Static FWM (8)
	Dual-band amplification (7)
4	Gain dependence on SOA length (3)
	Static FWM (8)
5	Gain dependence on SOA length (3)
	OOK and D(Q)PSK amplification (6)
	Static FWM (8)
	D(Q)PSK FWM (8)
6	OOK single and multi-channel amplification (6)

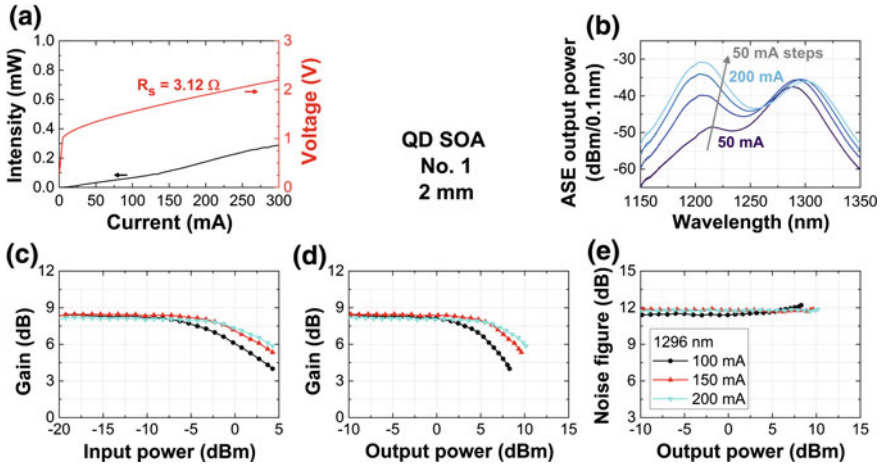

Fig. 3.7 Characteristics of QD SOA No. 1. **a** Single-facet in-fiber ASE power as well as voltage as a function of the current (LIV). **b** Spectrally resolved in-fiber ASE for different currents. The absolute power levels are not corrected by setup losses. **c**–**e** Fiber-to-fiber gain and noise figure as a function of the fiber **c** input power and **d**, **e** output power, both measured at a wavelength of 1296 nm and for different currents. The diagrams **c**–**e** share the same legend

3.3.2 Sample Series

This subsection presents details of the sample series, i.e. LIV curves, ASE spectra, gain and noise figure curves.

QD SOA No. 1–2 mm Long–Do 520

QD SOA No. 1 is a 2 mm long and 4 µm wide deeply etched ridge waveguide. The ridge is tilted with respect to the facet normal by 6.8°. The tilt and the facet AR coating suppress the onset of lasing resulting in negligible gain ripple in the ASE emission shown in Fig. 3.7b. The QD GS and ES emission are observed between 1240–1350 and 1150–1270 nm, respectively. The QD GS ASE emission saturates at a current of about 150 mA. The ASE peak wavelength is about 1296 nm. Increasing the current from 100 to 200 mA results in a device heating induced peak ASE wavelength shift of 7.9 nm whereas the ASE peak power is changed by less than 0.5 dBm/0.1 nm.

The device exhibit top-side n-contacts allowing to use a high-frequency probe head for electrical contacting. The SOA's LIV characteristic is depicted in Fig. 3.7a. A quite large series resistance of 3.1 Ω is observed in comparison to other samples presented in this thesis.

The device exhibits a peak linear fiber-to-fiber gain of 8.5 dB and a saturation input power P_{sat}^{in} of 4.1 dBm at a current of 150 mA (see Fig. 3.7c, d). Changing the current to 100 mA or 200 mA results in only minor linear gain changes but the P_{sat}^{in} is reduced to 1.7 dBm for a current of 100 mA whereas it is comparable for 200 mA. In the linear gain regime, a large fiber-to-fiber noise figure of about 11.8 dB is found

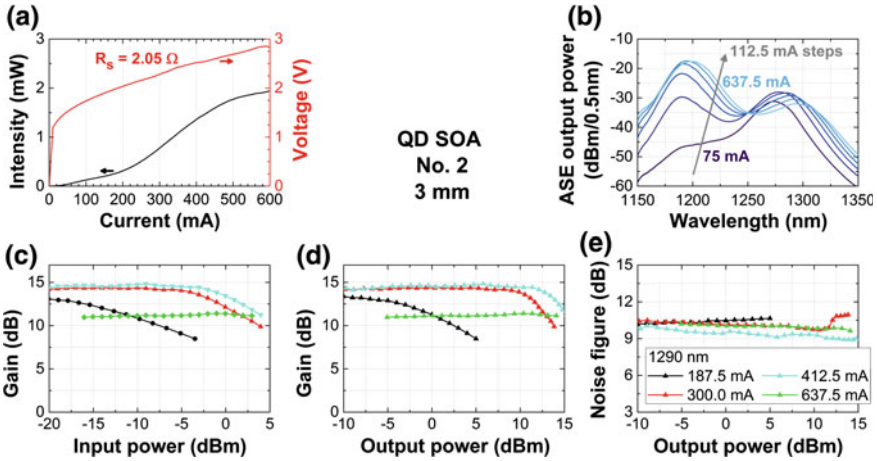

Fig. 3.8 Characteristics of QD SOA No. 2. **a** The single-facet in-fiber ASE power as well as voltage as a function of the current (LIV). **b** Spectrally resolved in-fiber ASE for different currents. The absolute ASE power levels are not corrected by setup losses. **c**–**e** Fiber-to-fiber gain and noise figure as a function of the fiber **c** input power and **d**, **e** output power, both measured at a wavelength of 1290 nm and for different currents. The diagrams **c**–**e** share the same legend

mainly caused by the limited gain and the side wall roughness of the deeply etched ridge waveguide.[2]

QD SOA No. 2–3 mm Long–Do 957

A 3 mm long QD SOA with a 4 µm wide shallow edged ridge waveguide was fabricated (QD SOA No. 2). The waveguide is tilted at 8° with respect the facet normal and the facets are AR coated. The series resistance is about 2.1 Ω as shown in Fig. 3.8a. The QD GS ASE emission saturates between a current of 190 and 300 mA (Fig. 3.8b). For currents above 450 mA the ES ASE emission saturates resulting in a saturation of the total emitted ASE intensity. For currents above 300 mA, the QD GS ASE emission suffers from device heating resulting in a continuous decrease of the emission with increasing current. In consequence, the GS ASE peak is reduced by 3.7 dB and the wavelength of the peak of 1284 nm at 300 mA is red shifted by 8.3 nm at 637 mA.

The GS peak fiber-to-fiber gain is 14.6 dB at a current of 412.5 mA. The corresponding 3-dB saturation input and output power are 3.3 and 14.9 dBm. Both power levels are further increased with increasing currents. The fiber-to-fiber noise figure is 9.4 dB at the maximum gain.[3]

QD SOA No. 3–3 mm Long–Do 1111

[2]Following Sect. 2.2.5, the chip noise figure is 7.3 dB, taking into account the 4.5 dB coupling losses. Further 3 dB can be attributed to the total inversion. Hence, a noise figure in the order of 4.3 dB can be assigned to the waveguide and the structure.

[3]In comparison to the deeply-edged QD SOA No. 1, a noise figure in the order of 1.9 dB can be assigned to the waveguide and structure of the shallow edged QD SOA No. 2.

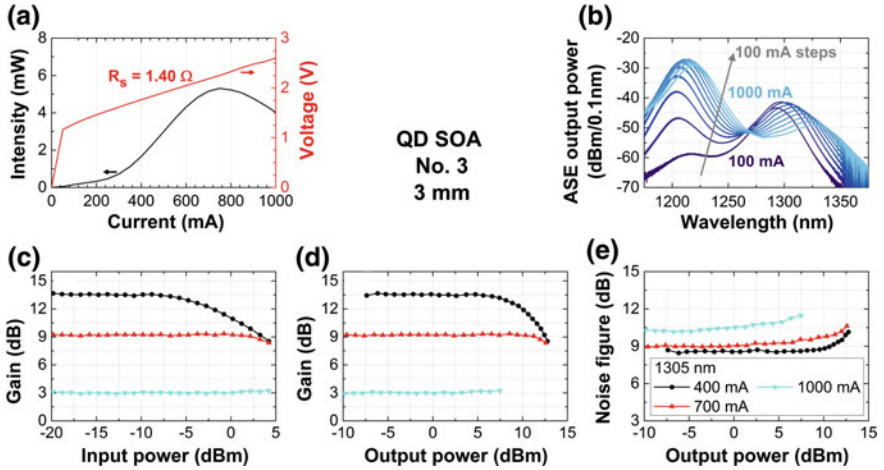

Fig. 3.9 Characteristics of QD SOA No. 3. **a** Single-facet in-fiber ASE power as well as voltage as a function of the current (LIV). **b** Spectrally resolved in-fiber ASE for different currents. The absolute ASE power levels are not corrected by setup losses. **c**–**e** Fiber-to-fiber gain and noise figure as a function of the fiber **c** input power and **d**, **e** output power, both measured at a wavelength of 1305 nm and for different currents. The diagrams **c**–**e** share the same legend

The QD SOA No. 3 is a 3 mm long and 4 µm wide shallow-etched ridge waveguide. The waveguide is tilted at 8° with respect the facet normal and the facets are AR coated. The improved mask design and processing result in a series resistance of 1.4 Ω which is lower than for QD SOA No. 2. As a result, a larger in-fiber ASE power as well as a reduced device heating caused ASE saturation is observed, see Fig. 3.9b. The in-fiber ASE emission is linearly increasing dominated by the QD GS emission up to a current of about 250 mA. For currents above 250 mA, the QD ES ASE emission overcomes the GS emission and dominates the integrated ASE emission. Therefore, the ASE emission increases linearly with a large slope due to the higher QD ES density of states with respect to the QD GS.

The GS ASE peak power saturates between 200 and 300 mA with a power variation below 0.2 dB (see Fig. 3.9b). The ASE saturation wavelength is around 1300 nm. The ASE peak power is reduced with respect to the saturation ASE peak power by about 0.9, 3.7 and 7.5 dB at a current of 400, 700 and 1000 mA, respectively. On average, the peak wavelength is red shifted by 1.8 nm per 50 mA current change.

The ES ASE peak power saturates about 15 dB above the GS ASE saturation power level at a current of 750–800 mA with a power variation around 0.3 dB. The ES ASE peak power is reduced with respect to the saturation ASE peak power by about 1.8 dB at a current of 1000 mA. The wavelength of the peak is blue shifted until a current of around 350 mA and afterwards red shifted with about 1.2 nm per 50 mA current change on average.

At a current of 400 mA and a wavelength of 1305 nm, the peak linear fiber-to-fiber gain is 13.5 dB. The corresponding fiber-to-fiber noise figure is 8.6 dB.

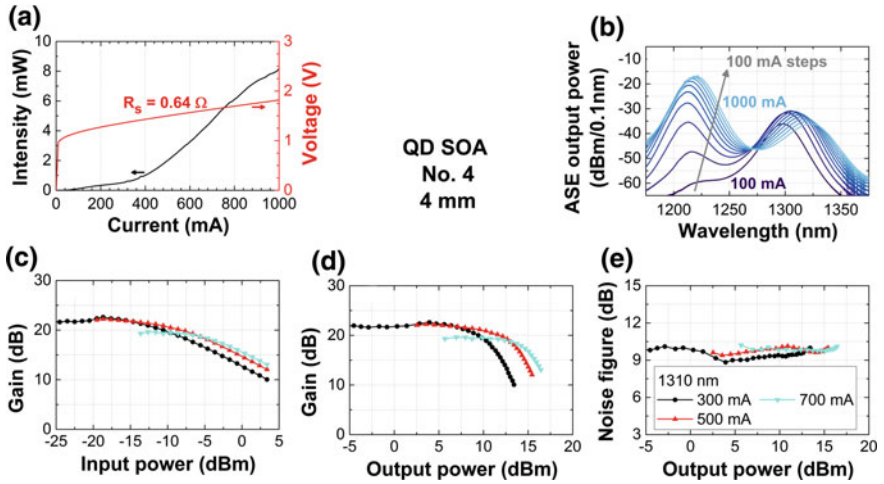

Fig. 3.10 Characteristics of QD SOA No. 4. **a** Single-facet in-fiber ASE power as well as voltage as a function of the current (LIV). **b** Spectrally resolved in-fiber ASE for different currents. The absolute ASE power levels are not corrected by setup losses. **c**–**e** Fiber-to-fiber gain and noise figure as a function of the fiber **c** input power and **d**–**e** output power, both measured at a wavelength of 1310 nm and for different currents. The diagrams **c**–**e** share the same legend

QD SOA No. 4; 4 mm Long; Do 1111

The 4 mm long, 4 µm shallow-etched ride waveguide QD SOA No. 4 is tilted at 8° and an AR coating on both facets was applied. A very low series resistance of 0.64 Ω was measured using a multi-tip DC probe head (Fig. 3.10). The in-fiber ASE output power exceeds 8 mW. The QD GS ASE emission saturates at a current of about 300 mA and peak wavelength appears at 1305 nm. The linear fiber-to-fiber gain was determined to 22 dB at currents of 300–500 mA. The corresponding in-fiber 3-dB saturation input (output) power are −8.7 dBm (10.3 dBm) and −6.3 dBm (12.8 dBm), respectively. The saturation output power can be increased to 15.2 dBm increasing the current to 700 mA but at the expense of a gain reduction to 19.4 dB. The noise figure is found to be about 9.5 dB within the linear gain regime.

QD SOA No. 5; 5 mm Long; Do 1111

The QD SOA No. 5 comprises a 5 mm long, 4 µm wide shallow edged ridge waveguide with an 8° tilt. Both facets are AR coated. The LIV characteristics were measured twice, both shown in Fig. 3.11a. Once the top-side p-contact is realized with two needle probes contacting pads with a distance of about 2.5 mm symmetrical to both sides of the SOA's center. In the other case, a multi-tip DC probe head was used contacting each of the ten p-pads independently. In both cases, the backside n-contract was used. Using the probe head halves the series resistance to a value of only 0.53 Ω and doubles the in fiber ASE emission to almost 12 mW. The GS ASE saturation power is almost comparable for both contacting methods whereas the ES ASE saturation power is improved by about 4 dB using the multi-tip DC probe head. This is

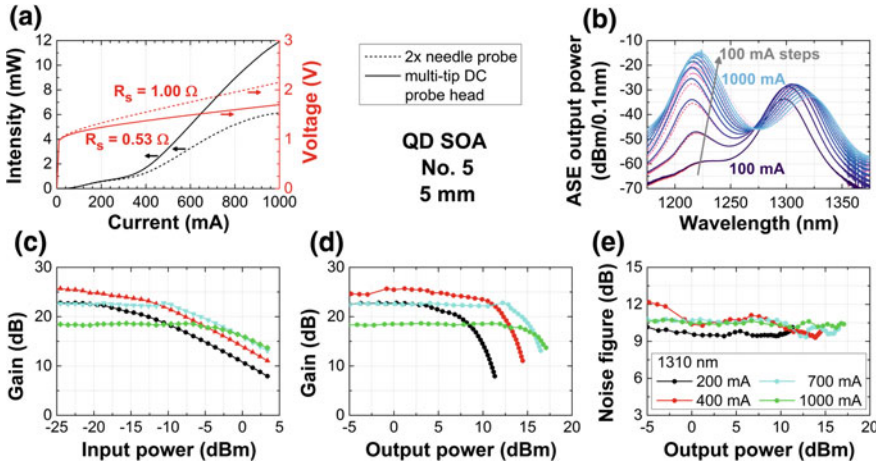

Fig. 3.11 Characteristics of QD SOA No. 5. **a** Single-facet in-fiber ASE power as well as voltage as a function of the current (LIV). **b** Spectrally resolved in-fiber ASE for different currents. The absolute ASE power levels are not corrected by setup losses. **c**–**e** Fiber-to-fiber gain and noise figure as a function of the fiber **c** input power and **d**, **e** output power, both measured at a wavelength of 1310 nm and for different currents. The diagrams **a**, **b** and **c**, **e** share the same legend

caused by the homogeneously pumped ridge resulting in a saturation at higher currents as well as an improved distribution of the heating over the entire device length. Consequently, QD SOA No. 4 and No. 5 are always contacted with the multi-tip head.

The QD GS ASE emission saturates at a current of around 350 mA. The peak wavelength is about 1306 nm. Increasing the current to 500 mA reduces the peak by about 0.7 dB and shifts the wavelength to 1310 nm. For currents up to 1000 mA, the QD GS ASE emission suffers from device heating resulting in a reduction of up to 5 dB and a wavelength red-shift to 1320 nm.

Linear fiber-to-fiber gain and 3-dB saturation input (output) power values as large as 25.5 dB and −11.5 dBm (11 dBm), respectively, are found at a current of 400 mA and a wavelength of 1310 nm. The corresponding fiber-to-fiber noise figure is about 10.5 dB.

QD SOA No. 6–4 mm Long–Do 1202

The 4 mm long QD SOA No. 6 has a 4 µm wide shallow-edged ridge waveguide with a tilt of 8°. The facets are AR coated. The series resistance is 1.5 Ω. The total in-fiber ASE intensity reaches 6 mW at a current of 800 mA and is still not saturating (see Fig. 3.12a).

The QD GS ASE emission saturates at a very large current of 640–730 mA whereas the ES ASE emission is still unsaturated at a current of 1000 mA. The GS ASE peak wavelength is red shifted by only 5 nm from a current of 460 to 1000 mA. These values indicate a mounting with a very good thermal conduction.

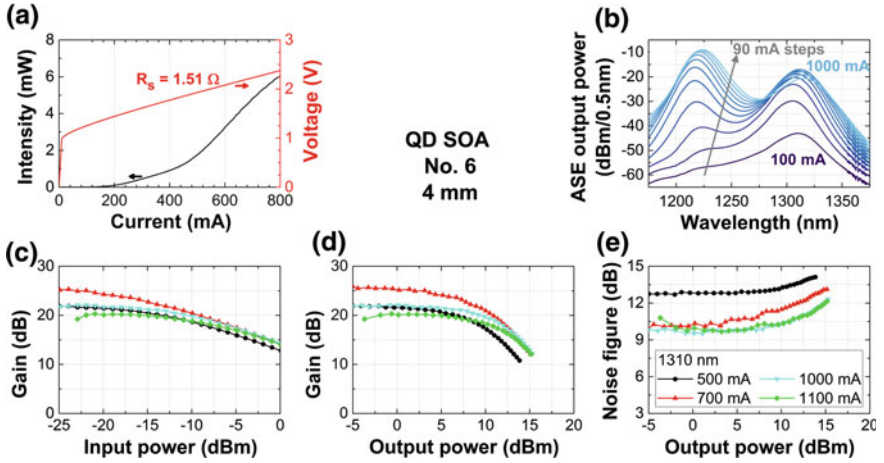

Fig. 3.12 Characteristics of QD SOA No. 6. **a** Single-facet in-fiber ASE power as well as voltage as a function of the current (LIV). **b** Spectrally resolved in-fiber ASE for different currents. The absolute ASE power levels are not corrected by setup losses. **c**–**e** Fiber-to-fiber gain and noise figure as a function of the fiber **c** input power and **d**, **e** output power, both measured at a wavelength of 1310 nm and for different currents. The diagrams **c**–**e** share the same legend

The maximal linear fiber-to-fiber gain is found to be as large as 25.5 dB at a current of 700 mA and a wavelength of 1310 nm corresponding to a chip gain of 35 dB. The fiber-to-fiber noise figure is about 10.2 dB. At this current, the in-fiber 3-dB saturation input and output power are −14.4 and 8.0 dBm, respectively. Increasing the current to 1000 mA reduces the gain by 3.6 dB but increases the 3-dB saturation output power to 11.2 dBm.

3.4 Comparison to Commercial O-Band Amplifiers

Three different commercial available O-band amplifiers are addressed and compared to the QD SOAs used in this thesis (called in this chapter TUB SOAs).

Commercial QD SOA

Commercial QD SOAs are offered by Innolume GmbH. All presented data in this thesis are extracted from the data sheet "Innolume GmbH, SOA-1250-110-yy-27dB, 08. August 2014" available on the company's homepage "www.innolume.com". The ASE and gain characteristics are depicted in Fig. 3.13. The QD GS ASE emission saturates at a current of approximately below 800 mA and no significant device heating induced wavelength red-shift is observed. The GS peak ASE emission is

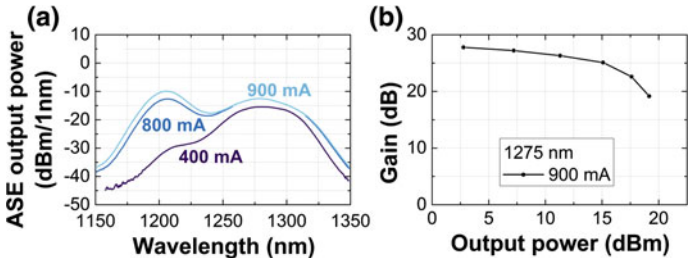

Fig. 3.13 Characteristics of a commercial QD SOA. All data are taken from the data sheet "Innolume GmbH, SOA-1250-110-yy-27dB, 08. August 2014". **a** Spectrally resolved in-fiber ASE for different currents. **b** Fiber-to-fiber gain as a function of the in-fiber output power determined at a wavelength of 1275 nm and a current of 900 mA

observed at a wavelength of 1277 nm. The dip between the GS and ES ASE emission is less pronounced than for the TUB SOAs. These devices exhibit either an increased inhomogeneously broadened QD ensemble in each QD layer or most likely different QD layers are grown with a slightly different center wavelength (called chirped gain layers) [18–20]. However, the device shows a broad QD GS ASE emission indicating a spectral 3-dB gain bandwidth of close to 50 nm. Additionally, the data sheet promises a 6-dB gain bandwidth of more than 110 nm taking into account the QD GS and ES gain. A fiber-to-fiber gain of up to 27.7 dB is observed. The 3-dB saturation input and output power can be roughly estimated to −8.8 and 15.7 dB, respectively. The noise figure is given to be 7.5 dB.

Commercial QW SOA

A commercial butterfly packaged InP (In: indium, P: phosphorus) QW-SOA was characterized, see Fig. 3.14. The peak ASE emission shows a band-filling effect induced blue-shift with increasing currents without a significant heating induced

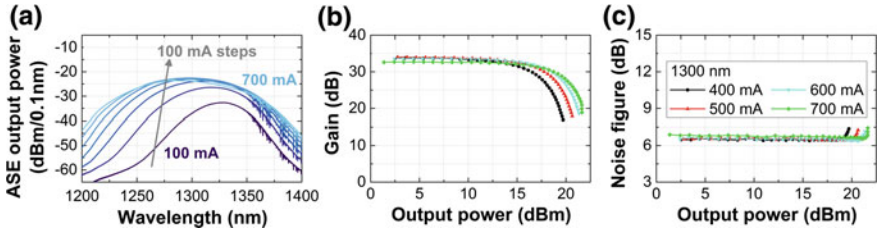

Fig. 3.14 Characteristics of a commercial available QW-SOA. **a** Spectrally resolved single-facet in-fiber ASE for different currents. The absolute ASE power levels are not corrected by setup losses. **b** Fiber-to-fiber gain and **c** fiber-to-fiber noise figure as a function of the in-fiber output power, both measured at a wavelength of 1300 nm and for different currents. The diagrams **b**, **c** share the same legend

red-shift (explanation see Sect. 2.1.2). The ASE peak emission is determined at a wavelength of 1296 nm for a current of 500 mA. The 3-dB and 6-dB ASE bandwidth are about 79 and 105 nm, respectively. Most likely a chirped multi-QW-layer active region is used, demonstrated e.g. in [21]. At a wavelength of 1300 nm, the linear fiber-to-fiber gain, 3-dB saturation output power and noise figure are measured to be 33.9, 17.2 and 6.4 dB, respectively. Increasing the current towards 700 mA slightly decreases the gain but increases the saturation output power by 1.9 dB similar to QD SOAs. The device has a polarization dependent gain which ratio cannot been measured due to the usage of polarization maintain fiber within the SOA's package. Preceding models of this QW-SOA without polarization maintaining fiber exhibited a polarization depended gain of 8–10 dB [17].

Commercial PDFA

A commercial praseodymium-doped fiber (PDFA) was characterized. The amplifier consists of two stages, each consist of a praseodymium-doped fiber optically pumped with two laser diodes in counter propagating configuration. The PDFA's currents refers to the sum of the four diode currents. The amplifier is polarization independent. The ASE spectra in Fig. 3.15 show an increasing peak emission with increasing currents but at the expense of the 3-dB ASE bandwidth. This bandwidth is reduced to 16.7 at the largest current of 3600 mA. At a wavelength of 1305 nm, the fiber-to-fiber gain is found to be as large as 42.4 dB with a 3-dB saturation output power of 17.3 dB. The fiber-to-fiber noise figure is found to be 6.8 dB. This noise figure is surprisingly large for a fiber amplifier usually offering noise figures in the order of 4–5 dB, e.g. [17, 22].

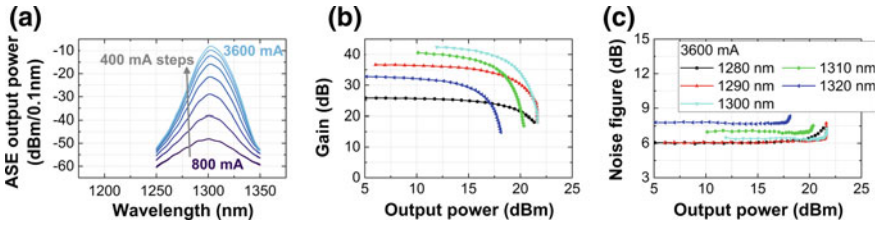

Fig. 3.15 Characteristics of a commercial available PDFA. **a** Spectrally resolved in-fiber ASE for different currents. The absolute ASE power levels depend on the resolution and are not corrected by setup losses. **b** Fiber-to-fiber gain and **c** fiber-to-fiber noise figure as a function of the in-fiber output power, both measured at a current of 3600 mA and for different wavelength. The diagrams **b**, **c** share the same legend

Comparison

Table 3.4 gives an overview of the most important parameters for the three commercial amplifiers and two exemplary TUB QD SOAs. The PDFA offers the largest gain and lowest 3-dB saturation input power but its 3-dB gain bandwidth is strongly limited. The QW-SOA exhibits the largest 3-dB gain bandwidth whereas the commercial QD SOA exhibits the largest 6-dB gain bandwidth. Implementing and improving the chirped layer technique to QD SOAs, also the 3-dB bandwidth can be tuned to 120 nm [23, 24].

The saturation output power levels of all three commercial amplifiers are on the same order of magnitude. The PDFA is the only tested polarization insensitive amplifier. But QW-SOAs and QD SOAs can be designed with low or no polarization sensitivity as well [25–29].

The lowest noise figure was expected for the PDFA but it is comparable to the QW-SOA. The gain and noise figure values of the TUB QD SOA suffer from the coupling losses of about 4–4.5 dB per facet. Based on the obtained noise figure values, the coupling losses of the commercial SOAs are expected to be about 1.5–3 dB per facet. The TUB QD SOA chip performance (in brackets in Table 3.4) is comparable with the values of the commercial SOAs corrected by the estimated coupling losses.

In consequence, the QD SOAs characterized in this thesis provide promising chip characteristics but have to be enhanced by technologies listed below to achieve or overcome the in-fiber performance of the commercial SOAs. Beside this, some of the improvements will also lead to a lower energy consumption. Each of the technologies

Table 3.4 Comparison of optical amplifiers fabricated at Technische Universität Berlin (TUB) and commercially available optical amplifiers

	TUB Lab		Commercial		
	QD SOA (No. 3)	QD SOA (No. 5)	QD SOA	QW-SOA	PDFA
Linear gain (dB)	13.5	25.5	27.7	33.9	42.4
	(22.5)	(34.5)			
3-dB ASE bandwidth (nm)	28.0	20.7	49.0	78.5	16.7
3-dB P_{sat}^{in} (dB)	1.0	−11.5	−8.8	−13.7	−22.1
	(−3.5)	(−16.0)			
3-dB P_{sat}^{out} (dB)	11.5	11.0	15.7	17.2	17.3
	(16.0)	(15.5)			
Linear noise figure (dB)	8.6	10.5	7.5	6.4	6.6
	(4.1)	(6.0)			
Current (mA)	400	500	900	500	3600
Polarization sensitive	Yes	Yes	Yes	Yes	No

The values for all QD SOAs are determined for the QD GS wavelength range. Numbers in brackets are chip values taking into account coupling losses of 4.5 dB per facet. The values for the commercial QD SOA are extracted from the data sheet (see text). Saturation input power (P_{sat}^{in}), Saturation output power (P_{sat}^{out})

have been demonstrated independently for QD-based devices or are in general well known technologies for laser and gain chips.

- The *mounting technologies* needed to be enhanced to improve the thermal conductivity which is the gain limiting factor at larger currents. The currently used technologies is in principle sufficient as demonstrated with QD SOA No. 6 but not reproducible as visible from the other QD SOAs. The thermal conductivity can be further improved by use of more efficient gluing and heat spreader technology and could be finally improved by implementing p-side down mounting. Both, the more efficient mounting technology as well as p-side down mounting are well known from high-power lasers, e.g. [30–34].
- The reduction of the *coupling losses* would increase the fiber-to-fiber gain and saturation power levels as well as lower the fiber-to-fiber noise figure. Especially an improvement of the last is mandatory for cascaded amplifiers [35]. The coupling losses of the current structure suffer mainly from the asymmetric out-coupled far-field caused by the rectangular waveguide cross section with an aspect ratio of about 1:10. A monolithic integrated spot-size converter on both facets is commonly used to symmetrize the far-field and to reduce the divergence. This can be realized either by vertical extension of the optical mode using a rib waveguide design [36] or a vertical taper structure [37–39], or by lateral contraction of the optical mode using lateral taper structures [40]. All methods are proved to reduce the coupling losses down to 1 dB per facet.
- The *top-side p-contact* has to be either connected on each pad (e.g. by bonding) or has to be realized with a broader and/or thicker metal contact layer. This will halve the series resistance, ensures a homogeneously pumped waveguide and reduces the device heating as demonstrated for QD SOA No. 5.
- The *polarization dependence on the wavelength* of the QD SOA and its origin are discussed in Sect. 3.5.2. A polarization insensitive QD SOA can be realized by growth of columnar QDs even with large gain as demonstrated in the 1.55 µm wavelength range [26, 28, 29].

3.5 Static Properties

This section addresses selected static properties of QD SOAs. First, Sect. 3.5.1 discusses the gain and gain bandwidth in dependence of the device length and presents a concept of a sectioned SOA. Subsequent, Sect. 3.5.2 discusses the polarization dependence of the gain for QD GS and ES.

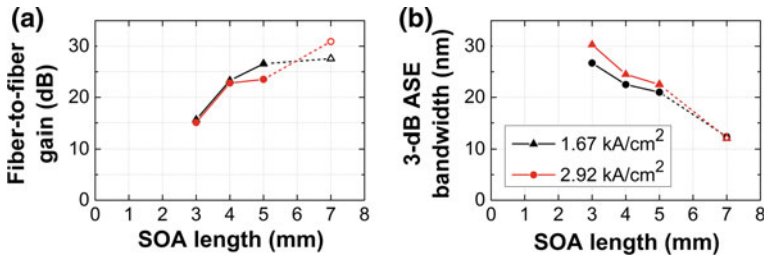

Fig. 3.16 **a** Peak fiber-to-fiber gain and **b** 3-dB ASE bandwidth versus SOA length for two different current densities. *Closed symbols* are measured with standard SOAs and *open symbols* for sectioned SOAs. The input wavelength was set for each SOA and current density to the QD GS ASE peak (see corresponding ASE spectra in Sect. 3.3.2)

3.5.1 Gain Saturation and Sectioned SOAs

The requirements to the gain and spectral bandwidth differ between the application. A linear fiber-to-fiber gain (per wavelength channel) larger than 10 dB (20 dB) is sufficient to extend the network reach by 29 km (57 km)[4] or to increase the power splitting ratio e.g. from 1:16 to 1:128 (1:1024). On the other hand, a larger gain bandwidth enables either an increasing of the number of wavelength channels or the channel spacing. Both allow a larger total network capacity. Various standards are defined within the O-band, e.g. [41], with bandwidths from 20 up to 100 nm. The following paragraphs discuss the gain and gain bandwidth in dependence of the device length.

The peak fiber-to-fiber gain was measured for QD SOAs with various lengths from 3 to 7 mm and is shown in Fig. 3.16a. The QD GS ASE peaks are obtained for a current density of around 1.67 kA/cm^2 whereas usually large current densities are used for the amplification of OOK signals to avoid pattern-effects [42]. Thus, also a larger current density of 2.92 kA/cm^2 was applied. At very large currents, the onset of lasing on the ES ASE was observed for the 5 mm long device, see Fig. 3.11. For the 7 mm long QD SOA,[5] a strong gain ripple larger than 0.5 dB and lasing appears on the GS ASE even at low current densities of 1.4 kA/cm^2 (400 mA). Hence, the gain is not evaluated.

The gain increases with the device length but runs into saturation due to the ASE self-saturation. The disadvantage of the increased gain is a narrowing of the spectral bandwidth, depicted in Fig. 3.16b. The gain is reduced at the larger current density due to device heating.[6] In contrast, the ASE bandwidth is increased. In comparison to

[4]Taking into account the O-band SMF loss of 0.35 dB/km discussed in Chap. 1.

[5]The design of this device is similar to QD SOA No. 3–5: Do 1111, shallow etched 4 µm ridge waveguide, 8° tilted, AR-coated facets.

[6]The stronger gain reduction observed for the 5 mm long device is caused by the onset of lasing on the ES ASE emission probably to a reflection from the setup. In contrast, the large-signal experiments in the subsequent chapters are all performed with the identical device without the onset of ES lasing.

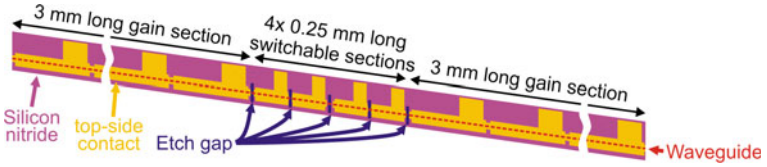

Fig. 3.17 Top-view sketch of the multi-section 7 mm long QD SOA chip design comprising two 3 mm long standard gain sections and in-between four 0.25 mm long sections which can be switched to different operating conditions. The used color code is identical to Fig. 3.2

the requirements listed above, the results of the 3–5 mm long QD SOAs are sufficient. However, other applications may require less bandwidth but more gain. Increasing the device length to 7 mm results in ASE self-saturation and lasing. Other options like cascading two fiber-coupled QD SOAs suffer from the coupling losses twice. A sectioned QD SOA concept is presented in the following to overcome both, the ASE self-saturation and lasing.

Sectioned SOA

The concept is based on the experiences obtained with saturable absorbers monolithically integrated in QD mode-locked lasers (MLLs) [5, 43–47]. The main idea is to place an absorbing section within the center of a long SOA chip to prevent the self-saturation and the onset of lasing. But, this section saturates in presence of an optical input signal and therefore allows larger gain values.

The sectioned QD SOA is sketched in Fig. 3.17. The device was fabricated similar to the QD SOAs No. 3–5[7] but comprises six electrically separated sections with a total waveguide length of 7 mm. The two outer sections are 3 mm long with a contact pad each 0.5 mm. The four mid sections are electrically separated from each other and the outer sections by 20 µm broad etch gaps (details see Sect. 3.1.2). The gap results in an resistance of 11 kΩ between the top-side p-contacts of the separated sections.

The device is contacted using the DC multi-tip probe shown in Fig. 3.5 (page 42). Both outer sections are driven with the same current source at the same current density as an standard SOA. The mid sections can be electrically connected independently either to the same source as the outer sections or to a second source which can apply a forward or reverse bias. Switching all mid sections to the outer sections the device is driven similar to a 7 mm long standard QD SOA.

Investigations of the ASE emission of the device are conducted in dependence of the current and different voltages applied to various numbers of the mid sections. Figure 3.18a exemplary shows such a measurement for a current density of 2.92 kA/cm^2 (700 mA) applied to the outer sections while the bias applied to all mid-sections is scanned. The largest applied bias of 1.3 V is close to the bias of 1.5 V on the outer sections. In consequence, this ASE spectrum is comparable to spectrum if all six sections are electrically connected to the same source and are thus driven

[7]This means: Wafer Do 1111, shallow etched 4 µm ridge waveguide, 8° tilted, AR-coated facets.

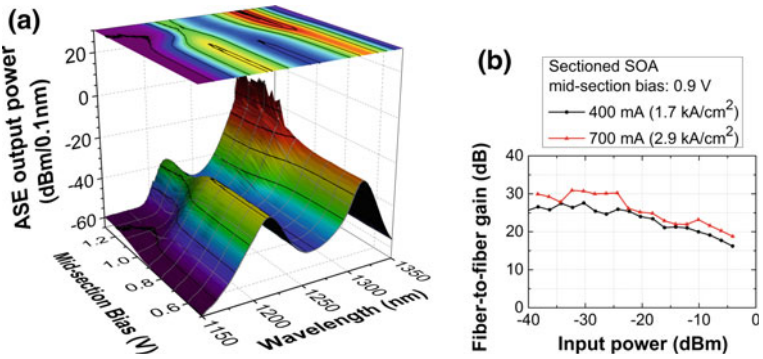

Fig. 3.18 **a** Spectrally resolved in-fiber ASE of a 7 mm long sectioned QD SOA for different bias levels of the central sections and for a current density of 2.92 kA/cm^2 (700 mA) for the outer sections corresponding to a bias level of 1.5 V. **b** Fiber-to-fiber gain measured for different current densities of the outer sections and a mid-section bias of 0.9 V. The input wavelength are aligned to the QD GS ASE peak and are 1303 and 1306 nm

with a current density of 2.5 kA/cm^2 (700 mA). Under these conditions a strong GS lasing is observed. Reducing the mid-section bias down to 1 V leads to only minor changes. But if the voltage is set below 1 V, the GS lasing is suppressed and the ES ASE increases and broadens. At a bias of 0.9 V, only a small gain ripple less than 0.4 dB remains. Further decreasing the bias reduces the ASE peak emission of both, the GS and ES. Increasing the currents towards 1000 mA while still scanning the bias leads partly to a switching of the lasing from the GS to the ES and in most cases to a lasing on both states. However, the GS lasing always disappears for bias levels close to 0.9 V.

The cavity for the gain ripple could be caused by a remaining reflectivity of the facets and would exhibit a mode separation of about 5.8 GHz.[8] The mode separation is characterized by analyzing an amplified signal (SOA in-fiber input power of −21 dBm) with a coherent detector.[9] The obtained radio frequency (RF) spectra are depicted in Fig. 3.19. In comparison to the exemplary input RF spectra, the peaks are visible in the spectra of the amplified signals. Applying an outer-section current density of 2.92 kA/cm^2 (700 mA) and a mid-section bias of 0.9 V, the peaks exceed the background by more than 10 dB. Reducing the mid-section bias continuously down to −3.0 V switches the mid-section finally into the absorption regime which attenuates the reflected signal while running through the waveguide but also lowers the gain. As a result, the peaks in the modulation spectra are strongly suppressed (compare Fig. 3.19b–d. But, the gain is reduced to values comparable or even below the 5 mm

[8] A QD mode-locked laser (MLL) with a cavity length of 1.012 ± 0.012 mm processed out of a comparable wafer like the sectioned QD SOA exhibits a pulse repetition rate of 39.85 ± 0.06 GHz [48, 49]. Hence, the repetition rate for a comparable 7 mm long laser would be 5.76 ± 0.06 GHz.

[9] A 40 GBd differential phase-shift keying (DPSK) modulated input signal is detected with an optical modulation analyzer (OMA). The DPSK modulation schema as well as the coherent detection are introduced in Chap. 4. A detailed setup description is given in Sect. 6.2.

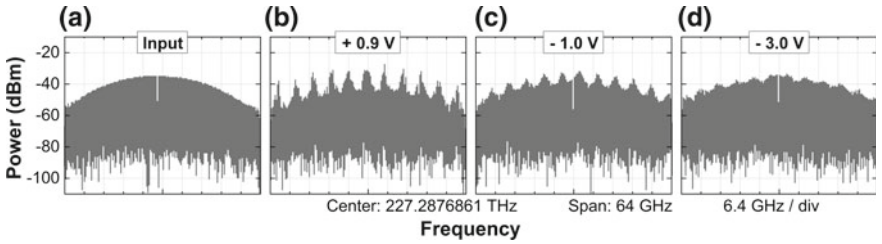

Fig. 3.19 RF modulation spectra of **a** exemplary input signal and **b–d** amplified signals using a 7 mm long sectioned QD SOA with an outer-section current density of 2.92 kA/cm^2 (700 mA) and a mid-section bias of **b** 0.9 V, **c** −1.0 V and **d** −3.0 V. The optical QD SOA in-fiber input power was −21 dBm

long QD SOAs. The peaks have an averaged frequency spacing of 5.9 ± 0.5 GHz and thus could be assigned to the facet-taper-cavity.

However, the fiber-to-fiber gain is shown in Fig. 3.18b. Fiber-to-fiber gain values up to 30.5 dB are achieved without the onset of lasing corresponding to an excellent chip gain of 39.5 dB. The in-fiber linear noise figure is about 11 dB. In comparison to the standard QD SOAs, the gain is increased by more than 4 dB with respect to the largest gain obtained for a 5 mm long device (see Fig. 3.16). The 3-dB ASE bandwidth is reduced to only 10.7 nm. This chip gain of the 7 mm long sectioned QD SOA exceeds the commercial QW gain and is close to the commercial PDFA gain of 42.5 dB.

In conclusion, the concept of long sectioned QD SOA with electrically separated mid-sections sufficiently prevents the onset of lasing in the ASE. Very large chip gain values up to 39.5 dB have been achieved but at the expense of a spectral bandwidth narrowing. The remaining gain ripple can be prevented by improving the AR coating of the SOAs and the fiber taper as well as by increasing the QD SOA waveguide tilt if necessary.

3.5.2 Wavelength Dependence of the Polarized Emission

The QD SOAs investigated in this thesis emit predominantly TE polarized light. The asymmetric and tilted waveguide privilege the TE polarized mode [11]. Additionally, the QD gain media itself predominantly emit TE polarized light. Multi-wavelength-channel amplification, dual-band amplification and wide-range wavelength conversion raise the question about the wavelength dependence of the polarization ratio. Thus, the polarization dependence of the QD SOA ASE is measured and discussed.

The setup stage described in Sect. 3.2 was modified by replacing the SMF components with polarization-maintaining fiber (PMF) components and adding a PMF polarization splitter. The PMF slow axis was aligned to the QD SOA TE axis. The obtained polarization dependent ASE emission is depicted in Fig. 3.20 measured for

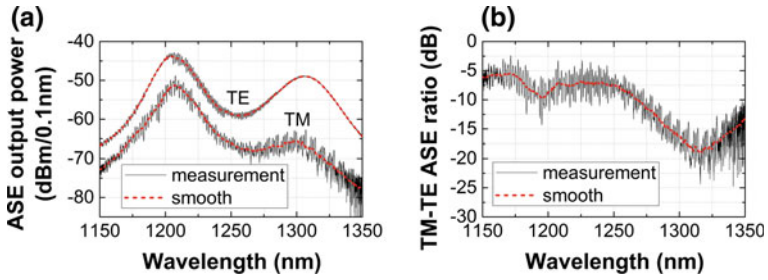

Fig. 3.20 **a** Polarization dependent ASE emission of QD SOA No. 3 at a current of about 350 mA. The visible ripples are caused by the PMF components. Smoothed versions of both curves are plotted in addition for easier comparison. **b** TM-TE ASE ratio calculated from (**a**)

QD SOA No. 3. At the GS ASE peak, the TM polarized emission is about 17.7 dB lower than the TE polarized emission. The largest difference of 18.8 dB is observed for larger wavelength corresponding to large QDs. In contrast, the TM-TE ratio is reduced by one order of magnitude to −7.5 dB for the ES ASE peak emission.

The difference in the polarization ratio of QD GS and ES can be explained by different contributions of the LH and HH to the QD hole ground and excited states as shown by $k \cdot p$ theory-based calculation [50]. The reduction of the TM-TE polarization ratio obtained on the red-wavelength part of the GS ASE emission could be attributed to a slightly increasing of the LH fraction for larger QDs. The polarization dependence can be designed by stacking several QD layers which was calculated e.g. in [51] and experimentally realized e.g. in [26, 29].

3.6 Gain and Phase Dynamics

The charge-carrier dynamics of SOAs have been discussed phenomenologically in Sect. 2.3. The charge-carrier dynamics for bulk, QW and QD-based gain materials have been investigated by many different groups during the past decades whereas the fastest carrier dynamics are found for QDs, e.g. [52–64]. The QD GS and ES carrier dynamics are investigated under various conditions as well. However, some conditions are not yet fully understood or investigated. But, an unambiguous knowledge of the relaxation path of the coupled QD-QW system is mandatory to understand and improve the performance of QD SOAs for system applications. The charge-carrier-dynamics-based gain and phase dynamics of the QDs will be discussed in this section under various conditions and by different measurement techniques.

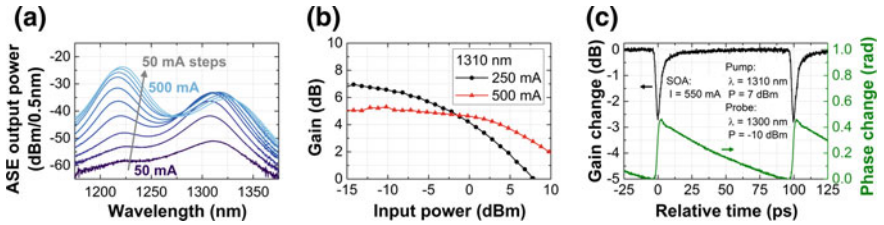

Fig. 3.21 Pump-probe trace of a 2 mm long QD SOA at a current of 550 mA. The wavelength, averaged in-fiber input power, temporal FWHM and pulse distance of the pump (probe) input pulses were 1310 nm (1300 nm), 5 mW (0.1 mW), about 1.6 ps (1.6 ps) and about 100 ps (100 ps). The data are kindly provided by Carsten Schmidt-Langhorst, Fraunhofer Institute for Telecommunications Heinrich-Hertz Institute (HHI)

3.6.1 QD GS Dynamics Under GS Perturbation

First, the QD GS gain and phase recovery is investigated in this section via single-color pump-probe measurements. Subsequently, the amplification of optical pulsed signals are investigated in terms of self-gain and self-phase modulation for conditions appearing in optical time-division multiplexing (OTDM)-based networks.

Pump-Probe Measurements

In a typical heterodyne pump-probe experiment, a strong pump pulse drives the QD SOA into the nonlinear gain regime and a weak pulse probes the nonlinear gain and phase change at different temporal delays with respect to the perturbing pump pulse. The probe can be used to scan the recovery of the energy state perturbed by the pump (single-color pump-probe) or a different energy state (two-color pump-probe).

The device under test is a 2 mm long QD SOA[10] exhibiting a linear fiber-to-fiber gain 5.1 dB for a current of 500 mA and a wavelength of 1310 nm. A pump-probe trace of the QD GS was measured at the Fraunhofer Institute for Telecommunications Heinrich-Hertz Institute (HHI) and is depicted in Fig. 3.21 for a temporal perturbation delay of 100 ps corresponding to 10 GHz pulse repetition rate. This duty cycle is on the order of typical optical communication symbol distances. A QD typical fast gain recovery is observed, indicated by a 90:10 % gain recovery time[11] below 10 ps. This fast gain recovery is enabled by the ultra-fast refilling of the QD GS from the carrier reservoir as long as the reservoir is sufficiently populated.

A peak phase change of 0.45 rad is found slightly time delayed with respect to the peak gain change which is caused by the temporal pulse width and the faster QD GS gain recovery. The phase does not recover between two subsequent perturbations. Typical, total 90:10 % phase recovery times much larger than 100 ps are observed. Usually, two different phase recovery times are observed [61, 62, 65].

[10] The design of this device is similar to QD SOA No. 6 (page 50): Do 1202, shallow etched 4 μm ridge waveguide, 8° tilted, AR-coated facets.

[11] The 90:10 % gain recovery time is the time required to recover from 90 to 10 % of the difference between original gain and peak gain change.

The dominating slow recovery time is caused by carrier density pilsation (CDP) in the carrier reservoir whereas the fast recovery time is correlated to the reservoir-QD carrier transitions [62, 66]. The slow phase recovery time is found to be rather independent of the current whereas the gain recovery gets faster with increasing currents [62]. In consequence, the QD SOA-based amplification of data signal is expected to cause minor or no amplitude patterning as long as the reservoir is highly populated but phase patterning occurs which strength is directly correlated to the signal input power via the nonlinear gain change.

Pulse Amplification and Self-phase Modulation

The amplification of ps-pulsed optical signals as used in optical time-division multiplexing (OTDM) systems is well known to change the pulse properties, such as spectral and frequency-chirp shifts as well as distortions of spectral and temporal pulse intensity profiles [67–69]. These are caused among others by nonlinear intensity-dependent phase changes during the pulse duration. For large input pulse energy the time dependent nonlinear reduction of the carrier density results in gain saturation and leads according to Eq. 2.12 (page 20) to a modulation of the temporal pulse phase. The temporal gain saturation depends on the relation of the pulse duration and the carrier-relaxation dynamics. Generally spoken, the pulse modulates its own amplitude and phase due to the gain saturation and consequently these effects are called self-gain modulation (SGM) and self-phase modulation (SPM) [67]. The value of the α-factor plays an important role for SPM. Due to the reduced α-factor of QD gain material in comparison to conventional gain material, SPM is expected to be low for QD SOAs, e.g. [70–74].

The appearance of SPM in the 3 mm long QD SOAs No. 2 (see page 46) is investigated using frequency-resolved second-harmonic generation (SHG) autocorrelation, called SHG Frequency resolved optical gating (FROG). This measurement technique allows to retrieving the complete pulse intensity and phase profile in the temporal and spectral domain. An introduction to this technique including a description of the retrieval algorithm used here are given in [75]. A description of the setup can be found in [46, 76]. All measurements were retrieved using a 256×256 grid size. root-mean square (rms) retrieval errors far below 0.01 are obtained proving that the results are very reliable.[12]

The pulse comb is emitted by a QD hybrid mode-locked laser (HMLL), amplified with a commercial QW-SOA and subsequently wavelength filtered to supress the SOA's ASE. The resulting pulse comb serves as the input of the QD SOA. The pulses are characterized without and with the QD SOA whereas the input power and current are scanned. Averaged input power levels from -10 to 5 dBm are tested corresponding to an energy of 2.5–79 fJ per pulse.

Figure 3.22 shows exemplary the retrieved pulse properties of the input and amplified pulse for a current of 500 mA and various averaged input power levels from -10 to 5 dBm. Only minor changes are observed for the pulse intensity profile and chirp which are within the retrieval error margin. The temporal chirp equals the nega-

[12] Details on the meaning of both values, please consider [75].

tive derivation of the temporal phase. However, the retrieved spectra show a slight wavelength red shift and a spectral narrowing with increasing input power levels.

The evaluation of the temporal and spectral FWHM as well as the linear part of the chirp (here the commonly used spectral chirp) is shown in Fig. 3.23 for various currents and input power levels. The input signal was characterized six times during the measurement period. Small variations occur due to either weak changes of the emitted pulse comb or the error margin of the retrieval algorithm. These fluctuations represent a minimal error margin for the obtained results and are depicted with the shaded area in Fig. 3.23.

The obtained values for the temporal FWHM and linear chirp are partly slightly increased with respect to the input values but no general trend for current or input power changes can be identified. A separate evaluation of the temporal e^{-2}-width (not shown here) shows a broadening below 30 % which could be caused by the fast QD gain recovery leading to a recovering during the trailing pulse parts (see Fig. 3.22). However, again, no trend can be identified within the error margin. Nevertheless, a slight spectral narrowing occurs with increasing input power due to the shape of the SOA gain spectra, two photon absorption or gain competition of the different spectral parts of the pulse like in lasers.

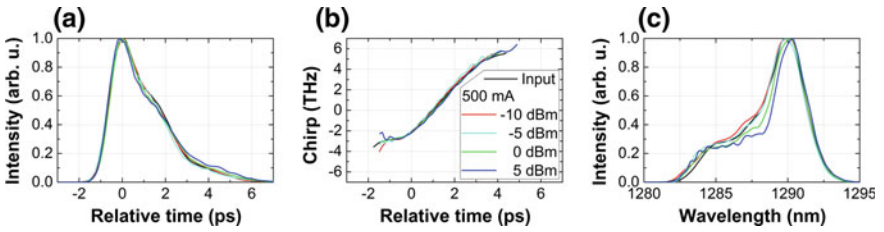

Fig. 3.22 Normalized **a** temporal and **c** spectral pulse intensity as well as **b** temporal chirp of the input pulse as well as the amplified output pulses for a current of 500 mA and various averaged input power levels. The pulse leading part is on the negative relative time axis. All three graph share the same legend

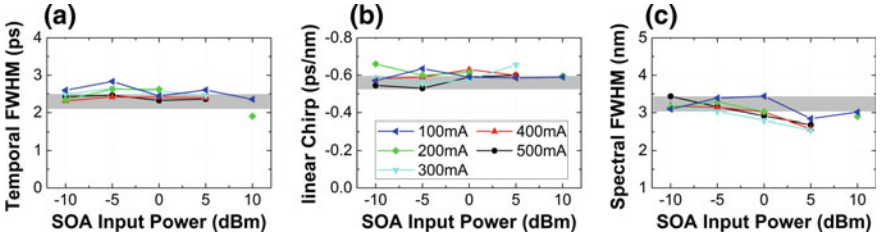

Fig. 3.23 **a** Temporal and **c** spectral FWHM of the normalized pulse profiles and **b** the linear part of the spectral chirp versus the QD SOA averaged input power level for various currents. Missing points are due to a failed retrieving of the measurements. The *shaded area* represents the error margin of the input signal. All three graph share the same legend

In conclusion, the QD SOA shows minor or no SPM for 40 GHz ps pulse combs for input power levels up to 5 dBm. Typical input power levels for optical communication systems are much below 5 dBm and QD SOAs are thus suitable for amplification of pulsed signals. For the sake of completeness, using very larger input power levels increases the SPM also in QD SOAs, which can be used for signal processing, e.g. [77].

3.6.2 QD GS Dynamics Under ES Perturbation

A QD laser-SOA hybrid was used to investigate the QD GS gain recovery under strong ES perturbation. The device is designed as an ES laser while preventing the onset of lasing on the GS. The original motivation for the development of this device was to identify relaxation pathways of the multi-state QD gain media as preparation for the multi-state amplification demonstrated in Chap. 7. The device was processed out of wafer Do 1791 featuring 5 QD layers and exhibits a 1.33 mm long and 6 µm wide shallow-etched ridge waveguide. In contrast to QD SOAs No. 1–6, this device was realized without a tilt of the ridge waveguide and one facet received a dichroic mirror coating whereas the other facet is as cleaved.

The device characterization as well as single-color pump-probe measurements have been performed by Yücel Kaptan and Bastian Herzog in the framework of their dissertation and Master thesis on a free-space optics stage at the Institute of Optics and Atomic Physics at the Technische Universität Berlin. The LIV characteristics and optical spectra are shown Fig. 3.24. The GS peak ASE emission is found at a wavelength of 1251 nm at a current of 80 mA. A gain ripple on the order of 0.5 dB is observed. Increasing the current up to 290 mA, the GS peak ASE is red-shifted by 11 nm. The onset of ES lasing at a current of about 195 mA represents a large perturbation which limits the number of charge carriers in the QD ES and reservoir refilling the QD GS. The center ES lasing wavelength is red shifted from 1177 to 1181 nm with increasing the current from 200 to 290 mA.

Pump-Probe Measurements

A detailed description of the pump-probe setup can be found in [78, 79]. A QD sub-ensemble with a GS emission wavelength of 1270 nm has been identified to be resonant to the ES lasing emission [78]. A control ensemble with a center GS

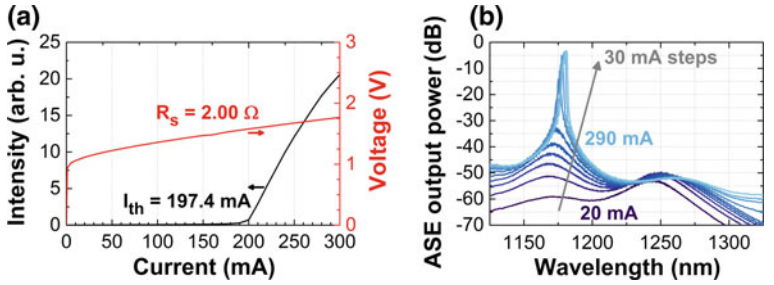

Fig. 3.24 Characteristics of the QD laser-SOA hybrid. **a** The optical power as well as voltage as a function of the current (LIV). **b** Spectrally resolved device emission for different currents. The power levels in both graphs are given in arb. units because the coupling and setup losses are unknown. The data are kindly provided by Yücel Kaptan, Technische Universität Berlin

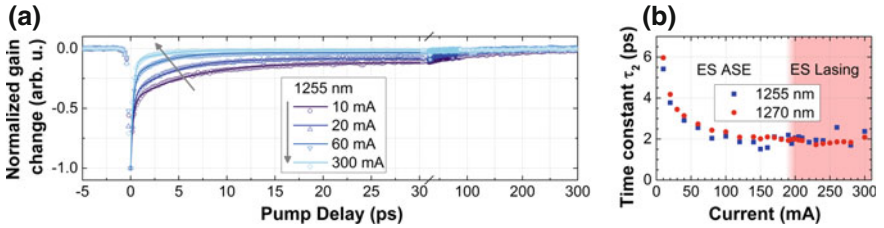

Fig. 3.25 **a** Exemplary measured single-color pump-probe traces (*symbols*) and fits (*straight line*) for time ranges from 0 to 30 ps for different DUT current. Please note the x-axis scale change after 30 ps. **b** time constant τ_2 extracted from fits of the single-color pump probe traces for QDs sub-ensemble being resonant with the ES lasing (1270 nm) and a QD control sub-ensemble (1255 nm). The data are kindly provided by Yücel Kaptan, Technische Universität Berlin

wavelength of 1255 nm was chosen for comparing the dynamics. The input energy per pulse, temporal FWHM and pulse distance of the pump (probe) input pulses were 6.6 pJ per pulse (0.66 pJ per pulse), 0.25 ps (0.35 ps) and about 13.3 ns (13.1 ns) corresponding to a pulse repetition rate of 75.4 MHz (76.1 MHz). The free-space to DUT coupling efficiency was below 10 %. Exemplary recorded single-color pump-probe measurements are shown in Fig. 3.25a. The recovery from the pump induced normalized gain dip can be described by the sum of three exponential functions

$$\Delta G|_{recovery} = \Delta G_0 + \sum_{i=1}^{3} \Delta G_i \cdot e^{t/\tau_i}. \tag{3.3}$$

The first time constant τ_1 is in the sub-picosecond regime and is determined by coherent effects of the pump and probe pulse with the gain media. Hence, is fixed to the experimental time resolution. The second time constant τ_2 is in the order of picoseconds and accounts for the carrier capture into the QDs. The third time constant τ_3 is a few hundred picoseconds and determines the recovery of the carrier

reservoir via current injection and thus attributes to CDP (see also Sect. 2.3.2). Fitting the pump-probe traces in the first 30 ps after the pump pulse, the third exponential function contributes approximately only a constant term to ΔG_0 and is thus neglected. Using the remaining free parameters ΔG_i with $i \in \{0, 1, 2\}$ and τ_2, all measured traces can be fitted with high accuracy.

The time constants τ_2 extracted from the fits is plotted in Fig. 3.25b in dependence of the current. The recovery time is decreased with increasing current starting at about 6 ps and saturates finally at about 2 ps at a current of about 100 mA consistent with previous measurements of similar QD SOAs [80]. The onset of ES lasing at a current of around 195 mA neither influences the recovery time of the control sub-ensemble (1255 nm) nor the resonant sub-ensemble (1270 nm).

Simulations

For a deeper understanding of the carrier dynamics, the device has been modeled by André Röhm in the framework of his Master's thesis at the Institute for Theoretical Physics at the Technische Universität Berlin. Detailed descriptions can be found in [81]. His microscopically based multi-rate equation model will be briefly introduced and subsequently the obtained results will be discussed. A detailed description of the model can be found in [81, 82].

Illustrations for the following theoretical description are given in Fig. 3.26a, b. The charge-carrier density of the two-dimensional carrier reservoir is given by w_b

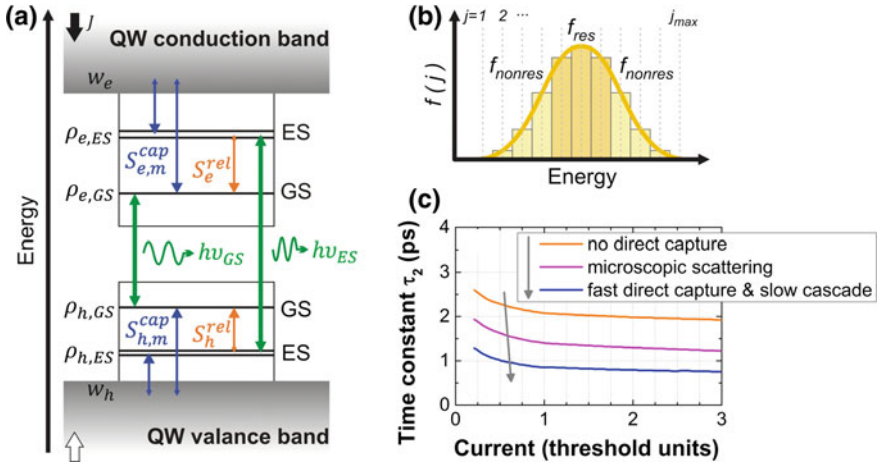

Fig. 3.26 **a** Sketch of energy band structure of a QD with a dot-in-a-well structure with QD state occupation probabilities $\rho_{b,m}$, w_b QW carrier reservoir density as well as scattering processes with scattering rates $S_{b,m}$ and optical transitions. **b** Sketch of the Gaussian probability mass function f of an inhomogeneously broadened QD ensemble distributed into j_{max} subgroups. The subgroups are separated into groups of optical active f_{res} and inactive f_{nonres} QDs. **c** Modeled time constant τ_2 with respect to the device current given in units of the ES laser threshold current for different dominating carrier capture paths. **a** and **b** are redrawn after [81, 83]. The data in **c** are kindly provided by André Röhm, Technische Universität Berlin and are redrawn after [81]

with $b \in \{e, h\}$ for electrons and holes. The occupation probability of the QD states is described by $\rho_{b,m}$ with $m \in \{GS, ES\}$ denoting the QD GS and ES. The model takes into account direct capture from the carrier reservoir into the QD states as well as carrier relaxation between the QD states. The corresponding scattering rates $S_{b,m}^{cap}$ and S_b^{rel} are microscopically calculated taking into account Auger-scattering processes and a detailed balanced condition. In this microscopic approach, the relaxation rates scale dynamically with the reservoir carrier density. The GS relaxation rate of the electrons (holes) is about 5–40 (25–200) times faster than the direct capture rate at reasonable operating currents for applications [83].

The inhomogeneous QD ensemble broadening is accounted by distributing the QDs into j_{max} subgroups. A Gaussian probability mass function $f(j)$ describes the ratio of QDs within the j^{th} subgroup in relation to the total number of QDs. The subgroups are divided into fractions f_x with $x \in \{res, nonres\}$ of QDs optically resonant f_{res} and non-resonant $f_{nonres} = 1 - f_{res}$ to the ES lasing. A ratio of 50 % was found to fit experimentally obtained data of QD lasers [84]. The set of material rate equations are then given by

$$\begin{aligned}
\frac{d}{dt} w_b &= \underbrace{\frac{J}{\epsilon_0}}_{CI} - \underbrace{R_{loss} w_e w_h}_{QW\ losses} - N^{QD} \sum_{x,m} \underbrace{2 v_m f_x S_{b,m,x}^{cap}}_{scattering}, \\
\frac{d}{dt} \rho_{b,m,x} &= - \underbrace{W_m\ \rho_{e,m,x}\ \rho_{h,m,x}}_{QD\ losses} + \underbrace{S_{b,m,x}^{cap} \pm \frac{1}{v_m} S_{b,x}^{rel}\Big|_{\substack{GS=+ \\ ES=-}}}_{scattering} - \underbrace{\frac{\partial \rho_{b,x}^m}{\partial t}\Big|_{st}}_{\substack{stimulated \\ recombination}},
\end{aligned} \tag{3.4}$$

with J: pump current density per layer, ϵ_0: vacuum permittivity, R_{loss}: effective reservoir loss rate, N^{QD}: QD density per layer, v_m: QD degeneracy excluding spin ($v_{GS} = 1$, $v_{ES} = 2$), W_m: spontaneous recombination rate. The stimulated emission term is given here by

$$\frac{\partial \rho_{b,x}^m}{\partial t}\Big|_{st} = \frac{2 g_{m,x}}{2 v_m f_x N^{QD}} (\rho_{e,m,x} + \rho_{h,m,x} - 1) N_m^{Ph}, \tag{3.5}$$

with g_m, x: gain coefficient, N_m^{Ph}: photon density per QD layer. The QW charge-carrier density is thus increased by carrier injection (CI) and decreased by scattering into the QD states and general losses. The occupation probability of the QD states is decreased by general QD losses and stimulated recombination as well as increased by scattering from the carrier reservoir into the QD states. In addition, the occupation probability of the QD GS is increased by scatting from the QD ES and the occupation probability of the ES is reduced correspondingly. The photon density per QD layer of the GS N_{GS}^{Ph} is modeled by a Gaussian pulse whereas the photon density per QD layer of the ES N_{ES}^{Ph} is given by a dynamic equation:

$$
\begin{aligned}
N_{GS}^{Ph} &= A_0 e^{-4log(2)(t/T_{FWHM})^2}, \\
\frac{d}{dt} N_{ES}^{Ph} &= (\underbrace{2g_{ES,res}(\rho_{e,ES,res} + \rho_{h,ES,res} - 1)}_{\substack{stimulated \\ recombination}} - \underbrace{2\kappa}_{\substack{optical \\ losses}}) N_{ES}^{Ph} \\
&\quad + \underbrace{4N^{QD}\beta W_{ES}\ \rho_{e,ES,res}\ \rho_{h,ES,res}}_{spontaneous\ emission},
\end{aligned}
\tag{3.6}
$$

with T_{FWHM}: pulse FWHM equal 180 fs, A_0: pulse amplitude, κ: cavity loss rate, β: spontaneous emission factor.

A simulation of the above described experiment was performed for the resonant QDs for three different carrier relaxation paths. First, the direct scattering from the carrier reservoir into the QD GS was neglected resulting in a cascaded refilling of the GS only. Second, the cascaded GS refilling was suppressed by drastically slowing the corresponding scattering rates resulting in a predominantly direct-capture-based refilling of the GS. Third, a mix of both paths was realized by using the microscopically calculated scattering rates. The modeled GS gain recovery time constant τ_2 is plotted in Fig. 3.26c in dependence of the current. The evolution of the experimental and modeled curves are in good agreement whereas the magnitude of the modeled curves could be adapted by changing all scattering channels with a constant factor without changing the relation between the different paths. However, the simulated recovery time constants show no change at the ES lasing threshold similar to the experiment. Thus, the relaxation path cannot been identified by this experiment.

The results of the GS gain dynamics under a strong ES perturbation allow inferences about the dual state amplification of data signals. The amplification of an optical data signal on the ES wavelength is therefore expected to introduce minor or nor signal degradations of a simultaneously amplified data signal on the GS wavelength.

3.6.3 QD ES Dynamics Under GS Perturbation

The identical device described in the previous Sect. 3.6.2 was used to get excess to the QD ES gain dynamics under a perturbation on the GS. The measurements have been performed by Yücel Kaptan, Bastian Herzog in the framework of their dissertation and Master thesis at the Institute of Optics and Atomic Physics at the Technische Universität Berlin. The corresponding simulation have been performed by André Röhm in the framework of his Master thesis at the Institute for Theoretical Physics at the Technische Universität Berlin. Detailed descriptions can be found in [79, 81, 85].

Time-resolved measurements of the ES emission have been conducted with a streak camera exhibiting a temporal resolution of 30 ps whereas a pump pulse was used to abruptly decrease the occupation of the GS. The pump pulse exhibited a temporal FWHM of 180 fs, spectral FWHM of 17 nm, a repetition rate of 75.4 MHz and an energy per pulse of about 40 fJ.

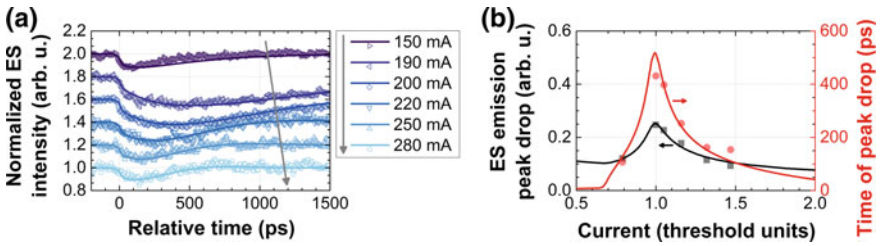

Fig. 3.27 **a** Experimentally (*symbols*) and simulated (*straight lines*) normalized intensity of the ES emission versus relative time with respect to the GS perturbation for different currents. The curves are shifted by 0.2 on the y-axis for an improved readability. **b** Experimentally (*symbols*) and simulated (*straight lines*) reduction of the ES emission and its appearance in time versus the current normalized to the threshold current. The data of both graphs are kindly provided by Yücel Kaptan and André Röhm, both Technische Universität Berlin

The measured and simulated time-resolved emission spectra are depicted in Fig. 3.27 for currents below, close to and above the ES laser threshold for a GS perturbation on resonant QDs. The GS perturbation leads for all driving conditions to a drop of the ES emission due to relaxation oscillations [85]. The depth and temporal position of the peak of this drop is strongly current dependent. Both, the drop depth and temporal position are determined by the relaxation oscillation frequency and damping factors [81]. Thus, the largest drop and temporal delay with respect to the GS perturbation are observed around the threshold current. Additional measurements and simulations performed for GS perturbations on non-resonant QDs show still a drop which is halved in its depth but the temporal position is nearly unchanged [85]. For these constellations, the relaxation oscillations have to be caused via the carrier reservoir. Indeed, the modeled carrier dynamics show that the picosecond refilling of the depleted non-resonant QD states reduces the carrier density in the reservoir. The new equilibrium condition results in an effective carrier escape from the resonant QD states into the reservoir again on a picosecond time scale. Thus, the system effectively redistributes the carriers from resonate to non-resonant QDs across the QW barrier in a picosecond time scale which leads to the experimentally observable relaxation oscillations.

The conclusions out of these results for the realization of QD-based dual-state amplifiers are restricted. On the one hand, the slow relaxation oscillations do not appear in amplifiers and the peak of the spectral-resolved photon density in the waveguide is usually smaller than in laser cavities. Additionally, amplifiers are usually driven in deeper saturation than lasers, which improves the ES dynamics. The obtained relatively slow ES dynamics is therefore limited by the special device design and cannot be transferred to amplifier dynamics.

On the other hand, the results also demonstrate a significant coupling of resonant and non-resonant QDs via the carrier reservoir which is of course a non-negligible factor for multi-channel and/or multi-state amplification. Pump-probe experiments in non-lasing devices obtained for all combinations of GS and ES gain recoveries and

perturbations published in [61] showed a slow ES gain recovery of up to 100 ps for unsaturated ES gain bias conditions. But a slow GS gain recovery can be observed for the unsaturated GS ASE emission as well, e.g. see Fig. 3.25. In contrast, a much faster ES gain recovery is observed for bias conditions pushing the ES emission close to saturation [57]. Indeed, the simulations also show a very fast gain recovery for the ES [81].

In conclusion, a fast gain recovery of both QD states and a decoupling of different QD sub-ensembles can be predicted for QD amplifiers if both states are saturated and the carrier reservoir is highly populated.

3.7 Summary

This chapter gave an overview of the fabrication as well as basic and dynamic characteristics of QD SOAs. First, the QD SOA design was introduced, in particular the p-i-n-diode structure, the realization of light guiding structures and the suppression of the cavity. Subsequently, the QD SOAs used throughout for characterization in the following chapters have been introduced.

QD SOAs exhibit excellent fiber-to-fiber gain values of up to 25.5 dB corresponding to chip gain values as large as 34.5 dB. A 3-dB ASE bandwidth of more than 20 dB is found for all SOAs with the largest bandwidth of 34 nm. A concept of a sectioned QD SOA was realized preventing the onset of ASE lasing. In contrast to standard single-section QD SOAs, the sectioned SOA offers a gain increase of 4 dB corresponding to a very large chip gain of 39.5 dB, but at the expense of a reduced gain bandwidth down to 10.7 nm. The gain is limited at larger currents for most of the QD SOAs chips by the thermal conductivity to the sub-mount. Hence, the QD SOAs characterized in this thesis provide promising chip characteristics, but the mounting technology has to be improved to access their full performance. Fiber-to-fiber noise figures down to 8.6 dB are found corresponding to excellent chip noise figures of 4.1 dB.

A comparison with commercially available QD and QW SOAs yields comparable chip gain values but lower fiber-to-fiber gain values due to the relatively high coupling losses. Additionally, the 3-dB ASE bandwidth was found to be smaller due to the gain dip between the QD GS and ES wavelengths. However, both states can be used for amplification of signals with a spectral separation of 100 nm which will be demonstrated in Chap. 7.

The last part of the chapter presented the emission and amplification of the two QD states in terms of polarization dependence and carrier dynamics. The GS ASE emission exhibits a TM-TE polarization ratio in the order of 18 dB whereas the ES ASE emission offers a reduced ratio of about 7.5 dB. QD SOAs exhibit very fast gain recovery of both QD states, and low self-phase modulation. Furthermore, the inhomogeneously broadened QD ensemble provides decoupled dynamics for currents saturating the QD emission and highly populating the carrier reser-

voir. Hence, QD SOAs are predestined for ultra-fast signal processing as well as single-, multi-channel and multi-state amplification of both, amplitude and phase-coded signals.

References

1. A.R. Kovsh et al., InAs/InGaAs/GaAs quantum dot lasers of 1.3 μm range with enhanced optical gain. J. Cryst. Growth **251**(1–4), 729–736 (2003)
2. Y. Nakata, Y. Sugiyama, M. Sugawara, Molecular beam epitaxial growth of selfassembled InAs/GaAs quantum dots, in *Self-assembled InGaAs/GaAs Quantum Dots, 1st end*, ed. by M. Sugawara (Academic Press, London, 1999), p. 368
3. D. Bimberg, M. Grundmann, N.N. Ledentsov, *Quantum Dot Heterostructures*, 1st edn. (Wiley, London, 1998)
4. D. Bimberg (ed.), *Semiconductor Nanostructures*, 2nd edn. (Springer, Berlin, 2008)
5. M. Kuntz, Modulated InGaAs/GaAs quantum dot lasers. Doctoral thesis. Technical University of Berlin (2006)
6. H.Y. Liu et al., P-doped 1.3 μm InAs/GaAs quantum-dot laser with a low threshold current density and high differential effciency. Appl. Phys. Lett. **89**(7), 073113 (2006)
7. A. Lenz et al., Limits of In(Ga)As/GaAs quantum dot growth. Phys. Status Solidi **246**(4), 717–720 (2009)
8. H. Eisele et al., Change of InAs/GaAs quantum dot shape and composition during capping. J. Appl. Phys. **104**(12), 124301 (2008)
9. H. Eisele et al., Atomic structure of InAs and InGaAs quantum dots determined by cross-sectional scanning tunneling microscopy. J. Cryst. Growth **248**, 322–327 (2003)
10. M. Laemmlin, GaAs-based semiconductor optical amplifiers with quantum dots as an active medium. Doctoral thesis (2007)
11. D. Marcuse, Reflection loss of laser mode from tilted end mirror. J. Lightw. Technol. **7**(2), 336–339 (1989)
12. B.R. Bennett, R.A. Soref, J.A. del Alamo, Carrier-induced change in refractive index of InP, GaAs and InGaAsP. IEEE J. Quantum Electron. **26**(1), 113–122 (1990)
13. J. Kischkat et al., Mid-infrared optical properties of thin films of aluminum oxide, titanium dioxide, silicon dioxide, aluminum nitride, and silicon nitride. Appl. Opt. **51**(28), 6789–6798 (2012)
14. Sh.A Furman, A.V. Tikhonravov, *Basics of Optics of Multilayer Systems*, 1st edn. (Editions Frontièeres, Paris, 1992)
15. L. Gao, F. Lemarchand, M. Lequime, Refractive index determination of SiO2 layer in the UV/Vis/NIR range: spectrophotometric reverse engineering on single and bi-layer designs. J. Eur. Opt. Soc. Rapid Publ. **8**, 13010 (2013)
16. J.R. Devore, Refractive indices of rutile and sphalerite. J. Opt. Soc. Am. **41**(6), 416–417 (1951)
17. C. Meuer, GaAs-based quantum-dot semiconductor optical amplifiers at 1.3 μm for all-optical networks. Doctoral thesis. Technical University of Berlin (2011), p. 155
18. N. Kirstaedter et al., Gain and differential gain of single layer InAs/GaAs quantum dot injection lasers. Appl. Phys. Lett. **69**(9), 1226 (1996)
19. A. Kovsh et al., Quantum dot laser with 75nm broad spectrum of emission. Opt. Lett. **32**(7), 793–795 (2007)
20. M. Hopkinson et al., High power broadband superluminescent diodes with chirped multiple quantum dots. Electron. Lett. **43**(19), 1045–1047 (2007)
21. T. Yamatoya et al., High power GaInAsP/InP strained quantum well superluminescent diode with tapered active region. Jpn. J. Appl. Phys. **38**, 5121–5122 (1999)
22. M. Yamada et al., Low-noise and high-power Pr/sup 3+/-doped fluoride fiber amplifier. IEEE Photonics Technol. Lett. **7**(8), 869–871 (1995)

23. L.H. Li et al., Wide emission spectrum from superluminescent diodes with chirped quantum dot multilayers. Electron. Lett. **41**(1), 41–43 (2005)
24. T. Akiyama et al., An ultrawide-band semiconductor optical amplifier having an extremely high penalty-free output power of 23 dBm achieved with quantum dots. IEEE Photonics Technol. Lett. **17**(8), 1614–1616 (2005)
25. Y.-S. Cho, W.-Y. Choi, Analysis and optimization of polarization-insensitive semiconductor optical amplifiers with delta-strained quantum wells. IEEE J. Quantum Electron. **37**(4), 574–579 (2001)
26. T. Kita et al., Polarization-independent photoluminescence from columnar InAs/GaAs self-assembled quantum dots. Jpn. J. Appl. Phys. **41**, L1143–L1145 (2002)
27. J. Jin et al., Fabrication and complete characterization of polarization insensitive 1310 nm InGaAsP-InP quantum-well semiconductor optical amplifiers. Semicond. Sci. Technol. **19**(1), 120 (2004)
28. T. Akiyama, M. Sugawara, Y. Arakawa, Quantum-dot semiconductor optical amplifiers. Proc. IEEE **95**(9), 1757–1766 (2007)
29. N. Yasuoka et al., Quantum-dot semiconductor optical amplifiers with polarizationindependent gains in 1.5 μm wavelength bands. IEEE Photonics Technol. Lett. **20**(23), 1908–1910 (2008)
30. M. Mikulla, Tapered high-power, high-brightness diode lasers: design and performance, in *High-Power Diode Lasers: Fundamentals, Technology, Applications*, 1st edn., ed. by R. Diehl (Springer, Berlin, 2000)
31. P. Loosen, Cooling and packaging of high-power diode lasers, in *High-Power Diode Lasers: Fundamentals, Technology, Applications*, 1st edn., ed. by R. Diehl (Springer, Berlin, 2000)
32. K. Boucke, Packaging of diode laser bars, in *High Power Diode Lasers: Technology and Applications*, 2nd edn., ed. by F. Bachmann, P. Loosen, R. Poprawe (Springer, Berlin, 2007)
33. S. Weiss, E. Zakel, H. Reichl, Mounting of high power laser diodes on diamond heatsinks. IEEE Trans. Componen. Packag. Manuf. Technol. Part A **19**(1), 46–53 (1996)
34. T. Kettler et al., High-brightness and ultranarrow-beam 850-nm GaAs/AlGaAs photonic band crystal lasers and single-mode arrays. IEEE J. Sel. Top. Quantum Electron. **15**(3), 901–908 (2009)
35. R. Bonk et al., Linear semiconductor optical amplifiers, in *Fibre Optic Communication: Key Devices*, 1st edn., ed. by H. Venghaus, N. Grote (Springer, Berlin, 2012), p. 682
36. C.M. Weinert, Design of fiber-matched uncladded rib waveguides on InP with polarizationindependent mode matching loss of 1 dB. IEEE Photonics Technol. Lett. **8**(8), 1049–1051 (1996). Aug
37. T.L. Koch et al., Tapered waveguide InGaAs/InGaAsP multiple-quantum-well lasers. IEEE Photonics Technol. Lett. **2**(2), 88–90 (1990)
38. H. Kobayashi et al., Tapered thickness MQW waveguide BH MQW lasers. IEEE Photonics Technol. Lett. **6**(9), 1080–1081 (1994)
39. Y. Tohmori et al., Spot-size converted 1.3 μm laser with butt-jointed selectively grown vertically tapered waveguide. Electron. Lett. **31**(13), 1069–1070 (1995)
40. K. Kasaya et al., A simple laterally tapered waveguide for low-loss coupling to singlemode fibers. IEEE Photonics Technol. Lett. **5**(3), 345–347 (1993)
41. ITU-T, *ITU-T G.989.1 03/2013, series G: transmission systems and media, digital systems and networks; digital sections and digital line system—optical line systems for local and access networks* (2013)
42. C. Schmidt-Langhorst et al., Quantum-dot semiconductor optical booster amplifier with ultra-fast gain recovery for pattern-effect free amplification of 80 Gb/s RZ-OOK data signals, in *European Conference and Exhibition on Optical Communication (ECOC)*, Vienna, Austria (2009), p. 6.2.1
43. M. Kuntz et al., High-speed mode-locked quantum-dot lasers and optical amplifiers. Proc. IEEE **95**(9), 1767–1778 (2007)
44. E.U. Rafailov, M.A. Cataluna, W. Sibbett, Mode-locked quantum-dot lasers. Nat. Photonics **1**(7), 395–401 (2007)

45. M.G. Thompson et al., InGaAs quantum-dot mode-locked laser diodes. IEEE J. Sel. Top. Quantum Electron. **15**(3), 661–672 (2009)
46. H. Schmeckebier et al., Complete pulse characterization of quantum-dot mode-locked lasers suitable for optical communication up to 160 Gbit/s. Opt. Express **18**(4), 3415–3425 (2010)
47. G. Fiol, 1.3 μm monolithic mode-locked quantum-dot semiconductor lasers. Doctoral thesis (2011), p. 169
48. M. Spiegelberg, Emission hochfrequenter Pulse von Nanostruktur-Lasern. Master thesis. Technische Universitaet Berlin (2015), p. 70
49. E. Rouvalis et al., 40 Ghz quantum quantum-dot mode-locked laser packaged module operating at 1310 nm, in *Asian Communication and Photonics Conference (ACP)*, 2014, AW3A.2
50. A. Schliwa, M. Winkelnkemper, D. Bimberg, Impact of size, shape, and composition on piezoelectric effects and electronic properties of In(Ga)As/GaAs quantum dots. Phys. Rev. B **76**(20), 205324 (2007)
51. A. Schliwa, Electronic properties of quantum dots. Doctoral thesis, Technische Universitaet Berlin (2007)
52. G. Eisenstein et al., Ultrafast gain dynamics in 1.5 μm multiple quantum well optical amplifiers. Appl. Phys. Lett. **58**(2), 158 (1991)
53. S. Weiss et al., Carrier capture times in 1.5 μm multiple quantum well optical amplifiers. Appl. Phys. Lett. **60**(1), 9 (1992)
54. F. Girardin, G. Guekos, A. Houbavlis, Gain recovery of bulk semiconductor optical amplifiers. IEEE Photonics Technol. Lett. **10**(6), 784–786 (1998)
55. P. Borri et al., Spectral hole-burning and carrier-heating dynamics in InGaAs quantumdot amplifiers. IEEE J. Sel. Top. Quantum Electron. **6**(3), 544–551 (2000)
56. T.W. Berg et al., Ultrafast gain recovery and modulation limitations in self-assembled quantum-dot devices. IEEE Photonics Technol. Lett. **13**(6), 541–543 (2001)
57. S. Schneider et al., Excited-state gain dynamics in InGaAs quantum-dot amplifiers. IEEE Photonics Technol. Lett. **17**(10), 2014–2016 (2005)
58. P. Borri et al., Ultrafast carrier dynamics in InGaAs quantum dot materials and devices. J. Opt. A Pure Appl. Opt. **8**(4), S33–S46 (2006)
59. A.J. Zilkie et al., Carrier dynamics of quantum-dot, quantum-dash, and quantum-well semiconductor optical amplifiers operating at 1.55 μm. IEEE J. Quantum Electron. **43**(11), 982–991 (2007)
60. T. Piwonski et al., Carrier capture dynamics of InAs/GaAs quantum dots. Appl. Phys. Lett. **90**(12), 122108 (2007)
61. I. O'Driscoll et al., Phase dynamics of InAs/GaAs quantum dot semiconductor optical amplifiers. Appl. Phys. Lett. **91**(26), 263506 (2007)
62. T. Vallaitis et al., Slow and fast dynamics of gain and phase in a quantum dot semiconductor optical amplifier. Opt. Express **16**(1), 170–178 (2008)
63. T. Erneux et al., The fast recovery dynamics of a quantum dot semiconductor optical amplifier. Appl. Phys. Lett. **94**(11), 113501 (2009)
64. J. Gomis-Bresco et al., Time-resolved amplified spontaneous emission in quantum dots. Appl. Phys. Lett. **97**(25), 251106 (2010)
65. J. Kim et al., Role of carrier reservoirs on the slow phase recovery of quantum dot semiconductor optical amplifiers. Appl. Phys. Lett. **94**(4), 041112 (2009)
66. A.V. Uskov et al., Carrier-induced refractive index in quantum dot structures due to transitions from discrete quantum dot levels to continuum states. Appl. Phys. Lett. **84**(2004), 272–274 (2004)
67. G.P. Agrawal, N.A. Olsson, Self-phase modulation and spectral broadening of optical pulses in semiconductor laser amplifiers. IEEE J. Quantum Electron. **25**(11), 2297–2306 (1989)
68. F. Romstad et al., Measurement of pulse amplitude and phase distortion in a semiconductor optical amplifier: from pulse compression to breakup. IEEE Photonics Technol. Lett. **12**(12), 1674–1676 (2000)
69. P.P. Baveja et al., Self-phase modulation in semiconductor optical amplifiers: impact of amplified spontaneous emission. IEEE J. Quantum Electron. **46**(9), 1396–1403 (2010)

70. D. Bimberg et al., InGaAs-GaAs quantum-dot lasers. IEEE J. Sel. Top. Quantum Electron. **3**(2), 196–205 (1997)
71. A.A. Ukhanov et al., Comparison of the carrier induced refractive index, gain, and linewidth enhancement factor in quantum dot and quantum well lasers. Appl. Phys. Lett. **84**(7), 1058–1060 (2004)
72. S. Schneider et al., Linewidth enhancement factor in InGaAs quantum-dot amplifiers. IEEE J. Quantum Electron. **40**(10), 1423–1429 (2004)
73. M. Gioannini, A. Sevega, I. Montrosset, Simulations of differential gain and linewidth enhancement factor of quantum dot semiconductor lasers. Opt. Quantum Electron. **38**(4–6), 381–394 (2006)
74. T. Vallaitis et al., Quantum dot SOA input power dynamic range improvement for differential-phase encoded signals. Opt. Express **18**(6), 6270–6276 (2010)
75. R. Trebino, *Frequency-Resolved Optical Gating: The Measurement of Ultrashort Laser Pulses*, 2nd edn. (Springer, Berlin, 2002)
76. H. Schmeckebier, Analyse von optischen Pulsen modengekoppelter Quantenpunkt-Halbleiterlaser. Diploma thesis (2009)
77. G. Contestabile et al., Regenerative amplification by using self-phase modulation in a quantum-dot SOA. IEEE Photonics Technol. Lett. **22**(7), 492–494 (2010)
78. Y. Kaptan et al., Gain dynamics of quantum dot devices for dual-state operation. Appl. Phys. Lett. **104**(26), 261108 (2014)
79. B. Herzog. Gaindynamik in Quantenpunktverstärkern und-Lasern. Master thesis. Technische Universität Berlin (2014)
80. S. Dommers et al., Complete ground state gain recovery after ultrashort double pulses in quantum dot based semiconductor optical amplifier. Appl. Phys. Lett. **90**(3), 033508 (2007)
81. A. Röhm, Dynamic scenarios in two-state quantum dot lasers. Master thesis, Technische Universität Berlin (2015)
82. A. Röhm, B. Lingnau, K. Lüdge, Understanding ground-state quenching in quantumdot lasers. IEEE J. Quantum Electron. **51**(1), 1–11 (2015)
83. B. Lingnau, Nonlinear and nonequilibrium dynamics of quantum-dot optoelectronic devices. Doctoral thesis, Technische Universität Berlin (2015)
84. B. Lingnau, W.W. Chow, K. Lüdge, Amplitude-phase coupling and chirp in quantum-dot lasers: inuence of charge carrier scattering dynamics. Opt. Express **22**(5), 4867–4879 (2014)
85. Y. Kaptan et al., Stability of quantum-dot excited-state laser emission under simultaneous ground-state perturbation. Appl. Phys. Lett. **105**(19), 191105 (2014)

Chapter 4
Introduction to System Experiments

The subsequent chapters in this thesis will demonstrate the suitability of QD-SOAs for generation, amplification and wavelength conversion of digital data signals coded in different physical properties of an optical wave. System experiments are widely used to test optoelectronic devices for optical communication applications under system-like operation. That means, that a defined digital test pattern is first converted from the electronic domain to the optical domain and transmitted (called: signal generation); secondly transmitted across a fiber span, amplified and/or processed and thirdly reconverted to the electronic domain and evaluated (called: detection). This chapter gives an introduction to the fundamentals of system experiments addressing in detail all three processes. Section 4.1 starts with an overview of the test patterns and modulation formats being relevant for this thesis. Subsequently, Sect. 4.2 discusses various configurations of test setups for the amplifier characterization and defines important terms and parameters. In addition, different transmitter and receiver types are introduced for various modulation formats. Section 4.3 discusses different methods and parameters used for evaluation of the signal quality. Finally, Sect. 4.4 addresses the input power dynamic range (IPDR) which is one important key parameter for optical amplifiers.

4.1 Test Pattern and Modulation Formats

This section first introduces the electrical test pattern used in this thesis and discusses its characteristics. Subsequently, optical modulation formats are introduced.

H. Schmeckebier, *Quantum-Dot-Based Semiconductor Optical Amplifiers for O-Band Optical Communication*, Springer Theses,
DOI 10.1007/978-3-319-44275-4_4

4.1.1 Pseudo-Random Bit Sequences

Particular well-defined bit sequences are used under laboratory conditions as they provide comparability and repeatability. Commonly a pseudo-random binary sequence (PRBS) (partially also called pseudo-random bit sequence) is used for test setups of two level modulation formats, such as OOK or binary phase-shift keying (PSK). The PRBS is a deterministic sequence and is specified by its degree x. A PRBS-x[1] has a length of $2^x - 1$ bits. Such a sequence can be generated for example with a shift register [1, 2]. A PRBS-x has the following characteristics [2, 3]:

- The PRBS-x contains all possible x-bit long words precisely once, except the word formed either only by zeros or ones.[2] The 2^x different words are given by permutations of zeros and ones.
- The PRBS-x contains 2^{x-1} ones and $2^{x-1} - 1$ zeros or vice versa.
- The frequency spectrum has a $sin^2(y)/y$ shape — with zero points at multiples of the bit rate — formed by discrete frequencies. The frequency density increases with increasing degree and the lowest frequency is given by $bit\ rate \cdot (2^x - 1)^{-1}$ and decreases with increasing degree.
- The derivation of a PRBS is again a PRBS. This is important for differential detection as no special pre-coding is required for the test setups.
- Interleaving two equal PRBS shifted by $\lceil (2^x - 1)/2 \rceil$ bits to each other results in the identical PRBS with the doubled bit rate. This can be used to simulated multiplexing data streams.

Typically, a PRBS-31 is used for system experiments as it is close to the characteristics of real traffic which is usually coded to restrict the maximum number of zeros and ones [3]. However, due to memory limitations of the measurements devices[3] or due to AC-coupling of electronic components, often PRBSs with a reduced degree are used. Most common are PRBS with the length of $2^{15} - 1$ (PRBS-15).

4.1.2 Modulation Formats

In digital optical communication, the logical channel (bit stream) is coded in the physical properties of an optical carrier wave, such as amplitude, phase, frequency and momentum, according to the used modulation format. This is called modulation channel. Multiple modulation channels can be interleaved in time (time division multiplexing, TDM), frequency (wavelength division multiplexing, WDM, orthogonal frequency-division multiplexing, OFDM) and/or polarization [4–8].

---

[1] This notation is used throughout this thesis instead of PRBS $2^x - 1$.

[2] The standard is typically, that the word formed only by zeros is missing.

[3] Recording a complete PRBS-31 requires a very fast 2 GB memory whereas a PRBS-23 requires only 8 MB memory [3].

A long time, simple two-level amplitude (or intensity) modulation, so called on-off keying (OOK) or sometimes two-level pulse amplitude modulation (PAM-2), was the dominating modulation format in optical communication systems [9]. Up to certain bit rates, this format is easy and cheap to generate via direct modulated lasers and to detect via simple direct detection. The increasing number of users, network capacity, transmission rate and required network flexibility first lead to a partial replacement of direct modulated devices by e.g. Mach-Zehnder modulator (MZM), due to bandwidth and performance limitation of the directly modulated lasers. In the next step, more advanced modulation arouse the interest, as they offer on the one hand performance and multiplexing improvements [9–11]. More important, they offer the capability to increasing data rates while keeping or even lower the required electrical bandwidth of the components which is an important cost factor.

Amongst others, advanced modulation formats include multi-level-amplitude modulation (PAM), x-phase-shift keying (PSK) modulation and m-ary amplitude-phase modulation (quadrature amplitude modulation, QAM). This thesis is focused on the generation and amplification of clear amplitude and phase-coded signals. Thus, only this formats are introduced in the following paragraphs whereas an introduction to the complete zoo of modulation formats can be found e.g. in [5, 6, 8, 9] or on Wikipedia.com [12].

In general, the modulated signal can be described as a complex carrier wave with a time dependent modulated amplitude and phase. Plotting the wave field in the complex plane with the real and imaginary field axes whereas neglecting the fast carrier amplitude oscillation results in the commonly used constellation diagram or IQ diagram. The real and imaginary axes are commonly called the in-phase (I) axis and the quadrature (Q) axis, respectively. Figure 4.1 sketches the constellation diagram of two and four-level amplitude and phase-coded signals. The signal vector is described by the vector magnitude and angle corresponding to the amplitude and phase. The information is presented by the scatter points (symbols) whereas the transition between the symbols are described by a change of the magnitude and/or angle of the field vector in the complex scatter diagram.

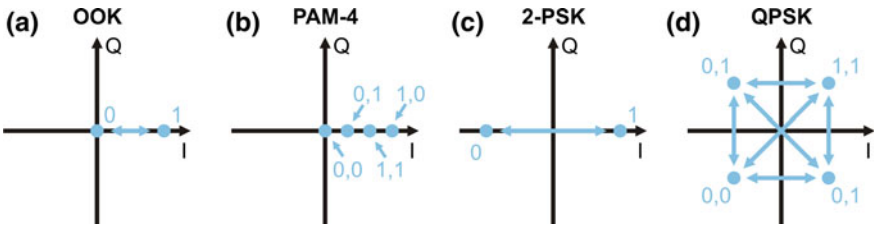

Fig. 4.1 Constellation diagram for various modulation formats. The *symbols* in the constellation diagram are represented by the *circles* whereas *each symbol codes* one or two bits. The transition between the *symbols* is sketched by the *arrow* except for the PAM-4 in which the transitions are omitted for the sake of clarity

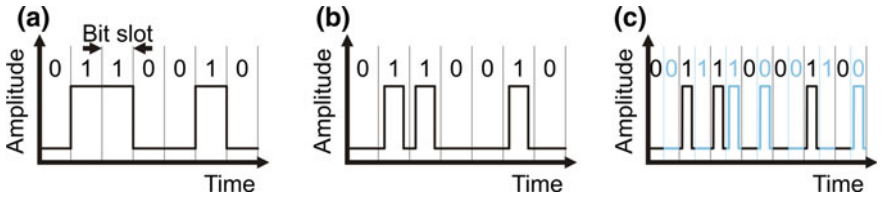

Fig. 4.2 Sketch of **a** NRZ and **b** RZ pattern as well as **c** two time-division multiplexed RZ patterns

For OOK modulated signals, the data are coded in low and high amplitude level often called space and mark level representing a logical zero and one, respectively. In contrast, the bits are coded in two different phase states e.g. 0 and π for 2-PSK modulated signals. Coding two instead of one bits per symbol doubles the number of required symbols. As a result, the bit rate is doubled while keeping the required symbol rate. The corresponding amplitude and phase-shift keying formats are called PAM-4 and quadrature phase-shift keying (QPSK).

Two types of OOK modulated signals are used within this thesis, i.e. non-return-to zero (NRZ) and return-to zero (RZ) signals. The amplitude returns always to the space level between the symbol slots for RZ patterns whereas it returns for NRZ signals only to the space level if the subsequent symbol lies on the space level as sketched in Fig. 4.2. Thus, RZ symbols are shorter than NRZ symbols for comparable symbols rates. If the uncoded temporal space between the RZ symbols is smaller than halve the symbol distance, two symbol streams can be place into each other as sketched in Fig. 4.2c. This OTDM is one advantage of RZ signals whereas NRZ signals require half the spectral bandwidth and are thus preferable for WDM [9].

4.2 Principles of Optical Test Setups

Setups for system experiments resemble parts of a transmission link. A typical optical test setup comprises a transmitter, inline components and a receiver as sketched in Fig. 4.3. The transmitter (Tx) converts the electrical data signal into the optical domain and transmits it to the line. The receiver (Rx) reconverts the signal back into the electrical domain and analyzes the signal quality. All components in-between the transmitter and receiver are summarized here as inline components, namely: power splitter, wavelength multiplexer and demultiplexer, fiber span, amplifier, etc.

In this thesis, three different inline scenarios are distinguished. Firstly, the back-to-back (BtB) configuration is used to characterize the transmitter-receiver setup in terms of signal quality and can be used as a reference. Secondly, inline amplification is required to compensate losses caused by other components, such as fiber spans and power splitters. Thirdly, wavelength converters are used to convert the information from the input wavelength to another wavelength provided by a new source. Altogether, inline components usually reduce the signal quality e.g. by adding noise,

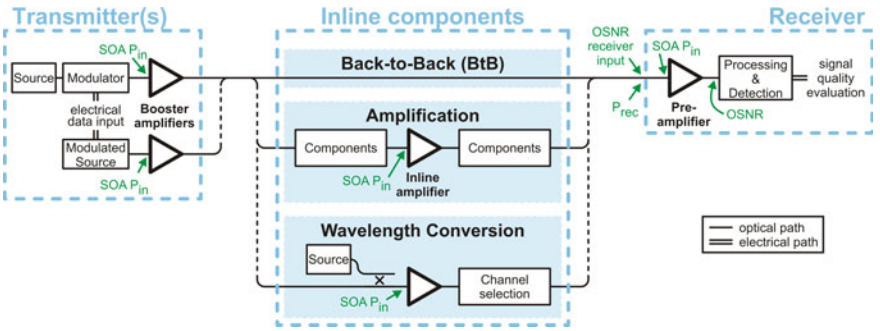

Fig. 4.3 Sketch of optical test setups with transmitter, inline components and receiver

dispersion, channel crosstalk and nonlinear effects.[4] Hence, the signal quality available at the receiver input is reduced in comparison to the BtB reference for comparable receiver input power levels. The different setup parts will be discussed in more detail in the following.

4.2.1 Transmitter

The transmitter converts the electrical data signal into the optical domain either by directly modulating an optical source, or by external modulation of the emission of a continuous wave source. Depending on the modulation format the external modulation is realized by phase modulators, Mach-Zehnder modulators (MZMs), IQ-modulators (see Fig. 4.4) or directly modulated semiconductor devices, such as electro-absorption modulators (EAMs) or SOAs. Within this thesis, the unique properties of QD-SOAs are used to demonstrate the directly modulated generation of phase-coded signals in Chap. 5. All tested amplification and wavelength conversion scenarios in Chaps. 6, 7 and 8 are based on the signal generation using modulators. Therefore, this introductory section will concentrate on the modulator-based signal generation.

Modulators commonly comprise a material whose refractive index depends on a local electric field, such as lithium niobate. Using this concept, the phase of an optical wave passing the material can be controlled by an external voltage applied to the material. This represents a phase modulator. Imbedding the material in a Mach-Zehnder interferometer structure, the output power of the MZM can be controlled by changing the voltage and thus the phase in one or both paths of the interferometer. A detailed review of common lithium niobate modulators can be found in [13]. A typical MZM transfer function is sketched in Fig. 4.4.

[4]Indeed, components regenerating the signal quality are available too, but will not be considered here.

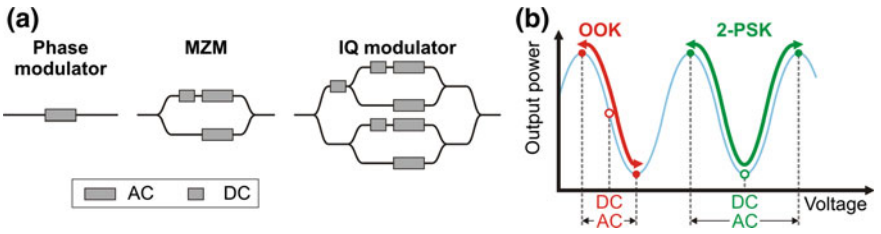

Fig. 4.4 **a** Sketch of different modulator types. **b** Transfer function of a single drive and dual-drive MZM with marked modulation ways for different modulation formats. *Open circles* mark the DC voltage whereas *closed circles* mark the final bit levels

Amplitude modulated signals are usually generated by aligning the DC voltage in one of the arms to half the maximal transmission output power and modulating both interferometer paths with the inverse voltage, whereas the modulation swing is adjusted to modulate between the maximum and minimum possible output power. 2-PSK modulated signals can be generated either with a phase modulator or MZM, whereas the latter usually offers a better performance. For PSK signals, the MZM DC voltage is aligned to the minimal output power and both interferometer paths are modulated with the doubled voltage in comparison to the OOK modulation. The resulting optical output has two possible states with equal power but with a phase difference of π, whereas the transition between the states runs through the minimal output power (see Fig. 4.1c). Using a phase modulator instead, the transition takes place on a circle without an amplitude change (not sketched in Fig. 4.1c). QPSK modulated signals could be generated using a phase modulator, but are commonly generated using an IQ-modulator, which is realized by two MZMs imbedded in super MZM structure. A more detailed description of all modulators and their modes of operation can be found e.g. in [14]. The modulated signal is finally often booster amplified.

4.2.2 Applications of Amplifiers

Optical amplifiers are divided into linear and nonlinear amplifiers. The former is characterized by large gain and large saturation output power levels and is typically used for signal amplification.

Linear amplifiers are subdivided into booster, inline and pre-amplifiers, depending on their position within the transmission link (see Fig. 4.3). Booster amplifiers are assigned to the transmitters and are designed for large output power levels at moderate input power levels. Inline amplifiers shall compensate inline losses caused by other components and are often cascaded in networks with a longer reach. Hence, these amplifiers are commonly designed with large gain and low noise. Finally, pre-amplifiers

are placed in-front of the detection and have to provide sufficient large output power for the subsequent photodiodes, even for very low input power levels.

System experiments for characterization of linear optical amplifiers typically use a variable optical attenuator (VOA) in front of the amplifier to investigate the signal quality in dependence of the input power levels. This allows to specify the input power dynamic range (IPDR), which is the key parameter of optical amplifiers for amplification of data signals amongst other static parameters like gain and gain bandwidth or noise figure. Hence, the IPDR is introduced separately in Sect. 4.4 and is characterized for various modulation formats and wavelength channel configurations in Chaps. 6 and 7.

In contrast to linear amplifiers, nonlinear amplifiers are optimized for low saturation output power levels. Hence, even moderate input power levels are sufficient to drive the amplifier in the gain saturation regime to benefit from nonlinear effects like four-wave mixing (FWM) or crossgain modulation (XGM). This is exploited for example for all-optical wavelength conversion (AOWC) further introduced in Chap. 8.

4.2.3 Receivers

The receiver processes (e.g. amplifies) and converts the optical signal into the electrical domain, processes the electrical signal and finally evaluates the signal quality in dependence of the receiver input power P_{rec} or optical signal-to-noise ratio (OSNR). Different receiver types are used within this thesis depending on the modulations format, see Fig. 4.5. All three receivers feature an optical pre-amplifier stage which allows a shot-noise limited detection of the photodiodes, which is achieved by keeping the optical power at the photodiodes constant on the optimal values independent of the receiver input power (P_{rec}). A detailed description of shot-noise limited detection and receivers can be found for example in [15–17].

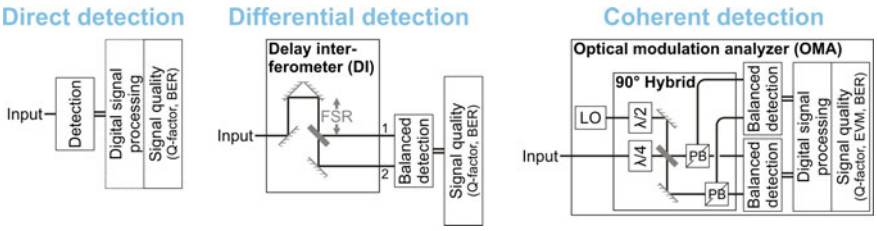

Fig. 4.5 Sketch of three different receiver types used to detect different modulation formats. *BER* biterror ratio, *EVM* error-vector magnitude, *FSR* free-spectral range, λ/x λ/x-plate, *LO* local oscillator, *PB* polarization beam splitter

OOK signals are converted using a pre-amplified direct detection. These receivers are the simplest and cheapest receivers as they usually consist of a fast photodiode and possibly a subsequent electrical amplifier.

Phase-coded signals require an optical processing before detection because the square law direct detection is insensitive to the optical phase. The optical signal processing converts the phase modulation into an amplitude modulation. Two receiver types are used in this thesis, i.e. differential and coherent detection receiver.

Differential Detection

The differential detection receiver is based on a delay interferometer (DI) in which one arm delays the optical signal with respect to the other branch [18]. This delay is characterized by the free-spectral range (FSR). The FSR equals the symbol rate and thus one beam is time delayed by one symbol duration with respect to the other. The two beams interfere. The DI processes both, the amplitude and phase whereas the phase difference is transformed to an amplitude modulation. The differential detection receiver evaluates the phase of the current symbol whereas the phase of the previous symbol is used as the reference. Thus, the data have to be coded as a symbol difference and the formats are than called differential phase-shift keying (DPSK) and differential quadrature phase-shift keying (DQPSK). The two output ports of the DI are normally detected with a balanced detector suppressing the DC component of the signal. For 2-PSK signals, the balanced detection offers a doubled level distance with respect to a single-ended detection of only one of the ports and an improved receiver sensitivity [19].

In contrast, a balanced detection is mandatory for QPSK signals. A detailed theoretical description of the DI can be found e.g. in [18]. The DI operation can be illustrated graphically by a projection line pinned to the point of origin in the IQ-diagram. All symbols and transitions are projected onto this line. The angle of the projection line is aligned by fine tuning of the delay, i.e. phase, between the DI arms on the order of the carrier wavelength. For 2-PSK signals, the processed output can be obtained at angles of 0° or 180° at which the projection line is parallel to the I-axis. QPSK signals show in addition a processed signal at angles of 90° or 270° (compare Fig. 4.1). QPSK signals are fully characterized by measuring two angles with a 90° difference. These two measurements are called tributaries in this thesis.

Coherent Detection

In contrast to the differential detection receiver, the coherent detection receiver uses a stable narrow linewidth continuous wave local oscillator (LO) as a reference to recover the full electric field of the signal [20]. A 90° optical hybrid is used to mix the signal twice with the LO whereas the LO is shifted in one case by 90° [21, 22]. As a result, the 90° optical hybrid provides four optical output ports with two respectively are balanced detected as sketched in Fig. 4.5. The resulting photo currents $I_I(t)$ and $I_Q(t)$ along the I and Q-axis, respectively, can be described as

$$\begin{aligned} I_I(t) &\propto \sqrt{|A_S|^2\,|A_{LO}|^2}\cos\left[\theta_S(t) - \theta_{LO}(t)\right], \\ I_Q(t) &\propto \sqrt{|A_S|^2\,|A_{LO}|^2}\sin\left[\theta_S(t) - \theta_{LO}(t)\right], \end{aligned} \tag{4.1}$$

with θ_S and θ_{LO}: phase of signal and LO, A_S and A_{LO}: amplitude of signal and LO [22]. If both photo currents are known, the complex amplitude of the signal I_c can be retrieved according to [22] by:

$$I_c(t) = I_I(t) + i\ I_Q(t). \tag{4.2}$$

Thus, the amplitude and phase modulation of the signal can be retrieved using digital signal processing (DSP). The coherent detection receiver is a very complex receiver as it requires e.g. DSP or phase-locked loops [20, 22]. However, the coherent detection receiver offers the largest flexibility since it can be used to detect various modulation formats and it offers in addition the best receiver sensitivity [15].

All receivers perform a signal quality evaluation which will be discussed in the next section. The coherent detection receiver including the signal quality evaluation is called optical modulation analyzer (OMA).

4.3 Signal Quality Evaluation

The previous section introduced modulation formats and the basics of setups used for system experiments, in particular receiver setups. In this section, three methods for evaluation of the signal quality are discussed based on different receivers.

4.3.1 Bit-Error Ratio

Various parameters have been developed as a figure of merit of the signal quality in optical test setups. The fundamental and finally only precise method is the bit-wise comparison of the electrical data input of the transmitter and the electrical data output of the receiver. The electrical receiver usually interprets the data stream by setting a decision level (or multiple e.g. for PAM-4) between the symbol levels and into the center of the symbol duration. The decision level is then used to decide for every received symbol whether it is above or below the decision level. The data stream is thus digitized. In case of a multi-level modulation format, the symbols are decoded into respective bits. The errors of the received bit stream are obtained by comparison with the known transmitted bit sequence. As a figure of merit, the bit-error ratio (BER) is defined as the number of wrong received bits divided by the total number of received bits.

$$BER = \frac{N_{wrong}}{N_{total}}. \tag{4.3}$$

The BER is measured as a function of the receiver input power (P_{rec}) and/or the optical signal-to-noise ratio (OSNR) (see Fig. 4.3). At very low P_{rec}, the receiver is not able to detect the signal. Increasing the P_{rec} decreases the BER as long as the

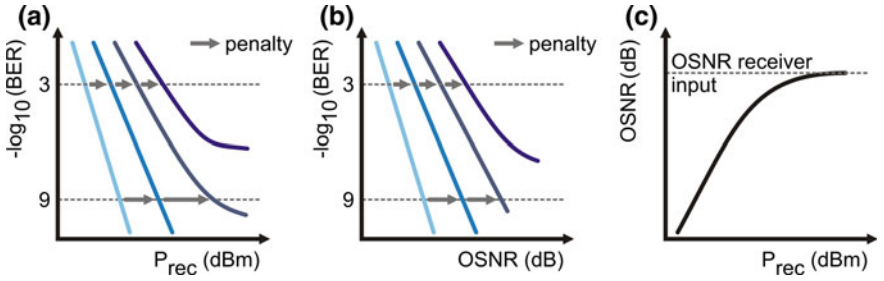

Fig. 4.6 Illustration of the bit-error ratio (BER) in a double logarithmic scale over the logarithmic. **a** P_{rec} and **b** OSNR. **c** Illustrates the dependence of the OSNR on the P_{rec}. Redrawn after [28]

OSNR is increased,[5] and hence improves the signal quality. At very large P_{rec} the BER increases with increasing P_{rec} due to overload effects [23]. A range of acceptable system performance can be defined in-between the two regimes in dependence of the required BER values [16].

Depending on the application scenario, different maximal acceptable BER levels are defined. For optical communication transmission experiments BERs of 10^{-12} and 10^{-9} are typically defined as "error-free" for short (up to a few hundred meters) and long (hundreds of km) transmission links, respectively. A statistically reliable estimation of the BER requires at least 100 counted bit errors [17]. Assuming a data rate of 10 Gb/s it would require a measurement time of 10^{-5} / 10 / 10^{4} s to prove a BER of 10^{-3} / 10^{-9} / 10^{-12}.

Applications using error correction codes, such as soft- or hard-decision forward-error correction (FEC), accept even larger BERs around 10^{-3} because the algorithm corrects the received BER to values below 10^{-12} [17, 20, 24–27]. However, only the low P_{rec} side will be discussed in the following.

Figure 4.6a illustrates a typical BER measurement in dependence of the P_{rec}, the so called BER curve. Assuming an optimized transmitter and a shot-noise limited receiver, the reduction of the P_{rec} results in a lower input power of the optical pre-amplifier sketched in Fig. 4.3. Assuming a linear gain, the amplified signal output is thus linearly reduced whereas the ASE remains constant or even increases. Accordingly, the optical signal-to-noise ratio (OSNR) is decreased with decreasing P_{rec} as sketched in Fig. 4.6c. Increasing the P_{rec} increases the OSNR until it saturates to the receiver input OSNR. According to [29] the OSNR is defined similar to the noise figure sketched in Fig. 2.5 (page 23) in logarithmic units as

$$OSNR\,[\mathrm{dB}] = 10\,log_{10}\left(\frac{P_{signal}\,[\mathrm{mW}]}{P_{ASE,\,0.1\,\mathrm{nm},\,at\,signal\,wavelength}\,[\mathrm{mW}]}\right). \tag{4.4}$$

[5] This is only valid for optically pre-amplified receivers as the optical amplifier changes the OSNR in front of the detection.

The BER depends linearly on the P_{rec} in the double-log over log plot if a reduction of the P_{rec} reduces only the received optical signal-to-noise ratio (OSNR) [28]. Introducing components in-between the transmitter and receiver can cause losses and degrades the signal quality e.g. due to noise adding, chirp, nonlinear effects, dispersion and patterning.

If the components cause only losses, the OSNR in front of the receiver remains constant whereas the receiver input power is reduced. Hence the BER curve with and without the component lay on each other but the maximal available P_{rec} and OSNR are reduced. In contrast, the BER curve will be shifted in case of degradation and larger receiver input power levels values are required to achieve a comparable BER level. The change of required receiver input power or OSNR is called penalty and is marked in Fig. 4.6a, b exemplary at a BER of 10^{-9} and 10^{-3}. A positive penalty represent a larger required receiver input power or OSNR and thus represents a decrease of the signal quality.

When the OSNR starts to saturate, the BER curve as a function of the receiver input power changes to a nonlinear slope. A further increase of the P_{rec} has diminishing returns on the BER due to the limited OSNR and finally an error-floor appears within the measured BER range. Taking into account that the OSNR is limited and not infinity, an error-floor can always be observed as long as the measured BER is low enough [17]. Several signal degradation, such as patterning, can also lead to a nonlinear slope of the BER curve in dependence of the OSNR whereas the adding of noise results in a penalty but still a linear slope. For the sake of completeness, it should be mentioned that the BER curve can be also shifted towards lower required P_{rec} or OSNR in particular cases, if the signal is regenerated which can be implemented by various configurations [30–33].

A BER measurement results in a number representing a clear statement whether the transmission is acceptable or not. The penalty between BER curves allow an interpretation of the signal degradation but the origin of the signal degradation has to be determined by other means. Performing eye diagram measurements and/or recording constellation diagrams give another access to the signal characteristics. Both will be discussed in the following.

4.3.2 Eye Diagram and Q-Factor

Eye diagrams represent a visualization of the signal waveform. They are generated by sampling the received data stream and overlaying different symbol slots in a single diagram [34]. An exemplary eye diagram is shown in Fig. 4.7. The above mentioned decision level for the BER measurements will be set in the center of the eye opening.

Signal degradations are directly visible in the eye diagram. Usually, two main OOK signal degradation are caused by optical amplifiers, both sketched in Fig. 4.8. On the one hand, the amplifier adds ASE to the signal and thus noise. On the other hand, a gain recovery slower than but still on the order of the symbol period results in the nonlinear gain regime into a gain of a given symbol in dependence of preceding

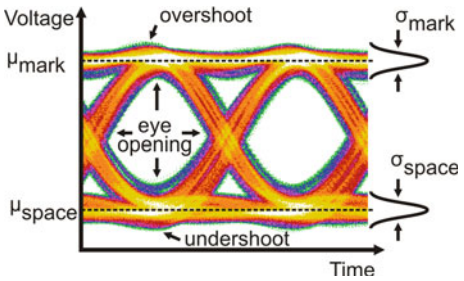

Fig. 4.7 Eye diagram with two eyes with *color coded* occurrence or density of sampled points within a specified voltage-time area. The mark and space level μ_y as well as their level broadening σ_y are highlighted. The *eye diagram* shows not only noise induced level brocading but also small time dependent overshoots and undershoots

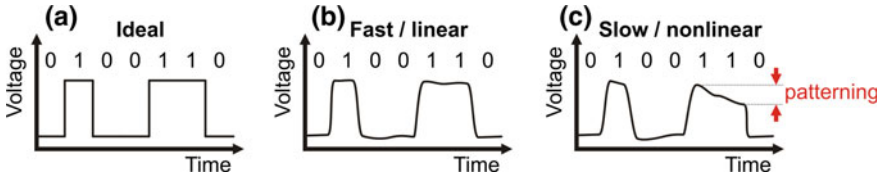

Fig. 4.8 The optical amplification of an **a** ideal input pattern will cause two main signal degradations. **b** A fast and/or linear amplifier adds noise to the signal due to the ASE and causes a broadening of the space and mark level distribution. **c** In addition, a slow amplifier driven in the nonlinear gain regime provides gain in dependence of the preceding bit(s) resulting in a broadening of the mark level

symbol(s). This effect is called patterning and describes a memory effect of the gain. An increase of the signal noise results in an increased broadening of both levels and the transitions between the levels. In contrast, pattern effects result in a reduced eye opening due to a broadening of the mark level. For purely phase-coded signals[6] no pattern effects can be observed as the signal magnitude remains constant. However, similar phase disturbing effects can be observed if the amplifier shows a time and symbol depended slow phase recovery as discussed in detail in Sects. 2.1 and 3.6.

Various characteristics, such as jitter, extinction ratio and Q-factor, can be extracted from an eye diagram characterizing the signal quality. However, in this thesis only the Q-factor will be used and is thus introduced. A definition of all other parameters can be found in e.g. [16, 34]. The Q-factor[7] describes the ratio of the eye size to the noise [34–36] and is defined as

$$Q = \frac{\mu_{mark} - \mu_{space}}{\sigma_{mark} + \sigma_{space}}, \tag{4.5}$$

[6]Please remember, the phase-coded signal can also exhibit amplitude changes in the symbol transitions as explained before.

[7]Q stands for quality.

with μ_{space} and μ_{mark}: mean value of the space and mark level, σ_{space} and σ_{mark}: standard deviation of the space and mark level. This definition assumes a Gaussian distribution of the noise and neglects other level broadening effects. A rough estimation of the BER can be calculated from the Q-factor [34, 36] by

$$BER = \frac{1}{2}\mathrm{erf}\left(\frac{Q}{\sqrt{2}}\right). \tag{4.6}$$

The calculated BERs become less accurate for increasing level broadening effects beside a Gaussian noise distribution, such as patterning. Consequently, calculated BER from Q-factors have to be taken with care, since they are just a rough estimation.

4.3.3 Error-Vector Magnitude

Using the coherent detection receiver, the constellation diagram can be obtained. The constellation diagram contains the scatter points (symbols in the IQ-plane) and all transitions between the symbols and thus represents another type of visualization of the signal. Figure 4.9 sketches various constellation diagrams with different signal degradations exemplary for a QPSK signal. An ideal signal provides tiny scatter points representing well defined symbols. Adding noise to the signal results in an symmetric increase of the measured distribution of the scatter points. In contrast, signal degradation only influencing the phase and amplitude results in a broadening of the measured distribution of the scatter points along the circle and radius, respectively. Thus, the constellation diagram enables to distinct between signal degradations occurring from phase or amplitude distortions whereas BER measurements for example obtained by the differential detection receiver cannot distinguish between them.

The deviation of the current measured symbol from the expected ideal symbol position yields the error vector as sketched in Fig. 4.10. The error vector is determined by contributions of the IQ phase error and the IQ magnitude error. As a figure of merit, the error-vector magnitude (EVM) is introduced describing the effective distance of

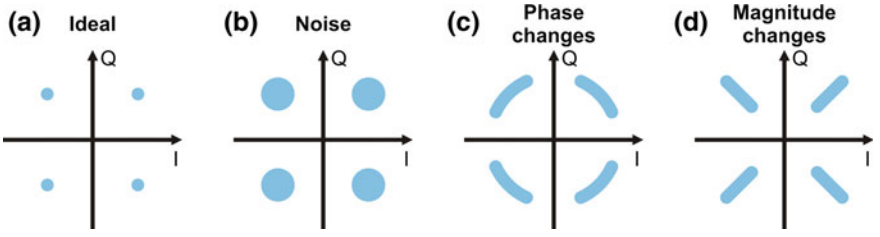

Fig. 4.9 Sketch of constellation diagrams of **a** ideal configuration as well as degraded signal quality due to **b** noise, **c** phase degradation and **d** magnitude degradation

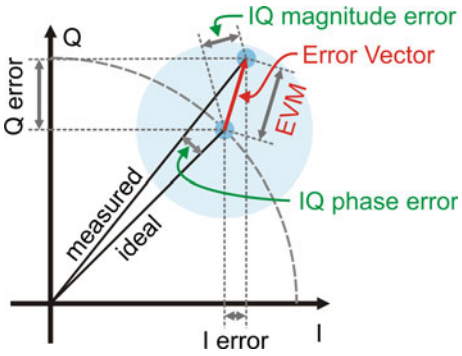

Fig. 4.10 Sketch of the complex signal field in the IQ diagram for the definition of the EVM describing the effective distance of the received from the ideal symbol

the received from the ideal symbol [37]. The EVM of N transmitted symbols is given by the square root of the averaged EVMs of each received symbol normalized to the largest ideal constellation vector magnitude $\left|E_{ideal,\,max}\right|$ [37, 38]:

$$EVM\,[\%] \equiv EVM_{RMS} = \frac{\sqrt{1/N\sum_{i=1}^{N} EVM_i}}{\left|E_{ideal,\,max}\right|} \qquad (4.7)$$
$$\text{with } EVM_i = \left|E_{Error\ Vector,\,i}\right|^2 = \sqrt{(I\ error)^2 + (Q\ error)^2}.$$

Similar to the Q-factor, the BER can be estimated from the EVM if additive white Gaussian noise dominates the EVM value [37].

4.4 Input Power Dynamic Range for Optical Amplifiers

Section 4.2.2 gave an overview of applications of optical amplifiers in optical communication systems. Section 4.3 introduced the evaluation of the signal quality. This section introduces a parameter that characterizes the performance of optical amplifiers with respect to the signal quality.

The optical input power into an amplifier varies with the application and the final network design. The amplifier has to amplify the signals within a specified range of input power levels with a specified performance. This ensures a large applicability of the amplifier. Hence, the quality of the amplified signal has to be characterized in dependence of the optical input power into the amplifier and the results have to be classified. The according figure of merit is the input power dynamic range (IPDR) [39]. It is defined as the range of input power in which the obtained BER is below a specific BER level:

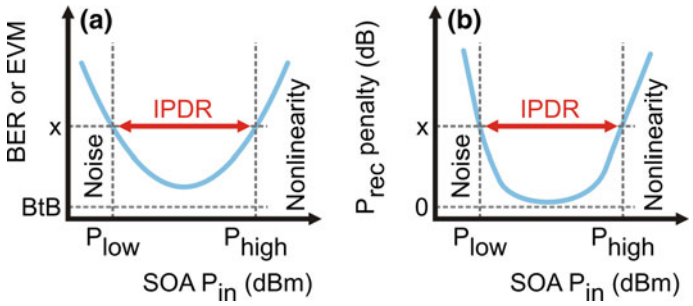

Fig. 4.11 Sketch of **a** BER or EVM and **b** P_{rec} penalty in dependence of the amplifier input power level P_{in}. The signal **a** quality and **b** degradation is better and smaller, respectively, than a specific value x within the IPDR

$$IPDR\,[dB] = P_{high}\,[dB] - P_{low}\,[dB]\,. \tag{4.8}$$

Commonly the "error-free" BER level of 10^{-9} and the FEC BER limit of around 10^{-3} are used as threshold levels. As the measured BER depends on the receiver input power, the receiver input power has to remain constant for all measurements. Typically, the receiver is operated 10 dB above the system sensitivity threshold [39], i.e. 10 dB above the receiver input power (called here $P_{rec}^{10\,dB}$) at which the BtB measurement achieved the BER threshold. The obtained BtB BER at the $P_{rec}^{10\,dB}$ represents the best achievable signal quality, i.e. lowest BER, for this system as long as no signal regenerate occurs. An exemplary IPDR measurement is sketched in Fig. 4.11a. The IPDR is limited towards low power levels by the low OSNR, i.e. noise. At high power levels, the IPDR is limited by nonlinear signal degradation, such as patterning or phase distortions. A theoretical discussion of the IPDR for amplitude and phase modulated signals can be found for example in [40].

BER characterizations require typically costly equipment and require a long time to be performed, particular at low BERs. Hence, Q-factor and EVM measurements are often preferred as they require significantly low measurement time but at the expense of accuracy as the attributed BER is based on statistical assumption. However, the decisive Q-factor or EVM thresholds are chosen according to the BER levels.

The above described IPDR is based on a constant receiver input power. Taking into account that a network usually contains several cascaded amplifiers over a complete transmission distance it could be more interesting to investigate the signal degradation directly in dependence of the input power, i.e. by the P_{rec} or OSNR penalty with respect to the BtB configuration. In this case, the IPDR is defined as the power level range in which the penalty at a specific BER is lower than a defined penalty value. The upper limit of the acceptable penalty per amplifier dependence on the application and the network and determines the power budget of the network. Penalties of 0.5, 1 or 2 dB could be defined.

Commonly, Q-factor and EVM-based IPDR are characterized using the first discussed method whereas BER-based IPDRs are characterized using the second

method. The results obtained for both IPDR definitions are usually not directly comparable. Hence, both definitions will be comprehensively investigated and compared in Sect. 6.2.

References

1. S.W. Golomb, *Shift Register Sequences. Revised* (Aegean Park Press, Walnut Creek, 1981)
2. F.J. MacWilliams, N.J.A. Sloane, Pseudo-random sequences and arrays. Proc. IEEE **64**(12), 1715–1729 (1976)
3. M. Müller, Pseudo-random binary sequences, in *Digital Communications Test and Measurement: High-Speed Physical Layer Characterization*, 1st edn., ed. by D. Derickson, M. Muller (Prentice Hall, Upper Saddle River, 2007), p. 976
4. M.P. Clark, *Data Networks, IP and the Internet: Protocols, Design and Operation*, 1st edn. (Wiley, London, 2003), p. 848
5. P.J. Winzer, R.J. Essiambre, Advanced optical modulation formats. Proc. IEEE **94**(5), 952–985 (2006)
6. P.J. Winzer, Modulation and multiplexing in optical communication systems. *IEEE LEOS Newsl*. http://www.photonicssociety.org/content/newsletters 2009, 4–10
7. P.J. Winzer, Modulation and multiplexing in optical communications, in *Conference on Lasers and Electro-Optics (CLEO) and Quantum Electronics and Laser Science Conference (QELS)*, 2009, CTuL3
8. M. Nakazawa, K. Kikuchi, T. Miyazaki (eds.), *High Spectral Density Optical Communication Technologies*, 1st edn. (Springer, Berlin, 2010)
9. G.P. Agrawal, *Fiber-Optic Communication Systems*, 4th edn. (John Wiley, London, 2012)
10. S. Ferber et al., Comparison of DPSK and OOK modulation format in 160 Gbit/s transmission system. Electron. Lett. **39**(20), 1458–1459 (2003)
11. A.H. Gnauck, P.J. Winzer, Optical phase-shift-keyed transmission. J. Light. Technol. **23**(1), 115–130 (2005)
12. Wikipedia. https://en.wikipedia.org/wiki/Modulation 2015
13. E.L. Wooten et al., A review of lithium niobate modulators for fiber-optic-communications systems. IEEE J. Sel. Top. Quantum Electron. **6**(1), 69–82 (2000)
14. M. Seimetz, *High-Order Modulation for Optical Fiber Transmission*, 1st edn. (Springer, Berlin, 2009), p. 251
15. T. Okoshi, K. Kikuchi, *Coherent Optical Fiber Communications*, 1st edn. (Springer, Berlin, 1988), p. 278
16. S.B. Alexander, *Optical Communication Receiver Design*, 1st edn. (SPIE Press, Bellingham, 1997)
17. S. Pachnicke, *Fiber-Optic Transmission Networks: Efficient Design and Dynamic Operation*, 1st edn. (Springer, Berlin, 2011)
18. J. Li et al., Free-space optical delay interferometer with tunable delay and phase. Opt. Express **19**(12), 11654–11666 (2011)
19. J.M. Kahn, K.-P. Ho, Spectral efficiency limits and modulation/detection techniques for DWDM systems. IEEE J. Sel. Top. Quantum Electron. **10**(2), 259–272 (2004)
20. E. Ip et al., Coherent detection in optical fiber systems. Opt. Express **16**(2), 753–791 (2008)
21. T.G. Hodgkinson et al., In-phase and quadrature detection using 90° optical hybrid receiver: experiments and design considerations. IEE Proc. Optoelectron. **135**(3), 260–267 (1988)
22. K. Kikuchi, Coherent optical communications: historical perspectives and future directions, in *High Spectral Density Optical Communication Technologies*, 1st edn., ed. by M. Nakazawa, K. Kikuchi, T. Miyazaki (Springer, Berlin, 2010), p. 338

23. E.E. Bergmann, J. Thompson, Sensitivity testing in optical digital communication, in *Digital Communications Test and Measurement: High-Speed Physical Layer Characterization*, 1st edn., ed. by D. Derickson, M. Muller (Prentice Hall, Upper Saddle River, 2007), p. 976
24. A. Malik et al., Network economics of optical transport networks with soft decision forward error correction (SD-FEC) technology. Photonic Netw. Commun. **28**(2), 115–122 (2014)
25. Infinera. Soft decision forward error correction for coherent super-channels. *WHITE PAPER* (2013)
26. I.P. Kaminow, T. Li, A.E. Willner (eds.), *Optical Fiber Telecommunications Volume VIB: Systems and Networks*, 6th edn. (Academic Press, London, 2013), p. 1148
27. K. Iniewski (ed.), *Convergence of Mobile and Stationary Next-Generation Networks*, 1st edn. (Wiley, London, 2011)
28. C. Meuer, GaAs-based quantum-dot semiconductor optical amplifiers at 1.3 μm for all-optical networks. Doctoral Thesis. Technical University of Berlin, 2011, p. 155
29. J. Thompson, E.E. Bergmann, Stress tests in high-speed serial links, in *Digital Communications Test and Measurement: High-Speed Physical Layer Characterization*, 1st edn., ed. by D. Derickson, M. Muller (Prentice Hall, Upper Saddle River, 2007)
30. M. Jinno, M. Abe, H. Liang, All-optical regenerator based on nonlinear fibre Sagnac interferometer. Electron. Lett. **28**(14), 1350–1352 (1992)
31. S. Radic et al., All-optical regeneration in one- and two-pump parametric amplifiers using highly nonlinear optical fiber. IEEE Photonics Technol. Lett. **15**(7), 957–959 (2003)
32. P.V. Mamyshev, All-optical data regeneration based on self-phase modulation effect, in *European Conference and Exhibition on Optical Communication (ECOC)*, 1998, p. 475
33. C. Porzi et al., All-optical regeneration of 40 Gb/s NRZ-DPSK signals in a single SOA, in *Optical Fiber Communication Conference (OFC) and National Fiber Optic Engineers Conference (NFOEC)*, 2013, JW2A.55
34. G.D. Le Cheminant, Characterizing high-speed digital communications signals and systems with the equivalaent-time sampling oscilloscope, in *Digital Communications Test and Measurement: High-Speed Physical Layer Characterization*, 1st edn., ed. by D. Derickson, M. Muller (Prentice Hall, Upper Saddle River, 2007), p. 976
35. Anritsu, Application note, Q factor measurement eye diagram measurement, SDHSONET pattern editing. *WHITE PAPER* (2000)
36. W. Freude et al., Quality metrics for optical signals Eye diagram, Q-factor, OSNR, EVM and BER, in *International Conference on Transparent Optical Networks (ICTON)*, vol. 1, 2012, Mo.B1.5
37. R. Schmogrow et al., Error vector magnitude as a performance measure for advanced modulation formats. IEEE Photonics Technol. Lett. **24**(1), 61–63 (2012)
38. R.A. Shafik, S. Rahman, R. Islam, On the extended relationships among EVM, BER and SNR as performance metrics. *International Conference on Electrical and Computer Engineering (ICECE)*, 2006, pp. 408–411
39. R. Bonk et al., The input power dynamic range of a semiconductor optical amplifier and its relevance for access network applications. IEEE Photon. J. **3**(6), 1039–1053 (2011)
40. R. Bonk, Linear and nonlinear semiconductor optical amplifiers for next-generation optical networks. Doctoral Thesis. Karlsruher Institut für Technologie, 2013, p. 278

Chapter 5
Concept of Direct Phase Modulation

This chapter[1] presents a concept of low-cost generation of phase-coded signals using a directly modulated QD-SOA. The concept exploits the unique decoupling of phase and gain dynamics of QD-SOAs. The basic idea and possible applications will be discussed in Sect. 5.1. The setup and the device under test are introduced in Sect. 5.2. Subsequently, Sect. 5.3 presents the experimental results. Finally, Sect. 5.4 summarizes and classifies the results.

5.1 Introduction and Concept

Directly modulated emitters are extensively used in optical communication networks as they simplify the network architecture, reduce the overall investment and maintenance costs. In long-haul transmission systems, directly modulated emitters are gradually replaced by a combination of continuous wave emitter and modulator due to the limited performance of directly modulated devices at ultra-high and speed high dense optical communications systems. However, in low cost optical communications systems like access networks (ANs) directly modulated devices are predominantly used. As the number of users and nodes and consequently wavelength channels are increasing especially in fiber-to-the home (FTTH) systems, a flexible network design is preferable as this could reduce the maintenance costs.

One possibility to enhance the flexibility of a network architecture is to realize a color-less or color-free up- and down-stream operation in passive optical networks [1–4]. In such networks, the up-stream wavelength of each optical network termination (ONT) is not defined by the ONT emitter but by the central office. Different approaches based on lasers, amplifiers and modulators have been demonstrated, e.g.

[1] Parts of this chapter have been previously published in [1, 2]. 1: Zeghuzi 2015a; 2: Zeghuzi 2015b.

H. Schmeckebier, *Quantum-Dot-Based Semiconductor Optical Amplifiers for O-Band Optical Communication*, Springer Theses,
DOI 10.1007/978-3-319-44275-4_5

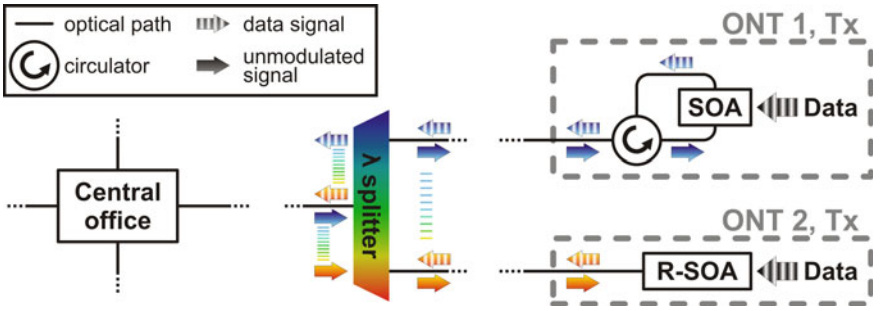

Fig. 5.1 Sketch of a color-free up-stream based on directly modulated SOAs in the ONT transmitter. ONT 1 is based on a standard SOA imbedded in a loop whereas ONT 2 is based on a reflective SOA (R-SOA). λ-splitter: arrayed waveguide grating

in [1–3, 5, 6]. A very simple approach is the use of a directly modulated SOA as sketched in Fig. 5.1. This can be realized either by a reflective SOAs (R-SOA) exhibiting one highly reflecting facet or by a standard SOA imbedded in a loop [4]. These operation was demonstrated for OOK signals e.g. in [7–9]. However, in comparison to OOK signals phase-coded signals, such as DPSK, offer a reduced OSNR requirement and are more robust to fiber nonlinearities [10, 11].

The separation of charge-carrier energy levels into optically active QD transitions and higher energy levels forming a carrier reservoir leads to a unique decoupling of phase and gain dynamics in QD-SOAs as discussed in Sects. 2.3 and 3.6. Indeed, larger QD-SOA drive currents lead to a saturated QD emission and a highly populated reservoir which results in a decoupling of the real and imaginary parts of the susceptibility as introduced in Sect. 2.1.2. A modulation of the current results in a change of the reservoir carrier density but has no or negligible influence on the occupation of the QD state(s) as long as the modulation does not underrun the saturation current. The change of the carrier density results in a refractive index change which can be probed by an optical wave. Hence, the phase of an optical input signal can be manipulated at the QD-SOA output by changing the carrier density via direct modulation. Within the linear gain regime, the optical wave is amplified with a negligible amplitude modulation but experiences a phase modulation.

5.2 Setup and Device Under Test

The setup is depicted in Fig. 5.2. The transmitter source is given by an external cavity laser (ECL) emitting at a wavelength of 1296 nm. The continuous wave optical signal is injected into the device under test (DUT) with its polarization being aligned to the TE axis. A variable optical attenuator (VOA) in front of the QD-SOA allows to adjust the optical input power level. The QD-SOA is contacted with a high-frequency probe head in signal-ground configuration. A DC current of 125 mA is superimposed with an electrical NRZ PRBS-7 signal generated by a 56 Gb/s bit-pattern generator (BPG) and applied to the DUT. The amplified and modulated QD-SOA optical output signal

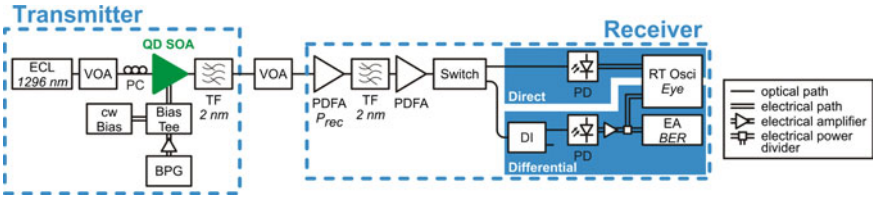

Fig. 5.2 Sketch for the setup for direct DPSK modulation. BPG: bit-pattern generator, *ECL* external cavity laser, *EA* error analyzer, *MZM* Mach-Zehnder modulator, *PC* polarization controller, *PD* photodiode, *QD-SOA* quantum-dot semiconductor optical amplifier, *PDFA* praseodymium-doped fiber amplifier, *Sa Osci* sampling oscilloscope, *SMF* single-mode fiber, *TF* wavelength tunable filter, *VOA* variable optical attenuator

is wavelength filtered using a wavelength tunable filter (TF) with a FWHM of 2 nm to prevent ASE loading of the receiver amplifiers.

The performance of the signal generation is tested in BtB configuration. The receiver input power is varied using a VOA in front of the receiver. The multi-format receiver contains an optical pre-amplifier stage and subsequently two different receiver types. The first PDFA is driven in constant gain mode whereas the second PDFA is operating in a constant output power mode, which ensures a constant averaged optical power on the photodetectors. A TF with a FWHM of 2 nm is used in-between the two amplifiers to suppress the ASE input into the second PDFA. An optical switch is used to detect the signal with one of the two receivers. The direct detection receiver is used to characterize the remaining amplitude modulation whereas the differential receiver is used to demodulate the phase-modulated signal.

The direct detection receiver comprises a 50 GHz photodiode (PD) and the signal quality is evaluated with eye-pattern measurements using an 80 GSa/s real-time oscilloscope exhibiting an analog bandwidth of 32 GHz.

The differential receiver comprises a delay interferometer (DI) and a subsequent 50 GHz photodiode (PD). The DI's free-spectral range (FSR) equals the symbol rate. A balanced detection as described in Sect. 4.2.3 would increase the receiver sensitivity by about 3 dB. The signal quality is evaluated with BER measurements using a 53.5 Gb/s error analyzer (EA) as well as eye-pattern measurements using the same real-time oscilloscope as for the direct detection receiver.

Device Under Test (DUT)

The DUT for the generation of phase-coded signals is the 2 mm long QD-SOA No. 1 (see page 39). The ASE peak is observed at a DC current of close to 150 mA at a wavelength of 1296 nm. At this wavelength, the ASE emission varies by only 0.6 dB when changing the current to 100 or 200 mA. This reduction is predominantly caused by device heating induced shift of the ASE peak wavelength. This power variation is expected to be even smaller for a modulated current because the modulation speed in optical communication systems is much faster than thermal effects in semiconductors. At a current of 150 mA, the device offers a small-signal fiber-to-fiber gain of 8.5 dB as well as a 3-dB saturation input power of 4.1 dBm.

5.3 Experimental Results

The optimal modulation point for the generation of directly modulated phase-coded signals, i.e. DC current and modulation amplitude, is given as a trade-off between different effects. On the one hand, a low DC current results in an unsaturated GS emission and consequently in a significant amplitude modulation. However, a large DC current causes device heating induced gain reduction and hence a lower signal quality at the receiver. On the other hand, a small modulation amplitude causes only a small variation of the carrier density and thus a small phase shift. Large modulations amplitudes increase the phase shift but can push the device out of the saturated regime resulting into amplitude modulation of the optical output signal. A suppressed amplitude modulation but significant phase modulation is expected from the DC characterization within a current range of about 100–200 mA.

For a DC current significantly below 100 mA and a modulation speed of 6 GBd, a disturbed OOK eye diagram was measured using the direct detection receiver. For currents above 100 mA no eye could be observed but still an amplitude modulation is observed as exemplary depicted in Fig. 5.3c for a modulation speed of 10 GBd. However, the generation of a 10 GBd phase-coded signal via directly modulating a QD-SOA is proved by measuring an open eye diagram at the delay interferometer (DI) output port 1, depicted in Fig. 5.3a. But no eye could be observed simultaneously at the DI port 2 as depicted in Fig. 5.3b. Changing the phase setting of the DI by 180° inverts the observed behavior of the DI ports, i.e. port 2 shows an open eye and port 1 not. This behavior was observed for all tested combinations of DC current, modulation amplitude and modulation speed.

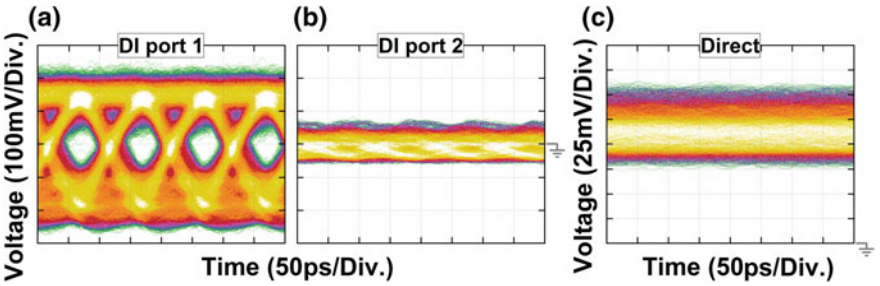

Fig. 5.3 Eye diagrams of the 10 GBd directly modulated phase-coded signal generation recorded at **a** DI port 1, **b** DI port 2 and **c** the direct detection pass. The P_{rec} was set to the BER threshold of 10^{-9}

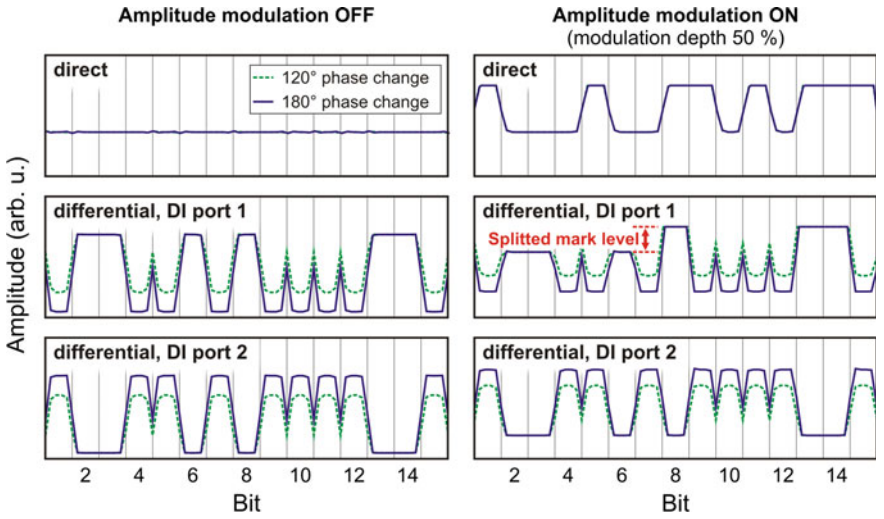

Fig. 5.4 Simulated detection of a DPSK signal using direct detection receiver and differential detection receiver. The differential receiver is simulated in single-ended detection independent for DI port 1 and port 2. The DPSK signal is simulated with a 120° and 180° phase change, both (*left*) without and (*right*) with a simulations amplitude modulation. The FSR of the DI equals the symbol rate. In presence of an amplitude modulation, DI port 1 exhibit two mark bit levels whereas port 2 shows only one mark level. All figures share the same legend

Influence of Amplitude Modulation on the DI Output

A simple simulation of the DI was performed to analyze the origin of the above described effect. The simulation takes a carrier wave field and modulates the phase and amplitude with a data signal without any bandwidth limitation. The modulated signal is either directly detected using a square-law detector or interferes with its one symbol delayed copy and both DI output ports are detected using square-law detectors. The bandwidth of real detectors is simulated by stepwise integration over a temporal interval (corresponding to the symbol rate), which simply filters out the fast carrier oscillation. The simulated results are shown in Fig. 5.4.

Starting with no amplitude modulation, the directly detected signal shows of course no modulation whereas both DI output ports exhibit clear space and mark levels. The extinction ratio is given by the phase change and reaches its maximum at 180°. A balanced detection is possible in this configuration and would result in an increased eye opening. Taking into account an additional amplitude modulation, different behaviors of the DI output ports are observed. Port 2 experiences only a reduction of the extinction ratio between mark and space level whereas port 1 experiences in addition a splitting of the mark level. A balanced detection would result in a decreased eye opening in comparison to a single ended detection of port 2.

Comparing directly detected eye diagrams for a symbol rate of 10 and 25 GBd depicted in Figs. 5.3c and 5.5c, the remaining amplitude modulation is damped with increasing symbol rate as indicated by the reduced amplitude swing. In consequence,

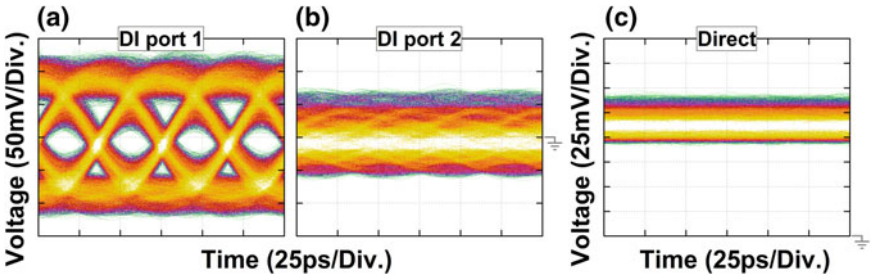

Fig. 5.5 Eye diagrams of the 25 GBd directly modulated phase-coded signal generation recorded at **a** DI port 1, **b** DI port 2 and **c** the direct detection pass. The P_{rec} was set to the BER threshold of 10^{-9}

the demodulated DI output shows a significantly improved eye diagram, i.e. demonstrated by the reduced space level variation (compare Figs. 5.3a, 5.5a).

In consequence, the experimentally observed behavior presumably results from a residual amplitude modulation of the QD-SOA. This could be reduced by decreasing the modulation amplitude which would also reduce the phase change and thus decrease the extinction ratio.

The differential detection processes only phase changes occurring between two subsequent symbols. According to Sects. 2.3 and 3.6, the effective time constant of the reservoir includes all carrier relaxation processes. This effective time constant is slower than the time constant of the current RF-signal transition induced adiabatic chirp in the reservoir. Consequently, the differential detection processes only those fast contributions to the total phase change within the reservoir. The remaining amplitude modulation especially at lower symbol rates could result into problems even for larger symbol rates like 25 GBd when using larger PRBS length.

Experimental Results

The optimal DC current and modulation amplitude for the direct phase modulation were adjusted by optimizing the eye diagram as well as the BER. A DC current of 125 mA and a modulation peak-to-peak voltage of 3 V were identified. BER measurements were performed for a fixed QD-SOA optical input power of −5 dBm and for increasing symbol rates from 10 to 25 GBd. All BER curves are shown in Appendix C. The BER curves are evaluated in terms of receiver input power P_{rec} penalty at a BER of 10^{-9} (error-free) and 10^{-3} with respect to the lowest symbol rate of 10 GBd. Doubling the symbol rate for an ideal transmitter-receiver setup would result in a 3-dB receiver input power P_{rec} penalty as the ideal receiver requires a constant received energy per symbol for comparable BERs. The penalty for a real non-ideal transmitter-receiver system is usually larger due to bandwidth limitations of the transmitter and/or receiver. The penalties are plotted in Fig. 5.6a.

The error-free generation of a phase-coded signal is achieved up to a symbol rate of 25 GBd. The receiver input power penalty is about 6.6 and 2.7 dB larger than the reference for a BER of 10^{-9} and 10^{-3}, respectively. The penalty follows the reference up to a symbol rate between 15 and 20 GBd which presumable corresponds to the

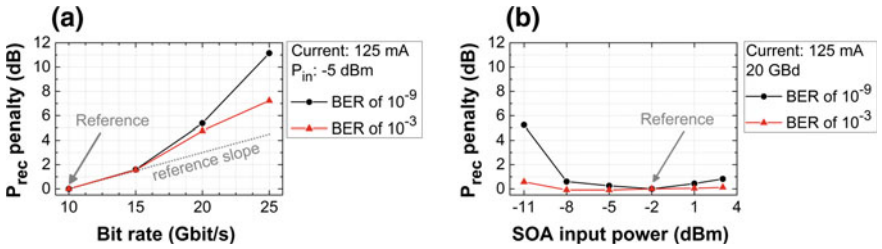

Fig. 5.6 Receiver input power P_{rec} penalty versus **a** the symbol rate and **b** the QD-SOA optical input power level. The optical input power was fixed to −5 dBm while scanning the symbol rate and the symbol rate was fixed to 20 GBd while scanning the optical input power level. The QD-SOA was driven in all case with a DC current of 125 mA. The penalty was determined at a BER of 10^{-9} and 10^{-3} with respect to the curve marked with "Reference"

small-signal modulation bandwidth of the QD-SOA. Nevertheless, despite the not optimized RF design, 25 GBd phase-coded signal generation is demonstrated for the first time.

At a given symbol rate of 20 GBd, the dependence on the input power level is investigated by changing the input power levels within a range of −11 to 3 dBm. The recorded BER curves (see Appendix C) and are evaluated in terms of receiver input power penalty with respect to the optimal input power of −2 dBm. The penalties are plotted in Fig. 5.6b. A penalty below 1 dB can be observed for QD-SOA input power levels from −8 to 3 dBm for both evaluated BER levels of 10^{-9} and 10^{-3}. A further reduction of the input power to −11 dBm leads only to a slight increase of the penalty at a BER of 10^{-3} whereas the penalty is larger than 5 dB for a BER of 10^{-9} caused by an error-floor. Hence, an error-free phase-coded signal generation is demonstrated within an input power range of more than 14 dB.

5.4 Summary

This chapter presented a QD-SOA-based concept for color-free low-cost generation of phase-coded signals. This concept has the potential to simplify the network architecture, improve the reliability, reduce the costs and possibly the energy consumption in comparison to alternative color-free configurations like OOK-based directly modulated SOAs or combinations of standard MZM or phase modulators with amplifiers required to overcome the modulator losses.

An error-free directly modulated QD-SOA has been demonstrated for the first time for phase-coded signal generation up to a symbol rate of 25 GBd. So far, DFB laser have been used to demonstrate up to 16 GBd directly modulated DPSK generation [12, 13], whereas SOAs have demonstrated only directly modulated OOK generation up to 10 GBd [7–9, 14]. Furthermore, error-free 20 GBd generation has been shown for input power levels within a range of more than 14 dB (−11 to 3 dBm) whereas

the QD-SOA has offered a fiber-to-fiber gain of up to 8 dB. A minor receiver input power penalty of 1 dB has been found within an input power range of at least 12 dB.

Hence, the proof of concept is given up to excellent symbol rates of 25 GBd demonstrating the suitability of directly modulated QD-SOAs for low-cost color-free networks realized with phase-modulated signal.

References

1. S.-M. Lee et al., Demonstration of a long-reach DWDM-PON for consolidation of metro and access networks. J. Lightwave Technol. **25**(1), 271–276 (2007)
2. S.-J. Park et al., An evolution scenario of a broadband access network using R-SOA-based WDM-PON technologies. J. Lightwave Technol. **25**(11), 3479–3487 (2007)
3. Y. Tian, Q. Chang, Y. Su, A WDM passive optical network enabling multicasting with color-free ONUs. Opt. Express **16**(14), 10434–10439 (2008)
4. P. Vetter, Next Generation optical access technologies, in *Communication (ECOC), European Conference and Exhibition on Optical* (2012), pp. 1–42
5. S.-G. Mun et al., A WDM-PON with a 40 Gb/s (32 × 1.25 Gb/s) capacity based on wavelength-locked Fabry–Perot laser diodes. Opt. Express **16**(15), 11361–11368 (2008)
6. H.-K. Lee, H.-J. Lee, C.-H. Lee, A simple and color-free WDM-passive optical network using spectrum-sliced Fabry–Pérot laser diodes. IEEE Photonics Technol. Lett. **20**(3), 220–222 (2008)
7. M. Omella et al., 10 Gb/s full-duplex bidirectional transmission with RSOA-based ONU using detuned optical filtering and decision feedback equalization. Opt. Express **17**(7), 5008–5013 (2009)
8. B. Schrenk et al., Direct 10-Gb/s modulation of a single-section RSOA in PONs with high optical budget. IEEE Photonics Technol. Lett. **22**(6), 392–394 (2010)
9. H. Kim, Transmission of 10-Gb/s directly modulated RSOA signals in single-fiber loopback WDM PONs. IEEE Photonics Technol. Lett. **23**(14), 965–967 (2011)
10. S. Ferber et al., Comparison of DPSK and OOK modulation format in 160 Gbit/s transmission system. Electron. Lett. **39**(20), 1458–1459 (2003)
11. A.H. Gnauck, P.J. Winzer, Optical phase-shift-keyed transmission. J. Lightwave Technol. **23**(1), 115–130 (2005)
12. R.S. Vodhanel et al., Performance of directly modulated DFB lasers in 10-Gb/s ASK, FSK, and DPSK lightwave systems. J. Lightwave Technol. **8**(9), 1379–1386 (1990)
13. A.S. Karar et al., Generation of DPSK signals using a directly modulated passive feedback laser, in *European Conference and Exhibition on Optical Communication (ECOC)* (Washington, DC, 2012), Tu.4.A.1
14. D.C. Kim et al., 2.5 Gbps direct modulation of reactive semiconductor optical amplifier for wavelength division multiplexing passive optical network colourless sources. Jpn. J. Appl. Phys. **48**, 120209 (2009)

Chapter 6
Signal Amplification

According to the introduction to future all-optical networks in Chap. 1, the individual customer premises are bidirectionally connected via access networks (ANs) to a central office, which are part of metropolitan area networks (MANs). Due to the desired increase of devices and longer reach, future all-optical ANs and/or converged MANs require SOA-based linear signal amplification [1–7]. In addition, a higher data rate is requested leading to the demand for either an increased symbol rate of OOK modulated signals or for the use of advanced modulation formats keeping the symbol rate but encoding multiple bits per transmitted symbol [5, 8]. Indeed, multiple modulation formats could be used in the same network to address individual requirements of the users. Hence, SOAs have to deal with various modulation formats and various symbol rates in multi-channel configurations to ensure flexible network architectures.

The gain bandwidth of the amplifier determines the number of supported wavelength channels and/or the channel spacing and thus the total network capacity. Within the O-band, the standards are defined with bandwidths from 20 up to 100 nm, e.g. [9]. A gain per wavelength channel larger than 10 dB (20 dB) is sufficient to extend the network reach by 29 km (57 km)[1] or to increase the power splitting ratio e.g. from 1:16 to 1:128 (1:1024). But, gain and gain bandwidth are connected as discussed in Sect. 3.5.1. Hence, the amplifier is designed as a trade-off between both properties, taking into account the requirements of the network. Furthermore, the optical amplifiers have to cope with data streams with various input amplitudes given by the specific topography of each network. For example, miscellaneous channels provided by the individual customer premises exhibit different amplitude levels due to individual reaches or losses of the respective transmission line.

[1] Taking into account the O-band SMF loss of 0.35 dB/km discussed in Chap. 1.

H. Schmeckebier, *Quantum-Dot-Based Semiconductor Optical Amplifiers for O-Band Optical Communication*, Springer Theses,
DOI 10.1007/978-3-319-44275-4_6

The range of input power levels in which the amplification allows an error-free transmission is called input power dynamic range (IPDR) and was introduced in Sect. 4.4. A larger IPDR allows a higher flexibility of the network architecture. The error-free definition depends on the modulation format and network implementation. Throughout this thesis, a BER of 10^{-9} and 10^{-3} (using forward-error correction (FEC)) will be used. The IPDR is thus the key parameter of the SOA for amplification of data signals with different amplitude levels amongst other static parameters like gain and bandwidth or noise figure. The IPDR is limited for low power levels by the amplifiers noise and for large input power levels by nonlinear effects. The IPDR is studied within this chapter for amplitude and phase-coded signals in single and multi-channel configurations.

The main issue for multi-channel transmission is the crosstalk between the channels at high input power levels describing the influence of other channel(s) on the signal performance of one channel. The crosstalk is particularly important for optical amplifiers as gain and phase dynamics of the gain media are determined by all wavelength channels. Within the linear gain regime, the crosstalk is expected to be low. But large SOA channel input power differences can still cause significant crosstalk on channels exhibiting a low input power. In addition, the crosstalk becomes strong in the nonlinear gain regime for a total input power – summed over all channels – significantly exceeding the 3-dB saturation input power. Indeed, the crosstalk within the slight nonlinear gain regime depends on the gain and phase dynamics of the gain material. QD SOAs have been demonstrated to show only small crosstalk even in the nonlinear gain regime, e.g. [8, 10–13].

Hence, this chapter[2] is focused on the IPDR for QD-SOA-based amplification of amplitude and phase-modulated signals in single and multi-channel configuration with per channel symbol rates of up to 80 GBd per wavelength channel. In detail, this chapter is organized as follows: Sect. 6.1 presents the amplification of multi-channel high symbol rate OOK signals, in particular the IPDR in single and multi-channel configuration. Section 6.2 first addresses the amplification of DPSK and DQPSK modulated signals in single-channel configuration, in particular the IPDR. In this context, the influence of the receiver type as well as the corresponding definition of the IPDR are discussed. Subsequently, the results of DQPSK amplification in the presence of a neighboring OOK channel are presented and discussed.

6.1 On-Off Keying (OOK) Signals

OOK modulated AN and MAN exhibit the most simple optical transmitter and receiver architecture and are thus preferred from the investment cost point of view up to per channel symbol rates of 20–40 GBd. However, even per channel symbol

[2]Parts of this chapter have been previously published in [1–4]. 1: Schmidt-Langhorst 2010; 2: Schmeckebier 2011; 3: Meuer 2011; 4: Zeghuzi 2015b.

rates up to 100 GBd, generated and demultiplexed via OTDM, can be interesting in particular cases.

IPDR investigations of SOAs with different gain media have been published e.g. in [8, 13–16] for OOK signals with various data rates. Typically, a significantly enlarged IPDR for QD-based SOAs has been observed mainly due to the strongly reduced pattern effects at larger input power levels. Hence, this section is focused on the amplification of OOK modulated signals with a high symbol rate of 80 GBd. The signal quality of the 80 GBd OOK signal is studied in absence and presence of three neighboring 40 GBd OOK channels in dependence of the QD SOA input power levels whereas the signal quality in case of bypassing the QD SOA serves as a reference. Thus, the IPDR in single and multi-channel configuration is compared. The collaborative measurements have been performed at the Fraunhofer Institute for Telecommunications Heinrich-Hertz Institute (HHI).

Setup

Figure 6.1 depicts the setup used to investigate the QD-SOA-based four-channel OOK amplification.

The 80 GBd RZ OOK data signal is based on a hybrid mode-locked laser (HMLL) emitting optical 1.5 ps broad pulses with a repetition rate of 10 GHz and a spectral center wavelength of 1310 nm. The HMLL output is amplified twice using two QW SOAs and in-between the pulse comb is two times multiplexed. The resulting 40 GHz pulse comb is modulated using a MZM which is driven by a 40 Gb/s NRZ OOK PRBS-31 generated by a BPG. The modulated 40 GBd RZ output is optical time-division multiplexed (OTDM) to an 80 GBd (80 Gb/s) RZ-OOK signal. This signal is finally booster amplified using a PDFA to ensure a large range of possible optical input power levels at the QD SOA.

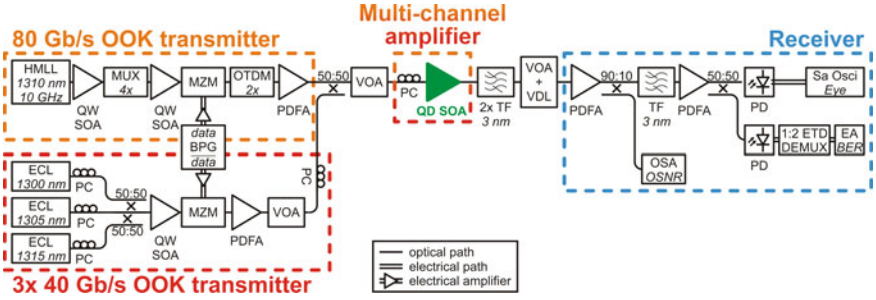

Fig. 6.1 Setup sketch for the multi-channel 80 GBd OOK amplification measurements. *BPG* bit-pattern generator, *EA* error analyzer, *ECL* external cavity laser, *ETD DEMUX* electrical time-domain demultiplexer, *HMLL* hybrid mode-locked laser, *MUX* multiplexer, *MZM* Mach-Zehnder modulator, *OSA* optical spectrum analyzer, *OTDM* optical time-division multiplexing, *QW SOA* quantum-well semiconductor optical amplifier, *PC* polarization controller, *PD* photodiode, *PDFA* praseodymium-doped fiber amplifier, *PWM* power meter, *Sa Osci* sampling oscilloscope, *TF* wavelength tunable filter, *VDL* variable delay line, *VOA* variable optical attenuator

The three 40 GBd NRZ OOK data signals are based on the output of three individual ECL emitting at a wavelength of 1300, 1305 and 1315 nm, respectively. The laser emissions are combined and their polarization is aligned equally. The combined signals are amplified using a commercial QW-SOA and afterwards modulated by a MZM which is driven by an inverted 40 Gb/s NRZ OOK PRBS-31 generated by the equivalent BPG. The three modulated 40 GBd (40 Gb/s) NRZ OOK signals are booster amplified using a PDFA to enable a large range of the QD SOA input power levels.

The 80 GBd RZ and the three interfering 40 GBd NRZ channels are combined and injected into the QD SOA under test with their polarization aligned to the TE axis. Two VOAs in front of the QD SOA enable various combinations of the per-channel input power of the 80 GBd signal and the interfering 40 GBd signals. The 40 GBd channels are intentionally NRZ modulated as well as are not time-delayed to each other. This represents a worst-case scenario for the device under test (DUT) with an enhanced crosstalk configuration on the 80 GBd channel.

The amplified QD SOA output signal to be analyzed by the receiver is chosen by two cascaded TF exhibiting a FWHM of 3 nm. Filtering out the 80 GBd channel, the three 40 GBd interfering channels are suppressed by more than 24 dB (see Fig. 6.2e). The receiver contains an optical pre-amplifier stage and a subsequent 3-dB splitter whose output ports are connected to PDs. 10 % of the first PDFA's output power is used to evaluate the OSNR using an OSA. A TF with a FWHM of 3 nm is used in-between the two amplifiers to suppress the ASE input into the second PDFA. The

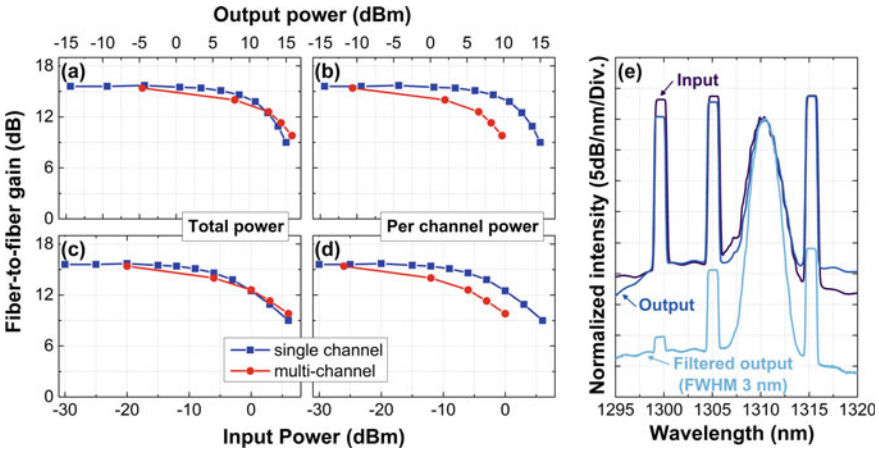

Fig. 6.2 Gain of the 80 GBd OOK signal in the absence ("single-channel") and in the presence ("multi-channel") of the three 40 GBd OOK interfering signals versus the **a** total output, **c** total input power, **b** per-channel output and **d** per-channel input power. The SOA current was 900 mA. The diagrams **a**–**d** share the same legend. **e** shows input and QD SOA output spectra before and after filtering exemplary for a total input power of 0 dBm. The spectra are normalized to the 80 GBd signal peak power

second PDFA is operating in a constant output power mode, which enables a constant averaged optical power on the 50 GHz PDs. The non-zero dispersion of the PDFAs results in a pulse broadening with finally a FWHM of 2.7 ps.

The signal quality is evaluated for the 40 and 80 GBd signals with eye-pattern measurements using a 70 GHz sampling oscilloscope. In addition, the 80 GBd signal quality is evaluated by BER measurements using a 1:2 electrical time-domain demultiplexer (ETD DEMUX) and a subsequent EA. The BER of the two demultiplexed 40 GBd (40 Gb/s) tributaries are measured timing the variable delay line (VDL) in front of the receiver. The 80 GBd BER is obtained by averaging both 40 GBd BER for equal OSNR values. The receiver input power and thus the OSNR is varied using a VOA in front of the receiver.

Device Under Test (DUT)

The DUT is the 4 mm long QD SOA No. 6 (see page 43). The QD SOA drive current has to be chosen as a trade of between the maximal available gain and a fast gain recovery due to device heating induced gain reduction at larger currents [11, 17]. Therefore, a current of 900 mA was chosen here. At this current the ASE peak emission is red-shifted to 1324 nm and decreased by 4 dB with respect to a current of 600 mA.

Figure 6.2a–d depicts the QD SOA fiber-to-fiber gain of the 80 GBd signal in the absence and in the presence of the three interfering 40 GBd channels. For a more detailed discussion, the gain is plotted versus the per-channel and total (sum over all channels) input and output power. Of course, in absence of the three interfering channels, the total and per-channel power levels are equal.

The 80 GBd signal gain plotted versus the total power is comparable for single- and multi-channel configuration (Fig. 6.2a, c). Plotting the gain versus the per-channel power, the gain saturation is shifted towards lower per-channel power levels in the multi-channel case. The linear gain, total 3-dB saturation input P_{sat}^{in} and output power P_{sat}^{out} for the 80 GBd signal are independent of the interfering channels and are measured to be 15.5 dB, 0.1 dBm and 12.6 dBm, respectively. In contrast to that, the per-channel 3-dB saturation input P_{sat}^{in} and output power P_{sat}^{out} are reduced by 6 dB to −5.8 dBm and 6.8 dBm, respectively, in the multi-channel case. This 6-dB reduction corresponds to the reduction of the per-channel input power P_{in} to $1/4$ of the total input power.

Experimental Results

The 80 GBd as well as an exemplary 40 GBd OOK QD SOA input eye diagrams (BtB configuration) are depicted in Fig. 6.3a, b for the maximal available OSNR. The eye diagrams of the other two 40 GBd channels are identical to that shown in the figure and are thus not shown. All input eyes are clearly open and show thin mark and space levels.

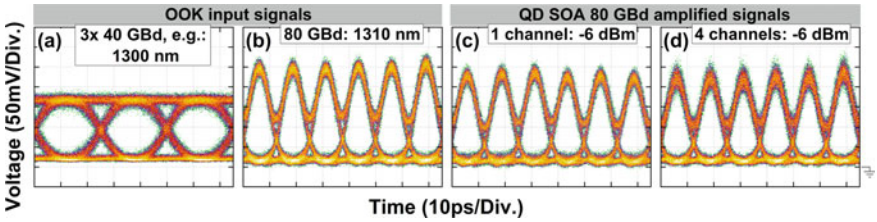

Fig. 6.3 Eye diagrams of **a** one exemplary 40 GBd OOK signal at a wavelength of 1300 nm and **b** the 80 GBd OOK signal, both in BtB configuration. The other two 40 GBd channels at a wavelength of 1305 and 1315 nm exhibit identical eye diagrams. Eye diagrams of the QD SOA amplified 80 GBd signal for a comparable per-channel input power level of −6 dBm in the **c** absence ("1 channel") and **d** presence ("4 channels") of the three interfering 40 GBd channels. All eye diagrams are measured at the maximal available receiver OSNR. The QD SOA drive current was 900 mA

Two exemplary eye diagrams of the amplified 80 GBd signal are shown in Fig. 6.3c, d in single and multi-channel configuration for the same per-channel QD SOA input power level of −6 dBm. The total input power is increased by 6 dB in the multi-channel case. In single-channel configuration, the amplified eye diagram is comparable to the input eye diagram. In comparison to the single-channel case, the eye diagram in the presence of the three interfering 40 GBd signals exhibit a slight broadening of the transitions and the mark level. This is caused on the one hand by the reduced gain and consequently the reduced maximal available receiver OSNR. On the other hand, a small pattern induced crosstalk appears because the total input power of 0 dBm reaches the 3-dB saturation input power and, thus, the mark level exceeds it by 3 dB.

The 80 GBd OOK BER measurements are listed in the Appendix C. The signal quality of the three 40 GBd signals have been verified but will be not discussed here in detail because the crosstalk on the 80 GBd channel is the strongest. The BER curves of the QD SOA amplified 80 GBd signal are evaluated in terms of OSNR penalty with respect to the BtB BER curve at a BER of 10^{-9} and 10^{-4}. The penalties are plotted in Fig. 6.4 with respect to the total and per-channel QD SOA input power levels.

A maximum OSNR penalty of 1.3 dB can be observed for the single-channel amplification for input power levels from −12 to 6 dBm. The penalty variation within this input power variation is small and nearly flat. Especially on the large-power side, the penalty is still small even for power levels far beyond the QD SOA 3-dB saturation input power of 0.1 dBm. Even for these very large QD SOA input power levels no significant patterning appears. Taking 2 dB penalty as a reference, the IPDR of the single-channel 80 GBd signal amplification is larger than 18 dB.

The 80 GBd multi-channel penalties show a large dependence on the QD SOA input power at a BER of 10^{-9}. The penalty for the lowest total input power of −6 dBm (per-channel −12 dBm) is only slightly larger than for the single-channel configuration. But the penalty significantly increases above 2 dB for the next measured larger total input power of 0 dBm (per-channel −6 dBm) which is equivalent to the total

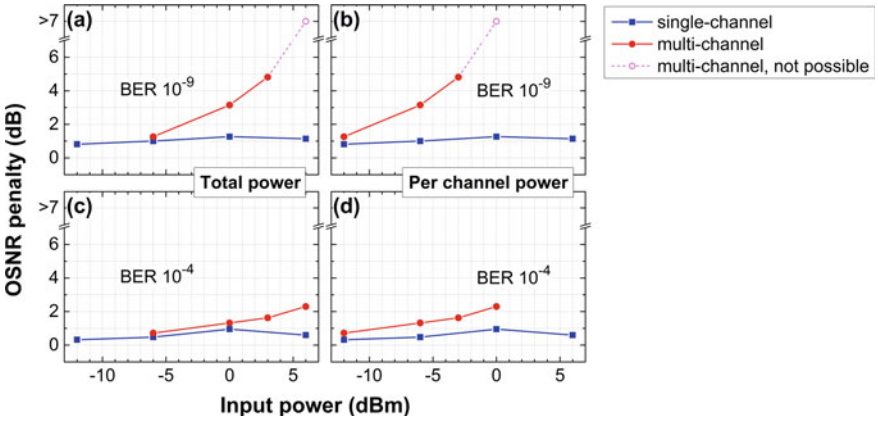

Fig. 6.4 OSNR penalty of the amplified 80 GBd OOK signal at a BER of **a**, **b** 10^{-9} as well as **c**, **d** 10^{-4} in the absence ("single-channel") and in the presence ("multi-channel") of three interfering 40 GBd channels. The OSNR penalty is plotted versus the **a**, **c** total QD SOA input power as well as the **b**, **d** per-channel input power. BER limits that have not been reached due to an error-floor are plotted at penalties labeled with ">7", and the connection to the measured penalties are dashed and the color is brighter. The characteristic of this connecting line is not valid and they are plotted to improve the readability as well as to symbolize the limit

3-dB saturation input power. For even larger input an error-floor appears and finally, the BER limit of 10^{-9} is exceeded for the largest tested per-channel input power of 0 dBm (total power 6 dBm).

Taking into account the broad homogenous linewidth (FWHM) of the QDs at room temperature of around 10 meV (14.0 nm at a wavelength of 1.32 μm) [18, 19] almost all three interfering signals used for this experiment lay within the homogenous linewidth of the QD providing the largest gain to the 80 GBd signal amplification. Hence, the observed signal degradation is presumable dominated by XGM on the QD GS levels. Addressing with each signal a QD subensemble which is not overlapping with the other subensembles could reduce the crosstalk. However, the crosstalk is weaker resulting in a large IPDR than for QW and bulk SOAs [8, 15, 20].

In contrast to the error-free threshold, the penalties for a BER limit of 10^{-4} are much less effected and are below 2 dB except for the largest total input power of 6 dBm (per-channel 0 dBm). Even for this large total input power the penalty remains moderate with a value of 2.3 dB. Hence, the signal quality at a BER limit of 10^{-9} suffers from cross-gain induced crosstalk which starts to appear at around the 3-saturation input power. The signal quality at a BER limit of 10^{-4} is more robust to the crosstalk effects.

Conclusion

In conclusion, the results demonstrate that the fast QD SOAs gain dynamics enable error-free 80 GBd RZ OOK single-channel amplification without pattern effects with a linear fiber-to-fiber gain of up to 15.5 dB and a QD SOA input power of 6 dBm far beyond the 3-dB saturation input power. The IPDR is found to be larger

than 18 dB limited by the measurement span. In addition, the crosstalk of three interfering 40 GBd NRZ OOK channels neighboring the 80 GBd channel in a 5 nm grid is found to be minuscule for input power levels within the linear gain regime. For larger input power levels around and even above the 3-dB saturation input power of 0.1 dBm, the crosstalk is increased, but still an error-free performance is proved for per-channel input power levels up to −3 dBm. Hence, QD SOAs are expected to be key components for future multi-wavelength-channel-based 400 Gb/s systems with a per-channel data rate of up to 100 Gb/s using OOK.

6.2 Differential (Quadrature) Phase-Shift Keying (D(Q)PSK) Signals

The previous sections covered the QD SOA amplification performance of amplitude modulated signals. This section treats the amplification of phase-modulated signals. In contrast to amplitude modulated signals, phase-coded signals cannot be detected directly. Instead, an optical and/or electrical processing is required to recover the phase of the optical signal. Phase sensitive receivers are thus more complex and consequently more expensive than direct detection receivers. The larger investment costs will be compensated by the improved performance and especially in case of a coherent detection receiver by a larger flexibility of the network in terms of scalability of the modulation format.

Phase-coded signals make lower demands on the performance of optical amplifiers than amplitude coded signals. Patterning can be neglected as the signal amplitude changes at least only for symbol transitions. However, this short amplitude changes can lead to a small variation of the carrier density and thus to a phase distortion as described by the α factor. Section 6.2.1 presents the basic setup and the device under test used for all D(Q)PSK measurements shown in this thesis. Subsequently, Sect. 6.2.2 presents QD SOA input power dynamic range (IPDR) results for DPSK and DQPSK modulated signals. Section 6.2.3 discusses the influence of an interfering OOK channel on a DQPSK in dependence of the input power of both signals.

6.2.1 Basic D(Q)PSK Setup and Device Under Test

The basic setup for all D(Q)PSK measurements in this thesis is sketched in Fig. 6.5. It is built of a 40 GBd D(Q)PSK transmitter, the DUT and a multi-format receiver. The precise setups of “inline 1” and “inline 2” vary depending on the measurement focus and are explained individually in the corresponding chapters.

The 40 GBd D(Q)PSK transmitter is based on an ECL emitting at a wavelength of 1308.5 nm (amplification) or 1311 nm (wavelength conversion in Sect. 8.4). Both wavelengths are chosen according to the QD SOA ASE GS peak emission, whereas

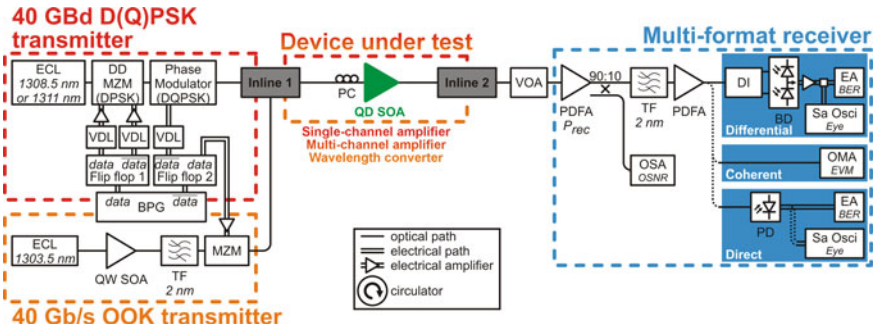

Fig. 6.5 Basic setup sketch for the D(Q)PSK signal amplification and wavelength conversion. Depending on the measurement the gray colored boxes "inline 1" and "inline 2" vary and are explained individually in the corresponding sections. The EA and RT-Osci were used only in one of the receivers at the time. *BD* balanced photo detector, *BPG* bit-pattern generator, *DD MZM* dual-drive Mach-Zehnder modulator, *DI* delay interferometer, *EA* error analyzer, *ECL* external cavity laser, *MZM* Mach-Zehnder modulator, *OSA* optical spectrum analyzer, *OMA* optical modulation analyzer, *QD SOA* quantum-dot semiconductor optical amplifier, *QW SOA* quantum-well semiconductor optical amplifier, *PC* polarization controller, *PD* photodiode, *PDFA* praseodymium-doped fiber amplifier, *Sa Osci* sampling oscilloscope, *TF* wavelength tunable filter, *VDL* variable delay line, *VOA* variable optical attenuator

the slight wavelength change for different applications is attributed to the available wavelength filters. The transmitter consist of a modulator cascade instead of an IQ-modulator, due to lack of commercially available O-band IQ-modulators. The output of the ECL is modulated using a dual-drive Mach-Zehnder modulator (DD MZM)[3] and a subsequent phase modulator. The electrical PRBS-7 data signals are generated by a 56 Gb/s BPG and are boosted, reshaped and retimed using two 56 Gb/s digital flip flops. The two outputs of flip flop 1 which are inverted to each other are used to drive the DD-MZM. The variable delay lines (VDLs) in front of the DD-MZM enable a fine tuning of the zero delay between the two DD-MZM input ports on the order of a few hundred femtoseconds. The optical output of the DD-MZM is a 40 GBd DPSK signal.

For generation of DQPSK signals, one output of flip flop 2 is used to drive the phase modulator. The VDL in front of the phase modulator is used to tune the delay between the optical and electrical input signals. The delay is chosen to be 108 bits for one of the DQPSK tributaries. This ensures that all transitions of the DQPSK signal are included. For DPSK signal generation, flip flop 2 is switched off. In case of multi-channel amplification, the 40 GBd OOK interfering channel is generated by modulating the amplified output of an ECL emitting at a wavelength of 1303.5 nm. The MZM is driven by the amplified second output of flip flop 2. This transmitter is only used in Sect. 6.2.3 and is switched off otherwise. Further components of

[3]This modulator is designed for the C-band but also operates in the O-band. But the device shows an increased wavelength dependent performance within the O-band in terms of e.g. extinction ratio. Due to a lack of commercial O-band DD-MZMs, this device is used.

the transmitter(s) like booster amplifiers, filters and signal combiners are part of "inline 1" and will be explained in detail in the corresponding sections.

The signal(s) are injected into the QD SOA with their polarization being aligned to the TE axis. Further components of the DUT like ASE suppressing filters for the amplification case or signal selecting filters for wavelength converters are part of "inline 2". Additionally, inline 2 can also contain inline components following the QD SOA, like wavelength channel selection filters for the receiver.

The receiver input power and thus the received OSNR is varied using a VOA in front of the receiver. The multi-format receiver contains an optical pre-amplifier stage and subsequently three different receiver types. The first PDFA is driven in constant gain mode whereas the second PDFA is operating with a constant averaged output power, which enables a constant averaged optical power into the three receivers. A TF with a FWHM of 2 nm is used in-between the two amplifiers to suppress the ASE input into the second PDFA. 10 % of the output power of the first PDFA is used to evaluate the OSNR using an OSA. Depending on the signal modulation format one of the three following receivers is used to evaluate the signal quality.

The direct detection receiver is used to detect OOK modulated signals (used only for multi-channel amplification presented in Sect. 6.2.3). It comprises a 50 GHz PD. The signal quality is evaluated with BER measurements using a 53.5 Gb/s EA as well as eye-pattern measurements using an 70 GHz Sa Osci.

The differential detection receiver comprises a delay interferometer (DI) and a subsequent 50 GHz balanced photo detector (BD). The signal quality is evaluated with BER measurements and eye measurements similar to the direct detection receiver. The differential detection receiver is used to measure BERs down to values of 10^{-12} and eyes of D(Q)PSK signals without offline processing.

In contrast, the optical modulation analyzer (OMA)[4]-based coherent detection receiver is used to measure constellation diagrams, EVMs and BERs down to 10^{-7} of D(Q)PSK signals with offline processing algorithms. If not explicitly stated differently, the coherent detection receiver is used throughout this thesis always with a software equalizer (EQ) to overcome bandwidth limitations of the transmitter and receiver. The settings of the EQ are chosen by an algorithm included in the OMA software,[5] that minimizes the EVM for the D(Q)PSK signals in BtB configuration over 99 symbols. The EQ settings are fixed after the algorithm has converged. All measurements with amplifiers are performed with the identical EQ settings like for the corresponding BtB configuration to display the influences. For each change of the BtB configuration, like wavelength or modulation format (DPSK to DQPSK), the algorithm is restarted.

[4]Due to lack of commercial available OMAs operating in the O-band, the world's first O-band OMA was developed and assembled at the Technische Universität Berlin by Dejan Arsenijević and Holger Schmeckebier and the support of Kylia and Keysight Technologies.

[5]"Keysight N4391A Software Optical Modulation Analyzer" version 4.1.11.17934 ©Keysight Technologies.

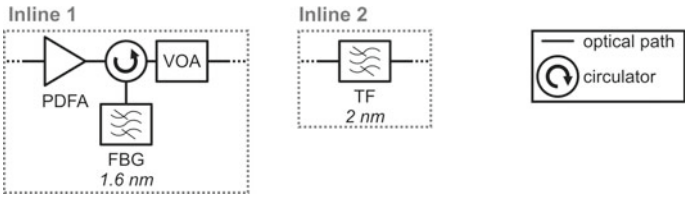

Fig. 6.6 Modification of the basic D(Q)PSK setup shown in Fig. 6.5 to investigate the QD SOA IPDR for a D(Q)PSK modulated signals. *FBG* fiber-Bragg grating, *PDFA* praseodymium-doped fiber amplifier, *TF* wavelength tunable filter, *VOA* variable optical attenuator

This section comprehensively uses both, the differential and coherent detection receivers as the use of both allow in-depth investigation of phase and amplitude effects, which are induced by the amplifier.

Device Under Test (DUT)
The DUT is the 5 mm long QD SOA No. 5 (see page 42). At a current of 500 mA, the SOA offers a peak small-signal fiber-to-fiber gain of 24.0 dB as well as a 3-dB saturation input and output power of −8.3 and 12.8 dBm, respectively.

6.2.2 Single-Channel (D(Q)PSK) Amplification—IPRD

This section presents first the modification of the basic D(Q)PSK setup followed by an introduction to the different methods for the IPDR evaluation based on the differential and coherent detection receiver. Subsequently, the sensitivity of both receivers are discussed by comparing the different IPDR methods obtained with an QD SOA. Finally, the IPDRs of D(Q)PSK signal amplification using the QD SOA are discussed.

Basic D(Q)PSK Setup Modification
In this section, the basic D(Q)PSK setup is modified as sketched in Fig. 6.6. The 40 GBd OOK transmitter is switched off. The generated D(Q)PSK signal is booster amplified in "inline 1" and subsequently wavelength filtered using a 1.6 nm broad FBG in combination with a circulator.[6] The QD SOA input power can be adjusted using the VOA in "inline 1". The QD SOA output is wavelength filtered to suppress the ASE using a TF with a FWHM of 2 nm in "inline 2".

Measurement Method for the IPDR
The 40 GBd DPSK and DQPSK signals are detected using both, the differential and the coherent detection receiver.

The *differential detection receiver* was used to perform BER measurements in dependence of the receiver input power P_{rec} without (back-to-back (BtB)) and with the QD SOA. The BER curves are fitted and the DQPSK BER curves of tributary 1

[6]Detailed information on this setup part can be found in the Appendix B.

and tributary 2 are averaged (more details see Appendix C). All measurements and fits are listed in Appendix C. The fitted BER curves are analyzed in terms of P_{rec} penalty at BERs of 10^{-9} and 10^{-3} with respect to the corresponding BtB measurement.

The *coherent detection receiver* was used to measure the EVM for a given P_{rec} or vice versa. For the DPSK modulation, the receiver input power levels was measured at an EVM of 23.4 and 30.0 % indicating a BER limit of 10^{-9} and 10^{-6}, respectively [21, 22]. Similar, EVMs of 16.4 and 20.0 % were chosen for the DQPSK modulation indicating a BER limit of 10^{-9} and 2×10^{-7}, respectively. Please notice, that the given indication of EVM and BER are only reliable for non-distorted signals.

As introduced in Sect. 4.4, the IPDR is determined for both receivers differently. In case of the differential detection receiver, the BER value is kept by changing the receiver input power (P_{rec}). In case of the coherent detection receiver, the P_{rec} is kept while measuring the EVM. The obtain IPDR values differ for both receivers due to the different definitions but also due to the different detection schema. This section uses both IPDR methods and, in addition, mixes both methods to enable a comparison and discussion of both receivers and methods. The following combinations are evaluated:

- P_{rec} penalty is evaluated at (shown in Fig. 6.7):
  - Constant BER thresholds using the differential detection receiver (labeled: "differential Rx at BER of 10^{-x}").
  - At constant EVM thresholds using the coherent detection receiver (labeled: "coherent Rx at EVM of x %").
- The EVM is measured for (shown in Fig. 6.8):
  - A variable P_{rec} at which the differential detection receiver achieves a BER of 10^{-9} (labeled: "P_{rec} variable, set to BER of 10^{-9}" or short "VP-curves").
  - A fixed P_{rec} value of 10 dB above the P_{rec} at which the differential detection receiver detects a BER of 10^{-9} in BtB configuration (labeled: "fixed P_{rec} to differential Rx").

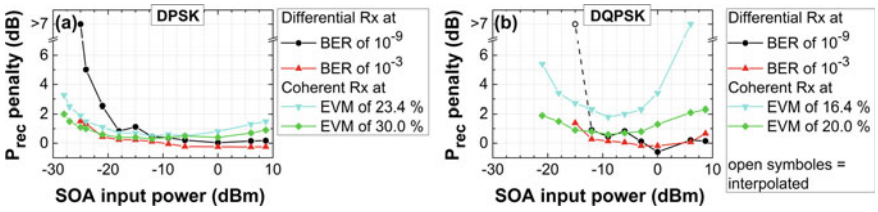

Fig. 6.7 Receiver input power P_{rec} penalty versus the QD SOA input power level for **a** the DPSK and **b** the DQPSK modulated signal. The P_{rec} penalty is evaluated at different BERs using the differential detection receiver as well as at different EVMs using the coherent detection receiver. The DQPSK BER curve recorded at a SOA input power of −15 dBm suffered from error burst on tributary 2 whereas tributary 1 showed a normal behavior (see Fig. 9.7, page 161). BER curves missing the BER limit of 10^{-9} by about or less than one order of magnitude are interpolated (marked with *open symbols*)

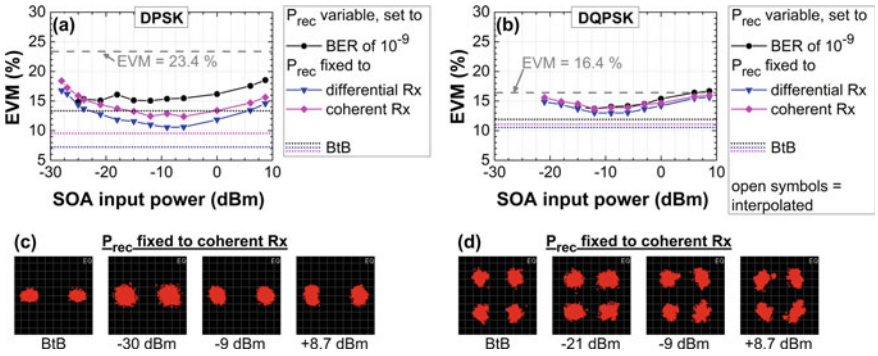

Fig. 6.8 EVM versus the QD SOA input power level for **a** the DPSK and **b** the DQPSK modulated signal. The P_{rec} is set differently for the three measured curves. The P_{rec} for the curves "P_{rec} variable..." were set individually for each QD SOA input power to the value at which a BER of 10^{-9} was achieved using the differential detection receiver (curves called "VP-curve" in text). These *curves* illustrates the difference between the two different receiver types. For DQPSK modulated signal, the point at −15 dBm has been performed at an interpolated P_{rec} (more details see text.). In contrast, the P_{rec} for "differential Rx" and "coherent Rx" was fixed to 10 dB above the BtB P_{rec} obtained at a BER of 10^{-9} and at an EVM of **a** 23.4 % and **b** 16.4 %, respectively. Exemplary **c** DPSK and **d** DQPSK constellation diagrams for the BtB configuration and for various QD SOA P_{in}, all measured at a fixed P_{rec} of **c** −26.5 dBm and **d** −20.9 dBm

– A fixed P_{rec} value of 10 dB above the P_{rec} at which the coherent detection receiver detects an EVM of 23.4 % (16.4 %) in BtB configuration for a D(Q)PSK signal (labeled: "fixed P_{rec} to coherent Rx").

The determined BtB Precs and the measured EVMs for the different receiver types and methods are listed in Table 6.1. The corresponding BtB constellation diagrams for the DPSK and DQPSK signals are depicted in Fig. 6.8c, d, respectively. Comparing the BtB DPSK and DQPSK Precs required for a BER of 10^{-9} and 10^{-3}, the difference is much larger than the ideal 3 dB. In addition, tributary 2 shows a 2 dB larger P_{rec} at a BER of 10^{-9} than tributary 1 and thus tributary 2 dominates the DQPSK P_{rec} (see Fig. 9.7, page 161). This asymmetry is caused either by misalignment of the DD-MZM drive signals or by the DD-MZM characteristics (not optimized for the O-band).

IPDR-Based Receiver Comparison

The P_{rec} penalties of the QD SOA amplified signals are plotted versus the QD SOA input power (P_{in}) in Fig. 6.7 for a BER of 10^{-9} and 10^{-3} as well as for two different EVM values. These curves are used to evaluate the QD SOA IPDR based on the differential detection receiver (measured BER) and based on the coherent detection receiver (measured EVM).

In the opposite to the P_{rec}-penalty-based IPDR in Figs. 6.7 and 6.8 shows the EVM-based IPDR measurements. The "VP-curve" represents a combination of the two receivers and two parameters as the BER-based differential detection receiver forces the P_{rec} at each individual point set to measure the EVM with the coherent

Table 6.1 List of modulation format dependent BtB receiver input power P_{rec} and measured EVM for different receiver types and methods

	P_{rec} (dBm)	EVM (%)
DPSK		
Differential Rx at BER 10^{-9}	−30.8	13.8
Differential Rx at BER 10^{-3}	−36.9	24.3
Coherent Rx at EVM of 23.4 %	−35.5	23.4
Coherent Rx at EVM of 30.0 %	−39.0	30.0
Fixed P_{rec} to differential Rx	−20.5	7.2
Fixed P_{rec} to coherent Rx	−26.5	9.5
DQPSK		
Differential Rx at BER 10^{-9}	−24.0	11.9
Differential Rx at BER 10^{-3}	−32.0	17.8
Coherent Rx at EVM of 16.4 %	−30.9	16.4
Coherent Rx at EVM of 20.0 %	−33.3	20.0
Fixed P_{rec} to differential Rx	−14.0	10.5
Fixed P_{rec} to coherent Rx	−20.9	11.1

detection receiver. If both receivers would show a similar dependence on noise and distortion, these "VP-curves" are expected to be flat.

For DPSK modulation, both receivers show a comparable P_{rec} penalty of less than 1 dB with respect to the BtB configuration for moderate QD SOA input power levels (P_{in}) of around −9 dBm (see Fig. 6.7a). Similarly, the "VP-curve" in Fig. 6.8a shows a flat behavior in this region of QD SOA input power levels (P_{in}). Increasing the QD SOA P_{in}, the differential detection receiver shows no P_{rec} penalty increase for both BER limits whereas the coherent detection receiver shows a slight increase (Fig. 6.7a). This behavior can be observed similar but more pronounced for the "VP-curve" (Fig. 6.8a). As a consequence, the performance of the differential detection receiver seems to be less sensitive to signal distortions which appear at large SOA input [8].

The coherent detection receiver exhibits a slow increase of the penalty with decreasing QD SOA input power. The differential detection receiver shows a similar behavior for a BER of 10^{-3} whereas it shows a strong increase for a BER of 10^{-9}. Therefore, the EVM-based coherent detection receiver performance seems to be less sensitive to noisy input signals than the BER-based differential detection receiver. The "VP-curve" reproduces this behavior by a flat non-increasing EVM. A proper explanation for the different sensitivities are the different receiver schemes. The coherent detection receiver on the one hand mixes the input signal with a low noise optical local oscillator (LO) whereas the differential detection receiver mixes the input signal with its one symbol delayed copy. The coherent detection receiver therefore acts more resilient to noisy input signals. On the other hand, the differential detection receiver compares only one symbol with the next and therefore is less sensitive to phase distortions on a larger time scale than the symbol rate. In contrast, the

coherent detection receiver experiences the full QD SOA phase recovery dynamics discussed in the Sects. 2.3.2 and 3.6.

The receiver dependent evolution of the P_{rec} penalty slopes for the DQPSK modulated signals are comparable to the DPSK modulated signals (see Fig. 6.7) with some restrictions at this point:

- The differential detection receiver power penalty increases nearly abruptly to values larger than 7 dB for a BER of 10^{-9} at the lowest SOA P_{in} of -15 dBm. This is cause by error burst of the BER reproducible observed only for tributary 2 at a SOA P_{in} of -15 dBm but not on tributary 1 (see Fig. 9.7, page 161). The origin for this is still under discussion. However, even without the error bursts, the strong increase is expected to appear at only slightly lower QD SOA input power levels.
- The minimal penalty measured at an EVM of 16.4 % indicating a BER of 10^{-9} (assuming no signal distortions) is increased and marginally below 2 dB.

However, the general comparability is confirmed by the "VP-curves" showing a complete similar behavior for both modulation formats (see Fig. 6.8).

In conclusion, the OMA-based coherent detection receiver in this thesis offers in-depth investigation of phase and amplitude effects of the amplifier. In contrast, the differential detection receiver can confirm directly an error-free operation without assumption about the signal, e.g. used to indicate a BER from the measured EVM.[7]

IPDR Evaluation and Discussion

After discussing the receiver differences, the QD SOA IPDR will be discussed in detail in the following.

The lowest EVM of the amplified signals is achieved for a QD SOA input power of around -9 dBm which is close to the 3-dB saturation input power, see Fig. 6.8. To study the IPDR limitations for decreasing and increasing SOA P_{in} from this optimal point, the change of the EVM, phase error and magnitude error are plotted in Fig. 6.9 with respect to the BtB measurement. The EVM increase for increasing SOA input power is dominated by the phase error (see also constellation diagrams in Fig. 6.8c, d). The EVM increase for low SOA P_{in} is driven by both, the phase and magnitude error. Hence, the amplified signal suffers with at large QD SOA input power from phase distortions. These are caused by the nonlinear gain and carrier dynamics at this very large input way above the 3-dB saturation input power of -8.3 dB. Nevertheless, measurements of the phase error performed for conventional SOAs (high α-factor) and QD SOAs (low α-factor) in [23] demonstrated a significantly improved performance of the QD SOAs at large SOA input power levels. The amplified signals with a low P_{in} run into the OSNR limitations resulting in more noisy signals visible with larger constellation points. The EVM-based IPDR evaluation is listed in Table 6.2. Unfortunately, the EVM value indicating a BER of 10^{-9} has not been reached. Hence, only a lower limit for the IPDR can be given.

[7] The OMA allows a direct BER evaluation down to about 10^{-5} limited by the length of the recorded traces of the OMA software. Lower BER values can be only estimated from the EVM.

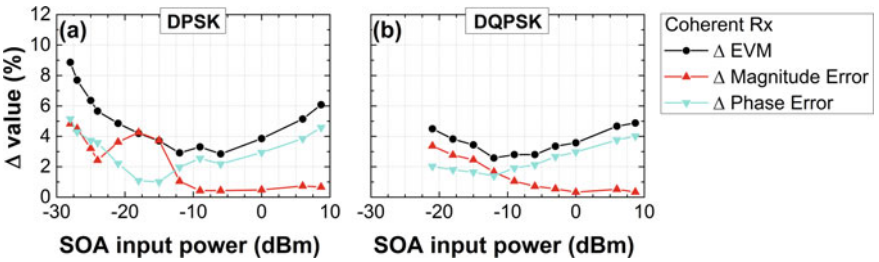

Fig. 6.9 Change of EVM, magnitude error and phase error versus QD SOA input power with respect to the BtB measurement for **a** DPSK and **b** DQPSK modulated signal

Table 6.2 List of modulation type dependent QD SOA IPDRs evaluated based on (left) 1, 2 and 3 dB receiver input power P_{rec} penalties as well as (right) different EVM for different receiver configurations

IPDR based on P_{rec} penalty					IPDR based on EVM		
	(dB)	(dB)	(dB)			(dB)	(dB)
DPSK							
	1 dB	2 dB	3 dB			23.4 %	30.0 %
BER 10^{-9}	>23.1	>28.8	>30.3				
BER 10^{-3}	>31.6	>33.7	>33.7				
EVM 23.4 %	22.7	>34.0	>36.4		Differential Rx	>36.7	>36.7
EVM 30.0 %	>32.7	>36.7	>36.7		Coherent Rx	>36.7	>36.7
DQPSK							
	1 dB	2 dB	3 dB			16.4 %	20.0 %
BER 10^{-9}	>18.0	>18.4	>18.8				
BER 10^{-3}	>22.7	>23.7	>23.7				
EVM 16.4 %	–	4.2	15.2		Differential Rx	>29.7	>29.7
EVM 20.0 %	13.7	~26.3	>29.7		Coherent Rx	>29.7	>29.7

The labels used in this table stand for following labels used in the text: "BER 10^{-x}" = "differential Rx at BER 10^{-x}"; "EVM x %" = "coherent Rx at EVM of x %"; "differential Rx" = "fixed P_{rec} to differential Rx"; "coherent Rx" = "fixed P_{rec} to coherent Rx"

Similar to the EVM, the optimal QD SOA P_{in} for the P_{rec} penalty is found around −9 dBm using the coherent detection receiver, see Fig. 6.8. Strongly decreasing or increasing the P_{in} leads to an increased penalty consistent to the EVM evolution. In contrast, the differential detection receiver shows no penalty increase even at very large input up to 8.7 dBm. However, the penalty increase for very low QD SOA input is comparable for a BER of 10^{-3} but much stronger for a BER of 10^{-9} as already described above.

Depending on the field of operation different acceptable P_{rec} penalty requirements have to be fulfilled by the amplifier. Therefore, the P_{rec} dependent IPDR has been evaluated for penalty thresholds of 1, 2 and 3 dB. The resulting D(Q)PSK IPDRs are listed in Table 6.2.

The EVM-based IPDRs are found to be larger than 36.7 dB (29.7 dB) for the D(Q)PSK signals. These obtained EVM-based IPDR values are larger or comparable to other published QD SOA values at 1.55 µm [23] despite the 42 % increased symbol rate from 28 to 40 GBd and simultaneously the drastically increased linear fiber-to-fiber gain from 13.5 dB to more than 24 dB. These results are very promising as the 1.3 µm QD SOA amplification is proven to be more robust despite the large gain induced reduction of the 3-dB saturation input power from 2 dBm [23] to −8.3 dBm.

For DPSK modulated signals, the penalty-based IPDR obtained with the differential detection receiver is a bit smaller than with the coherent detection receiver at a BER of 10^{-9} mainly caused by the different OSNR sensitivities discussed above. In contrast, the coherent detection receiver penalty IPDR is limited by a total offset penalty of close to 2 dB at a BER of 10^{-9} for DQPSK modulated signals. This offset is most likely caused by long-term phase changes resulting in an inter-symbol phase distortion. Taking into account the inter-symbol amplitude changes of the DQPSK signal (compare Fig. 4.1d, page 77), the reason for long-term phase changes could be an amplitude to phase conversion caused by the slow phase dynamics of the QD SOA reservoir. Hence, larger IPDRs are obtained with the differential detection receiver at this BER. However, the DPSK IPDR is, as expected, in all cases much larger than for the DQPSK signal but transmits also only half the information.

Comparing the different IPDR evaluations, the P_{rec} penalty-based IPDRs are at the most equivalent but smaller than the EVM-based IPDRs. This is related to the different P_{rec} at which the evaluation takes place. The penalty-based IPDR is performed at significantly lower receiver input power and is thus more sensitive to small signal changes.

In conclusion, the fast QD SOA gain dynamics and particular the decoupling of gain and phase dynamics result in predictable low α-factors and thus to an improved IPDR in comparison to conventional SOAs, as demonstrated in [8, 12, 23]. In comparison to the results in these publications, the QD SOA investigated in this chapter offers a larger IPDR despite the increased symbol rate and strongly improved gain. Combining the IPDR performance obtained for OOK and DQPSK signals, the QD SOAs are expected to support also modulations formats using amplitude and phase, e.g. QAM. First results published e.g. in [8, 23, 24] obtained for 1.55 µm QD SOA confirm this prediction. However, the large gain and large IPDR are very promising results and demonstrate the suitability of QD SOAs for future reach extended converged metro-access ring network scenarios base upon advanced modulation formats.

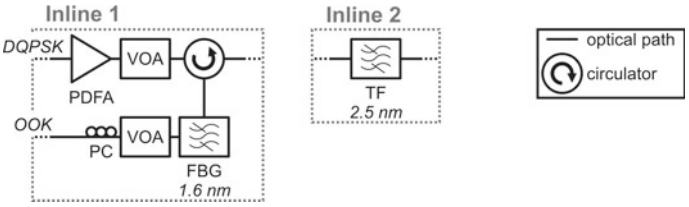

Fig. 6.10 Modification of the basic DQPSK setup shown in Fig. 6.5 to investigation the QD SOA 40 GBd DQPSK amplification in presence of a 40 GBd OOK signal. *FBG* fiber-Bragg grating, *PDFA* praseodymiumdoped fiber amplifier, *PC* polarization controller, *TF* wavelength tunable filter, *VOA* variable optical attenuator

6.2.3 DQPSK Amplification with One OOK Neighboring Channel

The previous subsection presented excellent IPDR results of D(Q)PSK signal amplification in single-channel configuration. However, under network conditions, the amplifier has to handle not only one but multiple wavelength channels simultaneously. The multi-channel OOK amplification was demonstrated in Sect. 6.1 for total input power levels even above the 3-dB Psat. Instead of investigating the multi-channel amplification of phase-coded signals, this chapter is focused on the mixed modulation format multi-channel amplification, in particular the amplification of a 40 GBd DQPSK signal in presence of a 40 GBd OOK interfering channel. This configuration is even more challenging than the presence of another DQPSK amplification, because the cross-gain modulation (XGM) and cross-phase modulation (XPM) induced crosstalk should be significantly stronger for OOK modulated signals.

Basic D(Q)PSK Setup Modification

The basic D(Q)PSK setup sketched in Fig. 6.5 (page 109) is modified by the components shown in Fig. 6.10. The 40 GBd OOK transmitter is switched on. The generated DQPSK signal is booster amplified in "inline 1" and subsequently wavelength filtered using a 1.6 nm broad FBG in combination with a circulator.[8] The same circulator-FBG combination is used to combine the OOK signal with the DQPSK signal. Both signals are injected into the QD SOA with their polarization being aligned to the TE axis. Using a VOA in each signal path allows a variation of the QD SOA input power (P_{in}) independent for each signal. A TF with a FWHM of 2.5 nm in front of the receiver ("inline 2") separates the channel to be characterized and suppresses the other channel by more than 30 dB.

Experimental Results

The crosstalk of the DQPSK signal on the OOK signal is expected to be much smaller than the crosstalk induced by OOK neighboring channels. Hence, the OOK channel signal performance is only validated by eye measurements. Exemplary amplified

[8] Detailed information on this setup part can be found in the Appendix B.

OOK eye diagrams are shown in Fig. 6.11 exhibiting a Q^2-factor between 15.5 and 16.3 dB indicating an error-free (BER $< 10^{-9}$) detection.

The 40 GBd DQPSK signal has been detected using both, the differential and the coherent detection receiver. The measurements have been performed in BtB configuration and different combination of the signal input. All BER measurements and fits are listed in Appendix C. The P_{rec} penalties are evaluated with respect to the BtB measurement and are plotted in Fig. 6.12 versus the interfering OOK signal input power. Figure 6.13 depicts the measured constellation diagrams and EVM values obtained at the P_{rec} at which the differential detection receiver has achieved a BER of 10^{-9}.

For a DQPSK QD SOA input power (P_{in}) of -9 dBm, the penalty increases above 3 dB at a BER of 10^{-9} for interfering OOK input up to -10 dBm. In this configuration, the total QD SOA input power of -6.5 dBm is already 1.8 dB above the 3-dB saturation input power. In contrast, the single-channel DQPSK penalty remains below 1 dB with up to an input power level of 10 dBm (see Fig. 6.7, page 112). Hence, the OOK signal causes XGM and XPM induce distortion of the DQPSK signal. The corresponding constellation diagrams shown in Fig. 6.13 exhibit significant phase distortions. Hence, these distortions also lead to a strong increase of the EVM at the DQPSK input power of -9 dBm. Finally, at an OOK P_{in} of -5 dBm the penalty is

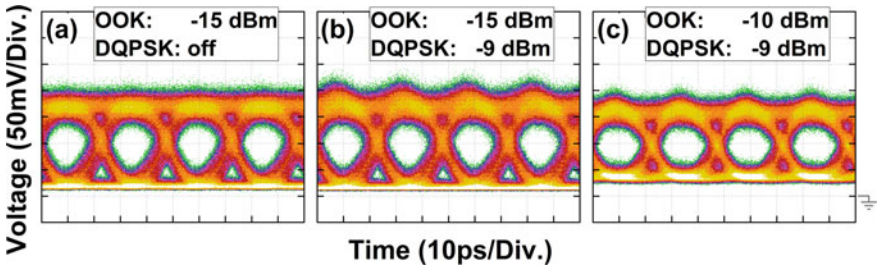

Fig. 6.11 Exemplary eye diagrams of the interfering 40 GBd OOK signal **a** in the absence as well as **b**, **c** in the presence of the 40 GBd DQPSK signal. The QD SOA input power levels are given in the figure. The Q^2-factor of the eye diagrams are between 15.5 and 16.3 dB indicating an error-free (BER $< 10^{-9}$) detection

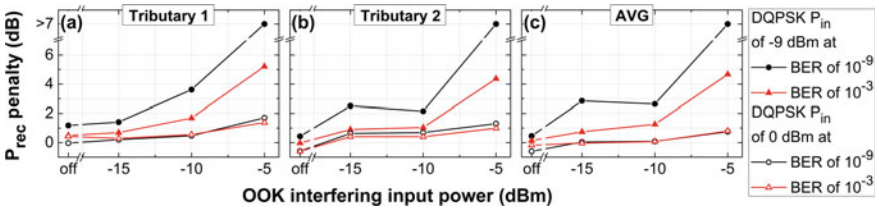

Fig. 6.12 Receiver input power (P_{rec}) penalty of the amplified 40 GBd DQPSK signal versus the interfering 40 GBd OOK signal input power (P_{in}) at a BER of 10^{-9} and 10^{-3} for **a** tributary 1, **b** tributary 2 and **c** the average of both. The DQPSK QD SOA P_{in} was set to -9 and 0 dBm

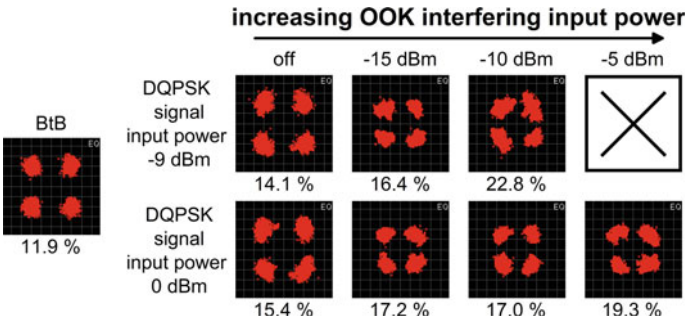

Fig. 6.13 Constellation diagrams and determined EVM values for the amplified 40 GBd DQPSK signal with a QD SOA input power of (*top row*) −9 dBm and (*bottom row*) 0 dBm, respectively. The interfering 40 GBd OOK signal input power increases from *left* to *right*. Constellation diagrams that could not been measured are crossed out

larger than 7 dB and the coherent detection receiver was not able to track the signal. Increasing the DQPSK P_{in} to 0 dBm the OOK induced penalty is below 1 dB up to an interfering OOK signal input power of −5 dBm. This configuration represents a total QD SOA input power of 1.2 dBm being nearly 10 dB above the 3-dB saturation input power. Similar to the penalty, the EVM increase is strongly reduced. But both, the penalty and the EVM slowly starts to rise when increasing the OOK P_{in} up to −5 dBm.

From the constellation diagram it can be deduces that interfering OOK input significantly lower than the DQPSK induce mainly phase distortions whereas comparable input also induce magnitude errors. The OOK signal amplification causes carrier density pulsation (CDP) resulting in a cross-phase modulation (XPM) and cross-gain modulation (XGM) of the DQPSK signal (see Sects. 2.3.2 and 3.6). The XGM and XPM intensity are determined by the carrier density within the reservoir, which is determined by the QD SOA drive current as well as the optical input. Operating the QD SOA below the total 3-dB saturation input power, XGM is negligible due to the ultra-fast QD gain recovery. In contrast, the CDP and carrier heating (CH) within the reservoir can cause phase changes resulting in a non-negligible XPM below the total 3-dB saturation input power.

In conclusion, the fast QD SOA gain dynamics enable the amplification of 40 GBd DQPSK in multi-channel configuration with 40 GBd OOK signals even in deep saturation as long as the OOK SOA input power level is significantly lower, e.g. by 3 dB, than the DQPSK input power level. Based on the experiences with multi-channel OOK amplification (e.g. [11]), this restriction could be cushioned by larger QD SOA drive currents leading to a reduced XGM caused crosstalk. This could enable DQPSK-OOK mixed multi-channel amplification with a QD SOA typical large input power dynamic range (IPDR). However, QD SOAs are very promising for multi-channel multi-format amplification up to the 3-dB saturation input power and even above.

6.3 Summary

This chapter evaluated the amplification of QD SOAs in terms of IPDR for amplitude and phase-coded modulation formats in single-channel and multi-channel configurations. For multi-channel configuration, the signal quality and particular the signal crosstalk in dependence of the QD SOA input power levels were discussed.

QD SOAs enabled error-free single-channel amplification of RZ OOK signals with a symbol rate of 80 GBd and a linear fiber-to-fiber gain up to 15.5 dB. The fast QD SOA gain dynamics enabled pattern-effect free amplification within a 2-dB penalty IPDR much larger than 18 dB, whereas the limits on both power sides were not reached and the largest tested QD SOA input power was already 6 dB above the 3-dB saturation input power of 0.1 dBm. The crosstalk of three interfering 40 GBd (40 Gb/s) NRZ OOK channels surrounding the 80 GBd (80 Gb/s) channel in a 5 nm grid was found to be minuscule for input power levels within the linear gain regime. For larger input power levels around and even above the 3-dB saturation input power, the crosstalk was increased but still an error-free performance is proved for per-channel input power levels up to −3 dBm (total power 3 dBm).

The fast QD SOA gain dynamics and particular the decoupling of gain and phase dynamics led to an excellent amplification of phase-coded signals, i.e. DPSK and DQPSK. The differential detection receiver and coherent detection receiver as well as different IPDR definitions were comprehensively discussed. Using both receiver types for characterization of the QD SOA IPDR enabled in-depth investigations of phase and amplitude effects as well as confirmed an error-free performance. For very small QD SOA input the signal quality is determined by the noise added by the QD SOA. In contrast, for QD SOA input significantly larger than the 3-dB saturation input power of −8.3 dB, the signal quality is determined by phase changes on a time scale longer than the symbol rate. However, single-channel error-free 2 dB receiver input power penalty and error-free EVM-based IPDRs are found to be larger than 28.8 dB (18.4 dB) and 36.7 dB (29.7 dB) for 40 GBd D(Q)PSK modulated signals, respectively. These values are significantly larger than previously published values for other QD or conventional SOAs [8, 12, 23] despite the significantly larger symbol rate of 40 GBd and linear fiber-to-fiber gain of 24 dB. The large IPDR is realized due to the low signal distortions even in very deep saturation represented by input of up to 17 dB above the saturation input power.

The fast QD SOA gain dynamics enables the amplification of a 40 GBd DQPSK signal even in the presence of a 40 GBd OOK neighboring channel. The error-free amplification of the DQPSK signal was demonstrated even in deep saturation as long as the OOK SOA input power level is lower, e.g. by 3 dB, than the DQPSK input power level. The crosstalk from the OOK channel on the DQPSK channel is caused by XGM and XPM. The power level restriction for both channels could be cushioned by larger QD SOA drive currents leading to a reduced XGM caused crosstalk. This could enable DQPSK-OOK mixed multi-channel amplification with a QD SOA typical large IPDR. Error-free amplification of the DQPSK signal was demonstrated for input power levels close to and above the total 3-dB saturation input

power in the presence of a 40 GBd OOK neighboring channel. Hence, QD SOAs are very promising for multi-channel multi-format amplification even in deep saturation.

In conclusion, QD SOAs enable the amplification of amplitude and phase-coded signals up to symbol rates of at least 80 GBd in single-channel and multi-channel configuration. The presented QD SOAs are well suitable for booster amplification due to their low-signal degradation at input power levels much larger than the 3-dB saturation input power. Due to their large gain, the investigated QD SOAs can be used as inline amplifiers or as pre-amplifiers used in low-cost receivers exhibiting a moderate sensitivity. Hence, QD SOAs are expected to be key components for future multi-wavelength channel multi-format-based all-optical reach-extended ANs and converged MANs.

References

1. L. Spiekman et al. “Semiconductor optical amplifiers for FTTx”. Int. Conf. on Transparent Optical Networks (ICTON). Vol. 2. 2007, Mo.D2.4
2. N. Suzuki, S. Yoshima, and J. Nakagawa. “Extended reach bidirectional optical amplified GE-PON with a high 46 dB span-budget for 64 far-end user ONUs”. Joint Int. Conf. on the Optical Internet (COIN) and Australian Conf. on Optical Fibre Technology (ACOFT). 2007, pp. 1–3
3. P.P. Iannone et al., Four extended-reach TDM PONs sharing a bidirectional hybrid CWDM amplifier. J. Lightwave Technol. **26**(1), 138–143 (2008)
4. P.P. Iannone et al. Bi-directionally amplified extended reach 40Gb/s CWDM-TDM PON with burst-mode upstream transmission. Optical Fiber Communication Conf. (OFC) and National Fiber Optic Engineers Conf. (NFOEC). 2011, PDPD6
5. H. Schmuck. Breitband-Zugangsnetze der nächsten Generation Verbundprojekt: CONDOR - Converged Heterogeneous Metro/Access Infrastructure (Project Report). 2013
6. K.C. Reichmann et al., “A symmetric-rate, extended-reach 40 Gb/s CWDM-TDMA PON with downstream and upstream SOA-Raman amplification”. J. Lightwave Technol. **30**(4), 479–485 (2012)
7. K. Taguchi et al. “40-km reach symmetric 40-Gbit/s λ-tunable WDM/TDM-PON using synchronized gain-clamping SOA”. Optical Fiber Communication Conf. (OFC) and National Fiber Optic Engineers Conf. (NFOEC). 2013, OW4D.6
8. R. Bonk. “Linear and nonlinear semiconductor optical amplifiers for next-generation optical networks”. Doctoral Thesis. Karlsruher Institut für Technologie, 2013, p. 278
9. ITU-T. ITU-T G.989.1 03/2013, series G: Transmission systems and media, digital systems and networks; Digital sections and digital line system - Optical line systems for local and access networks. 2013
10. R. Bonk et al. 1.3/1.5 μm QD-SOAs for WDM/TDM GPON with extended reach and large upstream/downstream dynamic range. Optical Fiber Communication Conf. (OFC) and National Fiber Optic Engineers Conf. (NFOEC). 2009, OWQ1
11. C. Schmidt-Langhorst et al. “80 Gb/s multi-wavelength booster amplification in an InGaAs/GaAs quantum-dot semiconductor optical amplifier”. European Conf. and Exhibition on Optical Communication (ECOC). 2010, Mo.1.F.6
12. T. Vallaitis et al., Quantum dot SOA input power dynamic range improvement for differential-phase encoded signals. Opt. Express **18**(6), 6270–6276 (2010)
13. R. Bonk et al., The input power dynamic range of a semiconductor optical amplifier and its relevance for access network applications. IEEE Photonics J. **3**(6), 1039–1053 (2011)
14. J. Leuthold et al. Linear and nonlinear semiconductor optical amplifiers. Optical Fiber Communication Conf. (OFC) and National Fiber Optic Engineers Conf. (NFOEC). 2010, OThI3

15. C. Meuer. “GaAs-based quantum-dot semiconductor optical amplifiers at 1.3 μm for all-optical networks”. Doctoral Thesis. Technical University of Berlin, 2011, p. 155
16. B.-H. Choi, S.S. Lee, Input power dynamic range analysis of SOA and EDFA link extenders on TDM-PON systems without burst effect control. Opt. Commun. **286**, 187–191 (2013)
17. C. Schmidt-Langhorst et al. Quantum-dot semiconductor optical booster amplifier with ultrafast gain recovery for pattern-effect free amplification of 80 Gb/s RZ-OOK data signals. European Conf. and Exhibition on Optical Communication (ECOC). Vienna, Austria, 2009, p. 6.2.1
18. M. Bayer, A. Forchel, Temperature dependence of the exciton homogeneous linewidth in In0.60Ga0.40As/GaAs self-assembled quantum dots. Phys. Rev. B **65**(4), 041308 (2002)
19. K. Matsuda et al., Homogeneous linewidth broadening in a In 0.5Ga 0.5As/GaAs single quantum dot at room temperature investigated using a highly sensitive near-field scanning optical microscope. Phys. Rev. B **63**(12), 121304 (2001)
20. R. Bonk et al. Single and multiple channel operation dynamics of linear quantum-dot semiconductor optical amplifier. European Conf. and Exhibition on Optical Communication (ECOC). 2008, Th.1.C.2
21. R.A. Shafik, S. Rahman, and R. Islam. On the extended relationships among EVM, BER and SNR as performance metrics. Int. Conf. on Electrical and Computer Engineering (ICECE). 2006, pp. 408–411
22. R. Schmogrow et al., Error vector magnitude as a performance measure for advanced modulation formats. IEEE Photonics Technol. Lett. **24**(1), 61–63 (2012)
23. R. Bonk et al., Linear semiconductor optical amplifiers for amplification of advanced modulation formats. Opt. Express **20**(9), 9657–9672 (2012)
24. S. Lange et al., Phase-transparent amplification of 16 QAM signals in a QD-SOA. IEEE Photonics Technol. Lett. **25**(24), 2486–2489 (2013)

Chapter 7
Concept of Dual-Band Amplifiers

The data up and down stream in current MANs and ANs are typically realized in two different optical communication bands to improve the network capacity and/or cushion the requirements, such as channel spacing. Approaches of future reach extended ANs and/or converged MANs are based on two communication bands. Hence, these approaches will require one conventional SOA per band. A reach extender could be implemented by wavelength splitter separating and combining the two bands with the amplifiers in-between as sketched in Fig. 7.1a.

Using a dual-band amplifier instead will considerably simplify the network architectures as sketched in Fig. 7.1b. Furthermore, the power budget will be increased as the losses of the network link are reduced, due to the lower number of required inline components. In addition, such amplifiers could allow a reduction of the energy consumption, because only one thermoelectric cooler (TEC) is required and the power consumption of a single device is presumable lower than pumping two individual devices. In total, such innovative dual-band amplifiers would reduce the overall investment and maintenance costs. Dual-band amplifiers have to provide the capability of simultaneously amplifying counter-propagating up-stream and down-stream data signals from different wavelength bands whereas each band carries multiple wavelength channels. As a proof of concept, this chapter will demonstrate the simultaneous amplification of two bidirectional amplitude-modulated signals with a spectral separation in the order of 100 nm.

In detail, this chapter is organized as follows:[1] First, Sect. 7.1 will introduce the concept for an ultra-broadband bidirectional dual-band QD SOA. The results presented in Chap. 6 as well as the fundamental device dynamics presented in Sect. 3.6 will be reviewed regarding the requirements for a dual-band QD SOA. Section 7.2 presents a first experimental proof of concept in 40 GBd OOK single-channel dual-band configuration. The IPDR of the bidirectional simultaneous signal amplification

[1] Parts of this chapter have been previously published in [1]. 1: Schmeckebier 2015.

H. Schmeckebier, *Quantum-Dot-Based Semiconductor Optical Amplifiers for O-Band Optical Communication*, Springer Theses,
DOI 10.1007/978-3-319-44275-4_7

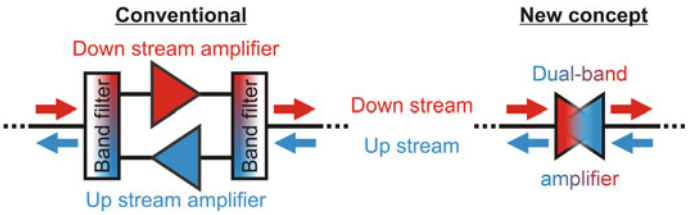

Fig. 7.1 Simplified sketch of a reach extender for up and down stream based on **a** conventional optical amplifiers and **b** a dual-band amplifier

is determined and discussed in dependence of the operating parameters. Finally, simulations of the experimentally obtained results are given in Sect. 7.3 based on a rate equation and traveling wave approach. The model allows to gain inside into the physical properties of the underlying complex carrier dynamics. In addition, the simulations allow a detailed scan of the operating parameters and hence an identification of the optimal operation conditions.

7.1 Concept of a Dual-Band QD SOA

The inhomogeneously broadened GS gain was used in Chap. 6 to prove the amplification performance in single- and multi-wavelength channel configurations for various modulation formats with symbol rates of up to 80 GBd. This represents amplification of signals within one band. In contrast, the dual-band QD SOA will use both, the QD GS and ES gain to amplify data signals representing now the up and down stream and thus the two bands. The results represent a conceptual study for a dual-band QD SOA. In a final device, the GS-ES energy distance matches two communication bands whereas the inhomogeneously broadened GS and ES gain will allow a multi-wavelength-channel amplification within both bands.

Similar to the multi-channel single-band amplification, the signals of one band act as interfering signals for the others. In worst case, crosstalk between intra- and inter-band channels will lead to signal degradation. The crosstalk between intra-band channels have been investigated in Chap. 6. The proof of concept of an ultra-broadband, bidirectional dual-band QD SOA will be performed exemplary for OOK modulated signals. This modulation format is expected to cause the largest possible inter-band crosstalk as demonstrated in Chap. 6. Two 40 GBd OOK signals with a wavelength spacing close to 100 nm represent the two bands.

Using both QD states simultaneously, the inter-state cross-gain modulation (XGM) and cross-phase modulation (XPM) will be the key issue for the dual-band QD SOAs concept. Fulfilling the demands of such a concept requires a deep understanding of the complex charge-carrier dynamics of the QD gain media in particular the coupling between the different classes of energy states. Parts of the interaction and dynamics have been addressed and investigated with various measurement techniques on time scales being relevant for optical communication as well as much

shorter ones in Sects. 2.3, 3.6 and Chap. 6. These explanations and results will be summed up in the following paragraphs and the remaining issues will be identified.

The dynamics of the QD gain media are determined by the charge-carrier dynamics of the different energy states and the external optical field. The amplitude- and/or phase-modulated optical field induces a dynamic change of the charge-carrier occupation of the different energy levels. The refilling of the states is determined by the carrier transitions between non-QD energy states and the QD states as well as by the transitions between the individual QD states, i.e. GS and ES. In this context, the term carrier reservoir defines commonly all higher energy states above the considered states. The energy states of the bulk matrix material and/or the QW surrounding the QDs as well as possible QD upper states serve as the reservoir for the QD ES. This reservoir serves similar together with the QD ES as an extended reservoir for the corresponding QD GS. In particular cases, the GS can also serve as a reservoir for the ES. However, this is commonly not the case under optical communication like conditions.

Single and multi-channel amplification experiments performed on the QD GS demonstrate a fast carrier refilling of the GS and thus a low channel crosstalk even in the nonlinear gain regime as long as the extended carrier reservoir is highly populated [1–4]. The XGM between wavelength channels addressing different groups of homogeneous broadened QD GS groups is mediated via the extended reservoir and can be negligible under these conditions. Based on pump-probe experiments and simulations [5, 6], similar results can be expected for multi-channel ES amplification. But to be correct, the XGM between different homogeneously broadened QD ES groups mediated via the reservoir could be increased as the ES-reservoir coupling is larger due to the lower energy separation. However, as long as the reservoir remains highly populated, XGM is negligible as well.

According to Sects. 2.3 and 3.6 the XPM in QD SOAs is dominated by the carrier reservoir but not by the QDs states. Hence, the XPM between the QD states is mediated via the reservoir and are thus comparable to XPM in single- and multi-channel single-band configuration like investigated in Sect. 3.6.

The remaining issue is the XGM between the states of the individual QDs. Investigations of the gain dynamics of the GS and ES under perturbation of the counter state discussed in Sects. 3.6.2 and 3.6.3 and e.g. [5, 7–9] suggest a low XGM for highly populated reservoirs. However, the experiments performed in the subsequent sections will deal with this remaining question using optical data signals.

7.2 Measurements

This section will presents the first experimental proof of concept of a bidirectional dual-band QD SOA using 40 GBd OOK signals in counter-propagating single-channel dual-band configuration. First, Sect. 7.2.1 introduces the experiential setup. Subsequently, Sects. 7.2.2 and 7.2.3 present the static gain and signal quality evaluation, respectively, in dependence of the operating conditions, i.e. QD SOA input power and drive current.

7.2.1 Setup

The setup used to demonstrate the dual-band amplification is built by five main units (see Fig. 7.2), the GS and ES transmitters and receivers as well as the dual-band amplifier.

The 40 GBd NRZ OOK GS data signal is generated by modulating the output of an ECL using a MZM. The ECL is emitting at a wavelength of 1305 nm. The MZM is driven by a 40 GBd OOK PRBS-7 generated by a 56 Gb/s BPG. The modulated GS signal is booster amplified using a PDFA to enable a large variation of the optical QD-SOA input power. Subsequently, a TF with a FWHM of 2 nm is used to suppress the ASE of the PDFA.

A QD Fabry-Pérot laser diode was used as the key component for the ES signal due to a lack of narrow linewidth laser sources for the ES wavelength of around 1210 nm. The QD laser emits at a wavelength of 1213.5 nm and has a spectral 3, 10 and 20 dB bandwidth of 5.5, 14.2 and 18.0 nm, respectively. The QD laser output is modulated with a second MZM driven by a 40 Gb/s OOK PRBS-7, which is generated by the identical BPG like for the GS signal.

Spectra of both signals are depicted in Fig. 7.3a. The spectral separation between the two signals is 91.5 nm representing the two different bands. The GS and ES signal are injected via CWDM filters in a counter propagating schema into the QD SOA whereas the polarization of both signals is aligned to the TE axis. The SOA input power can be adjusted using the VOAs before the CWDM filters. The path difference between the two signals was about 10 m in fiber from the modulator to

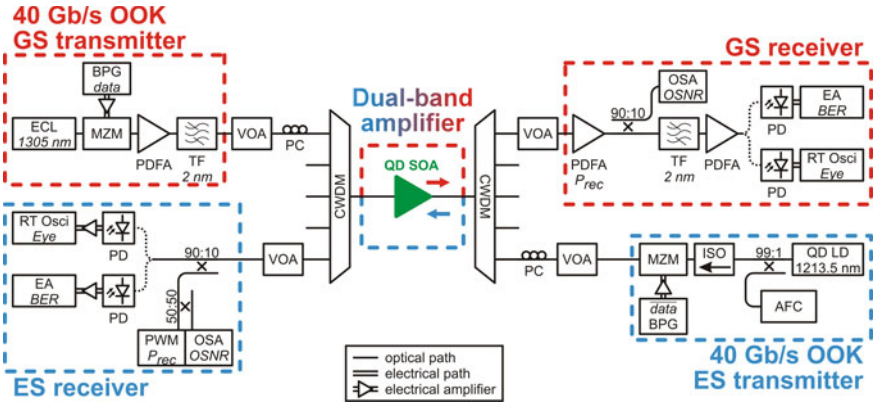

Fig. 7.2 Setup sketch for the dual-band amplification measurements. For the purpose of clarity, the BPG, EA and RT Osci are plotted twice in the sketch but they are actually identical. The BPG was used to modulate both transmitters simultaneously whereas the EA and RT Osci were used only in one of the receivers at a time. *BPG* bit-pattern generator, *CWDM* coarse-wavelength division multiplexing, *EA* error analyzer, *ECL* external cavity laser, *ISO* isolator, *LD* laser diode, *MZM* Mach-Zehnder modulator, *OSA* optical spectrum analyzer, *PC* polarization controller, *PD* photodiode, *PDFA* praseodymium-doped fiber amplifier, *PWM* power meter, *RT Osci* real-time oscilloscope, *TF* wavelength tunable filter, *VOA* variable optical attenuator

the input of the QD SOA. Thus, the two signals are decorrelated by several PRBS-7 lengths. The GS and ES output signals are separated by the CWDM filters from the counter propagating ES and GS input signals, respectively, and are detected by the corresponding receivers in dependence of the P_{rec} which can be varied by the VOAs in front of the receivers.

The GS receiver is set up in shot-noise-limited configuration and contains an optical pre-amplifier stage and a subsequent 50 GHz PD. The second PDFA is operating in a constant output power mode enabling a constant averaged optical power on the PD. 10 % of the first PDFA's output power is used to evaluate the OSNR using an OSA. A TF with a FWHM of 2 nm is used in-between the two amplifiers to suppress the ASE input into the second PDFA.

Due to a lack of appropriate optical amplifiers, the ES receiver is set-up in a direct detection configuration without optical pre-amplification. A 50 GHz PD and a subsequent electrical amplification is used.

In both receivers, the signal quality is evaluated with BER measurements using a 53.5 Gb/s EA as well as eye-diagram measurements using an 80 GSa/s RT Osci with an analog bandwidth of 32 GHz.

7.2.2 Device Under Test, ASE and Gain

The device under test is the 3 mm long QD SOA No. 3 (see p. 41). For further investigations of the bidirectional amplification three different operating regimes are identified by the ASE spectra (Fig. 7.3b). The ES ASE is unsaturated, close to saturation and saturated for a current of 400, 700 and 1000 mA, respectively. In contrast, the GS ASE is saturated for all three different currents. Due to device heating, the GS ASE peak power decreases and is red shifted by 0.035 nm/mA on average within this current range. In contrast, the ES ASE peak power first increased with increasing current from 400 to 700 mA and afterwards decreases similar to the GS ASE peak. On average, the ES peak is red shifted by about 0.026 nm/mA.

Figure 7.4 shows the GS gain characteristics for three different currents and for different interfering ES signal input power levels. The averaged linear GS fiber-to-fiber gain in the absence of the ES signal is given in Table 7.1. In the presence of the interfering ES signal the linear GS gain change for all currents is below ± 1.2 dB on average. For a low current of 400 mA the ES signal slightly decreases the GS gain whereas it increases the gain for the two larger currents (see Table 7.1). This behavior is identical for the interpolated ASE power level below the amplified GS signal (not shown here). Assuming an optical pumping of the QD ES for unsaturated currents would lead to the opposite behavior, meaning an increase of the GS gain with increasing interfering ES input power. In consequence, this effect is still under discussion. However, the GS gain experiences only a small influence of the interfering signal which is one requirement for the independent simultaneous amplification of the GS and ES signals.

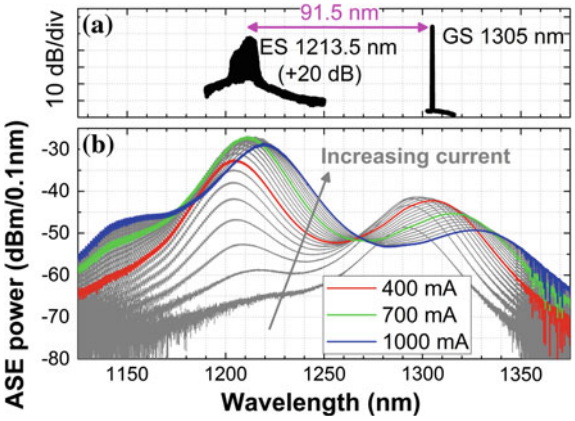

Fig. 7.3 **a** Optical spectra of the GS and ES signal. The ES signal is shifted by +20 dB in power. **b** Single-facet ASE spectra similar to Fig. 3.9 with three highlighted drive currents

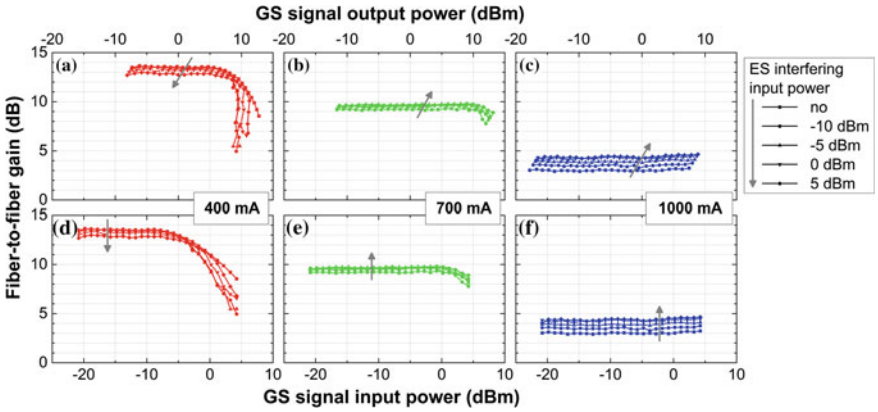

Fig. 7.4 Gain of the GS signal versus output power (*top row*) and input power (*bottom row*) for three different QD SOA currents. The gain is shown for different QD SOA input power levels of the interfering ES signal listed by the legend. The *arrow in each graph* shows the change of power according to the *arrow* in the legend. According to Sect. 3.3, the feedback fiber coupling setup losses are excluded

In opposite to the GS gain, the ES gain cannot be calculated using the definition introduced in Sect. 2.2, because the spectral bandwidth is too large. In consequence, the ES gain has to be calculated in a different way, which was developed for broadband signals. The details are discussed in "Appendix C". Figure 7.5 shows the ES gain characteristics ascertained for the three different currents and for different interfering GS signal input power levels. The averaged linear ES fiber-to-fiber gain in the absence of the GS signal is given in Table 7.1.

The influence of the GS signal on the gain behavior of the ES is more complex than vice versa. For a current of 400 mA the gain reduction caused by the interfering

Table 7.1 List of ASE, linear gain and saturation output power for the two different signals labeled with GS (1305 nm) and ES (1213.5 nm) for three different QD SOA drive currents

		Current (mA)		
		400	700	1000
ASE peak power level				
GS	(dBm/0.1 nm)	−42.2	−45.3	−49.3
ES	(dBm/0.1 nm)	−32.5	−27.0	−28.5
Difference	(dB)	9.7	18.4	20.7
Averaged linear noise figure w/o interfering signal				
GS	(dB)	8.6	9.1	10.4
ES	(dB)	10.4	10.2	10.1
Saturation input (output) power w/o interfering signal				
GS	(dBm)	0.7 (11.4)	Not reached	Not reached
ES	(dBm)	−7.4 (8.9)	−10.5 (12.3)	−5.7 (14.9)
Linear gain change under −10 to 0 dBm interfering input power				
GS	(dB)	−0.3	+0.4	+1.2
ES	(dB)	−9.6	−1.5	−1.2

The absolute ASE power levels depend on the resolution and are not corrected by setup losses. According to Sect. 3.3, the feedback fiber coupling setup losses are excluded for all values except the ASE related values. *w/o* without

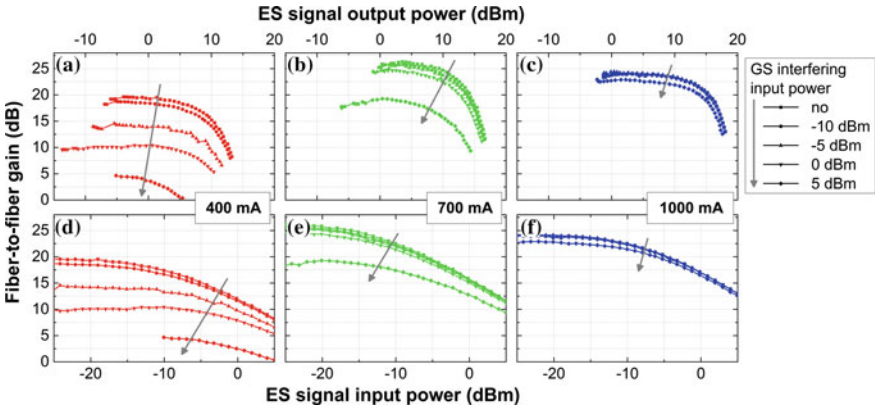

Fig. 7.5 Gain of the ES signal versus output power (*top row*) and input power (*bottom row*) for three different QD SOA currents. The gain is shown for different SOA input power levels of the interfering GS signal listed by the legend. The *arrow in each graph* shows the change of power according to the *arrow* in the legend. According to Sect. 3.3, the feedback fiber coupling setup losses are excluded. A failure of the QD SOA feedback fiber-coupling appeared for a current of 400 mA and an interfering GS input power of 5 dBm at low ES input power levels. The corresponding gain curve is therefore cut at ES input and output power levels below −10 and −5 dBm, respectively

GS signal exceeds 10 dB for the largest interfering input power level. Taking into account that:

– the ES ASE is unsaturated,
– the ES gain is influenced by the GS signal but not vice versa,
– the GS gain values are larger under perturbation of the ES than vice versa,

the effective GS carrier refilling from the carrier reservoir could expected to be more efficient than for the ES.

The ES gain performance is strongly improved for larger currents where the ES ASE emission is saturating as well. For a current of 700 mA the averaged linear gain reduction is small with values below 1.5 dB for interfering GS input power levels up to 0 dBm. Only at a very large interfering input power level of 5 dBm, again a gain drop of up to 7.5 dB is observed. Finally, at a current of 1000 mA, the ES gain is nearly independent of the interfering input signal demonstrated by a linear gain reduction of less than 1 dB for all GS input power levels. At these larger currents, especially at 1000 mA, the carrier reservoir is highly populated. This results in a very efficient simultaneous refilling of both states and is independent of the optical input power levels, which is also supported by the reduced GS gain.

However, taking into account XGM, saturation input and output power as well as the gain values (see Table 7.1), a current of about 700 mA is expected to be the most preferable drive current for the dual-band QD SOA.

7.2.3 40 GBd OOK Signal Amplification

The gain and cross-gain characteristics for continuous wave optical input signals have been presented and discussed in the previous paragraphs. Based on these results, different parameter combinations have been identified for the amplification of data signals in order to account for the dynamics of data signals. Figure 7.6 gives an overview of all combination of current, GS and ES input power levels tested for evaluating the quality of the amplified GS and ES 40 GBd OOK signals.

The GS signal is tested for all three currents (400, 700 and 1000 mA) and various GS input power levels from −15 up to 0 dBm in the absence of the interfering ES signal. No significant GS signal degradation is expected for low and moderate interfering ES input power levels, due to the small cross-gain effects of the interfering ES signal on the GS signal (see Table 7.1). Hence, only the largest available interfering ES input power of 0 dBm was used.

In contrast, a larger influence on the ES signal amplification is expected. Hence, a wider range of ES and GS input power levels are tested for the three currents, particularly for the unsaturated current of 400 mA. Tested parameter combinations resulting in closed eye diagrams are shown in addition in Fig. 7.6 to illustrate the limitations.

BER measurements have been performed in dependence of the P_{rec} without (BtB) and with the QD SOA. All measurements are listed in “Appendix C”. The BER curves

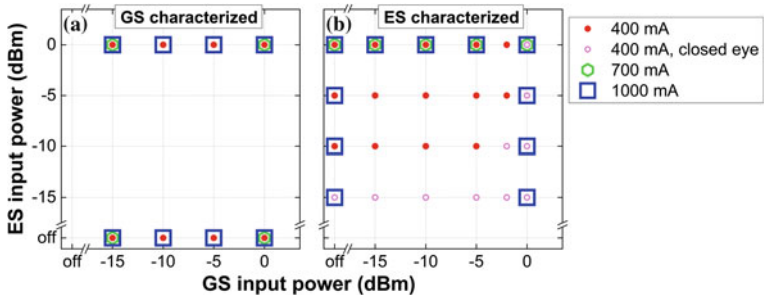

Fig. 7.6 Overview of 40 GBd OOK signal quality evaluation for the **a** GS signal and **b** ES signal, both with respect to the GS and ES signal input power levels

are analyzed in terms of P_{rec} penalty at a BER of 10^{-9} and 10^{-3} with respect to the corresponding BtB measurement. The BtB GS receiver input power required for a BER of 10^{-9} and 10^{-3} is found to be -26.7 and -33.8 dBm, respectively. The BtB ES receiver input power required for the same BERs are found to be -5.8 and -10.0 dBm, respectively.

40 GBd OOK GS Signal Quality Evaluation

The P_{rec} penalties for the GS signal are depicted in Fig. 7.7 with respect to the GS SOA P_{in} in the absence of an interfering signal. The penalty is nearly independent of the applied QD SOA current within the tested power range. A negligibly small P_{rec} penalty below 1 dB is found for both BER thresholds for all tested input power levels, except for the lowest input power of -15 dBm. Here, the penalty is slightly increased to about 1.5 dB at a BER of 10^{-9}. Exemplary eye diagrams are depicted in Fig. 7.8a, b showing minor pattern-effects for the largest tested GS input power of 0 dBm. However, for all characterized combinations of QD SOA input power levels and currents the penalty is well below 2 dB.

Figure 7.9 shows the penalties of the GS signal with respect to the QD SOA input power levels of the interfering ES signal. The results in the absence of the interfering signal are plotted at a x-axis value labeled with "off". The presence of the interfering

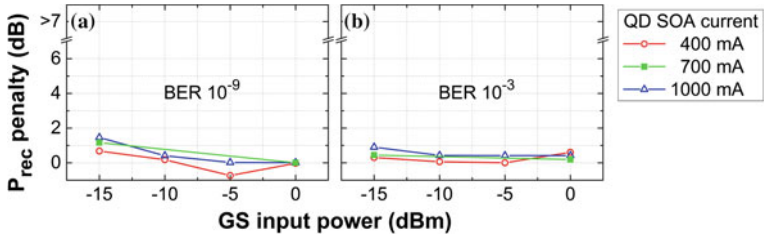

Fig. 7.7 Receiver input power P_{rec} penalty of the 40 GBd OOK GS signal at a BER of **a** 10^{-9} and **b** 10^{-3} in the absence of an interfering signal, both versus QD SOA input power levels of the GS signal and three different QD SOA currents

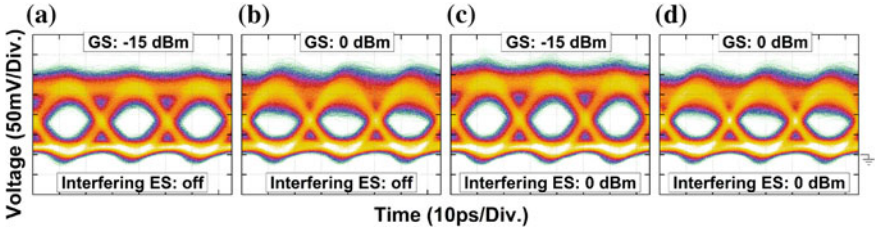

Fig. 7.8 Eye diagrams for the GS signal measured at a BER of 10^{-9} **a**, **b** in the absence and **c**, **d** in the presence of an interfering ES signal. The GS input power is **a**, **c** −15 dBm and **b**, **d** 0 dBm, respectively. The QD SOA current is set to 400 mA in all cases

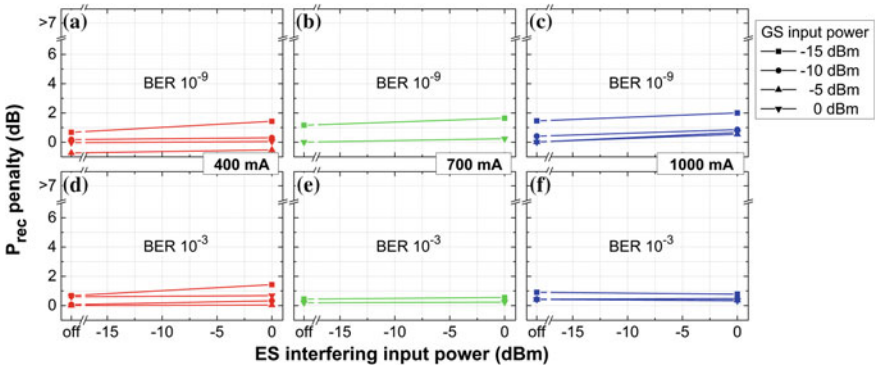

Fig. 7.9 Receiver input power P_{rec} penalty of the GS signal at a BER of **a**–**c** 10^{-9} and **d**–**f** 10^{-3}, all versus the QD SOA interfering ES input power. The QD SOA currents are **a**, **d** 400 mA, **b**, **e** 700 mA and **c**, **f** 1000 mA. The results in the absence of the interfering ES signal are plotted at a x-axis value labeled with "off"

ES signal leads at the most to a minor increase of the penalty by 0.7 dB at both BERs thresholds, despite the very large interfering input power of 0 dBm. Please note, that this power level is more than 5 dB above the ES 3-dB saturation input power (compare Table 7.1). Still, the GS penalty increase is small even for a small GS input power level of −15 dBm. Comparing the exemplary eye diagrams in the absence and presence of the interfering ES signal shown in Fig. 7.8, no additional signal degradation or patterning can be observed.

Hence, the GS penalty change in the presence of the ES signal is small and is in comparison to the BtB configuration below 2 dB for all tested configurations. This demonstrates a QD-SOA-based distortion-free amplification of the 40 GBd OOK GS signal nearly independent of the interfering ES signal, the investigated currents and the investigated GS input power levels.

40 GBd OOK ES Signal Quality Evaluation

The P_{rec} penalties for the ES signal are shown in Fig. 7.10 with respect to the ES SOA input power in the absence of an interfering GS signal. The penalties are negligible at

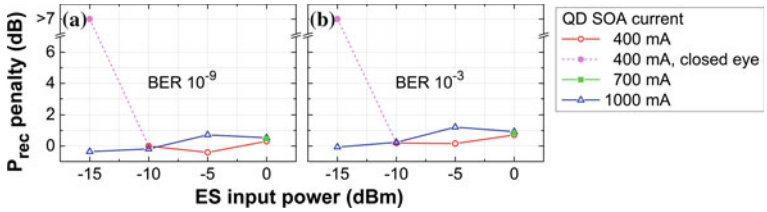

Fig. 7.10 Receiver input power P_{rec} penalty of the ES signal at a BER of **a** 10^{-9} and **b** 10^{-3} in the absence of an interfering signal, both versus the QD SOA input power of the ES signal and three different QD SOA currents. Measurements that could not been performed (*closed eye diagram*) are plotted at penalties labeled with ">7", and the connection to the measured penalties are dashed and the *color is brighter*. The characteristic of this connecting line is not valid and they are plotted to improve the readability as well as to symbolize the limit

a current of 400 mA and ES P_{in} from 0 down to −10 dBm. For an even smaller ES P_{in} of −15 dBm no BER measurements could been performed as mentioned above. This is probably caused by gain and noise limitations of the QD SOA at this unsaturated current in combination with the lack of an optical preamplifier for this wavelength resulting in a low ES receiver sensitivity. The QD SOA limitation is overcome at larger currents of e.g. 1000 mA where the penalties are minuscule for an input power of −15 dBm as well. The penalties are slightly lower for a BER of 10^{-9} than for a BER of 10^{-3}. But the differences are small and are within the error margin of the measurement method. The ES P_{in} of −5 and 0 dBm are much larger than the 3-dB saturation input power (see Table 7.1; Fig. 7.5) resulting in strong pattern effects at all currents exemplary shown by eye diagrams in Fig. 7.11c, d.

Figure 7.12 shows the penalties of the ES signal with respect to the QD SOA P_{in} of the interfering GS signal. Again, the penalties in the absence of the interfering signal are plotted at a x-axis value labeled with "off".

At a current of 400 mA, the ES P_{rec} penalty is strongly depending on the interfering GS P_{in} (see Fig. 7.12a, d). The penalty for low interfering input power levels of −15 and −10 dBm is comparable to the absence of the interfering signal. In contrast, the penalty is strongly increased for input power levels of −5 and −2 dBm. Furthermore,

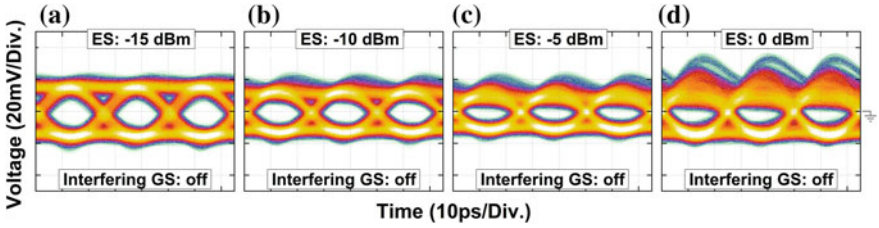

Fig. 7.11 Eye diagrams for the ES signal measured at a BER of 10^{-9} with an increasing input power from **a** −15 to 0 dBm in the absence of an interfering GS signal. The QD SOA current is set to 1000 mA in all cases

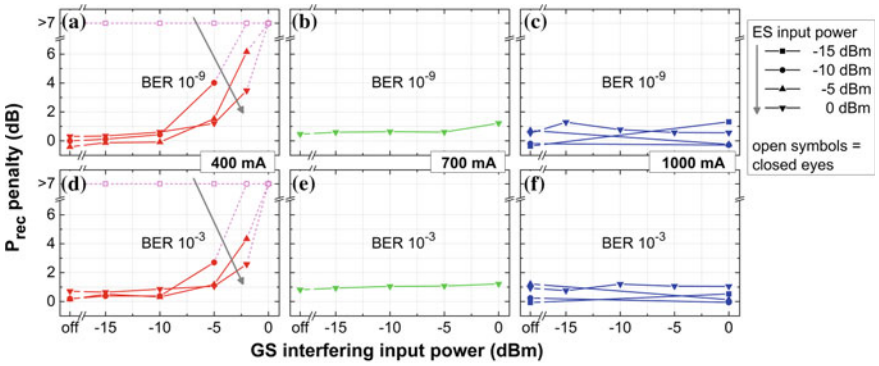

Fig. 7.12 Receiver input power P_{rec} penalty of the ES signal at a BER of **a–c** 10^{-9} and **d–f** 10^{-3}, all versus the QD SOA interfering GS input power. The QD SOA currents are **a**, **d** 400 mA, **b**, **e** 700 mA and **c**, **f** 1000 mA. Measurements that could not been performed (*closed eye diagram*) are plotted at penalties labeled with ">7", and the connection to the measured penalties are dashed and the color is brighter. The characteristic of this connecting line is not valid and they are plotted to improve the readability as well as to symbolize the limit

the penalties are strongly depending on the ES P_{in}. An increasing ES P_{in} reduces the penalty increase. The interfering GS signal induced penalty increase is larger at a BER of 10^{-9} than at a BER of 10^{-3}. However, no BER measurement could be conducted for an interfering GS input power of 0 dBm due to the large XGM visible by the strong patterning in the eye diagrams, see Fig. 7.13d. Hence, at 400 mA a simultaneous amplification of both signals is only feasible for low interfering input power levels up to −10 dBm.

This limitation is overcome with increasing current. At a current of 700 mA, the ES P_{rec} penalty is nearly independent of the interfering GS input power and a large ES input power of 0 dBm (Fig. 7.12b, e). This behavior is verified at a current of 1000 mA even for different ES input power levels from −15 up to 0 dBm (Fig. 7.12c, f). The largest observed penalty change is found at a BER of 10^{-9} and the combination of

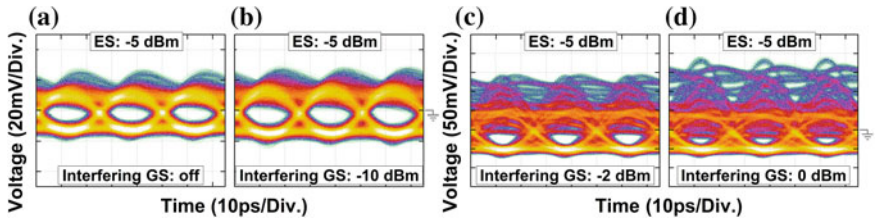

Fig. 7.13 Eye diagrams for the ES signal measured at a BER of 10^{-9} with an input power of −5 dBm. The QD SOA current is set to 400 mA. The interfering GS input power is increasing from (**a**) to (**d**). For an interfering input power of (**d**) 0 dBm no BER measurements could been conducted. Therefore, this eye diagram was at the largest available P_{rec}

lowest ES P_{in} of −15 dBm and largest interfering GS P_{in} of 0 dBm. This combination is the worst case scenario for the amplification, because the XGM probed by the ES is the possible strongest. But, still for this combination the P_{rec} penalty is below 1.4 dB.

The ES eye diagrams in the presence of an interfering GS input power of 0 dBm are comparable to the eye diagrams in the absence of the interfering signal at 1000 mA, shown in Fig. 7.11. Therefore, the 40 GBd OOK ES signal amplification is independent of the presence of an interfering GS signal as long as the QD SOA is driven with a current saturating the ES. The distortion-free amplification of the 40 GBd OOK ES signal is ensured up to ES input power levels of −5 dBm which is already larger than the 3-dB saturation input power.

Conclusion of Experimental Results
In summary, taking into account the current dependent gain performance as well as the large-signal quality evaluation of both signals, a QD SOA current of around 700 mA should be the optimum point of operation. For this current, the fiber-to-fiber gain of the GS and ES signal are about 10 and 26 dB, respectively. Especially the GS gain could be increased by a longer device and by an improved thermal electric cooling as discussed in Sect. 3.4. The signal quality evaluation demonstrates for both signals a P_{rec} penalty well below 2 dB independent of the respective interfering signal. In conclusion, the properties of the QD SOAs enable the distortion-free amplification of 40 GBd OOK signals with a spectral difference of more than 91 nm. This greatly proves the concept of a dual-band amplifier based on a QD SOA.

7.3 Simulation

The experimental results presented in the previous section are very promising. However, a detailed understanding of the underlying physics is mandatory to understand the origin of possible limitations. Hence, a numerical model was developed and implemented by Benjamin Lingnau in the framework of his dissertation at the Institute for Theoretical Physics at the Technische Universität Berlin [10]. His model reproduces the experimentally obtained results and allows excess to the complex carrier dynamics. In addition, the model allows a variation of the operating parameters in more detail and in a wide range which would be very time consuming for the experimental case.

First, the model will be briefly introduced in the Sect. 7.3.1, which closely follows the description in [10]. Subsequently, the Sects. 7.3.2 and 7.3.3 presents and discusses the modeled results.

7.3.1 Model Description

The QD SOA is described using a delay-differential-equation approach. The device with the length l is spatially discretized along the propagation axis into $Z+1$, $Z = 30$ points with a distance of $\Delta z := L/Z$. At the discretized point $z \in \{0, \ldots, Z\}$ the slowly varying forward $+$ and backward $-$ propagating electric field amplitudes are $E_{\pm}(z,t)$ with t: time. The propagating electric field amplitude for the QD GS and ES $E_{\pm}^{m}(z,t)$ with $m \in \{GS, ES\}$ are described by

$$E_{\pm}^{m}(z,t) = E_{\pm}^{m}(z \mp \Delta z, t - \Delta t) e^{\Delta t \, G^{m}(z,t)} + \eta_{\pm}^{m}(z,t), \tag{7.1}$$

with $\Delta t = \Delta z / v_g$: propagation time between two points with the group velocity v_g, $G^{m}(z,t)$: amplitude gain, $\eta_{\pm}^{m}(z,t)$: spontaneous emission source term. The amplitude gain and the spontaneous emission rate are determined from the active medium material equations introduced in Sect. 3.6.2. Thus, the charge-carrier dynamics is described by the microscopically calculated scattering rates whereas the field propagation is described by the delay-differential-equation. Taking into account the large current variation, the effective QW carrier reservoir losses r_{loss}^{w} are modeled here with a more sophisticated description by adding linear loss rates A^{S} to the bimolecular loss rates B^{S}.

$$r_{loss}^{w} = A^{S} \sqrt{w_e w_h} + B^{S} w_e w_h, \tag{7.2}$$

with w_e and w_h: electron and hole density in the reservoir. The active medium material equations are evaluated at each space discretization point. The total gain $g^{m}(z,t)$ for the GS and ES at a point z is then given by

$$g^{m}(z,t) = \Gamma \frac{h\nu}{\epsilon_{Bg}\epsilon_0} \frac{2N^{QD}}{h^{QW} v_m} \sum_{j} f(j) g_m^{j} \left(\rho_{e,m}^{j}(z,t) + \rho_{h,m}^{j}(z,t) - 1 \right), \tag{7.3}$$

with Γ: optical confinement factor which attributes to the number of QD layers, h: Planck constant, ν_m: optical wave frequency, ϵ_{Bg} or ϵ_0: background or vacuum permittivity, N^{QD}: QD density per layer, h^{QW}: QW layer thickness, v_m: degree of QD-state degeneracy, $f(j)$: contribution probability of the j-th QD subgroup, g_m^{j}: stimulated emission coefficient, $\rho_{e,m}^{j}$ and $\rho_{h,m}^{j}$: QD electron and hole occupation probability.

The resulting electric field amplitudes at point z therefore depend on the fields on the neighboring points on both sides and the spontaneous emission added at this point. The pure ASE output can be calculated by setting the device input electric field amplitudes to zero:

$$E_{+}^{m}(0,t) = 0 \quad \text{and} \quad E_{-}^{m}(L,t) = 0. \tag{7.4}$$

The measured ASE spectra (Fig. 7.3, p. 130) were fitted using the parameters A^{S}, B^{S}, w_e, w_h and the current dependent g_m^{j} to adjust the modeled device with the mea-

sured QD SOA. The experimentally observed wavelength red shift with increasing currents are attributed to Varshni-shift and energy band-gap renormalization. These are considered in the model by a current dependent lattice temperature. Additionally, a current dependence of the gain had to be implemented to address the ASE peak reduction correctly. Thus, the current dependent modeled gain is continuously rescaled from 100 % to finally 71 % at the largest applied current. No further measured characteristics like gain or signal quality evaluation have been used for adapting the model to the device.

The gain is calculated by replacing the input electric field condition in Eq. (7.4) by one or both following input signals assuming that the GS signal is injected at $z = 0$ and the ES signal is bidirectional injected at $z = L$.

$$\begin{aligned} E_{+}^{GS}(0,t) &= A_{in,GS}(t)e^{-i\nu^{GS}/2\pi t} \quad \text{and} \quad E_{+}^{ES}(0,t) = 0, \\ E_{-}^{ES}(l,t) &= A_{in,ES}(t)e^{-i\nu^{ES}/2\pi t} \quad \text{and} \quad E_{-}^{GS}(0,t) = 0, \end{aligned} \tag{7.5}$$

with $A_{in,GS}(t)$ and $A_{in,ES}(t)$: amplitude of the GS and ES input electric field. The amplitude $A_{in,m}(t)$ scales with the P_{in} into the device. In case of the data signal amplification, the amplitude is modulated with a 40 GBd NRZ OOK PRBS-7. The gain G^m is then calculated by

$$G^{GS}\left(P_{in}^{GS}\right) = \frac{|E_{+}(L,t)|^2}{|E_{+}(0,t)|^2} \quad \text{and} \quad G^{ES}\left(P_{in}^{ES}\right) = \frac{|E_{-}(0,t)|^2}{|E_{-}(L,t)|^2}. \tag{7.6}$$

In case of a data signal, the amplified GS and ES output signal quality is evaluate in terms of the optical Q-factor calculated by

$$Q := \frac{P_{mark} - P_{space}}{\Delta P_{mark} + \Delta P_{space}}, \tag{7.7}$$

with P_{mark} and P_{space}: optical power level of the mark and space level, ΔP_{mark} and ΔP_{space}: variance of the optical power level and the mark or space level. The Q-factor calculation is performed directly on the QD SOA output signals and hence the experimental occurring receiver characteristics like noise and bandwidth are neglected. The calculated Q-factor equals the experimental Q-factor in front of the receiver which is related to the P_{rec} for a given BER. Therefore, the modeled Q-factor is linked to the experimentally determined P_{rec} penalty. A reduction of the Q-factor due to a change of the QD SOA operating parameter corresponds to an increase of the P_{rec} penalty. The numerical algorithm slightly underestimates the Q-factor if the amplified data signal suffers from pattern effects.

A more detailed description and discussion of the model and its fitting to the measured device is given in [10].

7.3.2 ASE and Gain

The calculated current dependent ASE spectra are in excellent agreement with the measured ASE spectra for currents larger than 200 mA. The calculated GS and ES ASE peak follows the measured heating induced wavelength red shift with an accuracy well below 5 nm. The ASE peak power levels are reproduced with an accuracy better than 3 dB. Only the uninteresting measured shoulder at wavelengths below 1175 nm (see Fig. 7.3, p. 130) is not reproduced by the model as these optical transitions are not considered. This emission corresponds presumably to an QD upper state transition.

In opposite to the experiment, the modeled ES signal is a narrow bandwidth signal similar to the GS signal. Therefore, possible effects caused by the experimentally used broad bandwidth signal in comparison to a narrow bandwidth signal are neglected in the simulation. The data signal amplification is modeled by injecting the two counter propagating 40 GBd OOK signals into the model QD SOA, similar to the experiment. The calculated GS and ES fiber-to-fiber gain is plotted with respect to the input power levels of both signals in Figs. 7.14 and 7.15, respectively. The comparable measurements are shown in Figs. 7.4 and 7.5 (pp. 130, 131).

The modeled GS and ES gain are qualitatively in agreement with the measured gain values but a few deviation are observed, mainly for very large input power levels. The modeled GS and ES gain saturation occurs at lower input power levels. Increasing interfering ES input power levels reduce the modeled GS gain for all currents whereas the measured device shows a small increase at larger currents. At smaller currents, the modeled gain experiences a stronger reduction than the measured gain with increasing interfering input power levels, whereas both, the modeled and the measured gain, are nearly unaffected by the interfering input power at a current of 1000 mA. Hence, the gain behavior of both QD states is sufficiently reproduced by the model.

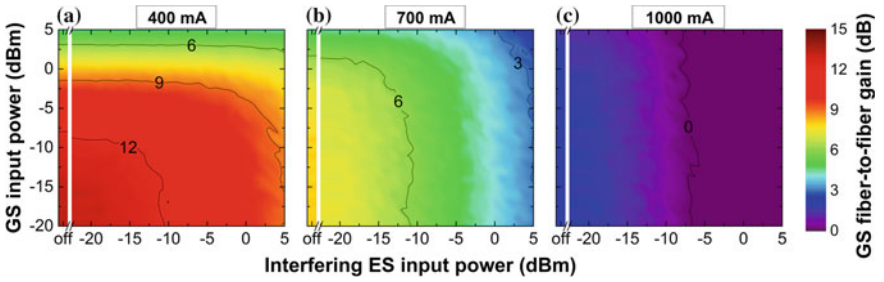

Fig. 7.14 Color coded gain of the GS signal versus GS and interfering ES input power for currents of **a** 400 mA, **b** 700 mA and **c** 1000 mA. Gain values smaller than 0 dB (effective loss due to coupling losses) have the same color code like 0 dB. The data are kindly provided by Benjamin Lingnau, Technische Universität Berlin

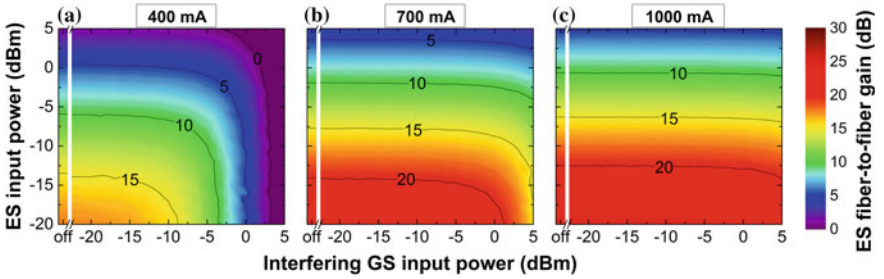

Fig. 7.15 Color coded gain of the ES signal versus ES and interfering GS input power for currents of **a** 400 mA, **b** 700 mA and **c** 1000 mA. Gain values smaller than 0 dB (effective loss due to coupling losses) have the same color code like 0 dB. The data are kindly provided by Benjamin Lingnau, Technische Universität Berlin

The strong influence of the interfering GS signal on the ES signal gain in contrast to the converse case can be explained by the intra-dot carrier scattering as well as the interaction of the QD states with the carrier reservoir as discussed in detail in the Sects. 3.6.2 and 3.6.3. According to [10], the ES signal amplification induced reduction of the QD ES occupation results only in a minor change of the quasi-equilibrium occupation of the QD GS. In contrast, an occupation reduction of the QD GS induces a considerable perturbation on the QD ES due to an increased intra-dot carrier scattering from the ES into the empty GS at a current of 400 mA. The reduced and finally abrogated perturbation with increasing current is caused by two effects. On the one hand, the reduced GS gain goes along with a decrease of the stimulated GS recombination resulting in a smaller intra-dot scattering rate. On the other hand, the reservoir carrier density is increased leading to more efficient refilling of the QD ES.

7.3.3 40 GBd OOK Signal Amplification

The modeled GS and ES Q-factors are depicted in Figs. 7.16 and 7.17, respectively, in dependence of the QD SOA operating conditions. As discussed above, the modeled Q-factors are linked to the experimentally determined P_{rec} penalties. A reduction of the Q-factor corresponds to an increase of the P_{rec} penalty. Therefore, the evolution of the modeled Q-factor and the experimentally determined penalty can be compared qualitatively.

The GS signal Q-factor is rather insensitive to variations of the GS input power, interfering ES input power and current demonstrated by a large area of Q-factor values larger than 10. GS input power levels beyond the experimental available 0 dBm lead to a slight reduction of the Q-factor at currents of 400 mA. Additionally, the combination of large interfering ES input power levels beyond −5 dBm—which is much larger than the 3-dB saturation input power (see Fig. 7.15)—and low GS

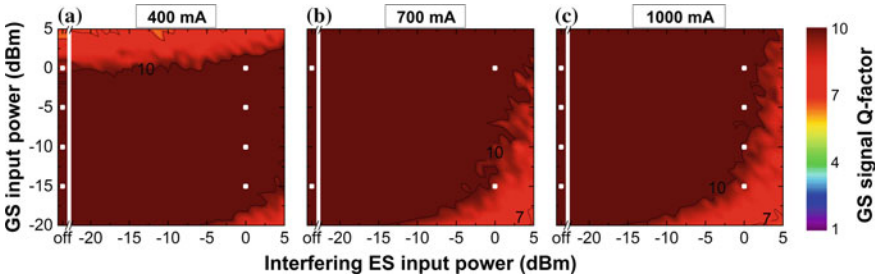

Fig. 7.16 Color coded Q-factor of the GS signal versus GS and interfering ES input power for currents of **a** 400 mA, **b** 700 mA and **c** 1000 mA. Q-factors larger than 10 have the same color code like 10. Experimentally investigated combinations of operating parameters are marked width with squares within the color plots. The data are kindly provided by Benjamin Lingnau, Technische Universität Berlin

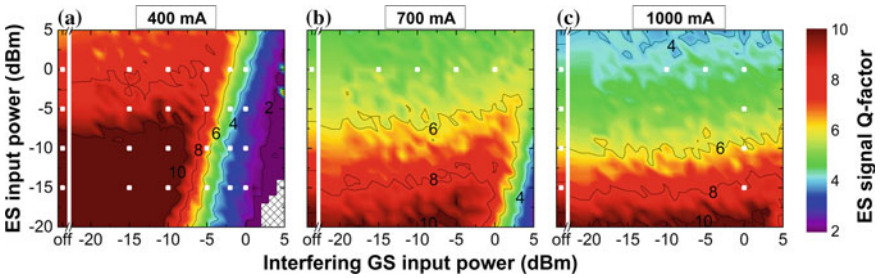

Fig. 7.17 Color coded Q-factor of the ES signal versus ES and interfering GS input power for currents of **a** 400 mA, **b** 700 mA and **c** 1000 mA. Q-factors larger than 10 have the same color code like 10. Experimentally investigated combinations of operating parameters are marked width with squares within the color plots. The data are kindly provided by Benjamin Lingnau, Technische Universität Berlin

signal input power levels leads to a Q-factor reduction below 10 at all currents. However, the modeled Q-factor is nearly completely independent of the operating parameter within the experimentally investigated area which matches very well to the experimental results of the P_{rec} penalty (see Figs. 7.7 and 7.9, pp. 133, 134).

The ES signal Q-factor depends strongly on the operating parameters. In contrast to the experimental results, the ES Q-factors are the largest for low ES input power levels (P_{in}) at a current of 400 mA (compare Figs. 7.10 and 7.17, pp. 135, 142). The measured P_{rec} penalty evaluation could not been performed for an ES input power level of −15 dBm because of an closed eye diagram even at the maximal available P_{rec}. The deviation between the calculated and measured results are caused by the neglected receiver characteristics in the calculation mentioned above. From the theoretical point of view a shot-noise limited detection like it was used in the GS receiver should allow the measurement for the low ES input power of −15 dBm and a current of 400 mA.

Beside this, the ES Q-factors show only small changes depending on the ES input power level for interfering GS input power levels up to −10 dBm. This performance is very similar to the experimental results, shown in Fig. 7.12a, d (p. 136). For even larger interfering GS input power levels, the Q-factor experiences a drop similar to the experimental P_{rec} penalty increase. Even the slight improvement with increasing ES input power for a given strong interfering GS input power is reproduced by the theory demonstrated by the slight improved Q-factor in vertical direction in Fig. 7.17. At larger currents of 700 and 1000 mA the modeled Q-factors show a lower performance with respect to increasing ES input power levels than for the unsaturated current of 400 mA. The reason for this is still under discussion. However, the modeled Q-factors show only a small dependence on the interfering GS input power similar to the experimental results.

In summary, the model qualitatively reproduces the measured gain values in terms of the dependence on the current and input power levels. The modeled Q-factors reproduce in most of the investigated cases the behavior of the experimentally investigated P_{rec} penalty. The model gave access to the complex carrier scattering processes within the device. Additionally, a much larger and more detailed range of GS and ES input power levels and currents were accessible by the models. As a result, the experimentally chosen current of 700 mA could be verified by the model has the optimum operating current taking into account the GS and ES gain and signal quality as well as the heating of the device. In addition, the model predicts input power levels of up to −7 and −13 dBm for the GS and ES signal as the optimum, respectively.

7.4 Summary

This chapter presented the concept of an ultra-broadband bidirectional dual-band amplifier using simultaneously the QD GS and ES for amplification. A large variation of the operating parameters, i.e. current and signal input power levels, have been tested experimentally and theoretically. The theoretical model allowed an analysis of the underlying carrier dynamics and thus the cross-gain effects. Additionally, a wider and more detailed scan of the parameters was assessable. An optimal current of 700 mA was identified at which both QD states are saturated exhibiting a linear fiber-to-fiber gain of the GS and ES signal of about 10 and 26 dB, respectively. As a the proof of concept, the distortion-free amplification of 40 GBd OOK signals with a spectral difference of more than 91 nm was demonstrated with a receiver input power penalty well below 2 dB for per-channel input power levels up to 0 dBm. Such an amplifier has the potential to drastically simplify the network architecture and reduce the power consumption resulting in reduced investment and maintenance costs of future reach extended ANs and converged MANs.

References

1. C. Schmidt-Langhorst et al., 80 Gb/s multi-wavelength booster amplification in an InGaAs/GaAs quantum-dot semiconductor optical amplifier, in *European Conference and Exhibition on Optical Communication (ECOC)*, 2010, Mo.1.F.6
2. H. Schmeckebier et al., Quantum dot semiconductor optical amplifiers at 1.3 μm for applications in all-optical communication networks. Semicond. Sci. Technol. **26**(1), 14009 (2011)
3. C. Meuer, GaAs-based quantum-dot semiconductor optical amplifiers at 1.3 μm for all-optical networks. Doctoral Thesis. Technical University of Berlin, 2011, p. 155
4. R. Bonk, Linear and nonlinear semiconductor optical amplifiers for next-generation optical networks. Doctoral Thesis. Karlsruher Institut für Technologie, 2013, p. 278
5. S. Schneider et al., Excited-state gain dynamics in InGaAs quantum-dot amplifiers. IEEE Photonics Technol. Lett. **17**(10), 2014–2016 (2005)
6. I. O'Driscoll et al., Phase dynamics of InAs/GaAs quantum dot semiconductor optical amplifiers. Appl. Phys. Lett. **91**(26), 263506 (2007)
7. Y. Kaptan et al., Gain dynamics of quantum dot devices for dual-state operation. Appl. Phys. Lett. **104**(26), 261108 (2014)
8. Y. Kaptan et al., Stability of quantum-dot excited-state laser emission under simultaneous ground-state perturbation. Appl. Phys. Lett. **105**(19), 191105 (2014)
9. A. Röhm, Dynamic scenarios in two-state quantum dot lasers. Master Thesis. Technische Universität Berlin, 2015
10. B. Lingnau, Nonlinear and nonequilibrium dynamics of quantum-dot optoelectronic devices. Doctoral Thesis. Technische Universität Berlin, 2015

Chapter 8
Signal Processing—Wavelength Conversion

A key functionality in future all-optical networks will be the processing of optical data signals, such as fast switching and wavelength conversion. The requirements for such nonlinear application components, particularly in future reach extended ANs and converged MANs, are cost efficiency, low power consumption and low footprint [1]. Performing signal processing in the optical domain rather than in the electrical domain has numerous advantages which are discussed in the following.

First, the optical signal has not to be converted into the electrical domain using a suitable receiver to allow electrical signal processing. This can be a large advantage particularly for inline-signal processing, because the processed signal has not to be reconverted again to the optical domain using a suitable transmitter. The electrical components are usually limited in terms of bandwidth and particular for advanced modulation formats the receiver and transmitter architecture is complicated and requires highly integrated components. In contrast, optical signal processing offers a significantly increased bandwidth, transparency to modulation formats and simple setups [2].

All-optical wavelength conversion (AOWC) in general describes the conversion of information from one wavelength to another wavelength. AOWC as the fundamental building block for optical signal processing, such as optical demultiplexing [3–5] and logical operations [6, 7], attracted great interest in the past decades. Beside these more advanced signal processing applications, AOWC can play an important role especially in large capacity, highly branched future reach extended ANs and converged MANs to avoid signal blocking issues as sketched in Fig. 8.1 [8–12]. The large density of multi-wavelength channel transmission in such networks in combination

H. Schmeckebier, *Quantum-Dot-Based Semiconductor Optical Amplifiers for O-Band Optical Communication*, Springer Theses,
DOI 10.1007/978-3-319-44275-4_8

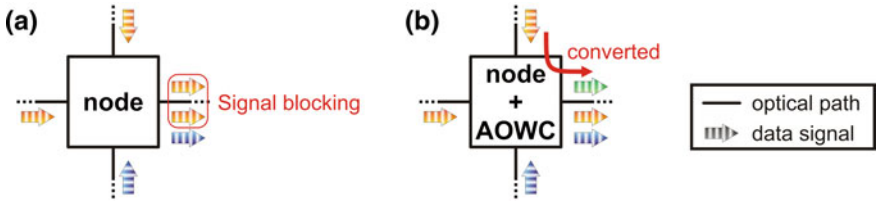

Fig. 8.1 Sketch of network node **a** without and **b** with all-optical wavelength conversion (AOWC) functionality for the case of two identical input wavelength channels (*left* and *top* signal). Signal blocking occurs at the node output without signal processing, because the two input signals with the same wavelength would overlap. In contrast, a node with AOWC functionality has the capability to convert the information of one of the interfering wavelength channels, e.g. the *top* signal, to a new wavelength channel. Redrawn after [2]

with the large number of users and network nodes could require reconfigurable optical networks nodes to increase the flexibility and capacity. In such configurations, the implementation of AOWC functionality into network nodes would allow a flexible conversion of the information between the wavelength channels.

Various schemes of AOWC have been developed and realized in the past decades [8, 13–17]. The vast majority of these schemes are based on the interaction of two or more signals in a nonlinear device, such as highly nonlinear fibers [15, 18–23], periodically poled lithium niobate [23–26], silicon waveguides [27–30], lasers [23, 31–34] and SOAs [13, 14, 16, 33, 35–38]. SOAs combine the properties of a small footprint, moderate to low optical input power requirements and positive conversion efficiencies due to the availability of gain as well as the capability of integration with other components.

This chapter[1] presents the performance of QD SOAs as wavelength converters based on the nonlinear four-wave mixing (FWM) in the gain material. Section 8.1 gives a brief overview of nonlinear effects in SOAs and discusses the advantages of FWM in comparison to other nonlinear effects. Subsequently, Sect. 8.2 gives an introduction to FWM in semiconductor gain material and defines the basic parameters and FWM schemes used in this chapter. Additionally, the advantages of QD gain materials will be addressed. Section 8.3 presents static FWM properties and their optimization for QD SOAs emitting within the O-band. QD-SOA-based large-signal wavelength conversion is presented and discussed for phase-coded signals, such as DPSK and DQPSK in Sect. 8.4. Finally, Sect. 8.5 summarizes the results.

[1] Parts of this chapter have been previously published in [1–8].
1: Bimberg 2010; 2: Meuer 2011a; 3: Meuer 2011b; 4: Meuer 2011d; 5: Bimberg 2011; 6: Schmeckebier 2011; 7: Schmeckebier 2012; 8: Zeghuzi 2015b.

8.1 Wavelength Conversion in SOAs

Three different nonlinear effects in semiconductor gain materials are commonly used for wavelength conversion, i.e. cross-gain modulation (XGM), cross-phase modulation (XPM) and FWM.

XGM is based on the gain saturation of the semiconductor gain material by an amplitude modulated pump signal and the resulting gain compression. The amplitude modulation of the data pump signal causes a modulation of the gain within a frequency bandwidth given by the carrier relaxation time constants of the gain media. The gain modulation can be probed by a weak continuous wave probe signal whose wavelength differs from the pump wavelength. The amplitude modulation of the pump signal is thus converted to the probe signal with an inverted bit logic.

As a change of the carrier density also changes the refractive index, XPM occurs simultaneously to XGM and vice versa [39]. Hence, XPM in SOAs can be used to transfer information from the amplitude modulated pump signals to the probe signal using a phase sensitive setup [8, 13, 14, 35, 38, 40].

XGM and XPM transfer the information from one SOA optical input signal to a second optical input signal. In contrast, FWM-based wavelength conversion generates new frequency components. The beating of two optical input signals in the semiconductor gain media generates a gain and index grating which is modulated with the frequency difference of the two input signals [41]. This beating induces the generation of new frequency components with a frequency shifted by the frequency difference with respect to the input signals as sketched in Fig. 8.2. The amplitude and/or phase modulation of the input signals is transferred to this new frequency components via modulation of the gain and index grating.

XGM, XPM and FWM have been investigated and compared in detail for various types of SOA gain material e.g. in [2, 8]. In devices with polarization independent gain, XGM and XPM offer the advantage of polarization insensitivity, large conversion range, and especially for XGM simple configurations. XGM-based wavelength conversion has been demonstrated in SOAs for OOK modulated signals up to 320 GBd [42–48]. However, the inability to convert phase-coded signals and the limited extinction ratio are drawbacks limiting the flexible use of this effect.

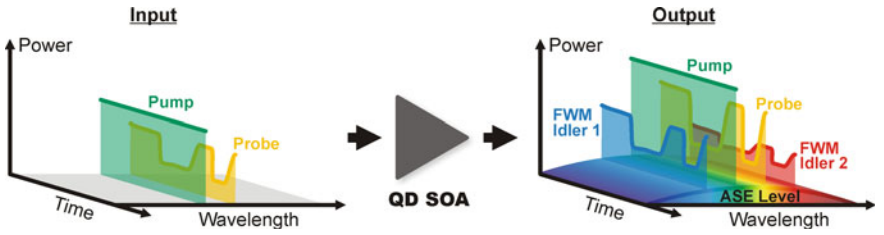

Fig. 8.2 Sketch of FWM-based wavelength conversion. New frequency components FWM idler 1 and 2 are generated due to the nonlinear interaction of the input pump and probe signal in the QD gain media. The modulation of the probe signal is transferred to both FWM idlers

FWM-based wavelength conversion offers a very large bandwidth, high extinction ratio, amplitude and phase sensitivity as well as a large conversion range if a multiple-pump configuration is used [2, 8, 49]. In addition, the spectrum and the spectral phase are inverted. FWM is a polarization sensitive process but this can be overcame by use of more sophisticated configurations demonstrated e.g. in [49–56]. The conversion efficiency and optical signal-to-noise ratio (OSNR) are often limited but can be also improved to positive conversion efficiencies and OSNR larger than 25 dB [49, 57–60]. FWM in bulk, QW and QD SOAs has been demonstrated with various modulation formats for data rates of up to 320 GBd [61–69]. FWM in semiconductor gain media can be used for applications, such as switching and demulitplexing [3–5, 13, 14], optical sampling [70], multi-channel wavelength conversion [71] as well as dispersion compensation via mid-span spectral inversion [54, 72].

In total, FWM-based AOWC offers the capability to convert amplitude- and phase-coded signals and is therefore of great importance for future flexible network designs.

This chapter concentrates on the FWM-based wavelength conversion in QD SOAs for phase-coded signals, i.e. DPSK and DQPSK. An investigation of similar samples with OOK modulated signals has been performed in [2, 73, 74].

8.2 Introduction to Four-Wave Mixing (FWM)

This section introduces the physics of FWM in semiconductor gain media and discusses the advantages of QD gain media. Subsequently, the basic parameters of FWM and two different FWM schemes are introduced.

8.2.1 Fundamentals of FWM in Semiconductors

FWM-based AOWC transfers the information from the probe signal to the target idler with a different wavelength. The idler results from the nonlinear interaction of the probe signal with an additionally injected pump signal in the semiconductor media. A brief semi-classical phenomenological description of the semiconductor-light interaction was given in Sect. 2.1.2. This section will follow up directly on Sect. 2.1.2 for a dielectric, non-magnetic, non-charged and isotropic semiconductor. For an improved readability, the dependency of the electric field and polarization field in terms of time t and space $\boldsymbol{r}$ will not be written in the following similar to Sect. 2.1.2. For the sake of simplicity, the fields are written in the following in scalar quantities. A complete description with field notation can be found e.g. in [75].

Injecting a pump and probe signal into the semiconductor, the superimposed electric field $\mathcal{E}$ is given by

$$\mathcal{E} = \mathcal{E}_{pump} + \mathcal{E}_{probe} \quad \text{with} \quad \mathcal{E}_x = \widetilde{E}_x exp(-i\omega_x t) + c.c, \tag{8.1}$$

with ω: light angular frequency, i: imaginary unit, c.c.: complex conjugate; [2, 75]. The response of the semiconductor to the electric field can be expressed by Eq. 2.8 (page 19). Assuming that the polarization only depends on the instantaneous value of the electric field amplitude and thus neglecting gain, loss and dispersion, the polarization can be Taylor expressed [75]:

$$\begin{aligned}\mathcal{P} &= \epsilon_0 \chi(\omega, \mathcal{E})\mathcal{E} \\ &=: \underbrace{\widetilde{\mathcal{P}}^{(1)}}_{=:\mathcal{P}_L} + \underbrace{\sum_{m=2} \widetilde{\mathcal{P}}^{(m)}}_{=:\mathcal{P}_{NL}}, \quad \text{with} \quad \widetilde{\mathcal{P}}^{(m)} = \epsilon_0 \chi^{(m)}(\omega)\mathcal{E}^m,\end{aligned} \tag{8.2}$$

with χ: susceptibility. In this notation, the polarization is often separated into the sum of a linear $\mathcal{P}_L$ and nonlinear $\mathcal{P}_{NL}$ contribution called m-th-order polarization [75, 76]. Accordingly, the susceptibility is separated into the linear susceptibility $\chi^{(1)}$ as well as m-th-order ($m > 1$) nonlinear susceptibilities $\chi^{(m)}$ whereas all orders do not depend on the electric field strength in this simplified contemplation. The second-order polarization $\mathcal{P}^{(m)}$ is responsible amongst others for SHG [75, 76] and is not considered here.

Inserting Eq. 8.1 into Eq. 8.2, the third-order polarization $\mathcal{P}^{(3)}$ can be expressed as the sum of polarization parts addressing different frequency components [75]:

$$\begin{aligned}\widetilde{\mathcal{P}}^{(3)} = &\underbrace{\mathcal{P}(\omega_{pump}) + \mathcal{P}(\omega_{probe})}_{\text{original frequencies}} + \underbrace{\mathcal{P}(3\omega_{pump}) + \mathcal{P}(3\omega_{probe})}_{\text{frequency triplication}} + \\ &\underbrace{\mathcal{P}(2\omega_{pump} + \omega_{probe}) + \mathcal{P}(2\omega_{probe} + \omega_{pump})}_{\text{sum-frequency}} + \\ &\underbrace{\mathcal{P}(2\omega_{pump} - \omega_{probe}) + \mathcal{P}(2\omega_{probe} - \omega_{pump})}_{\text{difference-frequency}}.\end{aligned} \tag{8.3}$$

Inserting this polarization term into the wave equation Eq. 2.7 (page 19), the complex solution for the electric field includes among the original frequency components various new frequency components. Frequency triplication and the sum-frequency components are not of interest here as the susceptibility $\chi(3)(\omega)$ strongly dependence on the frequency and thus the conversion efficiencies to these frequency components are low [2]. In contrast, the difference-frequency components are close to the pump and probe frequencies if the difference between these input frequencies is small. These components will represent the wavelength converted signals and are called here FWM[2] idlers. The output electric fields of these FWM components are given by [2, 75]:

[2] FWM in general is based on the interaction of three field generating a fourth frequency component. In case of a full degenerated FWM, all three frequency components are identical and thus the fourth frequency is. For a partly degenerated FWM used here for AOWC, two frequencies (usually the pump signal) are identical.

$$\mathcal{E}_{idler\,1} \propto \widetilde{E}^2_{pump}\widetilde{E}^*_{probe}exp(-i(2\omega_{pump} - \omega_{probe}t)),$$
$$\mathcal{E}_{idler\,2} \propto \widetilde{E}^2_{probe}\widetilde{E}^*_{pump}exp(-i(2\omega_{probe} - \omega_{pump}t)), \tag{8.4}$$

with $\widetilde{E}^*_x$: complex conjugation of $\widetilde{E}_x$. The electric field amplitude of the wavelength converted signal idler 1 thus depends linearly on the probe but quadratically on the pump amplitude. In contrast, amplitude of idler 2 depends linearly on the pump but quadratically on the probe amplitude. In most common configuration the probe signal carries the information and exhibit a smaller amplitude than the pump signal. Idler 1 is thus more intense than idler 2. Consequently, idler 1 is typically considered as the wavelength converted signal if not stated differently.

FWM in Semiconductors

So far, the above description is general and valid for all nonlinear media within the limitations listed above. However, in semiconductor gain media the carrier dynamics and the underlying processes determine the response of the gain media as described by the susceptibility. As introduced in Sect. 2.3, the carrier dynamics in semiconductor gain media are mainly determined by spectral hole burning (SHB), carrier density pulsation (CDP) and carrier heating (CH). FWM is thus mediated mainly by these processes for detuning up to a few THz [39]. For even larger detuning other processes like two photon absorption and the Kerr effect have to be taken into account [39]. However, the three dominating processes are typically considered to contribute independently to the partly degenerated FWM. Thus the third-order susceptibility $\chi^{(3)}$ can be expressed as a sum of the contribution of the individual processes [77–80]:

$$\chi^{(3)} = \chi^{(3)}_{SHB} + \chi^{(3)}_{CDP} + \chi^{(3)}_{CH}. \tag{8.5}$$

Based on Eq. 8.5, the optical output power of the partly degenerated FWM idler 1 can be derived with a simple model, which is valid within the following assumptions [78, 81]:

- Inverted gain media.
- Satisfied phase-matching.
- Single pass and co-propagating signals.
- Flat gain spectrum, i.e. the gain is constant across the entire spectral range considered by the pump, probe and FWM idlers.
- Short SOA, i.e. the SOA length does not influence the parameters.
- Unsaturated gain, i.e. input power levels are small with respect to the saturation input power levels.
- Weak idler intensities, i.e. the power level of the FWM idlers is weak with respect to the pump and probe power levels and thus doesn't change the properties of the gain media.

As a result, idler 1 is given by [81]:

$$P_{idler\,1} = \frac{1}{4}\, G_{probe}(G_{pump} - 1)^2 P_{in,\,pump}^2 P_{in,\,probe} \cdot \left| \sum_{m \in \{SHB,\,CDP,\,CH\}} \frac{1 - i\alpha_{H,\,m}}{P_{sat,\,m}} \widetilde{R}_m\,(\Delta\omega, \tau_m) \right|^2, \tag{8.6}$$

with $P_{Idler\,1}$: optical output power of FWM idler 1, G_x: unsaturated gain, $P_{in,\,x}$: optical input power of pump and probe signal, $P_{sat,\,m}$: saturation power level, i: complex unit, $\alpha_{H,\,m}$: α-factor or Henry factor or linewidth enhancement factor, $\widetilde{R}_m$: frequency response function, $\Delta\omega = \omega_{pump} - \omega_{probe}$: frequency detuning, and τ_m: time constant of the process as introduced in Sect. 2.1.2.

According to Eq. 8.6, the idler 1 output power goes cubically with the gain, quadratically with the pump input power and linearly with the probe input power but decreases with the frequency detuning of pump and probe signal. Additionally, the sign of the α-factor of the individual processes determine whether the corresponding third-order susceptibilities contributions are summed constructive or destructive.

The individual susceptibility components exhibit a different dependence on the frequency detuning. This dependence equals in the simplest case a low-pass characteristic like plotted e.g. in [82, 83]. Plotting the optical power of the FWM idler 1 with respect to the detuning allows an estimation of the time constants τ_m of the different processes, if the processes constructively interfere and if the time constant of the processes are significantly differ. This gives an independent access to the time constants in contrast to pump-probe-measurement-based evaluation e.g. discussed in Sect. 3.6. This was successfully demonstrated e.g. for the QD GS in [2, 84, 85] under various conditions.

Physically, the beating of the pump and probe signal within the gain media causes a modulation of the carrier density with the beating frequency $\Delta\omega$ [86]. This modulation generates a dynamic gain and index grating being responsible for the generation of new frequency components [41]. If the probe and/or pump signal carrier an amplitude or phase modulation, the grating is modulated similar and thus the generated FWM idlers.

Common experimental settings are beyond this simple model, i.e. the unsaturated gain condition. More sophisticated models including gain saturation and gain dispersion have been developed for more accurate FWM description [79, 81–83, 87]. These detailed models are beyond the scope of this thesis. However, the results of the simple model used here are sufficient to phenomenological describe the dependence of the FWM product.

FWM in Dependence of the Gain Material

Experimental and theoretical investigations demonstrated that conventional gain materials, such as bulk and QW, exhibit a strongly asymmetric FWM characteristic with respect to the sign of the frequency detuning $\Delta\omega$, e.g. [33, 58, 61, 77, 80, 82, 88–91]. At positive detuning $\Delta\omega > 0$ all three components of the third-order susceptibilities have the same sign and are summed constructively. At negative detun-

ing $\Delta\omega < 0$, the third-order susceptibilities of CDP and CH $\chi^{(3)}_{CDP} + \chi^{(3)}_{CH}$ interfere destructively with the third-order susceptibilities of SHB $\chi^{(3)}_{SHB}$ within the bandwidth of the SHB effect. Consequently, the FWM products are weaker in power for negative than for positive detuning, e.g. demonstrated in [77]. The large FWM asymmetry of QW gain materials can be reduced and the overall FWM efficiency can be improved by using strained QW as the active material [80]. However, the asymmetry remains large.

Gain materials with low or zero α-factor would allow a more symmetric FWM conversion with respect to the sign of the detuning. The lower α-factor of QD-based gain material with respect to bulk or QW gain material results in a more symmetric FWM conversion [59, 92–95]. Hence, the existence of a carrier reservoir enables the fast carrier dynamics and therefore a reduction of the influence of CDP. Additionally, the QD gain material exhibit a spectrally broader and improved conversion efficiency due to the fast time constants and broader gain spectra [59, 92, 94, 96–98].

For the sake of completeness, QD-based gain material emitting in the C-band has also found to exhibit large asymmetric FWM behavior e.g. [99]. The authors assumed a strong coupling between QD GS and the carrier reservoir, i.e. due to a tiny energy difference between the levels. Simulations in [93] showed a strong dependence of the FWM efficiency on the energy separation and number of states of the QD ES and reservoir. A small energy separation was identified by the authors to cause an increased carrier escape from the QD GS and thus reduces the conversion efficiency. Thus, not only the α-factor but also the inter-QD-state and QD-state-reservoir coupling plays an important role. However, the QD gain material used in [99] (C-band emission) differs from the QD gain material used in this thesis (O-band emission). The later exhibits a significant energy separation and thus a sufficient FWM conversion performance can be expected.

The FWM conversion for detuning larger than the homogenous linewidth of the QD states[3] has to be mediated via the carrier reservoir as tunneling between the QDs can be neglected [2]. The gain depletion of a specific QD sub-ensemble caused by the input pump and probe signal recovers via Auger scattering from the reservoir into the QD states. The reservoir carrier heating (CH) is modulated with the detuning frequency $\Delta\omega$ and thus the carrier capture into all QD sub-ensembles is modulated.

8.2.2 FWM Parameter Definition

The generation of FWM in active materials is characterized by two main parameters, i.e. the FWM conversion efficiency η and the signal-to-background ratio (SBR) [39]. Both depend on the input signal detuning. Figure 8.3 shows exemplary input and output spectrum measured for FWM generation in a QD SOA and sketches the parameters defined in the following. For the given detuning, the output spectrum

[3]The homogenous linewidth (FWHM) of the QDs at room temperature is around 10 meV corresponding to 14.0 nm at a wavelength of 1.32 µm [100, 101].

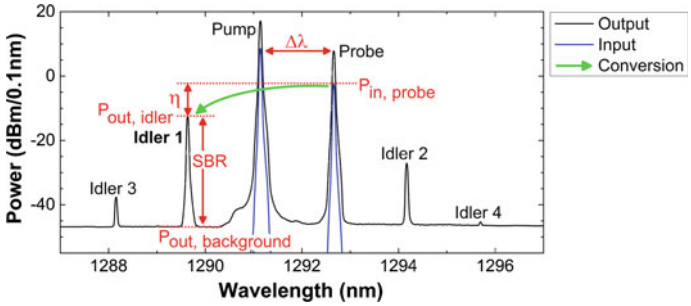

Fig. 8.3 Exemplary input and output spectra measured for FWM down-conversion in a QD SOA. The different signal peaks are labeled and the main parameters of FWM are sketched, i.e. detuning $\Delta\lambda$, conversion efficiency η and signal-to-background ratio (SBR). Detailed information are given in the text

shows four different FWM idlers. Idler 1 and idler 2 are generated by the mixing of pump and probe signal as described above. Idler 3 respectively idler 4 are generated by mixing pump and probe in addition with idler 1 respectively idler 2. Idler 1 is the strongest converted signal as already described above and will be solely considered in the following.

The frequency detuning is defined as the difference between the frequency of the pump signal and the probe signal $\Delta\omega = \omega_{pump} - \omega_{probe}$ [39]. The idler 1 is than generated at a frequency $\omega_{idler\ 1} = \omega_{pump} + \Delta f$. A positive and negative frequency detuning refers to a frequency up-conversion (towards larger frequency) and down-conversion (towards smaller frequency), respectively. Accordingly, the wavelength detuning can be defined as $\Delta\lambda = \lambda_{probe} - \lambda_{pump}$.[4] The idler 1 is than generated at a wavelength:

$$\lambda_{idler\ 1} = \frac{\lambda_{pump}\lambda_{probe}}{\lambda_{probe} + \Delta\lambda}, \tag{8.7}$$

which can be approximated by $\lambda_{idler\ 1} \approx \lambda_{pump} - \Delta\lambda$ for very small detuning ($\Delta\lambda \ll \lambda_{pump}$).

The FWM conversion efficiency η is defined as the ratio of the FWM-converted output power to the probe input power [39]:

$$\eta\,[\mathrm{dB}] = 10\ log_{10}\left(\frac{P_{out,\ idler}\ [\mathrm{mW}]}{P_{in,\ probe}\ [\mathrm{mW}]}\right). \tag{8.8}$$

[4]Please note, that the difference for the wavelength detuning is the opposite of the frequency detuning. Hence, a positive (negative) wavelength detuning refers similar to the positive (negative) frequency detuning to a frequency up-conversion (down-conversion) representing a wavelength down-conversion (up-conversion).

Please note that the probe input power and not output power is taken into account.[5] The noise performance of the converted idler is described by the signal-to-background ratio (SBR), which is given by [39]:

$$SBR\,[\mathrm{dB}] = 10\,log_{10}\left(\frac{P_{out,\,idler}\,[\mathrm{mW}]}{P_{out,\,background}\,[\mathrm{mW}]}\right). \tag{8.9}$$

Similar to the OSNR definition in Sect. 4.3, the power of the background noise $P_{out,\,background}$ has to be measured at the wavelength of the converted idler within a certain optical bandwidth [39]. The background noise power is interpolated similar to the ASE interpolation for the gain calculation described in Sect. 2.2.2, Fig. 2.5 (page 23).[6]

8.2.3 Wide-Range FWM Via Second Pump Signal

The spectral detuning range in which the single-pump FWM-based wavelength conversion exhibits a sufficient conversion efficiency is limited as will be presented in detail in the subsequent section. Typical, the FWM efficiency is reduced at least by 5–15 dB per 5 nm increase of the detuning. An improvement of the conversion range was demonstrated already in the past with the help of a second pump signal, e.g. [49, 64, 67, 103–107]. "Wide-range FWM" refers to the dual-pump scheme throughout this thesis.

The beating of the first pump and probe signal generates a gain and index grating modulated with $\Delta\omega$ via the modulation of the carrier distribution in the active material as described above. The additional injected second pump signal probes the phase and gain grating. Hence, additional FWM idlers are generated around the second pump with a frequency spacing of $\Delta\omega$ in the first order with respect to this second pump. Figure 8.4 shows exemplary input and output spectra measured for dual-pump FWM generation in a QD SOA. The FWM idler 1–4 are generated by pump 1 and probe (compare Fig. 8.3) whereas idler 2.1–2.4 are generated around pump 2. Similar to the single-pump scheme idler 2.1 is the strongest and will be considered in the following.

Please note, that the single-pump configuration (conversion of probe to idler 1) in Fig. 8.4 is set to down-conversion whereas the dual-pump configuration is up-converting (conversion of probe to idler 2.1). The spectral position of pump 2 can be changed independent of the single-pump configuration as long as idler 2.1 is not

[5] The output signal can experience positive or negative fiber-to-fiber gain strongly depending on the saturation degree of the gain media and the fiber-coupling losses. Using the probe output power instead of the input power could lead to an increase of the conversion efficiency by a large negative probe fiber-to-fiber gain (usually via increase of the pump and probe input power), whereas the idler output power remains constant or decreases more gently than the probe output power. This is often observed for FWM in DFB laser or Fabry-Pérot laser.

[6] According to [39, 102], the SBR does not equal the OSNR in general but for ASE dominated noise OSNR and SBR have a fixed relation.

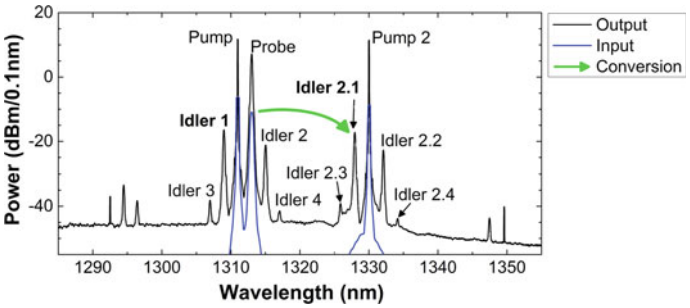

Fig. 8.4 Exemplary input and output spectra measured for dual-pump FWM up-conversion in a QD SOA. In additional to the FWM idler generated similar to the single-pump FWM configuration shown in Fig. 8.3 various new FWM idlers are generated around the second pump (pump 2). The weak group of peaks visible at both edges of the spectrum are generated by direct mixing of pump 2 and pump 1 as well as the probe

overlapping with one of the single-pump idlers. The dual pump-down conversion is realized here by placing pump 2 to a wavelength smaller than pump 1. The spectral position of idler 2.1 relative to pump 2 depends on the single-pump configuration. It will remain on the smaller wavelength side of pump 2 for down-conversion configuration of the single-pump configuration independent of the down- or up-conversion configuration of pump 2. The minimal conversion span in the dual-pump scheme is therefore typically slightly asymmetric per default for a given single-pump configuration. Opposite configurations of single- and dual-pump conversion[7] offer a slightly smaller minimal conversion distance than vice versa. However, at this small conversion distance, the single-pump conversion without the second pump would be preferable.

Finally, the output spectrum exhibits additional new peaks at both edges. These are generated by FWM of pump 2 and pump 1 as well as the probe signal. These components are weak as they represent a FWM in single-pump configuration with a large detuning. Therefore, these components will not be considered.

In summary, the dual-pump FWM scheme enables a wavelength tuning of the converted signal across a significantly larger span. In addition, the dual-pump FWM scheme allows also other applications like all-optical wavelength multicasting [23, 108]. A wavelength multicasting capable network node allows to transfer information from a single input wavelength channel to multiple output wavelength channels simultaneously. This signal processing functionality is realized by dual-pump FWM as multiple idlers a generated with a comparable output power, e.g. idler 2.1 and 2.2.

[7]This is for example the case if the single-pump configuration is set to down-conversion whereas the dual-pump configuration is set to up conversion like shown in Fig. 8.4. In this example, probe and pump 2 are on the same spectral side relative to pump 1.

8.3 Optimization of Static FWM

This section discusses the fiber-to-fiber FWM efficiency and SBR in QD SOAs in dependence of various parameters, such as detuning, spectral position relative to ASE peak, optical input power, gain via current and SOA length. In addition, the dual-pump efficiency and SBR are presented. The obtained results allow an optimization of the parameters for large-signal wavelength conversion presented in the subsequent section.

The polarization of the optical QD SOA input signals are adjusted to the TE axis in all subsequently presented configurations to ensure the maximal available gain.

8.3.1 Detuning Dependence

The FWM performance is characterized in single-pump configuration for 3 mm long QD SOA No. 2 (see page 40). The continuous wave pump wavelength is set to 1291 nm, which is close to the ASE peak emission for the tested current range whereas the continuous wave probe wavelength is scanned. The pump and probe input power level are set to 11 and 2 dBm, respectively. Figure 8.5 depicts the fiber-to-fiber FWM efficiency and the SBR in dependence of the pump-probe detuning for different QD SOA currents.

The converted idler 1 exceeds the noise floor within an detuning range of more than 50 nm for a current of 650 mA. The wavelength up-conversion (positive detuning) is less than 5 dB more efficient, i.e. very symmetric. Increasing the current towards and beyond the SOA gain saturating abrogates the asymmetry completely at large detuning. In addition, the larger current also increases the conversion efficiency in general. The maximum fiber-to-fiber efficiency is found to be −9 dB for a detuning of +0.5 nm and a current of 650 mA. This corresponds to a chip conversion efficiency of 0 dB chip considering coupling losses of 4.5 dB per taper.

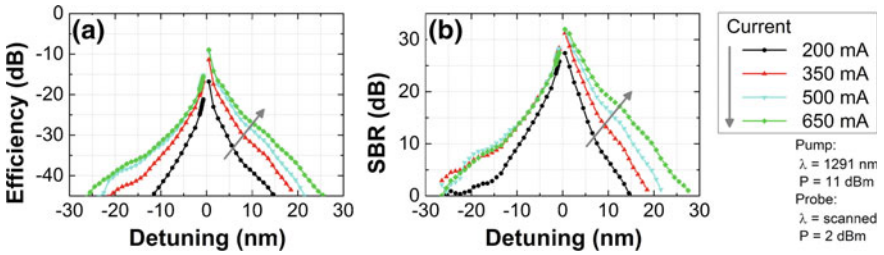

Fig. 8.5 FWM **a** fiber-to-fiber efficiency and **b** signal-to-background ratio (SBR) of FWM idler 1 as a function of the detuning for different QD SOA currents. The wavelength and in-fiber input power of pump and probe signal are given in the figure. Both figures share the same legend. The *arrow* shows the change of current according to the *arrow* in the legend

The SBR shows a slight asymmetric behavior similar to the efficiency. At a large operating current, the asymmetry also disappears at large detuning. A maximum SBR of 32 dB is found for a detuning of +0.5 nm and an operating current of 650 mA. For this current, the SBR exceeds 20 dB within an detuning range of 13.5 nm from −4.5 to +9 nm. The conversion efficiency is larger than −26 dB within this range.

Hence, the conversion efficiency and SBR in QD SOAs show a more symmetric performance for up and down-conversion consistence with e.g. [2, 49, 59, 92, 94, 109].

8.3.2 *Input Power Level Dependence*

The FWM conversion efficiency and SBR are shown in Fig. 8.6 in dependence of the in-fiber pump at different probe input power levels for a detuning of +1 nm and a QD SOA operating current of 650 mA.

Both, the efficiency and the SBR, follow the power increase first linearly and start to saturate at a power level of around 1 dBm. The efficiency is close to saturation and reaches a value of about −8.5 dB at a pump power of 11 dBm. Increasing the probe power by 10 dB results in an efficiency change of less than 1.5 dB whereas comparable saturation efficiencies are obtained. The probe power has thus only a small influence on the conversion efficiency. In contrast, the SBR is significantly increased by an averaged value of 4.8 and 4.4 dB if increasing the probe power in two steps by 5 dB.

In general, larger input power levels improve both, the conversion efficiency and SBR. For moderate and large input probe power levels of −3 and 2 dBm, the SBR exceeds 20 dB for pump input power levels larger than 3 and 0 dBm, respectively. Under these conditions, the conversion efficiency is larger than −15 and −21 dB, respectively.

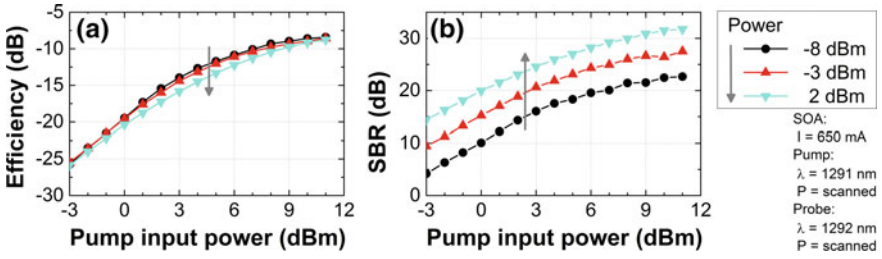

Fig. 8.6 FWM down-conversion **a** conversion efficiency and signal-to-background ratio (SBR) as a function of the in-fiber optical pump input power for three different in-fiber probe power levels. The pump and probe wavelength as well as SOA current are given in the figure. Both figures share the same legend. The *arrows* show the change of probe power according to the *arrow* in the legend

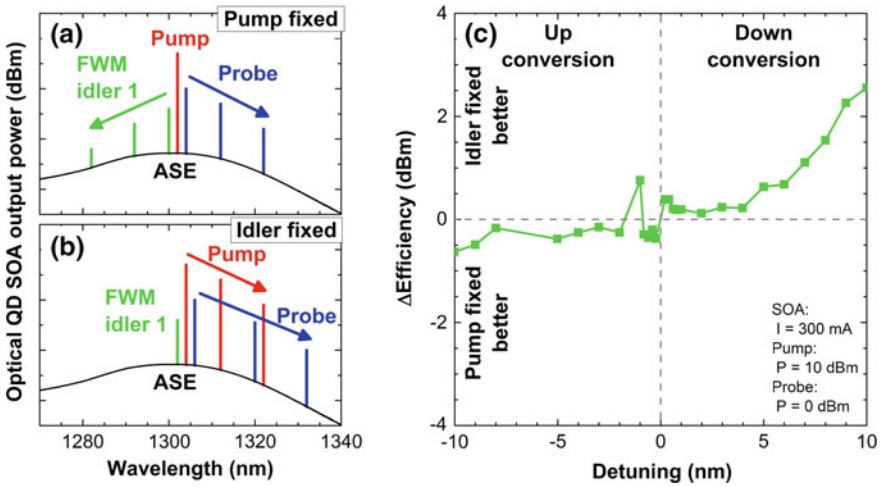

Fig. 8.7 Sketch of wavelength down-conversion for increasing detuning (*arrow* direction) with fixing **a** the pump wavelength and **b** the FWM idler 1 wavelength to the ASE peak wavelength. **c** FWM efficiency difference of both configurations

8.3.3 Dependence of Spectral Position Relative to ASE Peak

The FWM efficiency is characterized in Sect. 8.3.1 by centering the pump signal at the wavelength of the ASE peak and scanning the probe wavelength. With increasing detuning, FWM idler 1 is shifted towards spectral regions exhibiting lower gain as exemplary sketched in Fig. 8.7a for wavelength down-conversion. Instead of fixing the pump wavelength, the FWM idler could be fixed in wavelength to the ASE peak wavelength by scanning pump and probe wavelength as sketched in Fig. 8.7b. In this configuration, the FWM idler experiences a significantly larger gain but at the expense of shifting the probe wavelength forwards to spectral regions with even lower gain values (visible by the lower ASE in Fig. 8.7b).

The 3 mm long QD SOA No. 3 (see page 41) has been used to evaluate the FWM efficiency for both configuration. The SOA is driven with a current of 300 mA providing approximately the largest gain. The pump and probe in-fiber input power are 10 and 0 dBm, respectively. The FWM efficiency difference of both methods is presented in Fig. 8.7c.

Both methods show comparable performance for small detuning from −5 to 5 nm. The ASE and thus the gain are flat in this wavelength range, Hence, there is no difference between both methods. Increasing the detuning towards −10 nm indicates at least a slightly improved performance in case of the fixed pump configuration. In contrast, the fixed idler configuration exhibits an improvement of the down-conversion efficiency by 2.5 dB for a detuning of 10 nm. Hence, fixing the idler to the gain peak wavelength slightly improves the down-conversion efficiency at larger detuning.

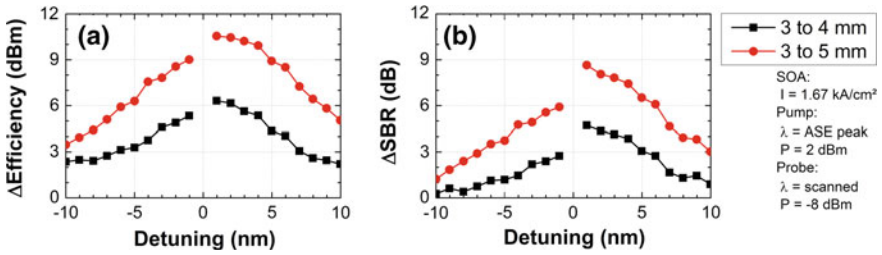

Fig. 8.8 FWM **a** efficiency and **b** signal-to-background ratio (SBR) improvement for increasing SOA length in dependence of the detuning. The wavelength and in-fiber input power of pump and probe signal as well as the SOA current density are given in the figure. Both figures share the same legend

8.3.4 QD SOA Length Dependence

The FWM conversion efficiency and SBR strongly depend on the QD SOA gain and thus the length of the SOA. The gain was discussed in dependence of the QD SOA length in Sect. 3.5.1 (page 55). Linear fiber-to-fiber gain values of 15.6, 23.3 and 26.6 dB were obtained for the 3, 4 and 5 mm long QD SOA No. 3, 4 and 5, respectively, all driven with a current density of 1.67 kA/cm^2. The improvement of the FWM efficiency and SBR with increasing SOA length are plotted in Fig. 8.8 in dependence of the detuning. The pump wavelength is positioned for each SOA to its ASE peak. The in-fiber pump and probe power levels are 2 and −8 dBm in all configurations. Hence, the SOAs with longer length are driven in deeper gain saturation due to the reduced saturation input power levels (compare Table 3.2, page 44).

The efficiency is increased at least by 2.2 and 3.5 dB within a 20 nm detuning range comparing the 3 mm long SOA with the 4 and 5 mm long SOA, respectively. The asymmetry of the up and down-conversion efficiency increases with increasing SOA length. A peak efficiency improvement of 10.5 dB is obtained with the 5 mm long SOA for a wavelength down-conversion of 2 nm (detuning +1 nm).

A slight increase of the SBR is obtained for large detuning probably due to the gain bandwidth narrowing caused by ASE self saturation of longer devices. However, the 5 mm long SOA offers an SBR improvement of more than 3 dB within a detuning range of 16.9 nm from −6.9 to +10 nm.

The FWM conversion efficiency and SBR significantly benefit from both, the larger gain and deeper saturation with increasing SOA length and for given input power levels. Hence, the 5 mm long SOA is most suitable for wavelength conversion with high efficiency and SBR.

8.3.5 Detuning Dependence for Dual-Pump Configuration

The detuning range in which the SBR exceeds 20 dB using the single-pump scheme is limited to about 15 nm (e.g. from −5 to +10 nm) depending on the QD SOA length and operating condition. Hence, the static wavelength conversion from probe to idler 1 is limited to less than −10 to +20 nm.[8] The conversion of modulated signals is often practical across an even smaller range due to additional required linear amplifiers and thus an further decrease of the SBR. The dual-pump scheme provides an extension of this range.

The FWM efficiency, SBR and peak power of the wide-range wavelength converted idler 2.1 (label see Fig. 8.4, page 155) is investigated for the 5 mm long QD SOA No. 5 (see page 42). The device under test is driven with a current of 900 mA. The pump 1 and probe wavelengths are set to 1311 and 1313 nm which are on the short wavelength side of the ASE peak obtained at 1319 nm. Positioning both signals at the ASE peak wavelength was prevented by the setup namely the number of suitable wavelength filters. The wavelength of pump 2 is scanned. The pump 1, pump 2 and probe input power levels are 15, 13 and 10 dBm, respectively.

Idler 2.1 is generated with a 2 nm detuning on the short wavelength side of pump 2 and follows its wavelength scan. Meanwhile, idler 1 remains at a 4 nm down-converted wavelength of 1309 nm since the wavelengths of pump 1 and probe are fixed. The FWM efficiency, SBR and peak power of idler 2.1 and idler 1 in dependence of the wavelength of idler 2.1 are depicted in Fig. 8.9. Additionally, the figure exhibits also a detuning equivalent $\overline{\Delta\lambda}$, which is defined based on the definition of the single-pump detuning $\Delta\lambda$ (Eq. 8.7, page 158) as follows:

$$\begin{aligned} \Delta\lambda &= \lambda_{probe} - \lambda_{pump\ 1} \approx \frac{\lambda_{probe} - \lambda_{idler\ 1}}{2}, \\ \overline{\Delta\lambda} &= \frac{\lambda_{probe} - \lambda_{idler\ 2.1}}{2}. \end{aligned} \tag{8.10}$$

The efficiency and SBR of idler 1 are nearly unaffected by the position of pump 2. Only at very small positive detuning, both values show a slight decrease possibly due to some cross-talk. This could be induced by direct interaction among the two pumps or the large number of additional FWM products and hence the reduced gain.

The idler 2.1 up and down-conversion efficiency is comparable for the smallest tested detuning equivalent of 5 nm. Both, the up and down-conversion efficiency, are reduced with increasing detuning equivalent but the up-conversion remains first more efficient than the down-conversion. This could be explained by the larger gain on the up-conversion side at smaller detuning indicated by the ASE peak wavelength at about 1319 nm. Both conversion efficiencies show only a difference of 2.5 dB for the largest tested detuning equivalent of ±15 nm. The idler 2.1 up and down conversion is thus much more symmetric than for idler 1 (compare e.g. Fig. 8.5) but

[8] Please note, that the conversion distance from probe to idler 1 is two times the detuning because the last is defined as the difference of probe to pump wavelength.

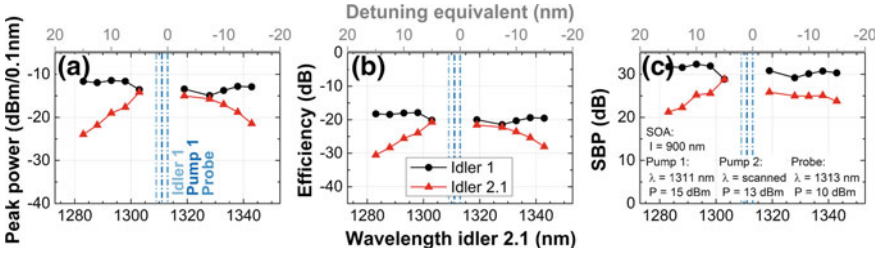

Fig. 8.9 FWM **a** peak power, **b** efficiency and **c** signal-to-background ratio (SBR) of idler 1 and idler 2.1 in dependence of the wavelength of idler 2.1. The fixed wavelength position of pump 1, probe and idler 1 are marked with the *vertical lines* (*dash-dot*) in the center of each graph. A detuning equivalent given by half the probe-idler 2.1 wavelength difference is plotted as the top x-axis in all three graphs to simplify the comparison to the single-pump detuning dependence e.g. shown in Fig. 8.5 (*note* the axis direction is inverted). All figures share the same legend

is not significantly improved for the down-conversion. In contrast, the idler 2.1 SBR is significantly improved for both, the up and down-conversion, and is in addition more symmetric than for idler 1. The SBR of idler 2.1 exceeds 20 dB in the entire detuning equivalent range of 30 nm (from −15 to +15 nm). The conversion efficiency exceeds −30 dB in nearly the entire detuning equivalent range. The converted idler 2.1 peak power exceed −30 dB (−24 dB) required for an error-free detection of D(Q)PSK using the differential detection receiver (see Table 6.1, page 114). Hence, the dual-pump scheme could enable a conversion in a wavelength range of up to 60 nm.

8.3.6 Conclusion

The conversion efficiency and SBR are optimized by large pump and probe input power levels, increase of gain and decrease of saturation input power levels e.g. by using longer QD SOAs as well as operating the QD SOAs at large currents. The single-pump wavelength conversion is preferable for short-range wavelength conversion within a detuning range of about 10 nm allowing a conversion within a range of 20 nm around the pump 1 wavelength. For even larger conversion distances across the entire spectral gain bandwidth, a dual-pump wavelength conversion is preferable. This enables an increased detuning range of about 30 nm corresponding to a conversion within a range of about 60 nm around the pump 1 wavelength.

8.4 Wavelength Conversion of Phase-Coded Signals

The static FWM was optimized in the previous section. Large-signal measurements have to be performed to demonstrate the suitability of QD SOAs as key component in

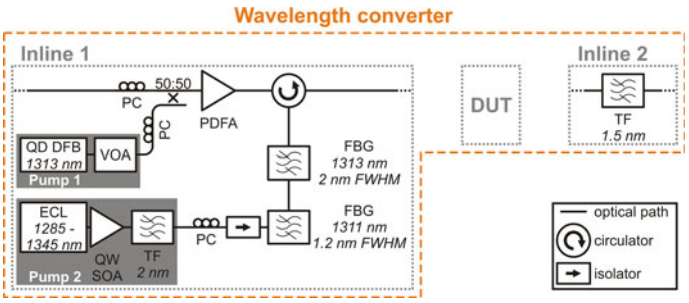

Fig. 8.10 Modification of the basic D(Q)PSK setup in Fig. 6.5 to investigation the QD SOA 40 GBd D(Q)PSK all-optical wavelength conversion. *ECL* external cavity laser, *DFB laser* distributed feedback laser, *FBG* fiber-Bragg grating, *PDFA* praseodymium-doped fiber amplifier, *PC* polarization controller, *QW SOA* quantum-well semiconductor optical amplifier, *TF* wavelength tunable filter, *VOA* variable optical attenuator

wavelength converters for all-optical networks. Using FWM in QD SOAs, sufficient wavelength conversion of high symbol rate OOK signals has been achieved in the past in amongst others also for devices comparable to the devices presented in this thesis e.g. in [2, 66, 73, 74]. However, future optical networks require modulation format transparent wavelength converters as these networks will use both, amplitude and phase-coded signals. The FWM-based wavelength conversion of phase-coded signals will require the generation of a sufficient fast phase grating similar to the fast gain grating used for OOK modulated signals. Up to now, the literature reports the conversion of up 40 GBd RZ-DPSK [110] and up to 25 GBd QPSK or DQPSK modulated signals using QD SOAs [68, 71, 111]. Hence, this chapter concentrates on the conversion of high symbol rate phase-coded signals, i.e. 40 GBd DPSK and DQPSK modulated signals.

Setup

The basic D(Q)PSK setup sketched in Fig. 6.5 (page 109) is modified by the components shown in Fig. 8.10. The D(Q)PSK transmitter generates a 40 GBd D(Q)PSK signal with a wavelength of 1311 nm.

The pump 1 signal is generated in "inline 1" by a QD DFB laser emitting at a wavelength of 1313 nm. The modulated signal and the pump 1 signal are combined with a 3-dB splitter and subsequently booster amplified using a praseodymium-doped fiber amplifier (PDFA). The output of the amplifier is wavelength filtered to suppress the ASE using a circulator and two cascaded reflective FBG,[9] one for each of the signals.

In case of wide-range wavelength conversion, the pump 2 signal is generated with an ECL, amplified using a QW SOA, and subsequently wavelength filtered to suppress the ASE of the amplifier. The pump 2 signal is combined with the pump 1 and probe signal using the circulator FBG cascade.

[9] See Appendix B for more details.

The device under test (DUT) follows "inline 1". All signals are injected into the device under test (DUT) with their polarization aligned to the TE axis. The QD SOA input power (P_{in}) can be adjusted for each signal using the VOA and the current of the PDFA and QW SOA. A TF following the DUT is used to separate the signal to be measured from the amplified input signals and the other generated FWM products. The blocked signals are suppressed by more than 30 dB with respect to the signal to be measured. The combination of "inline 1", DUT and "inline 2" represents the wavelength converted.

The 40 GBd D(Q)PSK signal is detected using the differential detection receiver only. A detection with the coherent detection receiver is not possible without changing the software EQ in case of the wavelength converted signal. Changing the EQ could mask signal changes caused by the QD SOA wavelength conversion. This is unwanted as the influence of the DUT is under investigation.[10] In addition, the performance of the available coherent detection receiver exhibits a stronger dependence on the wavelength than the differential detection receiver.

Device Under Test (DUT)
The DUT is the 5 mm long QD SOA No. 5 (see page 42). The SOA is driven with a current of 900 mA at the ASE peak appears at a wavelength of around 1319 nm. As described above, the pump 1 and probe signal are shifted to the smaller wavelength side of the ASE peak due to limitations of the setup. At a wavelength of 1310 nm, the linear fiber-to-fiber gain as well as a 3-dB saturation input and output power are approximately 21.5 dB and −3.6 dBm (14.9 dBm), respectively. The converted peak power, the conversion efficiency and the SBR were presented and discussed in Sect. 8.3.5.

8.4.1 Short-Range FWM

The 4 nm wavelength down-conversion of a 40 GBd D(Q)PSK signal is considered in the following in single-pump configuration, and thus in absence of the pump 2 signal. BER measurements are conducted in dependence of the receiver input power levels (P_{rec}) for the BtB configuration on the probe signal at a wavelength of 1313 nm and for the converted idler 1 at a wavelength of 1309 nm. The BtB configuration is given by bypassing the DUT whereas all other setup parts of the wavelength converter remain unchanged. The measured BER curves and fits are shown in Figs. 8.11 and 8.12 for DPSK and DQPSK modulated signals, respectively. The fitting procedure as well as the calculation of the averaged (AVG) DQPSK BER are explained in Appendix C.

The P_{rec} required for a BER of 10^{-9} are −30.4 dBm for the DPSK modulated signal. The wavelength converted signal shows a minuscule improved P_{rec} by −0.2 dB presumably caused by a marginal change of the receiver sensitivity at the 4 nm shifted

[10] See the description of the basic setup given in Sect. 6.2.1 for details about the software EQ.

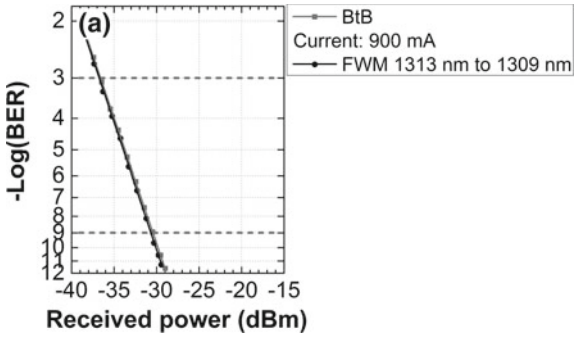

Fig. 8.11 40 GBd DPSK BER measurements versus receiver input power without (BtB) and with the QD-SOA-based wavelength converter operated in single-pump configuration. All BER curves are linearly fitted

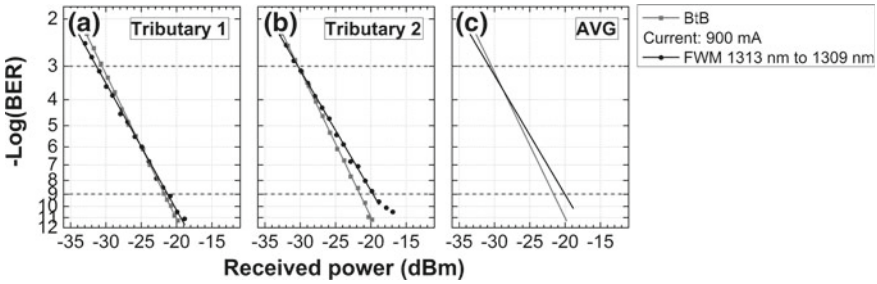

Fig. 8.12 40 GBd DQPSK BER measurements versus receiver input power without (BtB) and with the QD-SOA-based wavelength converter operated in single-pump configuration for **a** tributary 1 and **b** tributary 2. All BER curves are linearly fitted. **c** Averaged BER over both tributary

wavelength. Hence, the QD SOA enables a 4 nm wavelength down-conversion of a 40 GBd DPSK signal without any signal degradation.

The receiver requires a P_{rec} of -21.6 dBm to detect the DQPSK modulated signal with a BER of 10^{-9}. The wavelength converted signal shows a P_{rec} penalty of below 1.6 dB. This increase of the required P_{rec} is driven by tributary 2, whereas tributary 1 shows only a very small change. In addition, tributary 2 also exhibits an upcoming error-floor for a BER below 10^{-10}. However, the 40 GBd DQPSK signal can be converted by 4 nm from a wavelength of 1313–1309 nm with a P_{rec} penalty well below 2 dB.

8.4.2 Wide-Range FWM

The previous subsection presented wavelength conversion with a short distance of 4 nm. This section addresses the conversion across larger distances using the dual-

Table 8.1 List of modulation format dependent receiver input power P_{rec} of the differential detection receiver measured in BtB configuration for different wavelengths

	P_{rec} at 1288 nm BtB (dBm)	P_{rec} at 1313 nm BtB	P_{rec} at 1323 nm BtB (dBm)
DPSK			
BER 10^{-9}	−31.6	−30.4	−28.8
BER 10^{-3}	−37.7	−36.6	−34.8
DQPSK			
BER 10^{-9}	−23.6	−21.6	−21.2
BER 10^{-3}	−32.3	−30.4	−29.4

pump scheme. BER measurements of the 40 GBd D(Q)PSK are conducted in dependence of the receiver input power levels for the BtB configuration on the probe signal at a wavelength of 1313 nm and for the converted idler 2.1 at various wavelengths. The BtB configuration is given by bypassing the DUT, whereas all other setup parts of the wavelength converter remain unchanged.

System Characterization

In contrast to short-range FWM presented in the previous section, the wide-range wavelength conversion is accessible in a large spectral range of up to 60 nm using dual-pump FWM scheme. Hence, the strong wavelength dependence of the setup, i.e. the transmitter and receiver, has to be taken into account. BtB measurements show only the wavelength dependence of the coupled transmitter-receiver system but not the dependence of the individual parts. The latter would be required because the wavelength converter naturally leads to different wavelength of receiver and transmitter. Hence, one cannot distinguish between penalty changes caused by the wavelength converter and the system.

Typically, the receiver, in particular the optical amplifiers of the receiver, has a significantly stronger wavelength dependence than the transmitter. However, the transmitter used in this thesis is based on a DD MZM which was designed for the C-band and thus shows a larger dependence on the wavelength in the O-band, i.e. the extinction ratio. A valid discussion of phase distortion of the signal possibly caused by the wavelength converter is thus perhaps not feasible. However, to get an idea of the wavelength dependence of the system, two other BtB configurations are recorded by changing the probe wavelength to 1288 and 1323 nm, respectively. In this case, the circulator in the wavelength converter is bypassed[11] and a TF is used instead.

All BER measurements and fits are listed in Appendix C. The determined BtB P_{rec} required for a BER threshold of 10^{-9} and 10^{-3} are listed in Table 8.1 for the different BtB wavelength configurations. The fitted wavelength converted BER curves are analyzed in terms of P_{rec} penalty at a BERs of 10^{-9} and 10^{-3} with respect to the

[11] The bypassing is required because the FBGs would not reflect the signal. Hence, the probe signal would not reach the receiver.

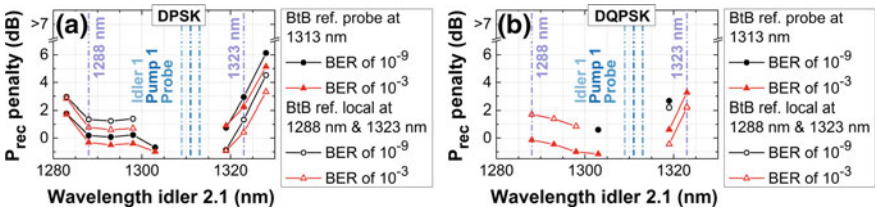

Fig. 8.13 Receiver input power P_{rec} penalty versus the wavelength of the converted idler 2.1 for **a** the DPSK and **b** the 40 GBd DQPSK modulated signal. The P_{rec} penalty is evaluated with the probe BtB measurement (wavelength at 1313 nm) as a reference across the entire converted wavelength span at BERs of 10^{-9} and 10^{-3} (*closed symbols*). In addition, the P_{rec} penalty is also evaluated for the short and long wavelength region using the 1288 and 1313 nm BtB measurement as a reference, respectively (*open symbols*). The fixed wavelength position of pump 1, probe and idler 1 as well as the alternative BtB signals are marked with the *vertical lines* (*dash-dot*)

BtB measurement. Figure 8.13 depicts the obtained penalties for 40 GBd D(Q)PSK wavelength conversion in dependence of the wavelength of idler 2.1.

40 GBd DPSK Modulated Signal

An error-free 40 GBd DPSK wavelength conversion is obtained within a wavelength range of 45 nm ranging from 1283 to 1328 nm. A conversion up to a wavelength of 1343 nm as demonstrated for the static wavelength conversion (see Fig. 8.9, page 160) is limited by the wavelength dependent receiver sensitivity due to the gain bandwidth of the optical amplifiers.[12]

The penalties for the wavelength down-converted signal obtained at a BER of 10^{-9} range from −0.6 to +1.8 dB if using the 1313 nm BtB measurement as the reference. In contrast, the penalties for the wavelength up-converted signal ranges from +0.8 to +6.1 dB. Using the references localized within the corresponding wavelength range, the penalties are increased by 1.2 dB and decreased by 1.6 dB for the down and up-conversion, respectively. Hence, the strong wavelength dependence of the transmitter-receiver system, particular the sensitivity of the receiver are large wavelength, presumably limit the conversion range and performance.

However, the 40 GBd DPSK wavelength conversion is achieved within a range of 40 nm (1283–1323 nm) with a penalty below 3 dB for both evaluated BER levels of 10^{-9} and of 10^{-3}. This range is extended to 45 nm with a lower restriction to the penalty requirements. The receiver sensitivity limits this range on the large wavelength side representing the wavelength up-conversion.

Using the 3-mm long QD SOA No. 2, the 40 GBd DPSK wide-range wavelength conversion was reported in [67, 112] within a range of 45 nm. The conversion of QD SOA No. 2 benefits from the use of a broadband receiver amplifier. Comparing the performance of QD SOA No. 2 and 5, both allow a conversion within a range of 45 nm whereas QD SOA No. 5 offers an improved idler 2.1 peak power

[12]The PDFA used within the receiver exhibit a gain reduction of 8 dB if increasing the wavelength from 1310 to 1320 nm (see Fig. 3.15). The shape of the ASE predicts an even larger gain reduction for changing the wavelength from 1320 nm towards 1340 nm.

(compare Fig. 8.9 on page 160 with [67, 112]). Based on the static FWM performance, in particular the peak power and SBR shown in Fig. 8.9a, c (page 160), and the down-conversion performance of the modulated signal (see Fig. 8.13 wavelength range 1280–1305 nm), an error-free conversion performance within the entire static conversion range of 60 nm seems to be feasible using a receiver with an improved spectral bandwidth. Especially, the wide-range conversion could be symmetric for up-and down conversion allowing to up or down-convert DPSK signals by 30 nm and more.

40 GBd DQPSK Modulated Signal

The detection of the converted 40 GBd DQPSK signal suffers from the similar receiver sensitivity problem as described above for the DPSK signal. But the consequence for the DQPSK signal is even worse as the receiver input power budget is significantly smaller than for the DPSK signal. However, an error-free BER of 10^{-9} can be reached for wavelength up and down-conversion to 1319 and 1303 nm, respectively, only limited by the available receiver input power. The penalties are below 3 dB.

The 40 GBd DQPSK signal can be converted within a range of 35 nm using a BER of 10^{-3}. This range is again limited on the large wavelength side by the receiver sensitivity. The observed penalties vary within in a range of -1.2 to 3.3 dB and -0.4 to 2.2 dB using the 1313 nm BtB and the localized BtB measurement as the reference, respectively. The penalties of the converted DPSK and DQPSK show a comparable performance at a BER of 10^{-3}. The full spectral range addressed by the DPSK signal is limited in case of the DQPSK by both, the receiver and the reduction of the output peak power of idler 2.1 with increasing conversion distance (see Fig. 8.9a).

However, the 40 GBd DQPSK wavelength conversion is achieved within a range of 16 nm (1319–1303 nm) and 35 nm (1288 nm to about 1323 nm) with a receiver input power penalty below 3 dB for a BER level of 10^{-9} and 10^{-3} (required approximately for forward-error correction (FEC)[13]). An improved receiver sensitivity could enable a DQPSK wavelength conversion across a wavelength range as large as obtained for the DPSK signal as the static SBR should be sufficient.

8.5 Summary

The symmetry of the FWM up and down-conversion efficiency in QD SOAs benefits from the low α-factor and thus the reduced influence of CDP. The asymmetry is less than 5 dB in agreement with e.g. [2, 49, 59, 92, 94, 109]. The static conversion efficiency and SBR in QD SOAs is optimized in well agreement with e.g. [2, 49, 59] by following the guidelines:

- Large pump and probe input power levels.

[13] See Sect. 4.3 for details.

- Increase of gain and decrease of saturation input power levels e.g. by longer QD SOAs and/or large currents.
- Single-pump wavelength conversion preferable for short-range wavelength conversion up to ± 10 nm.
- Dual-pump wavelength conversion preferable for wide-range wavelength conversion of up to ± 30 nm, only limited by gain-bandwidth of SOA.

The fast gain dynamics of QD SOAs even in deep saturation ensures a sufficiently fast modulation of the gain and refractive index grating. Thus, wavelength conversion of high symbol rate OOK signals is feasible [2, 66, 73, 74]. In addition, this chapter demonstrated that the phase grating is modulated sufficiently fast to convert high symbol rate phase-coded signals, i.e. 40 GBd (40 Gb/s) DPSK and 40 GBd (80 Gb/s) DQPSK modulated signals.

The error-free (BER $< 10^{-9}$) 4 nm wavelength down-conversion from 1313 to 1309 nm of a 40 GBd D(Q)PSK based on single-pump FWM in a QD SOA is demonstrated with a minuscule (low) receiver input power penalty of -0.2 dB (1.6 dB), respectively.

In dual-pump configuration, error-free 40 GBd DPSK wavelength conversion is demonstrate with a receiver input power penalty below 3 dB within a range of 40 nm (1283–1328 nm) covering 40 % of the entire O-band. Wide-range wavelength conversion of 40 GBd DQPSK signals is demonstrated within a range of 35 nm (1288–1323 nm) with a receiver input power penalty of about or less than 3 dB at a BER threshold 10^{-3} (approximately FEC limit). Error-free conversion is achieved within a reduced range of 16 nm (1319–1303 nm) with a penalty below 3 dB limited by the receiver sensitivity. These ranges are limited by the wavelength dependent receiver sensitivity and could be increased to at least 60 nm (35 nm) for D(Q)PSK modulated signals taking into account the static conversion properties.

In conclusion, QD SOAs enable short-range as well as wide-range wavelength conversion of at least 40 GBd phase-coded signals. This is the first time, that a 40 GBd DQPSK signal is converted using single and dual-pump FWM in a QD SOA. The results demonstrate that QD SOAs are very promising devices for AOWC, required for signal processing in modulation format transparent future ANs and MANs.

References

1. R. Bonk, Linear and nonlinear semiconductor optical amplifiers for next-generation optical networks. Doctoral thesis. Karlsruher Institut für Technologie (2013), p. 278
2. C. Meuer, GaAs-based quantum-dot semiconductor optical amplifiers at 1.3 μm for all-optical networks. Doctoral thesis. Technical University of Berlin (2011), p. 155
3. K. Uchiyama, S. Kawanishi, M. Saruwatari, 100-Gb/s multiple-channel output alloptical OTDM demultiplexing using multichannel four-wave mixing in a semiconductor optical amplifier. IEEE Photonics Technol. Lett. **10**(6), 890–892 (1998)
4. I. Shake et al., 160 Gbit/s full optical time-division demultiplexing using FWM of SOA-array integrated on PLC. Electron. Lett. **38**(1), 37–38 (2002)

5. S.L. Jansen et al., Demultiplexing 160 Gbit/s OTDM signal to 40 Gbit/s by FWM in SOA. Electron. Lett. **38**(17), 978–980 (2002)
6. A. Sharaiha et al., All-optical logic NOR gate using a semiconductor laser amplifier. Electron. Lett. **33**(4), 323–325 (1997)
7. H. Sun et al., XOR performance of a quantum dot semiconductor optical amplifier based Mach–Zehnder interferometer. Engl. Opt. Express **13**(6), 1892–1899 (2005)
8. S.J.B. Yoo, Wavelength conversion technologies for WDM network applications. J. Lightw. Technol. **14**(6), 955–966 (1996)
9. Y. Ueno et al., 3.8-THz wavelength conversion of picosecond pulses using a semiconductor delayed-interference signal-wavelength converter (DISC). IEEE Photonics Technol. Lett. **10**(3), 346–348 (1998)
10. T. Tripathi, K.N. Sivarajan, Computing approximate blocking probabilities in wavelength routed all-optical networks with limited-range wavelength conversion, in *Annual Joint Conference of the IEEE Computer and Communications Societies (INFOCOM)* (1999), pp. 329–336
11. H. Zang, J.P. Jue, B. Mukherjee, A review of routing and wavelength assignment approaches for wavelength-routed optical WDM networks. Opt. Netw. Mag. **1**, 47–60 (2000)
12. S. Sygletos, I. Tomkos, J. Leuthold, Technological challenges on the road toward transparent networking. J. Opt. Netw. **7**(4), 321–350 (2008)
13. C. Schubert, R. Ludwig, H.-G. Weber, High-speed optical signal processing using semiconductor optical amplifiers, in *Ultrahigh-Speed Optical Transmission Technology*, 1st edn., ed. by H.-G. Weber, M. Nakazawa (Springer, Berlin, 2007), p. 482
14. M. Usami, K. Nishimura, *Optical Nonlinearities in Semiconductor Optical Amplifiers and Electro-absorption Modulator: Their Applications to All-Optical Regeneration*, 1st edn., ed. by H.-G. Weber, M. Nakazawa (Springer, Berlin, 2007), p. 482
15. T. Yamamoto, M. Nakazawa, *Ultrafast OTDM Transmission Using Fiber Devices for Pulse Compression, Shaping, and Demultiplexing*, 1st edn., ed. by H.-G. Weber, M. Nakazawa (Springer, Berlin, 2007), p. 482
16. T. Sakurai, N. Kobayashi, New optical device technologies for ultrafast OTDM systems, in *Ultrahigh-Speed Optical Transmission Technology*, 1st edn., ed. by H.-G. Weber, M. Nakazawa (Springer, Berlin, 2007), p. 482
17. H. Ishikawa (ed.), *Ultrafast All-Optical Signal Processing Devices*, 1st edn. (Wiley, London, 2008), p. 258
18. S. Watanabe et al., Simultaneous wavelength conversion and optical phase conjugation of 200 Gb/s (5 times; 40 Gb/s) WDM signal using a highly nonlinear fiber four-wave mixer, in *International Conference on Integrated Optics and Optical Fibre Communications and European Conference on Optical Communications (ECOC)*. 1997, TH3A
19. T. Yamamoto, M. Nakazawa, Highly efficient four-wave mixing in an optical fiber with intensity dependent phase matching. IEEE Photonics Technol. Lett. **9**(3), 327–329 (1997)
20. B. Olsson et al., A simple and robust 40-Gb/s wavelength converter using fiber crossphase modulation and optical filtering. IEEE Photonics Technol. Lett. **12**(7), 846–848 (2000)
21. W. Wang et al., Raman-enhanced regenerative ultrafast all-optical fiber XPM wavelength converter. J. Lightw. Technol. **23**(3), 1105–1115 (2005)
22. H. Hu et al., 640 Gbit/s and 1.28 Tbit/s polarisation insensitive all optical wavelength conversion. Opt. Express **18**(10), 9961–9966 (2010)
23. A.E. Willner et al., Optically efficient nonlinear signal processing. IEEE J. Sel. Top. Quantum Electron. **17**(2), 320–332 (2011)
24. M.H. Chou et al., 1.5 μm-band wavelength conversion based on difference-frequency generation in LiNbO3 waveguides with integrated coupling structures. Opt. Lett. **23**(13), 1004–1006 (1998)
25. J. Yamawaku et al., Simultaneous 25 GHz-spaced DWDM wavelength conversion of 1.03 Tbit/s (103 x 10 Gbit/s) signals in PPLN waveguide. Electron. Lett. **39**(15), 1144–1145 (2003)
26. H. Furukawa et al., Tunable all-optical wavelength conversion of 160-Gb/s RZ optical signals by cascaded SFG-DFG generation in PPLN waveguide. IEEE Photonics Technol. Lett. **19**(6), 384–386 (2007)

27. R.L. Espinola et al., C-band wavelength conversion in silicon photonic wire waveguides. Opt. Express **13**(11), 4341–4349 (2005)
28. Q. Lin et al., Ultrabroadband parametric generation and wavelength conversion in silicon waveguides. Opt. Express **14**(11), 4786–4799 (2006)
29. H. Rong et al., High efficiency wavelength conversion of 10 Gb/s data in silicon waveguides. Opt. Express **14**(3), 1182–1188 (2006)
30. J. Leuthold, C. Koos, W. Freude, Nonlinear silicon photonics. Nat. Photonics **4**(8), 535–544 (2010)
31. M. Fisher, S.L. Chuang, Wavelength conversion using an integrated DFB laser-phase shifter. IEEE Photonics Technol. Lett. **16**(1), 197–199 (2004)
32. X.-H. Jia, Z.-M. Wu, G.-Q. Xia, Terahertz wavelength conversion based on four-wave mixing in $\lambda/4$-shifted dfb lasers: dynamic range and performance analysis. IEEE J. Quantum Electron. **43**(4), 334–342 (2007)
33. H. Kuwatsuka, Wavelength conversion devices, in *Ultrafast All-Optical Signal Processing Devices*, 1st edn., ed. by H. Ishikawa (Wiley, London, 2008), p. 258
34. J. Shi, S. Alam, M. Ibsen, Ultra-broadband wavelength conversion based on fourwave mixing in a Raman DFB fiber laser, in *Optical Fiber Communication Conference (OFC) and National Fiber Optic Engineers Conference (NFOEC)*. 2013, JW2A.23
35. T. Durhuus et al., All-optical wavelength conversion by semiconductor optical amplifiers. J. Lightw. Technol. **14**(6), 942–954 (1996)
36. D. Nesset, T. Kelly, D. Marcenac, All-optical wavelength conversion using SOA nonlinearities. IEEE Commun. Mag. **36**(12), 56–61 (1998)
37. D. Cotter et al., Nonlinear optics for high-speed digital information processing. Science **286**(5444), 1523–1528 (1999)
38. J. Leuthold et al., 100 Gbit/s all-optical wavelength conversion with integrated SOA delayed-interference configuration. Electron. Lett. **36**(13), 1129–1130 (2000)
39. S. Diez, Why and how to study four-wave mixing? in *Photonic Devices for Telecommunications*, 1st edn., ed. by G. Guekos (Springer, Berlin, 1999), p. 404
40. J.P.R. Lacey, G.J. Pendock, R.S. Tucker, All-optical 1300-nm to 1550-nm wavelength conversion using cross-phase modulation in a semiconductor optical amplifier. IEEE Photonics Technol. Lett. **8**(7), 885–887 (1996)
41. G.P. Agrawal, Population pulsations and nondegenerate four-wave mixing in semiconductor lasers and amplifiers. J. Opt. Soc. Am. B **5**(1), 147 (1988)
42. J. Leuthold et al., 160 Gbit/s SOA all-optical wavelength converter and assessment of its regenerative properties. Electron. Lett. **40**(9), 554–555 (2004)
43. Y. Liu et al., 160 Gbit/s all-optical SOA-based wavelength conversion and error-free transmission through two 50 km fibre links. Electron. Lett. **43**(25), 1447–1449 (2007)
44. Y. Liu et al., Error-free 320 Gb/s SOA-based wavelength conversion using optical filtering, in *Optical Fiber Communication Conference (OFC)*. 2006, PDP28
45. G. Contestabile et al., 160 Gb/s cross gain modulation in quantum dot SOA at 1550 nm, in *Communication (ECOC), European Conference and Exhibition on Optical* (2009), pp. 1–2
46. G. Contestabile et al., Cross-gain modulation in quantum-dot SOA at 1550 nm. IEEE J. Quantum Electron. **46**(12), 1696–1703 (2010)
47. D. Bimberg et al., Quantum-dot semiconductor optical amplifier for filter-assisted 80-Gb/s wavelength conversion, in *International Conference on Transparent Optical Networks (ICTON)*. 2011, We.B5.4
48. C. Meuer et al., 80 Gb/s wavelength conversion using a quantum-dot semiconductor optical amplifier and optical filtering. Opt. Express **19**(6), 5134–5142 (2011)
49. G. Contestabile, A. Maruta, K.-I. Kitayama, Four wave mixing in quantum dot semiconductor optical amplifiers. IEEE J. Quantum Electron. **50**(5), 379–389 (2014)
50. R.M. Jopson, R.E. Tench, Polarisation-independent phase conjugation of lightwave signals. Electron. Lett. **29**(25), 2216–2217 (1993)
51. G. Hunziker et al., Polarization-independent wavelength conversion at 2.5 Gb/s by dualpum four-wave mixing in a strained semiconductor optical amplifier. IEEE Photonics Technol. Lett. **8**(12), 1633–1635 (1996)

52. J.P.R. Lacey, S.J. Madden, M.A. Summerfield, Four-channel polarization insensitive optically transparent wavelength converter. IEEE Photonics Technol. Lett. **9**(10), 1355–1357 (1997)
53. A. Mecozzi et al., Polarization-insensitive four-wave mixing in a semiconductor optical amplifier. Appl. Phys. Lett. **72**(21), 2651 (1998)
54. U. Feiste et al., 40 Gbit/s transmission over 434 km standard fibre using polarisation independent mid-span spectral inversion. Electron. Lett. **34**(21), 2044–2045 (1998)
55. R. Schnabel et al., Polarization insensitive frequency conversion of a 10-channel OFDM signal using four-wave mixing in a semiconductor laser amplifier. IEEE Photonics Technol. Lett. **6**(1), 56–58 (1994)
56. L.Y. Lin et al., Polarization-insensitive wavelength conversion up to 10 Gb/s based on four-wave mixing in a semiconductor optical amplifier. IEEE Photonics Technol. Lett. **10**(7), 955–957 (1998)
57. M.A.A. Summerfield, R.S. Tucker, Optimization of pump and signal powers for wavelength converters based on FWM in semiconductor optical amplifiers. IEEE Photonics Technol. Lett. **8**(10), 1316–1318 (1996)
58. F. Girardin, T. Ducellier, S. Diez. Measurement techniques and results, in *Photonic Devices for Telecommunications*, 1st edn., ed. by G. Guekos (Springer, Berlin, 1999), p. 404
59. T. Akiyama et al., Symmetric highly efficient (0 dB) wavelength conversion based on four-wave mixing in quantum dot optical amplifiers. IEEE Photonics Technol. Lett. **14**(8), 1139–1141 (2002)
60. D. Nielsen et al., High-speed wavelength conversion in quantum dot and quantum well semiconductor optical amplifiers. Appl. Phys. Lett. **92**(21), 211101 (2008)
61. A.E. Kelly, D.D. Marcenac, D. Nesset, 40 Gbit/s wavelength conversion over 24.6 nm using FWM in a semiconductor optical amplifier with an optimised MQW active region. Electron. Lett. **33**(25), 2123–2124 (1997)
62. A.E. Kelly et al., 100 Gbit/s wavelength conversion using FWM in an MQW semiconductor optical amplifier. Electron. Lett. **34**(20), 1955–1956 (1998)
63. S. Arahira, Y. Ogawa, 160-Gb/s all-optical encoding experiments by four-wave mixing in a gain-clamped SOA with assist-light injection. IEEE Photonics Technol. Lett. **16**(2), 653–655 (2004)
64. A. Capua et al., Cross talk free multi channel processing of 10 Gbit/s data via four-wave mixing in a 1550 nm InAs/InP quantum dash amplifier. Opt. Express **16**(23), 19072–19077 (2008)
65. G. Contestabile et al., Investigation of transparency of FWM in SOA to advanced modulation formats involving intensity, phase, and polarization multiplexing. J. Lightw. Technol. **27**(19), 4256–4261 (2009)
66. M. Matsuura et al., 320 Gbit/s wavelength conversion using four-wave mixing in quantumdot semiconductor optical amplifiers. Opt. Lett. **36**(15), 2910–2912 (2011)
67. H. Schmeckebier et al., Wide-range wavelength conversion of 40-Gb/s NRZ-DPSK signals using a 1.3 μm quantum-dot semiconductor optical amplifier. IEEE Photonics Technol. Lett. **24**(13), 1163–1165 (2012)
68. G. Contestabile et al., Coherent wavelength conversion in a quantum dot SOA. IEEE Photonics Technol. Lett. **25**(9), 791–794 (2013)
69. L. Krzczanowicz, M.J. Connelly, 40 Gb/s NRZ-DQPSK data all-optical wavelength conversion using four-wave mixing in a bulk SOA. IEEE Photonics Technol. Lett. **25**(24), 2439–2441 (2013)
70. S. Diez et al., 160-Gb/s optical sampling by gain-transparent four-wave mixing in a semiconductor optical amplifier. IEEE Photonics Technol. Lett. **11**(11), 1402–1404 (1999)
71. M. Matsuura et al., Multichannel wavelength conversion of 50-Gbit/s NRZ-DQPSK signals using a quantum-dot semiconductor optical amplifier. Opt. Express **19**(26), B560–B566 (2011)
72. C. Schubert, R. Ludwig, H.G. Weber, High-speed optical signal processing using semiconductor optical amplifiers. J. Opt. Fiber Commun. Rep. **2**(2), 171–208 (2005)

73. H. Schmeckebier et al., Quantum dot semiconductor optical amplifiers at 1.3 μm for applications in all-optical communication networks. Semicond. Sci. Technol. **26**(1), 14009 (2011)
74. C. Meuer et al., 40 Gb/s wavelength conversion via four-wave mixing in a quantum-dot semiconductor optical amplifier. Opt. Express **19**(4), 3788–3798 (2011)
75. R.W. Boyd, *Nonlinear Optics*, 1st edn. (Elsevier, Amsterdam, 2013), p. 456
76. J.-C. Diels, W. Rudolph, *Ultrashort Laser Pulse Phenomena*, 2nd edn. (Academic Press, London, 2006), p. 680
77. K. Kikuchi et al., Observation of highly nondegenerate four-wave mixing in 1.5 μm traveling-wave semiconductor optical amplifiers and estimation of nonlinear gain coefficient. IEEE J. Quantum Electron. **28**(1), 151–156 (1992)
78. S. Diez, Vierwellenmischung in InGaAs-Halbleiterlaserverstärkern. Diploma thesis, Technische Universität Berlin (1996)
79. I. Koltchanov et al., Gain dispersion and saturation effects in four-wave mixing in semiconductor laser amplifiers. IEEE J. Quantum Electron. **32**(4), 712–720 (1996)
80. H. Kuwatsuka, T. Simoyama, H. Ishikawa, Enhancement of third-order nonlinear optical susceptibilities in compressively strained quantum wells under the population inversion condition. IEEE J. Quantum Electron. **35**(12), 1817–1825 (1999)
81. K. Obermann, A. Mecozzi, J. Mørk, Theory of four-wave mixing, in *Photonic Devices for Telecommunications*, 1st edn., ed. by G. Guekos (Springer, Berlin, 1999), p. 404
82. A.V. Uskov, J. Mørk, J. Mark, Wave mixing in semiconductor laser amplifiers due to carrier heating and spectral-hole burning. IEEE J. Quantum Electron. **30**(8), 1769–1781 (1994)
83. A. Mecozzi et al., High saturation behavior of the four-wave mixing signal in semiconductor amplifiers. Appl. Phys. Lett. **66**(1995), 1184–1186 (1995)
84. C. Meuer et al., Cross-gain modulation and four-wave mixing for wavelength conversion in undoped and p-doped 1.3 μm quantum dot semiconductor optical amplifiers. IEEE Photon. J. **2**(2), 141–151 (2010)
85. A. Zeghuzi, Characterisation of quantum dot based semiconductor optical amplifiers for optical communication applications. Master thesis, Technische Universität Berlin (2015), p. 77
86. G.P. Agrawal, Four-wave mixing and phase conjugation in semiconductor laser media. Opt. Lett. **12**(4), 260–262 (1987)
87. A. Mecozzi et al., Four-wave mixing in traveling-wave semiconductor amplifiers. IEEE J. Quantum Electron. **31**(4), 689–699 (1995)
88. J. Zhou et al., Terahertz four-wave mixing spectroscopy in a semiconductor optical amplifier for study of ultrafast dynamics. Appl. Phys. Lett. **63**(9), 1179–1181 (1993)
89. J. Zhou et al., Efficiency of broadband four-wave mixing wavelength conversion using semiconductor traveling-wave amplifiers. IEEE Photonics Technol. Lett. **6**(1), 50–52 (1994)
90. S. Diez et al., Related topics, in *Photonic Devices for Telecommunications*, 1st edn., ed. by G. Guekos (Springer, Berlin, 1999), p. 404
91. A. Bilenca et al., Broad-band wavelength conversion based on cross-gain modulation and four-wave mixing in InAs-InP quantum-dash semiconductor optical amplifiers operating at 1550 nm. IEEE Photonics Technol. Lett. **15**(4), 563–565 (2003)
92. M. Sugawara et al., Theory of optical signal amplification and processing by quantum-dot semiconductor optical amplifiers. Phys. Rev. B **69**(23), 235332 (2004)
93. O. Qasaimeh, Theory of four-wave mixing wavelength conversion in quantum dot semiconductor optical amplifiers. IEEE Photonics Technol. Lett. **16**(4), 993–995 (2004)
94. T. Akiyama, M. Sugawara, Y. Arakawa, Quantum-dot semiconductor optical amplifiers. Proc. of the IEEE **95**(9), 1757–1766 (2007)
95. N. Majer, Nonlinear gain dynamics of quantum dot optical amplifiers. Doctoral thesis, Technische Universität Berlin (2012)
96. T. Akiyama et al., Nonlinear gain dynamics in quantum-dot optical amplifiers and its application to optical communication devices. IEEE J. Quantum Electron. **37**(8), 1059–1065 (2001)
97. T.W. Berg, J. Mørk, J.M. Hvam, Gain dynamics and saturation in semiconductor quantum dot amplifiers. New J. Phys. **6**(178), 1–23 (2004)

98. D. Nielsen, S.L. Chuang, Four-wave mixing and wavelength conversion in quantum dots. Phys. Rev. B **81**, 035305 (2010)
99. M. Matsuura, N. Kishi, High-speed wavelength conversion of RZ-DPSK signal using FWM in a quantum-dot SOA. IEEE Photonics Technol. Lett. **23**(10), 615–617 (2011)
100. M. Bayer, A. Forchel, Temperature dependence of the exciton homogeneous linewidth in In0.60Ga0.40As/GaAs self-assembled quantum dots. Phys. Rev. B **65**(4), 041308 (2002)
101. K. Matsuda et al., Homogeneous linewidth broadening in a In 0.5Ga 0.5As/GaAs single quantum dot at room temperature investigated using a highly sensitive near-field scanning optical microscope. Phys. Rev. B **63**(12), 121304 (2001)
102. R. Ludwig et al., Ultrafast wavelength conversion and switching by four-wave mixing in semiconductor laser amplifiers, in *Ultrafast Electronics and Optoelectronics*. 1995, UMC2
103. G. Grosskopf, R. Ludwig, H.G. Weber, 140 Mbit/s DPSK transmission using an all-optical frequency convertor with a 4000 GHz conversion range. Electron. Lett. **24**(17), 1106–1107 (1988)
104. N. Schunk et al., Frequency conversion by nearly-degenerate four-wave mixing in travelling-wave semiconductor laser amplifiers. IEE Proc. Optoelectron. **137**(4), 209–214 (1990)
105. G. Contestabile et al., Efficiency attening and equalization of frequency up- and downconversion using four-wave mixing in semiconductor optical amplifiers. IEEE Photonics Technol. Lett. **10**(10), 1398–1400 (1998)
106. T.J. Morgan, J.P.R. Lacey, R.S. Tucker, Widely tunable four-wave mixing in semiconductor optical amplifiers with constant conversion efficiency. IEEE Photonics Technol. Lett. **10**(10), 1401–1403 (1998)
107. I. Tomkos et al., Performance of a reconfigurable wavelength converter based on dualpump-wave mixing in a semiconductor optical amplifier. IEEE Photonics Technol. Lett. **10**(10), 1404–1406 (1998)
108. G. Contestabile et al., All-optical wavelength multicasting in a QD-SOA. IEEE J. Quantum Electron. **47**(4), 541–547 (2011)
109. G. Contestabile et al., 100 nm-bandwidth positive-efficiency wavelength conversion for m-PSK and m-QAM signals in QD-SOA, in *Optical Fiber Communication Conference (OFC) and National Fiber Optic Engineers Conference (NFOEC)*. 2013, OTh1C.6
110. M. Matsuura, N. Kishi, 40-Gbit/s RZ-DPSK wavelength conversion using four-wave mixing in a quantum dot SOA, in *Optical Fiber Communication Conference (OFC) and National Fiber Optic Engineers Conference (NFOEC)*. 2011, JThA024
111. G. Contestabile et al., Ultra-broad band, low power, highly efficient coherent wavelength conversion in quantum dot SOA. Opt. Express **20**(25), 27902–27907 (2012)
112. C. Meuer et al., Wavelength conversion of 40-Gb/s NRZ DPSK signals within a 45-nm range using a 1.3 μm quantum-dot semiconductor optical amplifier, in *European Conference and Exhibition on Optical Communication (ECOC)*. 2011, We.10.P1.26

Chapter 9
Summary and Outlook

The present thesis investigated and demonstrated the suitability of GaAs-based QD SOAs for future metropolitan area networks (MANs) and access networks (ANs), featuring high symbol rate transmission in multi-wavelength channel configurations, using advanced modulation formats. These networks require optical amplifiers to compensate losses caused by the extended reach, larger splitting ratios and larger amount of in-line components. In addition, signal processing is imperative to enable all-optical wavelength conversion (AOWC) and all-optical switching.

Semiconductor optical amplifiers (SOAs) are particularly promising candidates for both, amplification as well as nonlinear optical signal processing, as they offer a small footprint, low power consumption, ease of integration in photonic integrated circuits, and broad gain spectra. Quantum dot (QD)-based SOAs exhibit unique properties in comparison to conventional bulk and/or QW base SOAs. QD gain material offer the separation of the energy states into gain providing QD states, i.e. ground state (GS) and excited state (ES), and carrier reservoir providing higher energy states. In case of a highly populated reservoir, this results in a decoupling of gain and phase dynamics as well as a presumably low α-factor. Hence, very fast gain dynamics is achievable even for strong gain depletion demonstrated by complete GS gain recovery on a picosecond time scale or even below. Furthermore, the inhomogeneously broadened QD ensemble leads to a broad gain bandwidth of both, GS and ES.

The ultra-fast gain recovery and broad gain bandwidth as well as the low α-factor predestine QD SOAs for multi-wavelength channel amplification and nonlinear wavelength conversion of both, high symbol rate amplitude and phase-coded signals. These have been demonstrated for symbol rates up to 80 GBd. In addition, based on the decoupling of phase and gain dynamics as well as the broad spectral separation of QD GS and ES in the order of 100 nm, two novel QD SOA-based concepts have been developed and demonstrated.

H. Schmeckebier, *Quantum-Dot-Based Semiconductor Optical Amplifiers for O-Band Optical Communication*, Springer Theses,
DOI 10.1007/978-3-319-44275-4_9

In detail, the present thesis has investigated:

Basic Characterization
QD SOAs with different designs and lengths have been presented. The deeply-edged ridge waveguide design provides a high-frequency capable contact design but at the expense of a high chip noise figure of 7.3 dB caused by the ridge roughness. Shallow-edged ridges offer significantly improved values down to 4.1 dB despite an increased length. 4–5 mm long single-section QD SOAs exhibit excellent chip gain values as large as 34.5 dB. Both, the chip noise figure and chip gain are comparable to commercially available SOAs. But, the fiber-to-fiber values suffer from the 4.5 dB coupling losses per facet and could be reduced by waveguide engineering. The gain values especially at larger currents are limited by thermal conductivity. Hence, an improvement of the mounting technology similar to commercial SOAs is desirable. Both, the QD SOAs and the commercial SOAs exhibit a polarization dependent gain. This can be overcome for both, e.g. shown for QD SOAs by using columnar QDs. However, the achieved fiber-to-fiber gain values of 13–26 dB and spectral 3-dB bandwidth of 34–21 nm are sufficient for applications in future all-optical ANs and MANs. Larger gain values for specialized applications can be realized at the expense of gain bandwidth narrowing. A concept of a sectioned QD SOA has been presented offering a very large chip gain up to 39.5 dB.

The gain dynamics have been investigated for both QD states. For the amplification of ps-pulses with communication typical symbol rates and power levels, neither self-phase modulation nor self-gain modulation have been found. The complete GS gain recovery has been confirmed to be faster than 10 ps even under a perturbation frequency on the order of typical optical communication symbol rates. In addition, a strong carrier depletion on the QD ES showed no influence on the GS gain recovery. Further measurements, simulations and discussions lead to a predicted fast gain recovery of both QD states and a decoupling of different QD sub-ensembles if both states are saturated and the carrier reservoir is highly populated.

Concept of Signal Generation
A novel concept exploits the unique decoupling of gain and phase dynamics of QD SOAs for directly modulated DPSK signal generation with the allocation of gain. Modulating the current of a QD SOA driven beyond the saturation bias results in a modulation of the carrier density of the reservoir and thus the refractive index. But, the gain of the QD GS remains constant. Hence, a QD SOA amplified optical signal experiences a time independent gain but a modulation of its phase.

Error-free direct DPSK modulation has been demonstrated up to symbol rates of 25 GBd using a QD SOA which offers a linear fiber-to-fiber gain of 8 dB. In addition, the error-free generation has been demonstrated within a 2 dB receiver input power penalty-based input power dynamic range (IPDR) larger than 12 dB at a symbol rate of 20 GBd. Differential detection has been used to benefit from the fast phase effects of the QD SOAs. These results excellently prove the concept. This is the fastest reported directly modulated DPSK generation for semiconductor edge emitters for optical communication applications. Hence, the obtained results

demonstrate the suitability of QD SOAs for a direct phase-modulated-based low-cost color-free networks like future ANs.

Amplification
Future reach extended ANs and converged MANs require multi-channel modulation-format-transparent optical amplifiers. In such networks, individual customer premises have individual paths to the central office with individual losses and thus the input power into the amplifier varies across the channels. The amplifier has to amplify all signals within a specific range of input power levels with low crosstalk. The according figure of merit is the IPDR. Beside gain, gain bandwidth and noise figure, the IPDR is a crucial amplifier parameter. Hence, the IPDR has been comprehensively investigated in this thesis for high symbol rate amplitude and phase-coded signal, i.e. OOK, DPSK and DQPSK modulated signals.

The fast gain dynamics of QD SOAs even in deep saturation enable pattern-effect free amplification of high symbol rate OOK signals as shown in the past. This has been confirmed in this thesis excellently by 15.5-dB amplification of a single-channel 80 GBd (80 Gb/s) RZ OOK signal within a 2-dB penalty IPDR much larger than 18 dB. The limits on both power sides have not been reached despite a large input power of already 6 dB beyond the 3-dB saturation input power of 0.1 dBm. Even in the presence of three neighboring 40 GBd (40 Gb/s) NRZ OOK channels, an error-free amplification is achieved up to a total input power of 3 dB above the 3-dB saturation input power. A negligible crosstalk on the 80 GBd channel has been found for smaller input power levels corresponding to the linear gain regime.

However, for the amplification of phase-coded signals, particularly with OOK neighboring channels, not only the fast gain dynamics have to be considered but also the phase dynamics. Hence, in the framework of this thesis, the IPDR for DPSK and DQPSK modulated signals as well as the influence of an OOK neighboring channel have been comprehensively investigated. The use of differential and coherent detection receivers allowed a comprehensive discussion of different IPDR definitions and enabled in-depth investigation of phase and amplitude effects as well as confirmed an error-free performance.

The fast QD SOA gain dynamics and particular the decoupling of gain and phase dynamics lead to an outstanding amplification performance of 40 GBd (40 Gb/s) DPSK and 40 GBd (80 Gb/s) DQPSK modulated signals with a gain of up to 24 dB. Error-free single-channel DPSK amplification has been demonstrated within an IPDR larger than 28.8 and 36.7 dB with a receiver input power penalty below 2 dB and an EVM below 23.4 %, respectively. In addition, the error-free single-channel DQPSK amplification has been demonstrated within an IPDR larger than 18.4 and 29.9 dB with a receiver input power penalty below 2 dB and an EVM below 16.4 %, respectively. The signal quality is determined by phase changes on a time scale longer than the symbol rate for large input power levels, whereas it is deteriorated by the amplifier noise for very small QD SOA input power levels. The phase distortion starts to increase for input power levels beyond the 3-dB saturation input power of −8.3 dB, but the error-free detection is demonstrated even for input power levels of 17 dB beyond the saturation input power. Hence, the phase dynamics of QD SOAs

are sufficiently fast or the phase effects are sufficiently suppressed to enable these IPDR results, which are significantly larger than previously published results.

The ultra-fast QD refilling and the suppressed phase effects enable the error-free 40 GBd DQPSK signal amplification even in the presence of a 40 GBd OOK neighboring channel as long as the DQPSK signal input power level is larger than for the OOK signal. And even this performance is achieved for input power levels far beyond the 3-dB saturation input power. The power distribution restriction can be cushioned by larger QD SOA currents leading to a reduced crosstalk as already demonstrated for OOK multi-channel amplification.

QD SOAs show an excellent amplification performance for high symbol rate OOK, DPSK and DQPSK signals even in multi-channel configuration. Hence, QD SOAs are suitable for modulation format transparent multi-channel amplification as required for future all-optical reach extended ANs and converged MANs.

Concept of Dual-Band Amplifier

Another novel concept, developed during the course of this thesis, exploits the inhomogeneously broadened QD GS and ES to amplify signals in dual-band configuration, i.e. with a large spectral separation. This concept requires a decoupling of GS and ES gain dynamics, which is achieved for saturating bias levels of both states as shown by simulations. Limited by the thermal conductivity, the bias has been chosen to saturate both QD states and to provide a sufficient linear fiber-to-fiber gain of close to 10 dB or more. The proof of concept has been demonstrated by distortion-free amplification of bidirectional 40 GBd (40 Gb/s) OOK signals with a spectral difference of more than 91 nm. The receiver input power penalty was found to be well below 2 dB for accessible per-channel input power levels up to 0 dBm. An IPDR larger than 15 dB has been presented for both signals, in which the receiver input power penalty is well below 2 dB.

This concept of a dual-band amplifier has the potential to drastically simplify the network architecture and thus reduce the power consumption or increase the power budget of the network. Both result in reduced investment and maintaining costs of future reach extended ANs and converged MANs.

Four-Wave-Mixing-Based Wavelength Conversion

AOWC as the fundamental building block for optical signal processing, such as optical demultiplexing and logical operations, is a key functionality for reach extended ANs and converged MANs. The fast gain dynamics even in the nonlinear gain regime predestine QD SOAs for AOWC. The most important nonlinear effects occurring in QD SOAs are cross-gain modulation (XGM), cross-phase modulation (XPM) and four-wave mixing (FWM). This thesis has focused on FWM as this is the only effect which is transparent to both, intensity- and phase-modulated signals. In comparison to conventional SOAs, FWM in QD SOAs allows a more symmetric wavelength up- and down-conversion efficiency due to the low α-factor and hence the suppressed influence of carrier density pulsation.

The static FWM performance has been optimized in terms of conversion efficiency and SBR for up- and down-conversion in single- and dual-pump configuration. Increasing saturation power levels, current and gain (via device length) lead to an improved performance. Conversion efficiencies as large as −9 dB have been found for a detuning of +0.5 nm. For the dual-pump configuration, the conversion efficiency and signal-to-background ratio (SBR) exceed −30 and 20 dB, respectively, in almost the entire detuning equivalent range of 30 nm (from −15 to +15 nm). This represents a wavelength up- or down-conversion by ±30 nm. This conversion span exceeds the homogenous linewidth of the QDs. Hence, the conversion has to be mediated via the reservoir, presumable via carrier heating.

However, FWM in QD SOAs was comprehensively used to wavelength convert high speed OOK signals which lead to impressive results. But, the conversion of phase-coded signals was only touched. Hence, this thesis has focused on the conversion of high symbol rate phase-coded signals, i.e. 40 GBd (40 Gb/s) DPSK and 40 GBd (80 Gb/s) DQPSK signals. In single-pump configuration, an error-free 4 nm DPSK wavelength down-conversion from 1313 to 1309 nm has been demonstrated with a marginal receiver input power penalty of −0.2 dB. The penalty for DQPSK was only 1.6 dB. This is the first time that a 40 GBd DQPSK is converted using a QD SOA.

In dual-pump configuration, the error-free 40 GBd (40 Gb/s) DPSK wavelength conversion has been demonstrated within a range of 45 nm (1283–1328 nm) covering 45 % of the entire O-band. Within a slightly smaller range of 40 nm, the receiver input power penalty has been found to be below 3 dB. Both ranges are limited by the receiver and could be increased to at least 60 nm taking into account the static conversion properties. The forward-error correction (FEC)-limit 40 GBd (80 Gb/s) DQPSK wavelength conversion has been demonstrated within a range of 35 nm (1288–1323 nm) with a receiver input power penalty below 3 dB. An error-free conversion has been achieved within a reduced range of 16 nm (1319–1303 nm) with a penalty below 3 dB, which was limited by the receiver sensitivity. Overcoming this limitation could enable an error-free conversion over the entire 35 nm range.

Hence, QD SOAs enable a short-range as well as wide-range wavelength conversion of at least 40 GBd phase-coded signals. Hence, QD SOAs are suitable for AOWC-based signal processing of both, intensity- and phase-coded signals.

Outlook

The QD SOAs can be improved in terms of growth and (post)-processing to decrease the noise figure, coupling losses and device heating. Polarization independent gain could be realized by applying the concept of columnar QDs GaAs-based QD devices. Furthermore, the larger gain of the QD ES can be exploited. Both, technological improvements as well as the use of the ES will enable to shorten the QD SOA length whereas keeping the fiber-to-fiber gain. This allows a reduction of the fabrication costs per device as well as reduce the remaining phase effects.

Besides the multi-level phase-coded modulation format addressed in this thesis, also multi-level amplitude modulated signals, i.e. pulse amplitude modulation with

four levels (PAM-4) are very interesting for future ANs and MANs. They allow low-cost direct detection receivers. Beside low patterning, these formats require very linear amplifiers. The fast gain dynamics as well as the large IPDRs obtained in this thesis predestine QD SOAs for this modulation format. Preliminary tests, performed with QD SOAs presented in this thesis, yield very promising results for the amplification of PAM-4 signals with symbol rates of up to 30 GBd (60 Gb/s).

The novel concept of directly modulated QD SOAs will be improved by larger gain values and/or shorter device lengths and an optimized HF design, allowing even larger modulation speeds than 25 GBd. Furthermore, this concept could be modified towards a gain providing all-optical demultiplexer for O-band optical time-division multiplexing (OTDM) signals. Upon imbedding the QD SOA in one arm of an interferometer structure, e.g. on chip integrated Mach-Zehnder modulator (MZM), current modulation changes the phase, whereas the interferometer structure analyze the induced phase change. Assuming that the phase change of the SOA is controllable on time scales on the order of the symbol rate of the OTDM signal, the OTDM signal could be demultiplexed at the output ports of the interferometer structure.

The present thesis demonstrated the amplification of multiple wavelength channels of intensity and phase-coded signals with QD SOAs with impressive performance. This low-crosstalk, low-penalty, large IPDR, multi-wavelength channel amplification can be combined with the novel dual-band amplifier concept. This will demonstrate an ultra-broadband, multi-channel, multi-format, dual-band amplifier utilizing the superior advantages of QD-based SOAs.

Another novel concept based on QD gain media can be realized by exploiting the QD GS and ES: AOWC between two bands. This can be realized on the one hand by XGM, assigning pump and probe signal to the different QD states. On the other hand, dual-pump FWM can be used by assigning pump and probe to one state and the second pump to the other state. The investigation of the nonlinear cross-state interactions, particularly across different QD subensembles will be subject of future work.

Appendix A
Gain Calculation of Broadband Signals

The gain for a narrow bandwidth signal (e.g. ECL) is defined as described in Sect. 2.2.1. In this case, the resolution of the OSA is set larger than the bandwidth of the signal. Thus, output power P_{out} and input power P_{in} can be derived directly from the measured peak power levels and ASE power level P_{ASE} can be determined by interpolating the ASE background below the signal. Unfortunately, this method is failing for a broad bandwidth source like a Fabry–Pérot laser diode because the spectral width is much larger than the resolution of the OSA. To calculate the gain for such an input signal, the method was adapted.

Equation 2.18 (p. 22) is still used to calculate the gain identical to the narrow bandwidth signals, but the determination of output power P_{out}, input power P_{in} and ASE power level P_{ASE} is modified. Input power is calculated by integrating the spectral power measured with the OSA taking into account the deconvolution of the internal OSA filter. The integrated input power P_{in} is calculated to be as close as 0.5 dB to the value measured directly with a power meter demonstrating that the integration method operates well. Output power is calculated similar to input power P_{in}, but the power integration is reduced to a spectral width called following "spectral limits". The reason for the introduction of the "spectral limits" is the determination of the ASE power level P_{ASE}. Measuring the ASE power level P_{ASE} in absence of an input signal and assuming that it remains constant is valid only for small input power levels. Thus, the ASE outside of the "spectral limits" is fitted with a polynomial of degree 5 and interpolated inside the "spectral limits" using the obtained fit. The ASE power level P_{ASE} below the output signal is determined by integration of the interpolated ASE within the "spectral limits" similar to output power P_{out} integration. As a result, the calculated broad-bandwidth signal gain is principally slightly underestimated because of the different integration limits of the input and output signal. Tests of the adapted method on narrow bandwidth signals and the comparison to results obtained with the conventional method were very promising. However, two different methods of setting the "spectral limits" have been tested and are discussed in the following.

In method "A", the "spectral limits" are fixed for all operating parameters and are set via the broadest measured output spectrum, which of course, correspond to the

H. Schmeckebier, *Quantum-Dot-Based Semiconductor Optical Amplifiers for O-Band Optical Communication*, Springer Theses,
DOI 10.1007/978-3-319-44275-4

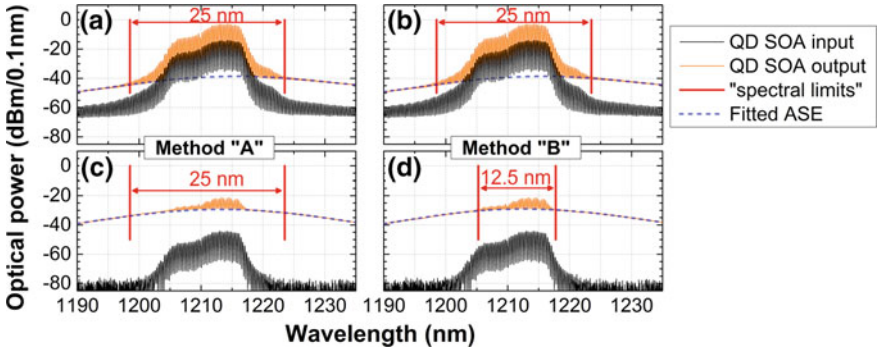

Fig. A.1 Optical spectra of QD SOA input, output, fitted and interpolated ASE as well as "spectral limits" for method "A" with **a/c** high/low input power levels and method "B" with **b/d** high/low input power levels. Method "A" uses fixed "spectral limits" whereas the "spectral limits" are set individually for each output spectrum to the outer visible laser modes for method "B". Comparing the fitted and interpolated ASE curve with the output signal demonstrates for example in a wavelength range from 1195 to 1205 nm, a slightly more accurate fit for method "B"

largest input power level. Hence, the center of the "spectral limits" was set to 1211 nm and the span was set to 25 nm. Figure A.1a, b shows exemplary two measurements with different QD SOA input power levels but fixed "spectral limits". In contrast to that, in method "B" the "spectral limits" are set individually for each output spectrum to the outer visible laser modes. An example for this method is shown in Fig. A.1c, d. Comparing the fitted and interpolated ASE curve with the output signal indicates for instance in a wavelength range from 1195 to 1205 nm a slightly more accurate fit for method "B".

A comparison of calculated gain for the two methods is shown in Fig. A.2. Except for very small input power levels, the gain value for both methods are comparable. Method "A" seems to fail at very low input power levels due to the large integration range of 25 nm with respect to the much narrower output signal resulting in a worse ASE interpolation. Thus, method "B" turns out to be more reliable and consequently, this method is used in this thesis.

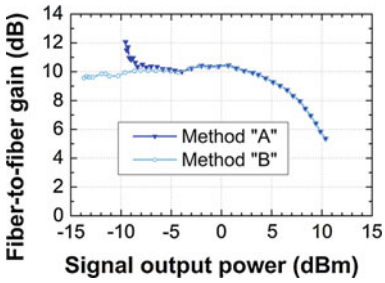

Fig. A.2 Gain versus SOA output power for a broad bandwidth signal calculated using method "A" and "B"

Appendix B
Device Setups

B.1 Low Loss Wavelength Filter and Signal Combiner

A circulator is a three port device which guides incoming light from port 1 to port 2 and incoming light from port 2 to port 3. All other transmissions like port 1 to port 3 or vice versa experience high losses (typically more than 60 dB) and thus the circulator acts like an isolator for these transitions.

The fiber-Bragg grating (FBG) is a distributed Bragg reflector realized by a periodic or aperiodic perturbation of the effective refractive index of the core of an optical fiber, e.g. a single-mode fiber (SMF). The perturbation leads to the reflection of the incoming light within the full-width at half maximum (FWHM) of the FBG satisfying the Bragg condition, whereas all other wavelengths are nearly unaffected and transmitted through the FBG.

Combining a circulator and a FBG enables the combination of (see also Fig. B.1):

- low loss filtering (typical less than 2.5 dB losses).
- sharp filter boundaries (typical 20 dB suppression reached at 1.8-times the FWHM).
- combining of signals (one reflected, the other transmitted).

which are superior advantages in comparison to e.g. a combination of a TF and a 3-dB splitter. The disadvantage is the low flexibility in terms of wavelength and bandwidth tunability.

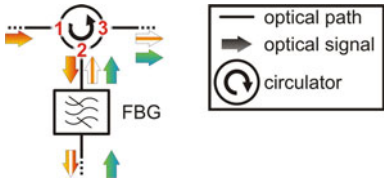

Fig. B.1 Setup sketch

H. Schmeckebier, *Quantum-Dot-Based Semiconductor Optical Amplifiers for O-Band Optical Communication*, Springer Theses,
DOI 10.1007/978-3-319-44275-4

Appendix C
Measured Bit-Error Ratio (BER) Curves

This chapter lists all BER measurements performed in Chaps. 5, 6 and 8 as long as they are not listed directly in these chapters. All BER curves have been fitted linearly with Eq. C.1. In case the BER curve is not linear, it was fitted stepwise linearly. The number of stepwise fits is given independently in each figure caption.

$$\begin{aligned} log(-log(BER)) &= a_0 + a_1 P_{rec}, \\ log(-log(BER)) &= a_0 + a_1 OSNR. \end{aligned} \tag{C.1}$$

The 80 Gb/s optical time-division multiplexing (OTDM) and 40 GBd (80 Gb/s) RZ- and DQPSK modulated signals are characterized according to Sects. 6.1 and 4.2.3, respectively, with two tributaries. The measured BER for both tributaries measured at an identical OSNR or P_{rec} are summed representing the BER of the total received signal. For the DQPSK measurements, tributary 1 and tributary 2 have not been obtained at identical P_{rec}. Additionally, their BER difference at comparable P_{rec} are large and thus a direct average would be wrong. As a consequence, the BER of both tributaries have been fitted independently. Using the fit parameters of both curves, an averaged (AVG) BER has been calculated for all measured P_{rec} of tributary 1 and tributary 2 using Eq. C.2.

$$BER(P_{rec}) = \frac{1}{2}\left(10^{-10^{A_{0,tr1}+A_{1,tr1}P_{rec}}} + 10^{-10^{A_{0,tr2}+A_{1,tr2}P_{rec}}}\right). \tag{C.2}$$

C.1 DPSK Signal Generation

Figure C.1 depicts all BER measurements performed for the direct modulated DPSK signal generation.

H. Schmeckebier, *Quantum-Dot-Based Semiconductor Optical Amplifiers for O-Band Optical Communication*, Springer Theses,
DOI 10.1007/978-3-319-44275-4

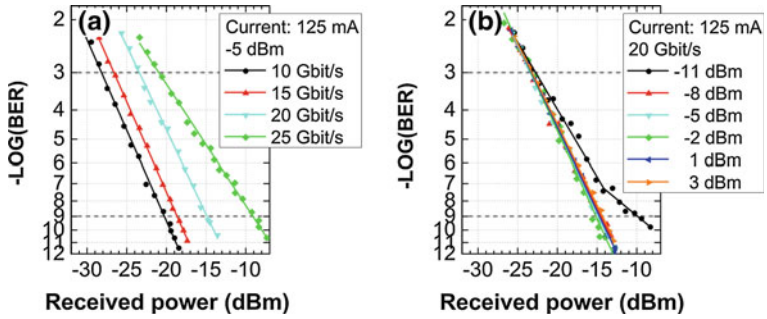

Fig. C.1 QD SOA direct modulated DPSK BER measurements versus receiver input power with **a** various data rates and fixed optical input power level of −5 dBm and **b** various optical input power levels and a fixed data rate of 20 Gb/s. The QD SOA DC current was in all cases 125 mA. All BER curves are linearly fitted, whereat the −11 dBm curve in **b** is stepwise fitted with 2 linear curves

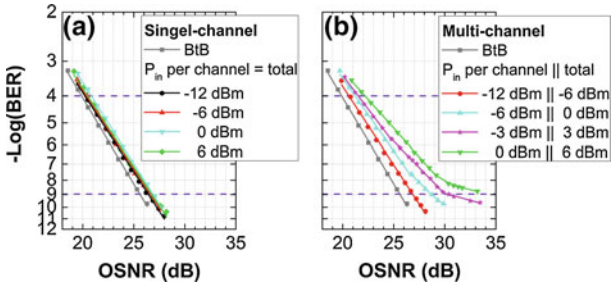

Fig. C.2 80 Gb/s BER measurements versus receiver input OSNR without (BtB) and with the QD SOA for various QD SOA input power levels **a** in the absence ("single-channel") and **b** in the presence ("multi-channel") of three interfering 40 Gb/s channels. The curves in (**a**) and (**b**) have equal symbols for equal per-channel input power levels and equal colors for equal total input power levels. The QD SOA drive current was 900 mA in both cases. The −6, −3 and 0 dBm BER curves in (**b**) are stepwise fitted with 2, 3 and 3 linear curves, respectively

C.2 OOK Amplification

Figure C.2 depicts all BER measurement performed for the multi-channel 80 Gb/s RZ OOK and 3-times 40 Gb/s NRZ OOK signal amplification.

C.3 D(Q)PSK Single-Channel Amplification

Figures C.3 and C.4 depict all BER measurements performed for the 40 GBd DPSK and DQPSK IPDR evaluation, respectively.

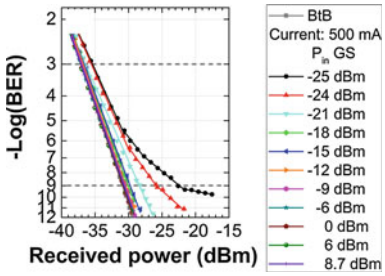

Fig. C.3 40 GBd DPSK BER measurements versus receiver input power without (BtB) and with the QD SOA for various QD SOA (P_{in}). All BER curves are linearly fitted

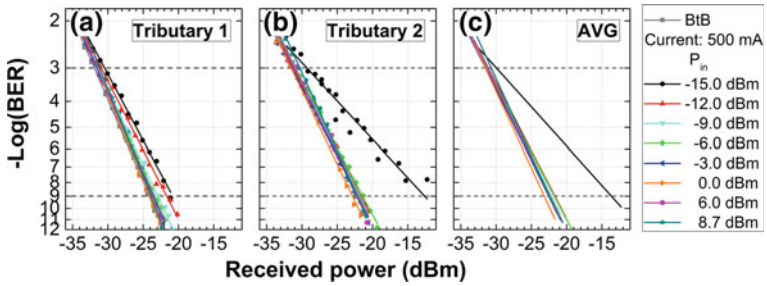

Fig. C.4 40 GBd DQPSK BER measurements versus receiver input power without (BtB) and with the QD SOA for various QD SOA input power (P_{in}) for **a** tributary 1 and **b** tributary 2. The −15.0 dBm curve for tributary 2 suffered from error-bursts which source could not been identified. All BER curves are linearly fitted. **c** Averaged BER over both tributary

C.4 D(Q)PSK Multi-Channel Amplification

Figures C.5 and C.6 depict all BER measurement performed for the multichannel 40 GBd DQPSK and 40 Gb/sOOK signal amplification.

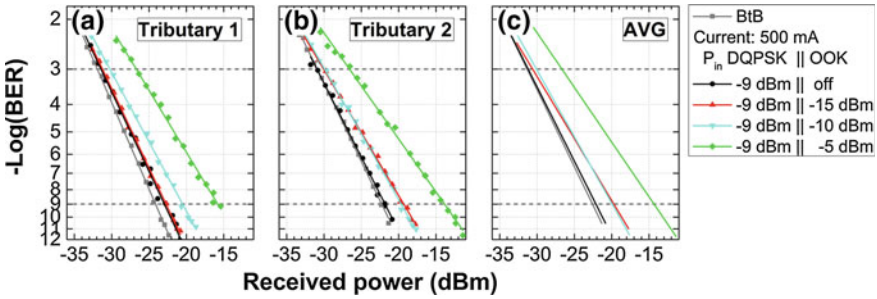

Fig. C.5 40 GBd DQPSK BER measurements versus receiver input power without (BtB) and with the QD SOA for a QD SOA input power (P_{in}) of −9 dBm and various interfering 40 Gb/s OOK QD SOA P_{in} for **a** tributary 1 and **b** tributary 2. All BER curves are linearly fitted. **c** Averaged BER over both tributary fits

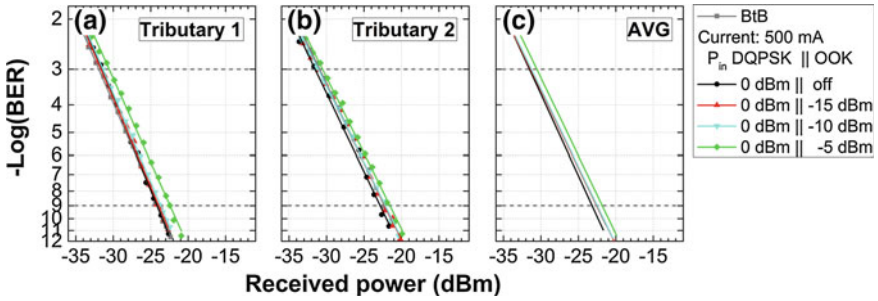

Fig. C.6 40 GBd DQPSK BER measurements versus receiver input power without (BtB) and with the QD SOA for a QD SOA input power (P_{in}) of 0 dBm and various interfering 40 Gb/s OOK QD SOA P_{in} for **a** tributary 1 and **b** tributary 2. All BER curves are linearly fitted. **c** Averaged BER over both tributary fits

C.5 Dual-Band Amplification

Figure C.7 depicts all BER measurements performed for the 40 Gb/s OOK GS signal evaluation with different combinations of current, GS input power levels and interfering ES input power levels.

Figure C.8 depicts all BER measurements performed for the 40 Gb/s OOK ES signal evaluation with different combinations of current, ES input power levels and interfering GS input power levels.

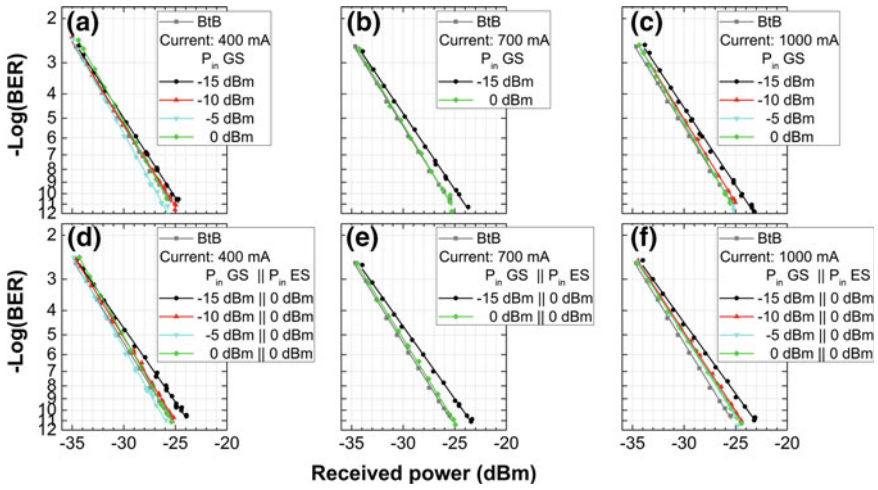

Fig. C.7 40 Gb/s OOK BER measurement versus receiver input power without (BtB) and with the QD SOA for currents of **a** and **d** 400 mA, **b** and **e** 700 mA and **c** and **f** 1000 mA, all with different GS input power levels "P_{in} GS". The *top row* (**a**–**c**) is measured in absence of the interfering ES signal. The *bottom row* (**d**–**f**) is measured for interfering ES input power levels "P_{in} ES" of 0 dBm

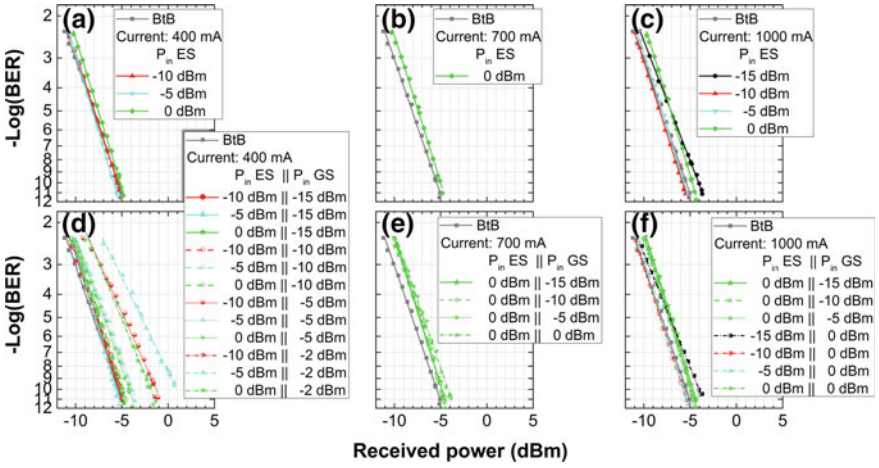

Fig. C.8 40 Gb/s OOK BER measurement versus receiver input power without (BtB) and with the QD SOA for currents of **a** and **d** 400 mA, **b** and **e** 700 mA and **c** and **f** 1000 mA, all with different ES input power levels "P_{in} ES". The *top row* (**a**–**c**) is measured in absence of the interfering GS signal. The *bottom row* (**d**–**f**) is measured for various interfering GS input power levels "P_{in} GS"

C.6 FWM-Based Wavelength Conversion

Figures C.9 and C.10 depict all BER measurements performed for the 40 GBd DPSK and DQPSK wavelength conversion in dual-pump configuration, respectively.

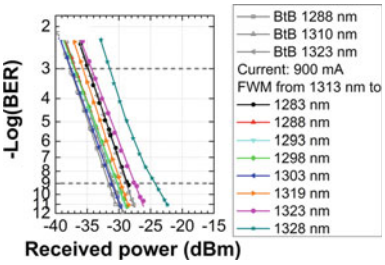

Fig. C.9 40 GBd DPSK BER measurements versus receiver input power without (BtB) and with the QD-SOA-based wavelength converter operated in dual-pump configuration. All BER curves are linearly fitted. The FWM converted curve 1328 nm is stepwise fitted with 3 linear curves

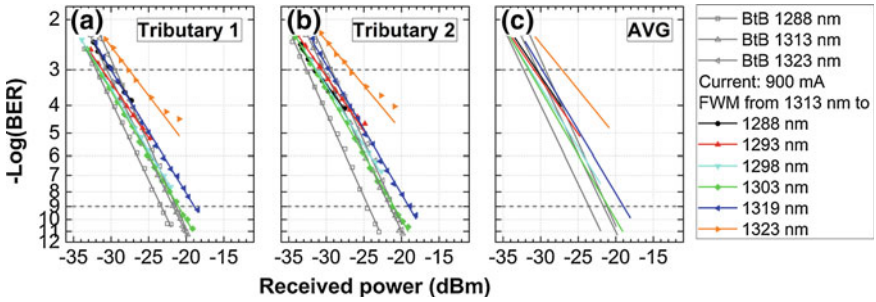

Fig. C.10 40 GBd DQPSK BER measurements versus receiver input power without (BtB) and with the QD-SOA-based wavelength converter operated in dual-pump configuration for **a** tributary 1 and **b** tributary 2. All BER curves are linearly fitted. **c** Averaged BER over both tributary